44th Journées des Actinides and 10th SPCA

Ein - Gedi - ISRAEL

Scientific Programme

Abstracts

List of participants

22-29/4/2014

SPCA10

22 April (Tuesday)

07:00-08:00	**Breakfast**
08:00-09:00	**Registration**
A – Physics I	*Arugot-hall*
09:00-09:35	**Itzhak Halevy** Opening and welcome to Israel
09:35-10:10	**Gerard Lander (INVITED)** Introduction to the physics of the condensed matter of the actinides
10:10-10:45	**Or Hen** Correlations in heavy nuclei
10:45-11:15	**Coffee break**
B – Chemistry I	*Arugot-hall*
11:15-11:50	**Norman Edelstein (INVITED)** The chemistry and electronic structure of Pa and its compounds
11:50-12:25	**Giora Kimmel** Symmetry and basics of X-ray diffraction
12:25-13:00	**Margarida Henriques** Synthesis of novel UC_x nanomaterials for online production of exotic isotope ion beams
13:00-14:00	**Lunch**
C – Physics II	*Arugot-hall*
14:00-14:35	**Amir Hen** X-Ray Magnetic Circular Dichroism and Mossbauer effect in Actinides
14:35-15:10	**Silvie Maskova (INVITED)** Basic concepts of hydrogenation
15:10-15:45	**Sharon May-Tal Beck/Or Hen** Positron annihilation as a scientific probe
15:45-16:10	**Coffee break**
D – Chemistry II and Physics III *Arugot-hall*	
16:15-16:50	**Zeev Karpas (INVITED)** Uranium in the nuclear fuel cycle
16:50-17:25	**Eyal Yahel** The shape of the melting curve and phase transitions in the liquid state
17:25-18:00	**Noah Shamir** Surface science in actinides
18:30-19:30	**Dinner** Reception SPCA10

23 April (Wednesday)

07:00-08:00	**Breakfast**
08:00-09:00	
E – Theory, electronic structure	*Arugot-hall*
09:00-09:35	**Nathan Argaman** Derivation of density functional theory from thermodynamics
09:35-10:10	**Silvie Maskova** Quantum criticality
10:10-10:45	**Silvie Maskova** Tuning physical properties in U-compounds by H: quantum criticality in $U_2(Ni,Fe)_2Sn$
10:45-11:15	**Coffee break**
F – Physics IV	*Arugot-hall*
11:15-11:50	**Gennady Rafailov** New ordered phase in the quasi-binary UAl_3-USi_3 system
11:50-12:25	**Chen Dubi** Passive neutron interrogation and neutron multiplicity counting
12:25-13:00	**Mykhaylo Paukov** Magnetism in hydrides of γ-uranium alloys
13:00-14:00	**Lunch**
G – Nuclear forensics I	*Arugot-hall*
14:00-14:35	**Yossi Almog** General police forensics
14:35-15:10	**Itzhak Halevy** What is nuclear forensics?
15:10-15:45	**Avi Sharon** Post blast nuclear forensics of a radiological dispersal device scene
15:45-16:10	**Coffee break**
H – Measuring systems I	*Arugot-hall*
16:15-16:50	**Vladimir Sechovsky** Facilities available for actinide research at Prague
16:50-17:25	**Gerard Lander** Research at big facilities on actinides: How neutrons and synchrotron x-rays can help our understanding
17:25-18:00	**Amir Hen** Mössbauer effect in Neptunium
18:00-18:30	**Ronit Kessel** Experimental constraints on processes in the Earth interior
18:45-19:45	**Dinner**
19:45-20:00	
20:00-20:40	**Gerard Lander** Discoveries that changed the world: 1932 – 1942: James Chadwick & Lise Meitner

24 April (Thursday)

07:00-08:00	**Breakfast**
08:00-09:00	
I – Measuring systems II, Physics V	*Arugot-hall*
09:00-09:35	**Antonio Pereira Gonçalves** Compounds, relations and properties in the U-Fe-Ge system
09:35-10:10	**Guy Makov** Atomistic studies of dislocation structure and motion
10:10-10:45	**Dan Berkovits (INVITED)** Soreq – Saraf
10:45-11:15	**Coffee break**
J – Nuclear forensics II	*Arugot-hall*
11:15-11:50	**Avi Sharon** A novel fireball analysis for an explosive aerosolization study
11:50-12:25	**Avi Sharon** Experiments and modeling the source term for RDD
12:25-13:00	**Itzhak Halevy/Shay Dadon** Micro-Copper radioactive survey demonstration
13:00-14:00	**Lunch**

JdA 44

24 April (Thursday)

13:00-14:00	**Lunch**
K – Reactors, nuclear fuel cycle, environment (Chairman: Itzhak Halevy)	*Arugot-hall*
14:00-14:20	**Halevy, Chorev, Danieli** Opening
14:20-14:40	**Chorev, Danieli** Opening Lecture
14:40-15:00	**Ksenia Lipkina** Metallic inert matrix fuel concept for minor actinides transmutation to achieve ultra-high burn-up
15:00-15:20	**Peri Landau** Effects of helium implantation on the mechanical behavior of 100nm-diameter iron nano-pillars
15:20-15:40	**Ilan Yaar** Prospects for a Future NPP in Israel
15:40-16:15	**Coffee break**
L – Theory, electronic structure (Chairman: Dariusz Kaczorowski)	*Arugot-hall*
16:15-16:35	**Alexander Shick** Non-magnetic ground state of PuO_2
16:35-17:55	**Nick Brincat** Ab initio investigation of the uranium-oxygen system
16:55-17:15	**Peter Oppeneer** Origin of the exceptional Ising behavior of quasiparticles in the hidden-order material URu_2Si_2
17:15-17:35	**Johann Bouchet** Vibrational properties of the light actinides
17:35-17:55	**Chen Dubi** Passive neutron interrogation in systems with poorly characterized detection efficiency
18:30-19:30	**Dinner** **Reception JdA44**

25 April (Friday)

07:00-08:00	**Breakfast**	
08:00-09:00		
	M1 – Inorganic, organometallic chemistry I (chairman: Israel Zilbermann) *Arugot-hall*	M2 – Materials Science I (chairman: Peter Oppeneer) *Hamichi-hall*
09:00-09:20	**Isabel-Sarah Karmel** Uranium(IV) imidazolin-2-iminato complexes: synthesis, structure and catalytic activity	**Gerard Lander** Experiments on thin films of uranium and UO_2 – an overview
09:20-09:40	**Philippe Raison** Coolant-fuel interaction in sodium-cooled fast reactors: structural investigations of the Na-An-O (An = U, Np, Pu) systems	**Mathieu Pasturel** XANES and RXES investigation of uranium aluminides
09:40-10:00	**Moris Eisen** New catalytic processes promoted by organoactinides	**Robert M. Harker** XRD, ellipsometry and Raman spectroscopy examination of uranium coupons exposed to low pressure of H_2 at ~ 80 °C
10:00-10:20	**Karsten Meyer (INVITED)** Uranium-Mediated Small Molecule Activation & a New Oxidation State in Uranium Chemistry	**Eric Colineau** Superconductivity: is there a problem in transuranics?
10:20-10:40		**Franz-Joseph Hambsch** Correlation of prompt fission neutron emission with fission fragment properties in ^{252}Cf(SF)
10:40-11:15	**Coffee break**	
	N – Chemistry II and Physics (chairman: Moris Eisen) *Arugot-hall*	
11:15-11:35	**Robert Baker (INVITED)** New reactivity of the uranyl ion	
11:35-11:55		
11:55-12:15	Israel ZILBERMANN Novel bi-metallic uranyl complexes - Redox chemistry in aqueous solutions	
12:15-12:35	**Roberto Caciuffo** Molecular nanomagnetism in actinide-based coordination complexes	
13:35-12:55	**Moshe Friedman** ^{235}U prompt fission neutron spectrum measurement via activation technique with DONA detector at SARAF	
13:00-14:00	**Lunch**	
14:00- dinner	Dead Sea tour	
18:30-19:30	**Dinner**	

26 April (Saturday)

07:00-08:00	**Breakfast**
08:00-09:00	
09:00-dinner	**Jerusalem tour** A Tour Day in Jerusalem 1. We will start our tour by viewing Old City of Jerusalem from the promenade of The Olive Mountain. 2. From there we will walk downhill and visit the Church of Gethsemane. 3. Then we will drive around the walls of the Old city. 4. We will enter Old City through Jaffa Gate. 5. Walking in the allies of Old City will include following sites: The Holy Sepulcher Church (The Holy Grave Church), the Muslim quarter and the Jewish quarter. 6. We will visit some archeological sites such as the Kardo and the Wailing Wall. 7. If we have enough time we will go to the Last Supper hall – the Cenaculum in Mount Zion. Orly Cabilly Licensed tour guide #8719 Phone 0507601096 Tel. +972-50-7601096 olycabilly@gmail.com www.orlycabilly.com
18:30-19:30	**Dinner**

Church of Gethsemane

Jaffa Gate

Holy Sepulcher Church

Kardo

Wailing Wall

Cenaculum

27 April (Sunday)

07:00-08:00	**Breakfast**	
08:00-08:40		
08:40-09:20	**Robert Troc, Gerard Lander, Jan Genossar, Ilana Kuznietz** In memorial of Dr. Moshe Kuznietz *Arugot-hall*	
	O1 – Materials Science II (In memorial of Dr. Moshe Kuznietz) (chairman: Robert Troc) *Arugot-hall*	O2 – Forensics (chairman: Israel Zilbermann) *Hamichi-hall*
09:25-09:45	**Evgeniya Tereshina** Exchange bias in UO_2/Py thin films	**Avi Sharon (INVITED)** High explosive RDD: time and distance multiscale study
09:45-10:05	**Anna Adamska** Growth and characterization of uranium-alloy thin films	**Avi Sharon (INVITED)** Fast multispectral radiometry for particles analysis
10:05-10:25	**Roman Gumeniuk** Crystal structure and physical properties of $(Th,U)_3Ir_4Ge_{13}$	**Gustavo Haquin** Nuclear forensics in Israel
10:25-10:45	**Eitan Tiferet/Itzhak Orion** New calculation method for electron inelastic mean free path in thin films: measurements and Monte Carlo transport	**Itzhak Halevy** Aerial survey, Aerial survey demonstration
10:45-11:15	**Coffee break**	
11:15-11:35	**Joe Gal, Gerard Lander** In memorial of Prof. Bernard R. Cooper *Arugot-hall*	
	P1 – Materials Science III (In memorial of Prof. Bernard R. Cooper) (chairman: Roberto Caciuffo) *Arugot-hall*	P2 – Large measuring systems (chairman: Itzhak Orion) *Hamichi-hall*
11:40-12:00	**Dariusz Kaczorowski** On the search for a Lifshitz point in UPd_2Si_2	**Amir Hen** Recent progress in the investigation of the electronic and magnetic properties of $NpNi_5$
12:00-12:20	**Denis Gorbunov** High pressure effects on the itinerant 5*f* ferromagnet U_2Fe_3Ge	**Sharon May-Tal Beck** Positron Annihilation as a probe for actinides research
12:20-12:40	**Aviva Melchior** Pressure induced amorphization of $La_{1/3}(Nb,Ta)O_3$	**Bent Pedersen** Detection of SNM by pulsed neutron interrogation
12:40-13:00	**Joe Gal** Melting curves under high pressure of some light actinide metals	**A. Ocherashvili** Fissile mass estimation by pulsed neutron source
13:00-14:00	**Lunch**	
	Q – Materials Science IV (In memorial of Prof. Oscar Vogt) (chairman: Joe Gal) *Arugot-hall*	
14:00-14:20	**Joe Gal, Gerard Lander** In memorial of Prof. Oscar Vogt	
14:20-14:40	**Antonio Pereira Gonçalves** Studies on the $UFeSb_2$ uranium antimonide	
14:40-15:00	**Tsachi Livneh** Correlating the effects of temperature and pressure on Raman scattering in uranium dioxide	
15:00-15:20	**Malgorzata Samsel-Czekala** Electronic structure of cage-like compound UFe_2Al_{10} – Theory and XPS experiment	
15:20-15:40	**Igor Izosimov** Multi-step excitation schemes in laser spectroscopy of actinides and lanthanides in solutions	
15:45-17:15	R – Botanical garden tour (chairman: Amir Hen)	
17:15-18:30		
18:30-19:30	Dinner	
19:30-21:30	S – Poster session (chairman: Silvie Maskova)	

28 April (Monday)

07:00-08:00	**Breakfast**
08:00-09:00	
T – Materials Science V *Arugot-hall* (chairman: Noah Shamir)	
09:00-09:20	**Robert Troc** Physical properties and XPS spectra of cage-like compound UB_{12}
09:20-09:40	**Eyal Yahel** Self-induced radiation damage in thin metallic films
09:40-10:00	**Fabrice Wilhelm** XMCD studies of ferromagnetic $AnFe_2$ Laves-phase systems
10:00-10:20	**Stanislav Melchakov** Separation factors of U and Pr or Nd in LiCl-KCl-CsCl melt – liquid gallium, indium or gallium-indium eutectic alloy system
10:20-10:40	**Alexander V. Andreev** Magnetic properties of a $U_3Cu_4Ge_4$ single crystal
10:40-11:15	**Coffee break**
U – Surface science *Arugot-hall* (chairman: Eyal Yahel)	
11:15-11:35	**Noah Shamir** The interaction of H_2O with strained uranium metal surfaces
11:35-11:55	**Noah Shamir** Inhibition of hydrogen chemisorption on uranium surfaces by traces of water vapor
11:55-12:15	**Thomas Gouder** Integrated surface science approach for study of spent fuel corrosion processes
12:15-12:35	**Danielle Schweke** Monitoring the in-situ oxide growth on uranium by UV-visible reflectance spectroscopy
12:35-12:55	**Shimon Zalkind** Amorphous carbon enhancement of hydrogen penetration into UO_2
13:00-14:00	**Lunch**
14:00-15:45	V – New perspective for actinide science, conference summary *Arugot-hall* (Chairman: Itzhak Halevy)
15:45-16:15	
16:15-18:00	W – Visiting Masada (Chairman: Itzhak Halevy)
18:00-19:00	
19:00-23:00	X – Conference dinner at Masada (Chairman: Itzhak Halevy)

Changes after Abstract book deadline

P2-1 Amir Hen
Recent progress in the investigation of the electronic and magnetic properties of NpNi5

Q4 Malgorzata Samsel-Czekala .....was N2
Electronic structure of cage-like compound UFe2Al10 – Theory and XPS experiment

N2 I. ZILBERMANN
Novel bi-metallic uranyl complexes - Redox chemistry in aqueous solutions

H4 Ronit Kessel
Experimental constraints on processes in the Earth interior

Posters 44th JdA

1. **Rami Batrice**

Selective Oli gomerisation and [2+2+2] Cy cloaddition of Term inalAlkynes from Sim ple Actinide Precatalysts

2. **Dmitry Maltsev, Vladimir Volkovich, EvgenyVladykin and Boris Vasin**

Electrochemistry of uranium in fused LiCl-KCl-CsCl eutectic

3. **Ioana-Carmen Popescu (Hoştuc), Petru Filip, Doina Humelnicu, Ionel Humelnicu,Thomas Bligh Scott and Richard Andrew Crane**

Chemical as pects of the interactions occurred in the aqueous sy stem U(VI)-zero valent iron nanoparticles - carboxy- methyl – cellulose-H_2O

4. **Andrey V.Shchetinskiy, Viktor A. Ivanov and Vladimir A. Volkovich**

Reaction of uranium dioxide with copper-containing chloride melts

5. **Avraham I Bram, Arie Venkert and Louisa Meshi**

Towards Prediction Of Crystal Structure Of Al-Rich Intermetallides Formed In Al-T-A Systems

6. **Anna Adamska**

Growth and characterization of uranium-alloy thin films

7. **Keith R Hallam and Michael Ling**

X-ray Diffraction Analysis of High-Purity Cerium-Lanthanum Alloys

8. **Antonios Banos, Camille Stitt and Tom Scott**

The influence of surface cleaning preparation on the initiation of uranium hydride sites

9. **Gennady Rafailov, Gili Shalev, Isaac Dahan and Louisa Meshi**

Study of the $U(Al,Si)_3$ vertex location in the 400 ºC isothermal section of the U-Al-Si phase diagram

10. **Gennady Rafailov, Asaf Uziel, Avner White, Itzhak Dahan, Louisa Meshi**

Towards construction of quasi-binary UAl_3-USi_3 phase diagram

11. **A.P. Gonçalves, M.S. Henriques and L. Havela**

Studies on the U-Fe-C ternary phase diagram

12. **Vladimir A. Volkovich, Dmitry Maltsev, Leonid F. Yamschikov, Alexander G. Osipenko and Mikhail V. Kormilitsyn**

Solubility of uranium in liquid gallium, indium and their alloys

13. **A. Savchenko**

Conceptual study of m ultiphase struc ture of high uranium de nsity alloy s to reduce che mical interaction

14. **A. Savchenko, M.Skupov, A.Vatulin, A.Glushenkov, G.Kulakov and K.Lipkina**

Fuel Cycle Concept with Advanced METMET and Composite Fuel in LWRs

15. **Oleksandr Bednarchuk, Mathieu Pasturel and Dariusz Kaczorowski**

Thermodynamic and transport properties of $U_3Cu_4Si_4$ and $U_3Cu_4Ge_4$

16. **Filanovich A.N., Povzner A.A and Nogovitsyna T.A.**
A self-consistent thermodynamic modeling of thermal and elastic properties of $PuCoGa_5$ and $PuRhGa_5$

17. **Pablo Maldonado, Lena Zetterström Evins and Peter M. Oppeneer**
Ab initio amomistic thermodynamics of water reacting with UO_2 surfaces

18. **Amir Hen**
Progress in the magnetic study of Np_2Co_{17}

19. **A. Hen, E. Colineau, R. Eloirdi, J.-C. Griveau, I. Halevy, I. Orion, J.-P. Sanchez and R. Caciuffo**
Structural, electronic and magnetic properties of $NpNi_5$ see P2-1

20. **A. Hen, L. Martel, Y. Tokunaga, E. Colineau, J.-C. Griveau, and R. Caciuffo**
Mössbauer and NMR spectroscopy of $U_{0.15}Np_{0.85}O_2$

21. **Volkov A.G., Oskina V.A. and Povzner A.A.**
Superconductivity of strongly correlated 5f- electron systems with a magnetic instability (on example of americium)

22. **Povzner A. A., Volkov A. G. and Golubeva L. R.**
Magnetic susceptibility and features of electronic structure of $PuRhGa_5$

23. **M. Vališka, J. Pospíšil and V. Sechovský**
Evolution of the ferromagnetism in UCoGe induced by Ru doping

24. **Arno Hiess**
New scientific possibilities provided by the ESS for neutron scattering experiments on actinide-based compounds

25. **I. Halevy** see O2-4
Israeli arial radiation survey system

26. **I. Halevy, M. Ghelman, Y. Yehuda-Zada, A. Manor, A. Sharon and I. Yaar**
Radioactive contamination estimation from micro-copters or helicopter airborne survey : simulation and real measurements see J3

27. **Eitan Tiferet, Alon Givon and Itzhak Orion**
Electron transport in solids – inelastic mean free path measurements in the 5 to 15 keV energy range

28. **A. Shor, D. Berkovits, Y. Eisen, G. Feinberg, A. J. M. Plompen, G.Giorginis, M. Hult, A. Krása, M. Friedman, D. Cohen, M. Paul and M. Tessler**
Towards measurement of the $^{209}Bi(n,\gamma)^{210m,g}Bi$ cross sections at SARAF

29. **M. Paukov, I. Tkach, Z. Matěj, L. Havela**
Magnetism in hydrides of Gama-Uranium alloys. see F3

30. **M.S. Henriques, A. Cruz, J. Marçalo, T. Stora, L. Havela, Z. Weishauptová, A.P. Gonçalves**
Synthesis of novel UCx nanomaterials for online production of exotic isotope ion beams see B3

Opening and welcome to Israel
For the 10th SPCA

Itzhak Halevy

In the opening Session for the 10th SPCA the program of the school will be presented.

The sessions of the 10th SPCA are:

- Physics
- Chemistry
- Theory, electronic structure
- Nuclear forensics
- Measuring systems

While the 10th SPCA lectures on crystallography, Physics, Chemistry and basics of actinides research.

Special lecture will be given in the evening of the second day by Gerard Lander

"Discoveries that changed the world: 1932 – 1942: James Chadwick & Lise Meitner"

This 10th SPCA will be an introduction to Actinides research and will be followed by the 44th Journées des Actinides.

The reception for the 10th SPCA will take place on the balcony of lecture Hall "Amichi", with music, wine and more…., everything on the background of the pastoral mountains of Judea desert and Dead Sea.

Introduction to the physics of the condensed matter of the actinides

G. H. Lander[1]

[1]*European Commission, JRC, Institute for Transuranium Elements, D-76125 Karlsruhe, Germany and Institut Laue Langevin, Grenoble, France*
e-mail: lander@ill.fr

The actinides were essentially “born” in the fiery birth of the Manhattan Project in the 1940s. All elements beyond U were discovered in that program and its aftermath. At the end of WWII there was a huge legacy of properties of these materials that were not understood at all. Without the crash program of the war, the number of people working on the fundamental problems reduced. Progress was slow on what has turned out to be one of the most complex series of elements in the periodic table. On Pu metal, for example, it has taken us 50 years to even understand the absence of magnetism in this complex element.

This talk will describe some of these problems that confronted the early researchers, and the progress that has been made. Today, the problems are different, but many of the same features – especially the duality of the 5*f* states – are strikingly reminiscent of those early challenges.

Now we have new tools to study these materials and – perhaps even more significantly – we have theory that may soon be able to make meaningful predictions for new actinide materials.

Proton-neutron correlations in medium and heavy asymmetric nuclei

Or Chen

Hebrew University of Jerusalem

The high momentum tail (p>KF) of the nuclear wave function is one of its most intriguing, though elusive, parts.
Experiments conducted over the last decade have shown that in symmetric nuclei such as12C, the high momentum tail (p>KF) of the nuclear momentum distribution is dominated by nucleons belonging to Short Range Correlated (SRC) pairs and that these pairs are primarily proton-neutron (pn) pairs.
In this talk I will present new measurements of short-range correlations in medium and heavy asymmetric nuclei using the A(e,e'p) and A(e,e'pp) reactions on C, Al, Fe, and Pb conducted at Jefferson Lab. From these measurements we extracted the number of proton-proton (pp) pairs in nuclei relative to C and the number of pn pairs relative to pp pairs. The number of pp pairs increases much more slowly than simple combinatorics, evidence that pp pairing is highly selective. Neutron-proton correlated pairs dominate over pp pairs, even in heavy asymmetric nuclei where the existence of a large number of nuclear shells allow for non-trivial pairing of pairs from different shells.

The chemistry and electronic structure of Pa and its compounds

Norman M. Edelstein

Chemical Sciences Division, MS70A-1150, Lawrence Berkeley National Laboratory, 1 Cyclotron Road,Berkeley, CA 94720, USA
e-mail: nmedelstein@lbl.gov

Protactinium, element 91, is one of the least studied of the actinide elements that is available on the mg to gram scale. The reason is the difficulty in handling due to the daughter activities from itsmajor isotope ^{231}Pa, which has a half-life of 32,760 y. From the point of view of its electronic configuration in the tetravalent state (Pa^{4+}), where it has one 5f electron in its ground configuration, it is one of the simplest to analyze. In addition the excited $6d^1$ configuration is low-lying; for Pa^{4+} diluted in the crystalline host Cs_2ZrCl_6, this configuration begins around 20,000 cm^{-1} [1,2].

In this talk the known chemistry of Pa^{5+} will be briefly outlined. The spectral and magnetic properties of Pa^{4+} diluted in Cs_2ZrCl_6 will be reviewed. A method will be outlined for producing $PaCl_5$ which is readily soluble in common organic solvents. From these solutions, Pa^{4+}compounds can be readily obtained and characterized [3].

A few molecular compounds of Th^{3+} are known with a $6d^1$ ground configuration, and of course many molecular compounds of U^{3+} have been characterized with a $5f^3$ ground configuration. To date, no known compounds of Pa^{3+} have been characterized. Furthermore, it is not certain what the ground electronic configuration of a Pa^{3+} compound would be. It will certainly be a configuration containing two unpaired electrons, and could be either $5f^2$ or $5f^16d^1$.

References

[1] D. Piehler, et al.,*J. Chem. Phys.***94**, 942 (1991).
[2] N. M. Edelstein, et al.,*J. Chem. Phys.*, **96**, 1 (1992).
[3] W. K. Kot, et al., *New J. Chem.*, **19**, 641 (1995).

Symmetry and Basic X-Ray Diffraction

Giora Kimmel

Ben-Gurion University of the Negev

The talk will deal with the elements of crystallography, x-ray scattering, diffraction, kinematic theory, correlation between crystal structure and diffraction patterns, absorption, characterization of real crystals, problems in x-ray diffraction of actinides, examples.

Synthesis of novel UC_x nanomaterials for online production of exotic isotope ion beams

M.S. Henriques,[1] A. Cruz[1], J. Marçalo[1], T. Stora[2], L. Havela[3], Z. Weishauptová[4], A.P. Gonçalves[1]

[1] *Nuclear and Technological Campus-IST, University of Lisbon, 2695-066 Bobadela, Portugal*
e-mail: mish@ctn.ist.utl.pt
[2] *ISOLDE-CERN, CH-1211 Geneva 23, Switzerland*
[3] *Dept. Condensed Matter Physics, Faculty of Mathematics and Physics, Charles University, 121 16 Prague, Czech Republic*
[4] *Institute of Rock Structure and Mechanics, ASCR, V Holešovičkách 41, 182 09 Prague, Czech Republic*

Radioactive ion beams (RIBs) provide unique opportunities to study nuclear, atomic, surface and solid-state physics, astrophysics, nuclear forensics, medicine, and biology. The isotope separation online (ISOL) method is used at ISOLDE - CERN [1] to create RIBs through the bombardment of thick high-temperature targets by an accelerated primary proton beam. As a result, radionuclides are generated in the target material via induced spallation, fragmentation and fission nuclear reactions. Once produced, the isotopes must first diffuse from the interior of the target to the surface and then evaporate from it, followed by ionization, acceleration, mass separation and further beam manipulation until delivered at the final user. From the experimental point of view, high intensity RIBs can be obtained by increasing the overall efficiencies, high isotope diffusion and short delay times, or by increasing the power of the primary beam. Minimum delay times can be achieved in targets with highly-permeable, low-density, open-structures operating at high temperatures. However, increased driver beam intensity might carry serious concerns for the target as thermal loads, radiation damage, or physical integrity under irradiation. Thus to find the ideal material for a thick target is a tremendous technological challenge for the ISOL technique. Nearly five decades after the first irradiation tests, micrometric uranium carbide-based materials are still the reference materials for radioactive ion-beam production. Nevertheless, it was recently proved that a significant increase of the release and yields of exotic isotopes can be obtained on submicron and nanostructured porous materials [2]. The objective of this study is to produce submicron structured carbides of U to be tested as target materials at ISOLDE.

For this purpose, three different approaches were tested: (1) solid - gas reaction between U metal and CH_4, (2) electrospinning of precursor solutions containing U salts (Fig. 1), and (3) mechanical alloying in liquid medium of pre-alloyed uranium carbide.

In the path (1), U sub-micron powders were prepared by hydrogen decrepitation: UH_3 was first prepared by reaction of U with H_2, followed by its decomposition at 250ºC under vacuum. The UC_x nanopowders were then prepared by the reaction of the uranium powders with CH_4 at 700ºC, with a crystallite size in the range 20 – 30 nm, but upon heat treatment they are very reactive with oxygen, and a mixture of UC + UO_2 forms readily.

In the approach (2), an exploratory work was first made with lanthanides and then extended to U. Acetate salts and/or acetylacetonate were synthesized for the different metals (M = Eu, Er, Yb and U) and mixed with cellulose acetate. The solutions were then electrospun in different conditions. The dried electrospun materials were subsequently heat-treated at temperatures from 800 to 1550ºC in a flowing argon atmosphere. Scanning electron microscopy observations show that for the same M/C = 4 ratio the spinnability of the solutions is dissimilar for each M and changes for the different salts of the same element. For 4f metals, micrometric fibers are well formed for the Er case, while for Eu the fibers are nanometric and exhibited many and large beads. For Yb no fibers are formed. In the case of U, the formation of nanometric fibers was only achieved for the acetylacetonate solutions (Fig. 1). The heat treatment of the electrospun materials lead to the material densification and to the formation of highly porous samples, with an open porosity and large distribution of pore sizes. CO_2 adsorption isotherms have shown that the Er sample treated at 800ºC has a

surface area of 527 m^2/g. X-ray diffraction indicated the formation of MC_2 or MC for all studied samples, with estimated average crystallite sizes of 13, 10 and <10 nm for ErC_2, EuC_2 and YbC_2, respectively. For U carbides, the starting crystallite size is <10 nm for the acetate salt and 28 nm for the acetylacetonate solution, increasing with annealing temperature up to 66 nm for the maximum temperature tested (1550ºC).
In the method (3), after an exploratory trial with Y and graphite, a powdered pre-alloyed UC was mixed with excess of graphite together with an organic solvent. The mixture was then inserted in a WC carbide crucible containing WC carbide balls in a ratio 1/18 and milled in a planetary ball-mill. The evolution of the milling procedure was followed by X-ray diffraction analysis at regular intervals of time.
The results have shown that nanostructured UC_x materials can be successfully produced by all the techniques. Yet electrospinning is the most versatile method to tune the desired surface-interface features for these materials. However, serious drawbacks are the low yields, the complicated production of precursors and polymeric solutions. Batches of some of these materials are now under preparation for in-situ proton irradiation.

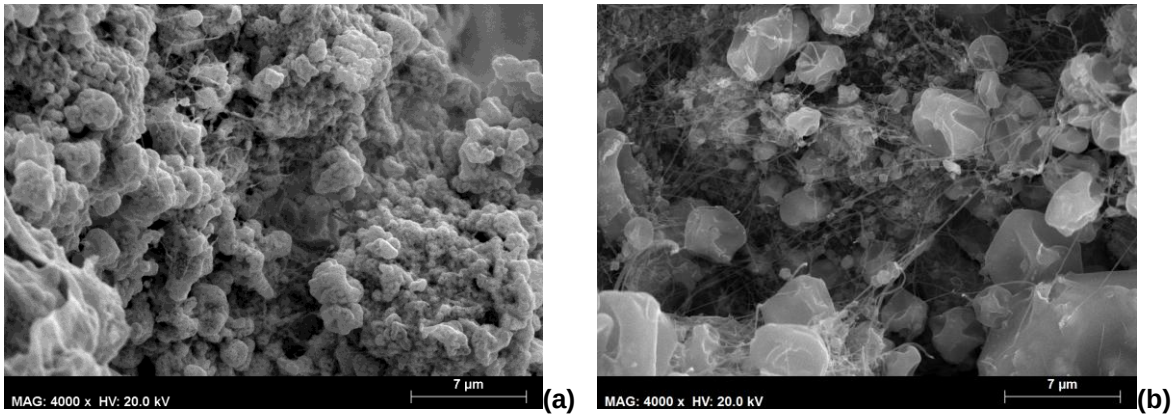

Fig. 1. Scanning electron microscopy images of a U precursor solution produced by electrospinning, showing the formation of nanofibers: as electrospun (a) and after heat treatment (b).

References

[1] A. Herlert, *Nuclear Phys. News* **20**, 4 (2010).
[2] T. Stora, *Nucl. Instr. Meth. B* **317**, 402 (2013).

Acknowledgements: This work was carried within the financial support of FCT, Portugal, through the project CERN/FP/123588/2011 and the grant SFRH/BD/66161/2009 (MSH).

X-Ray Magnetic Circular Dichroism and Mossbauer effect in Actinides

A. Hen,[1,2]

[1]*European Commission, Joint Research Centre, Institute for Transuranium Elements, Postfach 2340, D-76125 Karlsruhe, Germany*
[2]*Nuclear Engineering Department, Ben Gurion University, IL84105 Beer-Sheva, Israel*
E-mail: amir.hen@mail.huji.ac.il

X-ray magnetic circular dichroism (XMCD) has the exceptional property of being able to discern between the contributions to the total magnetization of the different elements of a complex sample. This magnetic characterization tool is considered as the best suitable technique to probe the orbital and spin magnetism and to isolate those different contributions separately. XMCD is not only an element but also a shell-specific probe involving the excitation of core-level electrons to unoccupied states of symmetry defined by dipole selection rules for optical transitions. For a magnetic material, XMCD is the difference between the absorption of left and right circularly polarized X-rays. This difference can be correlated to the magnetic moment of the atoms involved in the absorption process using magneto-optical sum-rules under given assumptions regarding the magnetic dipole contribution.

The interaction between polarized light and the charge and current distributions in materials have been known since the Faraday (1845), Kerr (1875) and Voigt (1902) effects were discovered. The extension of these techniques to the X-ray energy range was much more recent. De Bergevin and Brunel (1972) used a conventional X-ray source for the first X-ray magnetic diffraction measurements [1]; Erskine and Stern (1975) predicted that a magneto-optical effect should occur in polarized XAS on the $L_{2,3}$ edge of nickel [2]. Thole et al. (1985) predicted much larger effects on the line shape of the $M_{4,5}$ absorption edges of a rare-earth ion whose ground state is split by an external magnetic field, the line shape depends on the relative orientation between the magnetization direction and the polarization vector of the X-rays [3]. The first X- ray dichroism experiment was performed by Van der Laan et al. [4] on terbium iron garnets by using linearly polarized light. Schütz et al. [5] performed the first experiments with circularly polarized X-rays were they found a small circular dichroism signal (~ 0.1% of the total signal) at the Fe K edge. Chen et al. (1990) have found much more significant effect (as large as 20%) while measuring XMCD at the $L_{2,3}$ edges of Ni [6], Co, and Fe [7], due to the fact that transitions at these edges take place directly to the empty 3d states, which are strongly polarized. Meanwhile Thole et al. [8] and Carra et al. [9] established sum-rules that allow one to separately determine orbital and spin contributions of these states to the total magnetic moment carried by the absorbing atom by using the integrated intensities of the XMCD and of the total absorption spectra. XMCD experiments have been reported for a great number of uranium compounds [10] Np and Pu ferromagnetic Laves phases [11] and intermetallic Np compound [12].

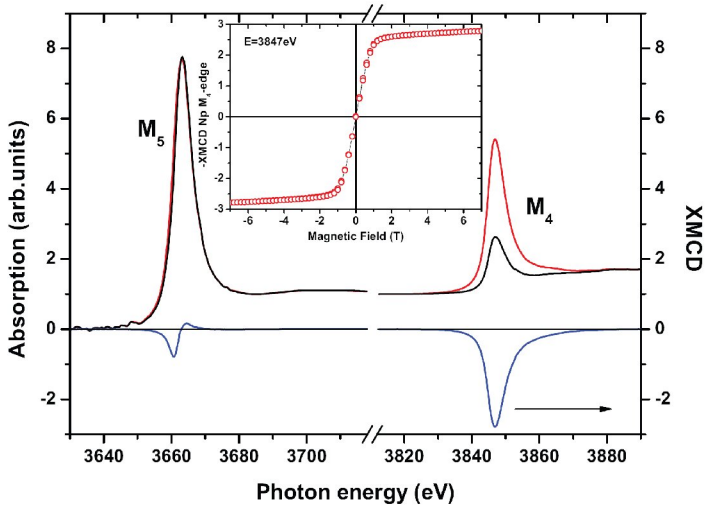

Fig. 1: X-Ray absorption spectra μ^+ (red line), μ^- (black line) measured at 50 K and H_{ext} = 7 T at the Np $M_{4,5}$ absorption edges;
The XMCD signal (Blue line) is given by $\mu^+ - \mu^-$, the inset shows the field dependence of the XMCD signal at the Np M_4 edge.

Mössbauer effect is yet another unique experimental technique that is elemental specific, however while the X-rays used in XMCD are interacting with the electrons of the probed samples, the Mössbauer effect is measured by recording the recoil free resonance absorption of gamma rays radiation by a specific nucleus within the probed sample.

Discovered by Rudolf Mossbauer (1929-2011) in 1958 (Nobel prize in 1961) the effect and the spectroscopy based on it became a unique and powerful tool not only in fundamental physics research but also in chemistry and even biology. The high resolution in energy of the Mössbauer spectroscopy can be derived from the lifetime uncertainty of the excited state of the source nuclei (about ~10^{-8}eV). Such high resolution allows one to resolve the so called hyperfine energy-splitting of the nucleus caused by electronic and magnetic fields and gain insight on the electric monopole interactions (isomer/chemical shift), the electric quadrupole interaction (Stark splitting) and magnetic dipole interaction (hyperfine field B_{hf}). The measuring of these interactions gives an insight on the chemical environment, electrical and magnetic properties of the probed ion.

The Mössbauer effect has been observed in more than 40 elements, most popular among them are ^{57}Fe and ^{119}Sn. In actinides, the Mössbauer effect was observed and measured for all the light actinides (Th-Am). However, only ^{237}Np is a suitable Mössbauer element for a systematic and feasible research [13]. The 60 keV electric dipole (E1) Mössbauer resonance of the ^{237}Np nucleus is a unique microscopic tool among the actinides for gaining information on the electronic and magnetic properties of Np systems [14].

In this communication it will be shown how synchrotron radiation XMCD technique, developed in the last years exploit the high brilliance, tunable polarization and energy available to probe element and shell specific magnetization in magnetic samples along side with the basics of Mössbauer effect and principles of Mössbauer spectroscopy in actinides with focus on ^{237}Np compounds and demonstrate how the two techniques could complement each other [12].

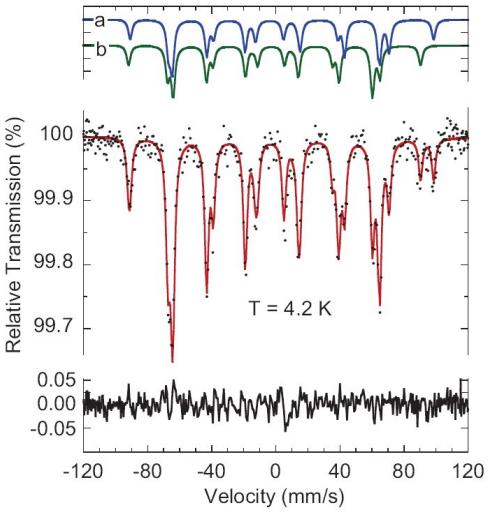

Fig. 2: ^{237}Np Mössbauer spectrum measured at 4.2K the spectrum is composed of two split sub-spectra indicating two slightly different Np crystallographic sites and the presence of magnetic hyperfine field.

References

[1] F. de Bergevin and M. Brunel, *Phys. Lett.* A **39**, 141 (1972) 159, 161
[2] J. L. Erskine and E.A. Stern, *Phys. Rev. B* **12**, 5016 (1975) 159, 163
[3] B. T. Thole et al., *Phys. Rev. Lett.* **55**, 2086 (1985) 159, 163
[4] G. van der Laan et al., *Phys. Rev. B* **34**, 6529 (1986) 159, 163
[5] G. Schütz et al., *Phys. Rev. Lett.* **58**, 737 (1987) 163
[6] C. T. Chen et al., *Phys. Rev.* B **42**, 7262 (1990) 163
[7] F. Sette et al., *AIP Conf. Proc.* **215**, 787 (1990) 163
[8] B. T. Thole et al., *Phys. Rev. Lett.* **68**, 1943(1992)
[9] P. Carra et al., *Phys. Rev. Lett.* **70**, 694 (1993) 165
[10] V. N. Antonov et al., *Phys. Rev. B* **68**, 214424 (2003); *ibid* 214425, A. N. Yaresko et al., *Phys. Rev. B* **68**, 214426 (2003).
[11] F. Wilhelm et al., *Phys. Rev. B* **88**, 024424 (2013).
[12] I. Halevy, A. Hen et al., *Phys. Rev. B* **85**, 014434 (2012).
[13] B. D. Dunlap and G. M. Kalvius, in Handbook on the Physics and Chemistry of the Actinides, edited by A. J. Freeman and G. H. Lander (North-Holland, Amsterdam, 1985), Vol. 2
[14] J. P. Sanchez et al., *J. Alloys Compd.* 275, 154 (1998).

Basic concepts of hydrogenation

S. Mašková

Department of Condensed Matter Physics, Charles University, Ke Karlovu 5, 12116 Prague 2, The Czech Republic, e-mail: maskova@mag.mff.cuni.cz

The sensitivity of the interactions in the *f*-electron systems to modification of the crystal structure makes the experimental techniques involving alternation of the atomic arrangement especially important. Various studies under hydrostatic or uniaxial compression are well-known examples of such methods. From this point of view hydrogenation can be treated as a complementary technique that provides „negative“ pressure. In the narrowest sense, the term hydride is used just in cases when metal lattice is changed upon hydrogen absorption. However we will use this term in wider sense. We will define hydrides as compounds for which the hydrogen absorption leads to the modifications of the crystal structure, such as pure lattice expansion or the formation of a new structure. Hydrogen absorption can be used to modify magnetic properties of the intermetallics. After interstitial hydrogen doping the crystal lattice can be several percent larger than before hydrogenation.
Hydrogenation of U compounds often leads to dramatic variations both in size and stability of magnetic moments and their interactions. Doping by hydrogen, which occupies interstitial positions, leads to a unit-cell expansion in some cases exceeding 10%. This affects the U–U spacing considered to be the most critical parameter tuning magnetic properties in U intermetallics. Therefore the H absorption can be used to tune magnetic properties. E.g. in the case of U_2Co_2In which exhibits no magnetic ordering and the susceptibility curve is almost temperature independent, the hydrogenation leads to the enhancement of magnetic interactions in the hydride. $U_2Co_2InH_{1.9}$ was found to be an antiferromagnet with T_N = 2.4 K. The possibility to tune magnetic properties is also manifested during hydrogenation of U_2Co_2Sn which is a paramagnet. Magnetic susceptibility curve for α-$U_2Co_2SnH_x$ (small amount of hydrogen) shows that it orders ferromagnetically around 33 K with a very small detected moment. Further increment of absorbed hydrogen leads to antiferromagnetic order in $U_2Co_2SnH_{1.4}$ [1].

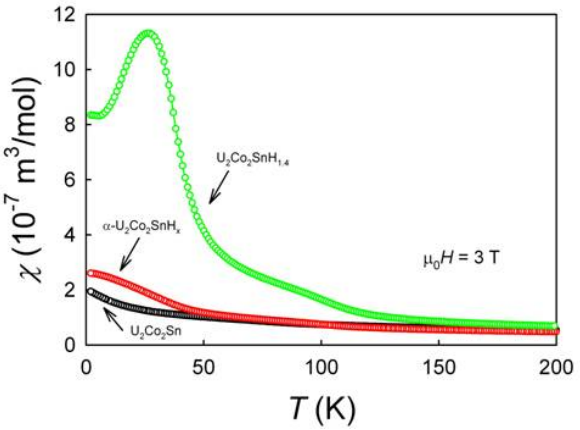

Figure 1. Magnetic susceptibility of U2Co2Sn compared with its hydrides.

In order to make a prediction whether particular material would form a hydride it is necessary to take into account various conditions: geometry of the atomic arrangement in the unit cell, electronic factors, diffusive kinetics, surface properties, etc. One of the possible approaches [2] is based on the comparison of the contributions to the formation energy of the hydride. The first contribution is the energy to convert the crystal structure of the parent compound to the crystal structure formed in the hydride. A second contribution, which for some materials is dominant, is the loss of cohesive energy when the structure is expanded to form a hydride. This expansion lowers the cohesive energy. The final contribution to the hydride formation

energy is the chemical bonding between the hydrogen and other elements in the compound. This is the only contribution which is negative and hence favorable to hydride formation. These contributions are relatively high competing with each other. The more negative the total enthalpy of hydride formation is, the more probable the hydrogenation is. These calculations are not easy for systems more complicated than pure metal hydrides. Easier predictions can be made when examining the crystal structure of the parent compound. Some geometrical criteria have to be fulfilled to make the hydride formation possible. Geometrical requirements include sufficient size for the interstitial positions and their arrangement in space.

1. Westlake's criterion states that available interstitial sites must have a spherical volume with the radius ≥ 40 pm [3-7].
2. The minimum H-H distance should be 210 pm.
3. According to the "Shoemaker's exclusion rule" two tetrahedra sharing the same face cannot be occupied simultaneously [8-10].

Some of the sites that do not satisfy these criteria in the parent compound may become suitable for filling with hydrogen due to the lattice expansion after the first stage of the hydrogenation. Despite the simplicity of these criteria they are very useful as the first estimate of hydrogen absorption possibility. However one should keep in mind that there are always some exceptions from these rules due to the fact that the stability of the hydride is determined by many factors and none of them predominates in all cases.

This work was supported by the Grant Agency of the Czech Republic under the grant No. 204/12/0285.

References

[1] K. Miliyanchuk et al., *Phys.* B **359–361**, 1042 (2005).
[2] H. Smithson et al., *Phys. Rev.* B **66** 144107 (2002).
[3] D.G. Westlake, *J. Less-Common Met.* **75** (1980) 177.
[4] D.G. Westlake, *J. Less-Common Met.* **90** (1983) 251.
[5] D.G. Westlake, *J. Less-Common Met.* **91** (1983) 1.
[6] D.G. Westlake, *J. Less-Common Met.* **91** (1983) 275.
[7] C.E. Lundin et al., *J. Less-Common Met.* **56** (1977) 19.
[8] B. Hjörvarsson et al., *J. Phys.: Cond. Mater* **11** (1999) L119.
[9] D.P. Shoemaker and C.B. Shoemaker, *J. Less-Common Met.* **68** (1979) 43.
[10] X.W. Wang and C.F. Chen, *Phys. Rev. B* **56** (1997) R7049.

Materials research using Positron Annihilation Spectroscopy (PAS)

Sharon May-Tal Beck,[1] D Cohen[2], O Hen[3], J Dumas[2], A Ocherashvili[1], E Piasetzky[3], N Pilip[3], G Ron[2], I Sabo-Napadensky[4] and R Weiss-Babai[4]

[1] *Physics department, NRCN, P.O.Box 9001, Beer-Sheva , 84190, Israel*
e-mail: smtbeck@gmail.com
[2] *Racah Institute of Physics, Hebrew University of Jerusalem, Jerusalem, 91904, Israel*
[3] *School of Physics and Astronomy, Tel-Aviv University, Tel-Aviv, 69978, Israel*
[4] *Soreq NRC, Yavne, 81800, Israel*

Positron Annihilation Spectroscopy (PAS) is a well-established method used in the fields of condensed matter physics, nuclear physics, chemistry, materials science and materials engineering [1]. In PAS, positrons are typically injected into the bulk of a material where they rapidly thermalize and are likely to be trapped in neutral or negatively charged crystallographic defects. After a time interval that can vary from ~100ps to few ns, depending on the material's type and its defects, the positrons annihilate with that material electrons, each such process results in the emission of two almost back to back photons carrying each approximately 511 keV. Due to momentum and energy conservation, the momentum distribution of the annihilating electrons reflects in angular distribution around the 180° between the two emitted photons (ACAR – Angular Correlation of Annihilation Radiation) and in the broadening of their energy distribution (DB – Doppler broadening). The electron density in the positron proximity before annihilation defines the lifetime of positron in the material [2], with measurable differences between mean lifetimes in the bulk region and in defect traps.
The relatively high energy photons emitted from annihilation events penetrate the material under study, allowing non-destructive measurements.
The distinguishable differences between the electron characteristics at point defects as opposed to the undamaged bulk region, and the high affinity of positrons to the defects, make them useful as a probe for point defects, the smallest of which are single atoms vacant from their lattice sites (mono-vacancies), down to very low concentrations, of ~10^{-6} a^{-1} and up [3]. Comparison to sensitivity regions of other research methods is shown in Fig. 1, taken from [4]. The very good resolution of ACAR measurements allow detailed exploration of Fermi surfaces in single-crystal materials.

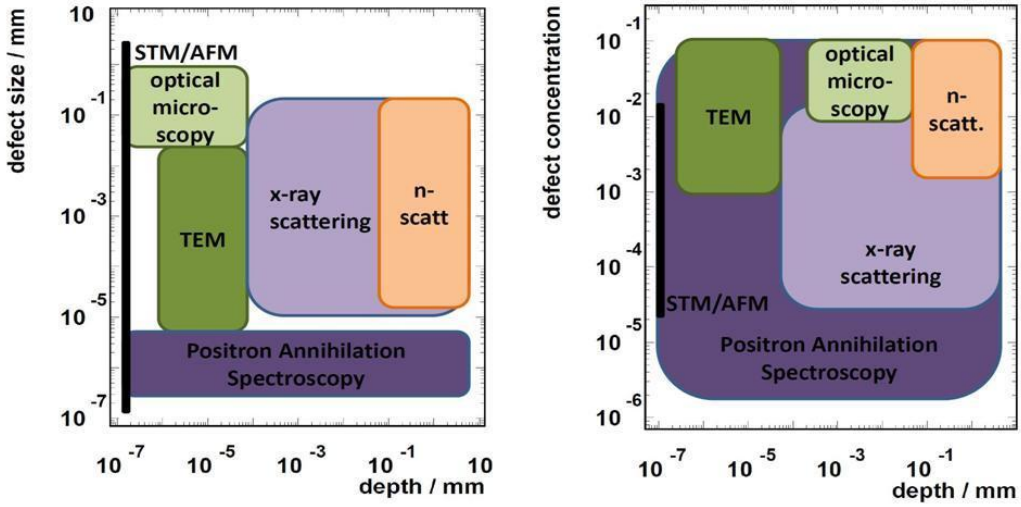

Fig. 1 Sensitivity regions accessible to various standard techniques: optical microscopy, neutron scattering (n-scatt), transmission electron microscopy (TEM), scanning tunnelling microscopy (STM) / atomic force microscopy (AFM), x-ray scattering, and positron annihilation.

The two most common PAS measurement systems are based on table-top gamma spectrometers, and slow positron beams. In table top measurements, positrons from a ^{22}Na

source (mean energy ~200 keV) [5] probe materials to depths of hundreds of microns, giving integrative information on their interior. In slow positron beams the source positrons are moderated, low energy positrons are selected and accelerated to create a mono-energetic beam with energy varying from tens of eV to ~25-50 keV. It is possible to scan the material from its surface to a depth of few microns and profile damage or thin layer characteristics [6].

The positron group at NRCN has built a table-top positron lifetime spectrometer [7], which with a unique data analysis method gets to a state of the art time resolution, of ~140ps. An Israeli collaboration, including researches, students and technicians from the Hebrew University, Tel-Aviv University, NRCN and Soreq NRC, is currently building the first slow positron beam in Israel [8]. The beam will be the center of the newly formed **S**low **PO**sitron facili**T**y (SPOT) at the Hebrew University. This beam, together with the PAL spectrometer of NRCN, will bring new material research capabilities to the Israeli community. The SPOT positron beam will serve as a tool for both fundamental and industry-oriented applied materials research.

PAS measuring methods and their applications will be discussed in more detail and the positron beam design concepts and challenges will be described.

References

[1] A. Dupasquier, A.P. Mills, Jr . (Eds.), *Positron Spectroscopy of Solids*, IOS, Amsterdam, (1995).
[2] M. J. Puska et al*. Journal of Physics F: Metal Physics* **13**, 1091 (1983).
[3] R. H. Howell et al. *Applied Surface Science* **116**, 7-12 (1997).
[4] S. May-Tal Beck, et al., *Defect and Diffusion Forum* **331** (Ed. B.N Ganguly and G. Brauer), 95-112 (2012).
[5] P.J. Foster et al.,*Journal of Applied Physics* **101**, 043702 (2007).
[6] W. Anwand et al., *Defects and diffusion forum* **331**, 25 (2012).
[7] S. May-Tal Beck et al., *Material Science Forum* **445-446**, 495-497 (2004).
[8] S. May-Tal Beck et al., to be published in *Journal of Physics: Conference Series* (2014).

Uranium in the nuclear fuel cycle

Zeev Karpas

Chemistry Department (Retired), Nuclear Research Center, Negev, Beer Sheva, ISRAEL,
e-mail: zeevkar44@gmail.com

Uranium plays an essential role in the nuclear fuel cycle. The presentation will give an overview of this role from the cradle (prospecting for uranium deposits) to the grave (disposal of spent nuclear fuel). The main methods used for prospecting uranium bearing minerals and the technologies for excavation of uranium will be surveyed. Then the milling operations, usually carried out close to the mine, that are used for production of "yellow cake" (usually in the form of U_3O_8) will be described. The processing stages of uranium ore concentrates (UOC) that are deployed at the uranium conversion facility (UCF) to produce the materials used for nuclear fuel based on natural uranium (UO_2 powder), feed material for isotope enrichment facilities (UF_6 mainly) and metallic uranium for some type of research reactors will be presented. The methods used for isotope enrichment and for fabrication of fuel elements will be briefly discussed. Finally, the treatment of irradiated fuel (spent nuclear fuel) and its disposal will be described.

The shape of the melting curve and phase transitions in the liquid state

Eyal Yahel

Physics Department, Nuclear Research Center - Negev, Israel

The phase diagram of elemental liquids has been found to be surprisingly rich, including variations in the melting curve and transitions in the liquid phase. The effect of these transitions on the shape of the melting curve is reviewed and analyzed. First-order phase transitions intersecting the melting curve imply piecewise continuous melting curves, with solid-solid transitions generating upward kinks or minima and liquid-liquid transitions generating downward kinks or maxima.

For liquid-liquid phase transitions proposed in the literature i.e., for carbon, phosphorous, selenium, and possibly nitrogen, we find that the melting curve exhibits a kink. Continuous transitions imply smooth extrema in the melting curve and the curvature of which is described by an exact thermodynamic relation. From this expression we find that a minimum in the melting curve requires the solid compressibility to be greater than that of the liquid, a very unusual situation. This relation is employed to predict the loci of smooth maxima at negative pressures for liquids with anomalous melting curves. The relation between the location of the melting curve maximum and the two-state model of continuous liquid-liquid transitions is discussed and illustrated by the case of tellurium [1].

Sound velocity is a fundamental measure of the thermodynamic state of the liquid. It has long been suspected that deviations from normal behavior, i.e., linear decrease of the sound velocity with temperature, are indicative of structural rearrangements. It is well documented that liquid antimony (l-Sb) exhibits an anomalous temperature dependence of the sound velocity with a maximum value attained at approximately 900^0C. We have measured the pair correlation function in l-Sb at relatively small temperature intervals across a wide temperature range and obtained the temperature dependence of the parameters of the structure. We find that the temperature dependence of the structure is correlated with that of the sound velocity. We also find that similar correlations exist in other liquid metals [2]. A simple thermodynamic relation, which relates the temperature dependence of the sound velocity in the liquid with other thermodynamic quantities, was derived. It is seen that in normal liquids the temperature dependence is related to the volume expansion coefficient. In anomalous liquids the increase in temperature is seen to originate in an entropy term and may be associated with structural rearrangements. A microscopic model for anomalous liquid metals is proposed. These structural rearrangements of the liquid suggest a kind of continuous transition in the liquid phase.

The pressure-temperature phase diagram of bismuth present multiple transitions in the solid and liquid phases. Therefore, bismuth provides the possibility to further explore the phase transitions in liquids. The thermodynamic properties of liquid bismuth have been

and the static structure factor. These physical properties display a number of anomalies. In particular, we have observed evidence for the presence of a temperature-driven liquid-liquid structural transformation that takes place at ambient pressure [3]. The latter is characterized by a density discontinuity that occurs at 740^0C. Differential thermal analysis measurements revealed the endothermic nature of this transformation. A rearrangement of liquid Bi structure was found by neutron diffraction measurements, supporting the existence of a liquid-liquid transformation at high temperatures.

References

[1] Makov, G. & Yahel, E. Liquid-liquid phase transformations and the shape of the melting curve. *J. Chem. Phys.* **134,** 204507 (2011).

[2] Greenberg, Y. *et al.* On the relation between the microscopic structure and the sound velocity anomaly in elemental melts of groups IV, V, and VI. *J. Chem. Phys.* **133,** 094506 (2010).

[3] Greenberg, Y. *et al.* Evidence for a temperature-driven structural transformation in liquid bismuth. *Eur. Lett.* **86,** 36004 (2009).

Surface science in actinides

Noah Shamir

59 Rotem St., Omer 84965, Israel. noah.shamir@gmail.com

The common surface science tools, having selective sensitivity for the upper atomic surface layers, will be presented. Examples of a "cold" system, for non or low radioactivity materials (at the NRCN) and a "hot" system, for studies of radioactive materials (at the ITU) will be presented. A special emphasis will be given to the Direct Recoils Spectrometry (DRS), which directly monitors hydrogen and hydroxyls on the surface.

Examples of studies of the interaction of gases with the surface of uranium metal, performed at the NRCN, will be presented.

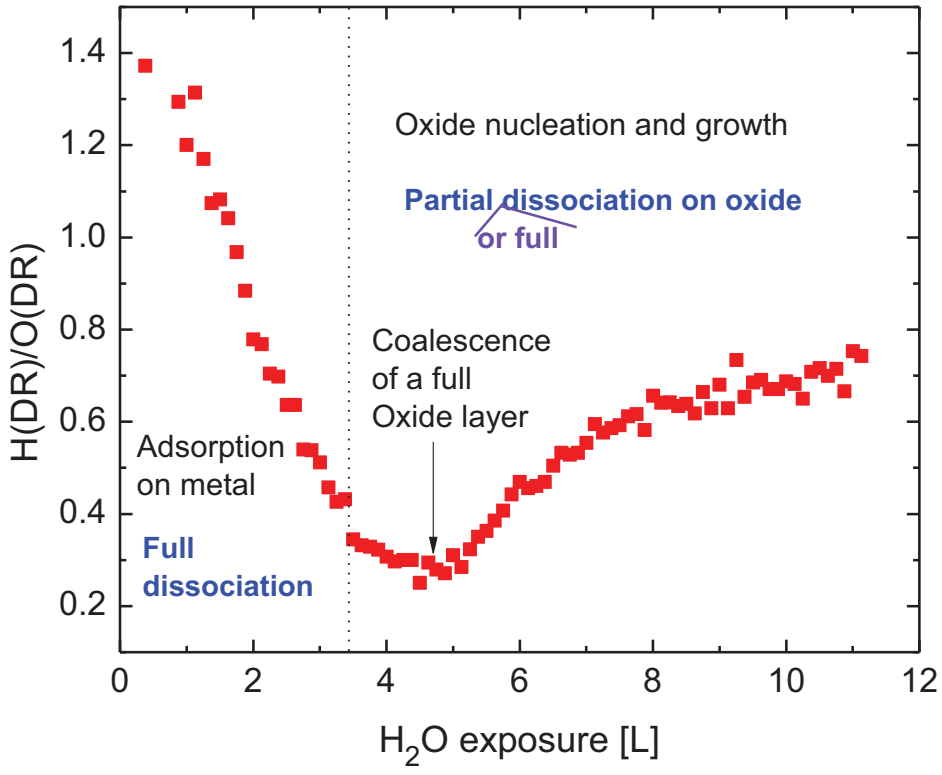

Fig. 1: H(DR)/O(DR), derived from a DRS spectrum of exposure of a clean uranium surface to H_2O.

Thermodynamics as a Foundation for Density Functional Theory

Nathan Argaman

Department of Physics, Nuclear Research Center – Negev, P.O. Box 9001, Be'er Sheva 84190, ISRAEL
e-mail: argaman@mailaps.org

Density Functional Theory (DFT) is the method of choice for an ever increasing number of electronic structure computations (recently reaching 30,000 publications per year). It was founded in the sixties on the basis of the Hohenberg-Kohn theorem and the Kohn-Sham equations, which were originally proved and derived for electronic ground states. Alternatively, one may use thermodynamics to derive DFT for finite-temperature ensembles, with the ground-state theory recovered in the zero temperature limit. Specifically, the transformation from chemical potential μ to electron number N as a free variable may be directly generalized to clarify how DFT uses the density distribution $n(\boldsymbol{r})$, rather than the external potential $v(\boldsymbol{r})$, to specify a particular inhomogeneous electronic system. Relating interacting and non-interacting systems with the same $n(\boldsymbol{r})$ distribution, one recovers not only the Kohn-Sham formulation, but also the so-called adiabatic connection theorem, which gives an explicit expression for the exchange-correlation energy in terms of the "exchange-correlation hole." This derivation has the advantage of being constructive, rather than being based on a *reductio ad absurdum* argument. It thus serves as an excellent basis for a discussion of the approximations which are inevitably introduced, including the Local Density Approximation (LDA) and the Generalized Gradient Approximation (GGA).

Reference:

[1] N. Argaman and G. Makov, "Density Functional Theory – an Introduction," *Am. J. Phys.* **68**, 69 (2000).

Quantum criticality

S. Mašková, L. Havela

Department of Condensed Matter Physics, Charles University, Ke Karlovu 5, 12116 Prague 2, The Czech Republic, e-mail: maskova@mag.mff.cuni.cz

Current condensed-matter physics is successful in description of weakly interacting electrons in metals as well as of localized electrons in e.g. 4*f* shell of lanthanides. The problems start between the two limits, where we should interpolate between two incompatible descriptions, and where the electron-electron correlations start to dominate. Some part of interactions is included in the Fermi liquid theory, which leads to renormalization of coefficients of some electronic properties, leaving the type of dependence unchanged from the non-interacting electron model. The focus here will be the situation around the onset of formation of magnetic moments and magnetic ordering, where the universal Fermi liquid picture collapses, several types of so called non-Fermi liquid scaling take over.

Quantum criticality in U_2Ni_2Sn doped by Fe and/or H

S. Mašková[1], L. Havela[1], K. Miliyanchuk[2], A. Kolomiets[1,3], H. Nakotte[4], J. Peterson[4]

[1] *Department of Condensed Matter Physics, Charles University, Ke Karlovu 5, 12116 Prague 2, The Czech Republic, e-mail: maskova@mag.mff.cuni.cz*
[2] *Faculty of Chemistry, Ivan Franko National University, 79005 Lviv, Ukraine*
[3] *Department of Physics, Lviv Polytechnic National University, 12 Bandera Str., 79013 Lviv, Ukraine*
[4] *Department of Physics, New Mexico State University, Las Cruces, USA-NM 88003*

Several compounds of $U_2(Ni_{1-x}Fe_x)_2Sn$ series with various concentrations of Fe were prepared. Their magnetic properties and impact of hydrogenation on the crystal structure and magnetic properties were studied, starting from U_2Ni_2Sn, which is an antiferromagnet with T_N = 26 K [1]. A rapid suppression of AF order with increasing Fe concentration is evidenced by temperature shift of the feature at T_N in C/T (not shown here). For $U_2(Ni_{0.8}Fe_{0.2})_2Sn$, for which the magnetic order is already vanished, the low-temperature C/T reveals behavior that is reminiscent of non-Fermi-liquid scaling (fig. 1). A pronounced upturn in C/T vs. T at low temperatures is often described by two different microscopic models: either using a paramagnon term $\delta T^2 \ln T$ or the term $-AT^{½}$, predicted for weakly interacting spin fluctuations. In our case, we found that the $-AT^{½}$ term provides a better fit of the low temperature specific heat (between 3 and 11 K). However, for lower temperatures (below 3 K), the upturn saturates and it now resembles more a paramagnon term, i.e. $\delta T^2 \ln T$. The rather sudden change in C/T around ≈ 3 K would usually be taken as evidence for some kind of magnetic ordering. However, no pronounced anomaly of magnetic susceptibility χ (T) appears in this temperature range. Instead, χ (T) has a monotonously increasing tendency (with decreasing T), which becomes gradually more and more field dependent. Comparison of the C/T data of $U_2(Ni_{0.8}Fe_{0.2})_2Sn$ with the ones of U_2Co_2Sn and $U_2Co_2InH_{1.9}$ (see fig. 1) reveals quite similar behavior for the compounds, except that there is no saturation tendency in U_2Co_2Sn [2] nor $U_2Co_2InH_{1.9}$ [3].

The Sommerfeld coefficient, which measures the electronic contribution to the specific heat, increases with increasing Fe concentration. It reaches a maximum value of ≈ 430 mJ/mol.K^2 for $U_2(Ni_{0.8}Fe_{0.2})_2Sn$ (fig. 2). With further increment of Fe concentration, γ decreases again.

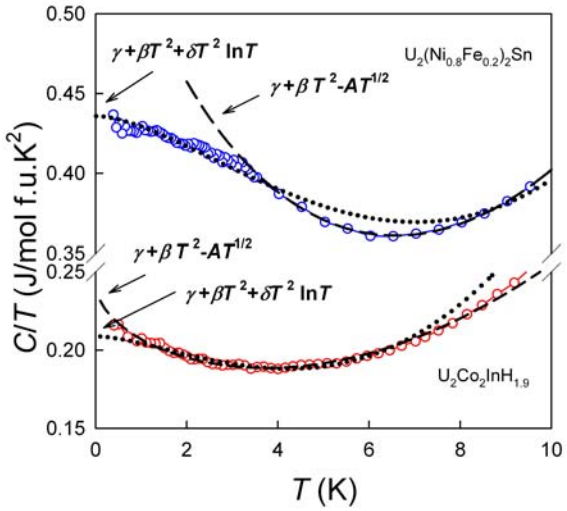

Figure 1. Low temperature part of the specific heat in the C/T vs. T representation of $U_2(Ni_{0.8}Fe_{0.2})_2Sn$ measured in zero field compared with $U_2Co_2InH_{1.9}$. Different fits marked by the dashed and dotted lines help to distinguish between the two different microscopic models.

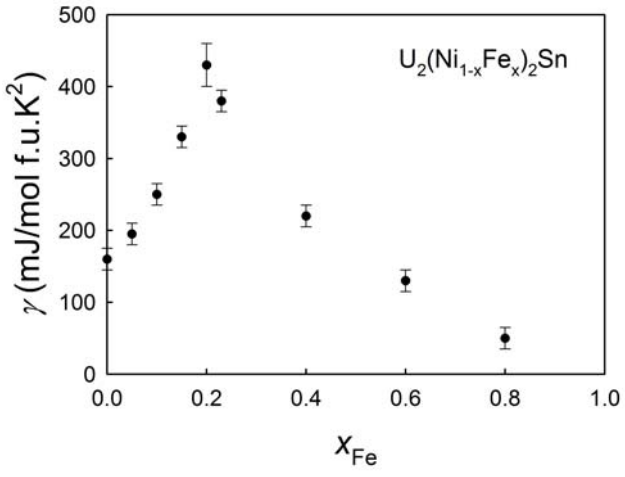

Figure 2. Concentration dependence of Sommerfeld coefficient of specific heat of $U_2(Ni_{1-x}Fe_x)_2Sn$.

$U_2(Ni_{1-x}Fe_x)_2Sn$ compounds can absorb up to 2 H/f.u. similar to other U_2T_2X compounds [3]. The hydrogenation of AF compounds leads to an increase of the Néel temperature, nevertheless the ordering temperature also rapidly decreases with increasing Fe concentration. Antiferromagnetic order disappears at approximately the same Fe concentration as in the case of parent alloys. It should be noted that there is no pronounced upturn in the low-temperature specific heat seen in the hydride of $U_2(Ni_{0.8}Fe_{0.2})_2Sn$. It seems that the lattice expansion upon hydrogenation in the $U_2(Ni_{1-x}Fe_x)_2Sn$ has only little influence on magnetic properties around $x \approx 0.2$. The low sensitivity to lattice expansion in this alloy is different than in U_2Co_2Sn, where hydrogen absorption of small amount of hydrogen to U_2Co_2Sn led to ferromagnetic α-hydride (T_C = 33.5 K) and larger amounts to an antiferromagnetically ordered β-hydride (T_N = 27 K) [4]. The hydrogenation of Fe-rich alloys leads to an unexpected development of ferromagnetic order between x = 0.23 and 0.8 (T_C = 38 K at x = 0.6) with low U moments.

The studies of physical properties of $U_2(Ni_{1-x}Fe_x)_2Sn$ and their hydrides allow us to build magnetic phase diagram as a function of Fe concentration (see fig. 3). Taking the anomalies observed in C/T and χ, we find that the ferromagnetic phase in Fe-rich hydrides is isolated from the antiferromagnetic phase for Fe-low hydrides.

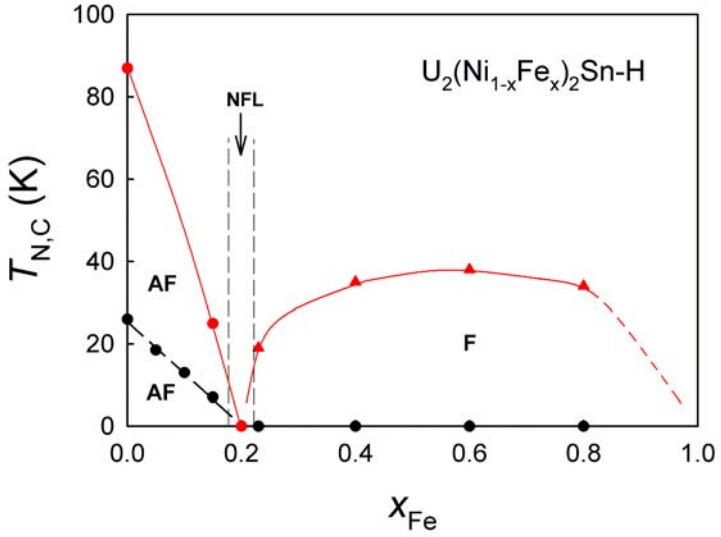

Figure 3. Magnetic phase diagram of $U_2(Ni_{1-x}Fe_x)_2Sn$ and their hydrides (circles denote the Néel temperature, triangles the Curie temperature). Black color corresponds to parent compounds, red to the hydrides.

The type of phase diagram exhibits, for the hydrides, an unusual situation. A singular point exists between different types of magnetic order. A study to reveal more details of this situation is under way.

This work was supported by the Grant Agency of the Czech Republic under the grant No. 204/12/0285.

References

[1] F. Bouree et al., *J. Magn. Magn. Mater.* **138**, 307 (1994).
[2] J. S. Kim et al., *Phys. Rev.* B **62**, 6986 (2000).
[3] K. Miliyanchuk et al., *Physica* B **378-380**, 983 (2006).
[4] K. Miliyanchuk et al., *Physica* B **359– 361**, 1042 (2005).

New ordered phase in the quasi-binary UAl3-USi3 system

Gennady Rafailov[1,2], Isaac Dahan[1] and Louisa Meshi[2]

[1]Materials Department, Nuclear Research Center of Negev (NRCN), Beer-Sheva P.O.Box 9001, 84190, Israel, refelov@bgu.ac.il
[2]Department of Materials Engineering, Ben-Gurion University of the Negev, Beer-Sheva, 50148*, Israel*

Industrial importance of U-Al-Si system stems from the fact that during processing – Al-based alloy (containing Si as impurity), used for cladding of U (fuel in nuclear reactors), undergo heat treatment which stimulates the diffusion among the fuel and the cladding. One of the possible ways to represent ternary U-Al-Si phase diagram is construction of UAl_3-USi_3 quasi-binary phase diagram. On the one hand, since both UAl_3 and USi_3 phases are isostructural - an isomorphous phase diagram is expected, on the other hand - some researchers observed miscibility gap at lower temperatures. During our study of the UAl_3-USi_3 quasi binary phase diagram, new stable $U(Al_x,Si_{(1-x)})_3$ phase was identified. The structure of this phase was determined using a combination of electron crystallography and powder X-ray diffraction methods as tetragonal (I4/mmm (No.121) space group), with lattice parameters of a=b= 0.8347(1) nm, c= 1.6808(96) nm. Its unit cell has 64 atoms and it can be described as an ordered variant of the $U(Al,Si)_3$ solid solution. The ordering can be explained and atom positions re-calculated by means of Bärnighausen tree which was constructed using the original $U(Al,Si)_3$ structure as an aristotype.

Neutron multiplicity counting in passive neutron interrogation for fissile mass estimation

Chen Dubi[1]

[1] *Dep. Of Physics, Nuclear Research Center of the Negev (NRCN). POB 9001, Beer Sheva, Israel*
e-mail: chendb331@gmail.com.

Non Destructive Testing (NDT) for fissile mass estimation in a polluted samples is one of the many challenges facing both the safety and the safeguard nuclear community. In my talk I will introduce one of the procedures that is currently considered a standard NDT procedure: Passive neutron interrogation, relying on neutrons coming from spontaneous fission events in the tested sample.
On one hand, since most structure materials are (relatively) transparent to neutron radiation, passive neutron interrogation is considered highly effective in the analysis of dirty, poorly characterized samples, or in the case where the sample is shielded. On the other hand, since a typical passive interrogation assembly is based on ^{3}He detectors, neutrons from additional neutron sources (mainly (α,n) reactions and induced fissions in the tested sample) cannot be separated from the main spontaneous fission source through energetic spectral analysis.
There for, the noise to source ratio must be evaluated through a mathematical "filter". One way for doing so is to utilize the fact that the different neutron sources have a very different statistical nature, and then, by studying the higher moments of the detection rate (or, equivalently, time correlations between consecutive detection), we may gain knowledge about the noise to source ratio. Such considerations are commonly known as **N**eutron **M**ultiplicity **C**ounting (NMC) methods.
The most well-known NMC method is the Multiplicity method [1], which correlates the noise to source ratio with the so called Singles, Doubles and Triples in the detection train. In recent years, a new method, referred to as the SVM method (standing for **S**kewness, **V**ariance, **M**ean), has been introduced by the author [2]. While it has been shown that the two methods share the same model assumptions and the same statistical error, the SVM method enjoys both a relative simplicity and a theoretical flexibility, enabling us to extend the capabilities of NMC in a fairly simple manner.
In the talk, I will introduce the SVM method and discuss, through both theory and real life measurement, the general need for NMC methods and the capabilities of the SVM method.
The talk will be aimed to a general audience, and will not assume any prior experience in the field.

References

[1] N. Ensslin, W. Harker, M. Krick, D. Langner, M. Pickvell: Application guide to neutron multiplicity counting*, Los-Alamos manual*, LA-13422-M (1998).
[2] C. Dubi, T. Ridnik, I. Israelashvili, J. Bagi, J. Huszti: A method for the estimation of fissile mass by measuring the number of neutron signals within a specific time interval, *Nuclear Instruments and methods A (NIMA)* **186-187**, 1658 (1989).

Magnetism in hydrides of γ-Uranium alloys.

M. Paukov, I. Tkach, Z. Matěj, L. Havela

Department of Condensed Matter Physics, Faculty of Mathematics and Physics, Charles University, Ke Karlovu 5, 121 16, Prague 2, Czech Republic
e-mail: Michael.Paukov@gmail.com

The *bcc* form of Uranium metal, its alloys, and their hydrides have been used in various applications, such as low-enriched nuclear fuel. The γ-Uranium metal is stable at elevated temperatures. The only possibility to retain this phase to low temperatures is to combine doping (by Mo, Zr, Ti, Nb, Re, Ru, Pd, or Pt) with quenching. It opens the possibility to study the ground state properties in this form of U. We have been testing the possibility to reduce the necessary amount of the dopant using ultrafast cooling [1].

As next, we decided to test the interaction with hydrogen. The common α-U phase is known to react readily with H at low pressures already, producing a fine pyrophoric powder of β-UH_3, which is ferromagnetic with the Curie temperature around 170 K. Experiments revealed that the Mo stabilized γ-U absorbs H only at elevated pressure. The product is surprisingly not powder. We obtained brittle but compact pieces of hydrides denoted as UH_3Mo_x with practically amorphous crystal structure, most likely related to β-UH_3 [2]. Varying the Mo concentration, we found that the Curie temperatures increase up to 200 K. The Curie temperature has a maximum for $UH_3Mo_{0.18}$ (see Fig. 1a).

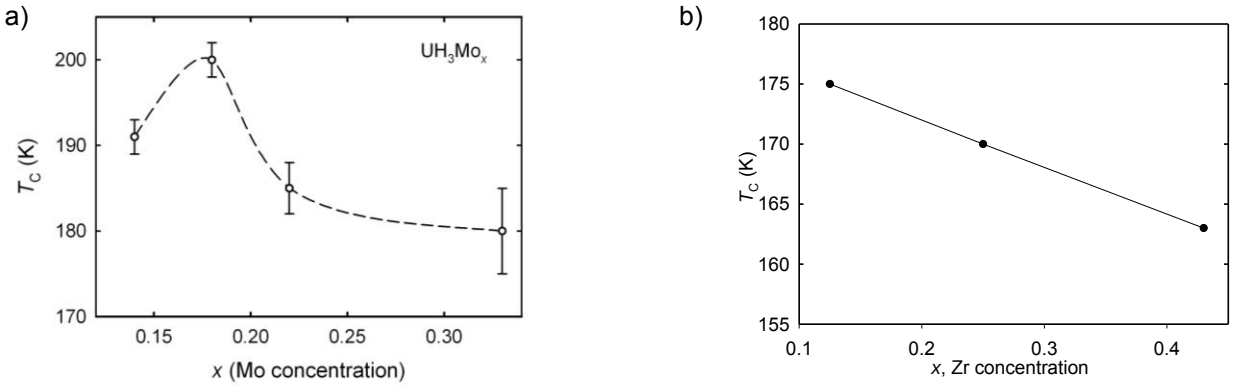

Fig. 1. The dependence of Curie temperature on a) Mo, b) Zr concentration.

The magnetic moment per U atom increases, as well [2]. The saturation magnetization of the U-Mo hydrides is higher than that in β-UH_3 (see Fig. 2a).

The type of hysteresis loops at T = 2 K can be associated with pinning of domain walls in highly disordered systems with high anisotropy (see Fig. 2b). There exists extended evidence of similar behavior among such materials, called as High Anisotropy Random Distribution, for example on the basis of $SmCo_5$ or amorphous $TbFe_2$. With increasing concentration of Mo the coercive force increases extremely up to 5 Tesla.

For comparison with U-Mo, we undertook the same type of study with *bcc* U doped by Zr. The U-Zr alloys absorb hydrogen (pressures above 5 bar H_2 are necessary) up to the stoichiometry UH_3Zr_x, forming a crystalline material with the cubic structure corresponding to α-UH_3, which represents a *bcc* U lattice filled with H.

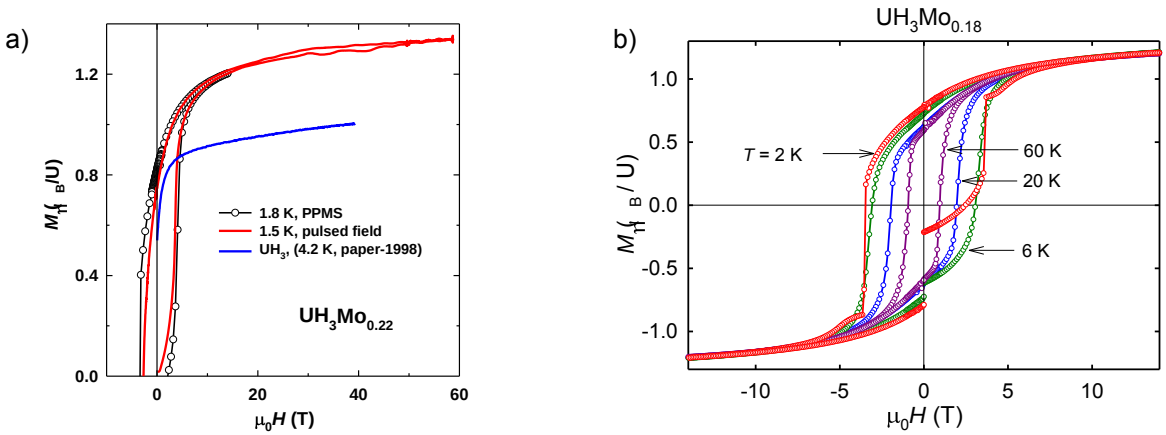

Fig. 2. a) Approach to saturation in high magnetic fields for $UH_3Mo_{0.22}$ compared with β-UH_3
b) temperature variations of hysteresis loop for $UH_3Mo_{0.18}$.

We assume that Zr occupies randomly the U lattice sites, as the atomic radius of Zr and U are similar. $T_C \approx 175$ K slightly exceeds that of β-UH_3 for low Zr concentrations, but decreases with increasing Zr concentration (see Fig. 1b). U moments remain on the level of 1 μ_B. The study reveals a surprising fact that magnetic properties of α-UH_3 and β-UH_3 are similar, despite different atomic spacing. A striking feature of UH_3Zr_x systems is enormous magnetic coercivity, with the width of hysteresis loop exceeding 11 T at low temperatures (see Fig. 3).

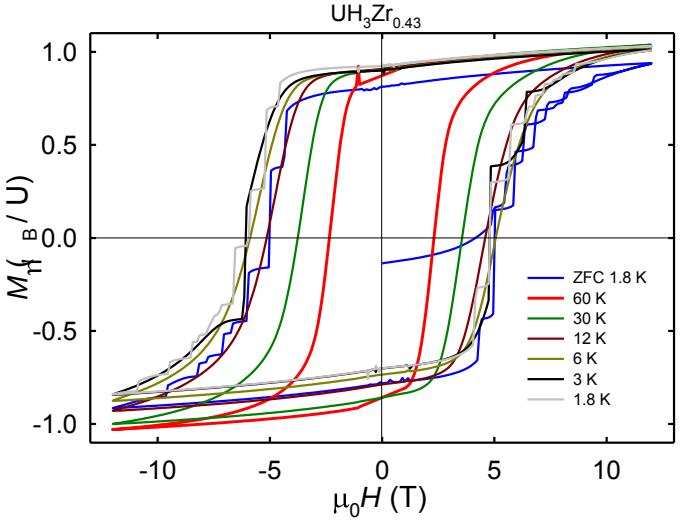

Fig. 3. Hysteresis loops of $UH_3Zr_{0.43}$ measured at various temperatures.

It can be again attributed to the statistical distribution of Zr leading to randomness of easy-magnetization direction.

Our results indicate that interestingly large variability can be achieved for the UH_3 hydrides. The amorphous phase may allow for diverse other dopants tuning magnetic properties. At present we try to dope U by both Mo and Zr.

[1]. I. Tkach, N.-T. H. Kim-Ngan, S. Mašková, M. Dzevenko, L. Havela, A. Warren, C. Stitt, T. Scott, J.Alloys Comp. 534 (2012) 101-109.
[2]. I. Tkach, S. Mašková, Z. Matěj, N.-T. H. Kim-Ngan, A.V. Andreev and L. Havela, Phys. Rev. B 88 (2013) 060407(R).

FORENSIC CHEMISTRY

Joseph Almog

Forensic chemistry is a new discipline in the Casali Institute. It deals with the use of chemical methods to resolve crimes and furnish courts of law with scientific evidence. The main research areas are:

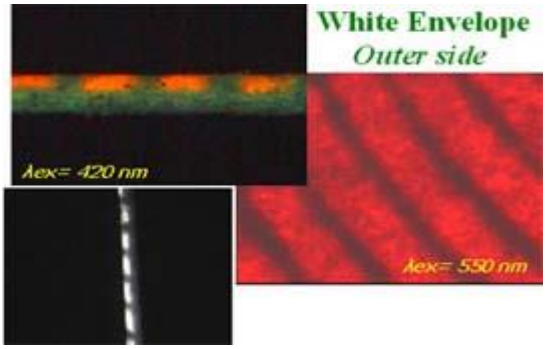

Latent fingerprint visualization Chemical development of latent fingerprints is expressed by a visual chemical reaction between an appropriate reagent and one or more constituents of human secretion, to yield a colored, luminescent, or radioactive product, which can be visualized. The research concentrates on developing improved reagents and instrumentation for this purpose, particularly on more sensitive "mapping" of the amino acids and lipids that are present in small amounts in fingerprint deposits. The work is done in cooperation with the Latent Fingerprint Laboratory of the Division of Identification and Forensic Science (DIFS) of the Israel Police.

Advanced techniques for detection and identification of explosives Cutting-edge techniques for diagnostic determination of explosives are studied and compared. Another research direction is the preparation of novel color reagents for the chemical detection of explosives. The work is done in collaboration with the Explosives Identification Laboratory of the DIFS.

Field tests for crime-scene examination The goal is to provide forensic technicians with better tools for scientific examination of scenes of crime. Research problems include: Shooters' detection (color and fluorescence techniques) and enhancement of faint contact impressions (e.g. shoe-print, tire-prints, indented writing). The work is done in collaboration with the Toolmarks and Materials Laboratory and the Questioned Documents Laboratory of the DIFS.

What is nuclear forensics?

Itzhak Halevy

Department of Physics, NRCN, Israel
e-mail: halevyi@caltech.edu

Nuclear forensics is the investigation of nuclear materials to find evidence for example the source, the trafficking, and the enrichment of the material. The material can be recovered from various sources including dust from the vicinity of a nuclear facility, or from the radioactive debris following a nuclear explosion.
Results of nuclear forensic testing are used by different organizations to make decisions. The information is typically combined with other sources of information such as law enforcement and intelligence information.
The first seizures of nuclear or otherwise radioactive material were reported in Switzerland and Italy in 1991. Later, reports of incidents of nuclear material occurred in Germany, the Czech Republic, Hungary and other central European countries. Nuclear Forensics became a new branch of scientific research with the intent of not only determining the nature of the material, but also the intended use of the seized material as well as its origin and about the potential trafficking routes. Nuclear forensics relies on making these determinations through measurable parameters including, but not limited to chemical impurities, isotopic composition, microscopic appearance, and microstructure. By measuring these parameters, conclusions can be drawn as to the origin of the material. Identification of these parameters is an ongoing area of research; however, data interpretation also relies on the availability of reference information and on knowledge of the fuel cell operations.
The lesson will include the Analysis, Counting Techniques, Mass Spectrometry and Additional Nuclear Forensic Methods.

The IAEA definition
Nuclear forensics is the analysis of intercepted illicit nuclear or radioactive material and any associated material to provide evidence for nuclear attribution. The goal of nuclear analysis is to identify forensic indicators in interdicted nuclear and radiological samples or the surrounding environment, e.g. the container or transport vehicle. These indicators arise from known relationships between material characteristics and process history. Thus, nuclear forensic analysis includes the characterization of the material and correlation with its production history.

Examples to Nuclear Forensic events.

Analysis of swipe samples – bulk analysis is shown in figure 1.

Fig 1: swipe samples Analysis.

Analysis of single particles by LA-ICP-MS technique is a knowen tecniqe for nuclear forensic, see figure 2.

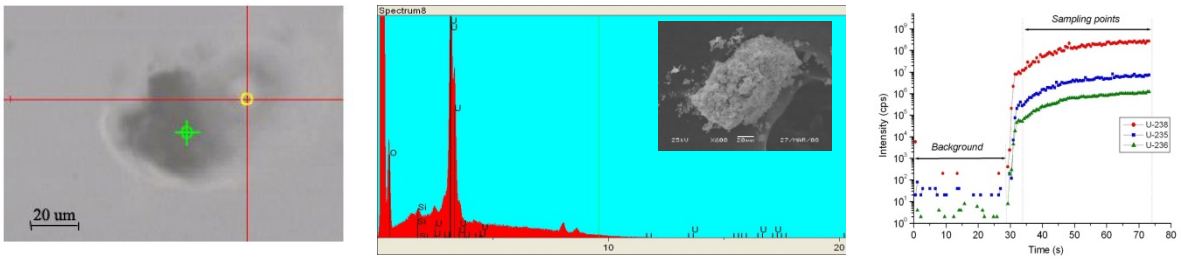

Fig 2: Analysis of single particles by LA-ICP-MS technique

"NUCLEAR FORENSICS SUPPORT REFERENCE MANUAL" [1] is a basic tool for nuclear forensics research and studies.

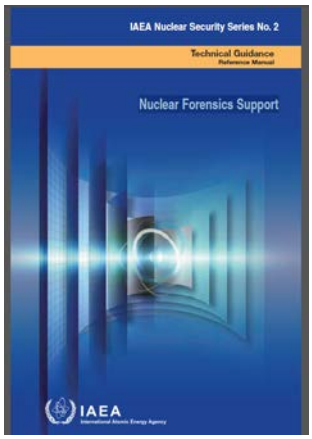

Fig 3: NUCLEAR FORENSICS SUPPORT REFERENCE MANUAL - IAEA

References

[1] NUCLEAR FORENSICS SUPPORT REFERENCE MANUAL, IAEA Nuclear Security Series No. 2, IAEA

Post Blast Nuclear Forensics of a Radiological Dispersion Device Scene

A. Sharon[*1], I. Halevy[1], D. Sattinger[1], L. Krantz[2], U. Admon[1], P. Banaim[1], I. Yaar[1]

[1]Nuclear Research Center Negev (NRCN),P.O.Box 9001, Beer- Sheva, Israel
[2]IAEC, Tel-Aviv, Israel

"Green Field" (GF) project conducting in Israel, between the years '06-'14, aimed at increasing the preparedness for outdoor terrorism events, where a radioactive (RA) material is dispersed by an explosive charge. Under the project framework a wide experimental program was established and conducted. The experimental plan included set of about 150 detonation tests that were done in order to close some gaps of knowledge mainly relating to the "source term" characterization. Experiments were done using wide range of different source term parameters. Among these are: explosive types, dispersed materials (both, stable simulants and short live radio isotopes), device geometries, ground surfaces, detonation heights and orientation, atmospheric stability situations etc. Field data collection and documentation used some of the "state of the art" detectors, cameras etc. Based on a comprehensive data analysis and complementary simulations, a methodology for post blast forensic using data collected from the close vicinity of the detention point was developed.

1. Introduction

Realistic source term characterization plays as a "necessary condition" for reliable atmospheric dispersion model predictions. Source term characterization means all the necessary input data needed for the initiation of the atmospheric transport model. This include the final RA particles size distribution, the isotopes involve (single or a mix), the cloud top height ("effective height"- where it is in a thermal equilibrium with the ambient atmosphere), and the distribution of particles along the cloud up to the effective height. Much of the final health and environmental consequences of an explosive RDD event depend on these parameters.

Cloud top height is a function of the explosive type and amount, the surface below HE charge, the local atmospheric stability above the detonation point and the local wind speed.

Particles size distribution following detonation depends the explosive type used (less on the amount), the surface below the detonation, the type(s) of the RA material(s) and the device geometry.

Particles distribution along the cloud is a function of the cloud vertical velocity up to the effective height (depend the HE type, atmospheric stability, wind speed etc.) and the fraction of aerosols out of the total RA material.

The main idea behind the offered "post blast nuclear forensics (NF)" process is that much of the essential data needed for reliable nuclear forensics can be collected from the arena just few meters around the detonation point without looking for long distance downwind deposition.

The immediate area around the detonation point ("ground zero"- GZ) is rich enough to supply much of the necessary data for reconstruct a reliable picture of the event. This include the RA material(s) involved, the HE type and amount and the device geometry.

The data collecting process is of an extreme importance for that. Here there is a citation from the ITWG guidelines for evidence collection: "Obtaining reliable NF conclusion is only possible if the entire process from sample collections at the incident site through the analysis and data interpretation is laboratory controlled and technically rigorous".

Data collecting include smears from the ground below detonation (for radiation spectroscopy, particles size distribution, particles morphology and agglomerates, HE chemistry etc.), measured dimensions of craters below detonation and evidences on the cloud height, if possible.

Once the RA material(s) type(s) and the size distribution are recover (SEM and EDS) one can conclude about the device geometry (the terrorists capabilities). Other classical forensic

information relating the HE can be easily concluded by the police demolition units. This include the type and amount of the HE used.
Figure 1 present SEM pictures of particles sample from the GZ area of detonation tests where stable CsCl (left) and $SrTiO_3$ (right) powders were dispersed.

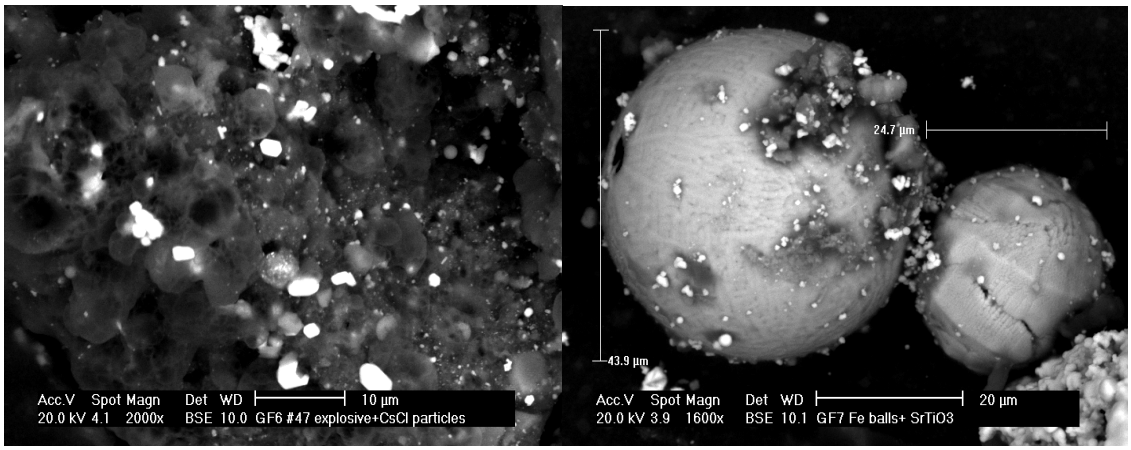

Fig. 1: SEM pictures of smear samples collected from a GZ point of two tests where stable CsCl and $SrTiO_3$simulant sources were dispersed in “dirty bomb” like event.

One can see that in the case of the CsCl test there is a large amount of unburned explosive remnants which evident a deflagration rather than detonation situation. The CsCl final particles remained almost as before the “detonation” with no shock sintering evidence.
On the right picture there are $SrTiO_3$ particles that were agglomerated to Fe sintered balls of the electric wires used for the detonation. In both of the cases the RA particles size distribution can be measured and compared to the original used in order to be able to conclude the possible device geometry and the quality of detonation.
Fig. 2 present an example of two caters remains after detonation tests on asphalt and steel surfaces. The amount of ambient dirt entrained into the fireball is highly depending on the surface type below the detonation. In a case where no dirt entrained the fraction of
fine aerosols created (respirable and non respirable) will be higher than for the case “dirty shots” where agglomerates of RA particles and ambient dirt will change the size distribution.

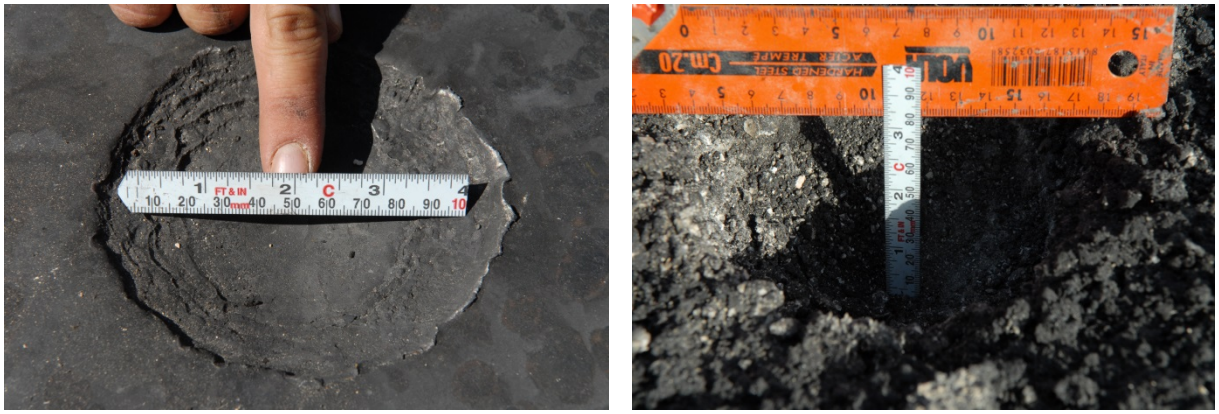

Fig. 2: Craters remained following detonation of the same charge on different surfaces types: Steel (clean) on the left and Asphalt (dirty) on the right.

Figure 3 present the predicted detonation (TNT) cloud top heights for different local atmospheric conditions and HE amounts, based on a model developed for such an events [1, 2].

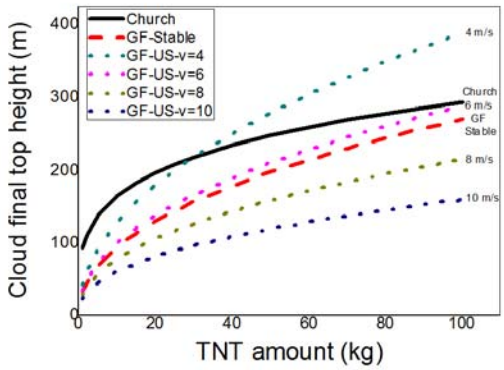

Fig. 3: Cloud top height for different HE amounts and micro-meteorology situations.

3. Summary

Reasonably reliable post detonation nuclear forensics can be made based on a simple data collection out of the immediate area around the GZ point. HE type and amount, RA mix and device geometry can be concluded out of this analysis.

References

1. Hotspot 2.07.2, Health physics and atmospheric dispersion code, LLNL-USA, Sep. 2011. See also in Hot Spot user guide Sharon et al.
2. A. Sharon, I. Halevy, D. Sattinger, I. Yaar, Cloud rise model for RDD events, Atmospheric Environment 54 (2012) 603-610.

Facilities available for actinide research in Prague

V. Sechovský

DCMP, Faculty of Mathematics and Physics, Charles University,
Ke Karlovu 5, 12116 Prague 2, Czech Republic

Since June 2012 the Prague group at the Charles University operates a Czech research infrastructure *Magnetism and Low Temperature Laboratories* (MLTL - http://mltl.eu orhttp://lmnt.cz)which is financially supported by the Government of Czech Republic. The main mission of MLTL is to provide broad scientific community unique possibilities for comprehensive experimental studies of physical phenomena and properties of materials in multiextreme conditions.MLTL offer *open access* to a wide range of experimental facilities for sample preparation (SSE refinement of staring metals, synthesis of bulk polycrystals, growth of single crystals), characterization (XRD, SEM + EDX) and measurements of various physical properties in high magnetic fields up to 20 T, temperatures from 30 mK to 1000Kand external pressures up to 25 GPa). Anybody can apply for experimental time with his proposal on the *user portal* of http://mltl.eu.

The main strategic objective is the excellence of the infrastructure on the international scale. Therefore the MLTL Panel evaluation the proposals and allocation of experimental time is based primarily on the quality of intended research. The proposals of students for experiments needed for their theses are promoted within the evaluation process.

The research opportunities offered by MLTL will be demonstrated during the lecture with emphasis on methodology.

Research at big facilities on actinides: How neutrons and synchrotron x-rays can help our understanding

G. H. Lander[1]

[1]European Commission, JRC, Institute for Transuranium Elements, D-76125 Karlsruhe, Germany and Institut Laue Langevin, Grenoble, France
e-mail: lander@ill.fr

Neutron scattering was a by-product of the Manhattan Project, as it started by using neutron beams emerging from the reactors produced by that project. Seventy years later, neutron scattering is a tool used by many scientists, across many different disciplines, to try to understand the microscopic properties of materials. It can also give unique answers to problems involving actinides.

X-rays, of course, date even further back, but it was not until the 1970s that synchrotron radiation was widely available. Now synchrotron radiation is a tool widely used in the study of actinides across a variety of different fields.

The basic properties of these two probes will be presented and contrasted. Some of the ways these techniques have helped us understand the actinides will be presented.

Experimental constraints on processes in the Earth interior

Ronit Kessel

Institute of Earth Sciences, The Hebrew University of Jerusalem

Direct observations on deep Earth composition, mineralogy, and processes are limited. Drilling is available up to 15 km and direct, although sporadic, samples are brought to the surface from depth of up to 300 km in the form of xenoliths or mineral and fluid inclusions in diamonds. Information on deeper areas within the Earth is derived from indirect observations, such as seismology and high pressure and temperature experimental petrology. The most common experimental techniques to study deep Earth processes are piston cylinder, relevant to pressures up to 3 GPa, and multi-anvil, up to 10 GPa.
My group and I run experiments on a rocking Multi-Anvil apparatus in order to reduce chemical zonation and enhance equilibrium in the capsule. We use the diamond trap setup in order to physically isolate the liquid phase from the solid phases while keeping chemical communication during the experiment. The liquid phase is analyzed using the laser-ablation ICP-MS, following the freezing technique in order to prevent exsolution during capsule preparation for analysis. The solid phases are analyzed using the electron probe micro-analyzer and X-ray diffraction.

Discoveries that changed the world: 1932 – 1942

James Chadwick & Lise Meitner

G. H. Lander[1]

[1]*European Commission, JRC, Institute for Transuranium Elements, D-76125 Karlsruhe, Germany and Institut Laue Langevin, Grenoble, France*
e-mail: lander@ill.fr

From the discovery of the neutron (1932) to the first demonstration of controlled fission (1942) was just ten years; a period that took physics from an occupation of a small number of eccentric gentlemen and (even fewer) ladies to something of concern to, and funding decisions of, Governments all over the world. The shadows of those tumultuous years are still with us, for better or worse.

This talk will recount those ten years through the lives of James Chadwick (1891-1974) and Lise Meitner (1878-1968), contemporaries who played pivotal roles in the events, even though, partly because of their retiring personalities, they are often over-shadowed by "larger" figures.

James Chadwick (left) with General Leslie Groves (Head of the Manhattan Project) at Los Alamos 1945

Lise Meitner with President Truman when she was honoured as “Woman of the Year” in Washington 1946

Compounds, Relations and Properties on the U-Fe-Ge System

A.P. Gonçalves,[1] M.S. Henriques[1], D. Berthebaud[2], O. Tougait[3], L. Havela[4]

[1] *C2TN, Instituto Superior Técnico/CFMC, Universidade de Lisboa, Estrada Nacional 10, 2695-066 Bobadela LRS, Portugal*
e-mail: apg@ctn.ist.utl.pt
[2] *CRISMAT UMR6508, 6 Boulevard du Maréchal Juin - F-14050 Caen cedex 4, France*
[3] *Lab. Chimie Solide Matériaux, UMR CNRS 6226, Univ. Rennes I, Rennes, France*
[4] *Faculty of Mathematics and Physics, Charles University, Ke Karlovu 5,12116 Prague, Czech Republic*

Uranium compounds show a wide variety of properties that depend on the U electronic structure and the position of the 5*f* levels, which usually can be changed by external factors (like temperature, pressure, magnetic field,…) and internal factors (as composition, structure,…). Therefore, the study of such compounds frequently leads to the identification of original crystal structures and ground-states. The case of uranium germanides is paradigmatic: examples of unique crystal structures are not uncommon and they comprise one of the most puzzling ground-states, the coexistence of superconductivity and ferromagnetism, as first reported for UGe_2 under pressure [1] and after observed on URhGe [2] and UCoGe [3].
One of the best ways to identify new compounds is the study of phase diagrams, which provides important information about the formation and stability of compounds and their phase relations. The ternary lanthanide systems containing Fe and Ge were intensively studied due to the discovery of the giant magnetocaloric effect in pseudo-binary compounds such as $Gd_5Si_xGe_{4-x}$, or in similar systems when substituting Si and Ge by other non-metals or transition metals. For actinide-containing phase diagrams, a systematic search was started some years ago, the U-Fe-X X= B, Al, Si, Sn, and Ga isothermal sections being already reported [4-8]. Following our previous works, we decided to explore the U-Fe-Ge system and characterize the existing compounds. Here we present a review on the structure and physical properties of these uranium-iron germanides.

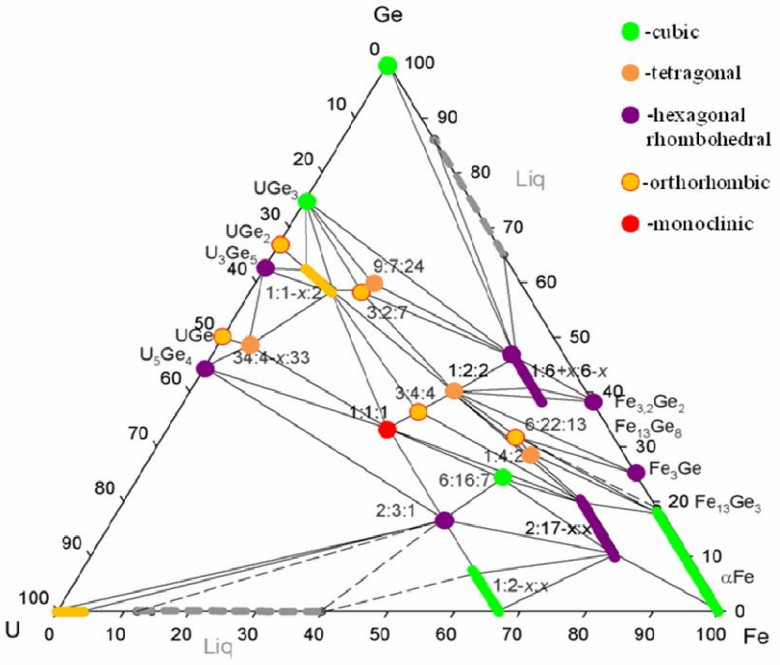

Figure 1 - Isothermal section at 900ºC of the U-Fe-Ge system emphasizing the different crystal symmetries (see text).

The isothermal section at 900ºC was observed to contain fourteen ternary stable phases (ten intermetallic compounds and four homogeneity ranges), nine of them discovered for the first time: ten stoichiometric ternary compounds, (A) UFeGe, (B) UFe_2Ge_2, (E) $U_{34}Fe_{3.32}Ge_{33}$, (G) $U_3Fe_2Ge_7$, (H) $U_9Fe_7Ge_{24}$, (I) U_2Fe_3Ge, (J) $U_6Fe_{16}Ge_7$, (K) $U_3Fe_4Ge_4$, (L) UFe_4Ge_2, and (M) $U_6Fe_{22}Ge_{13}$; three intermediate solid solutions, (D) $U_2Fe_{17-x}Ge_x$ ($2<x<3.7$), (F) $UFe_{1-x}Ge_2$ ($0.58<x<0.79$), (C) $UFe_{6+x}Ge_{6-x}$ ($x<0.7$); and (N) one extension of the binary UFe_2 into the ternary system ($UFe_{2-x}Ge_x$, $x<0.2$),. Within these, three original structure types, $U_{34}Fe_{4-x}Ge_{33}$, $U_9F_7Ge_{24}$ (both tetragonal, space group I4/mmm) and $U_6Fe_{22}Ge_{13}$ (orthorhombic, space group Pbam) were observed. Typically, there is a decrease of the symmetry in the ternary phases, when compared with the binary ones. However, many motifs observed in the binary compounds also exist in the ternary phases revealing a clear connection between them.
In this ternary system the hybridization usually leads to a decrease of the magnetic moments and magnetic ordering temperature. However, the Hill rule is only partially followed, U_2Fe_3Ge being an obvious exception. In the Fe-rich corner an evident predominance of ferromagnetic interactions, induced by Fe, exists.

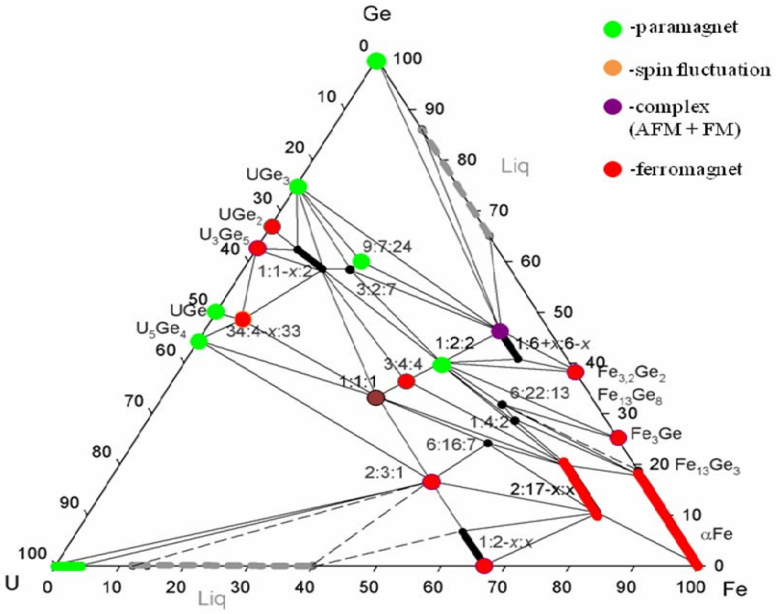

Figure 2 – Magnetic ground-state of compounds from the U-Fe-Ge system (see text).

Acknowledgements
M.S.H. acknowledges FCT for the SFRH/BD/66161/2009 grant.

References

[1] S. S. Saxena, P. Agarwal, K. Ahilan, F. M. Grosche, R. K. W. Haselwimmer, M. J. Steiner, E. Pugh, I. R. Walker, S. R. Julian, P. Monthoux, G. G. Lonzarich, A. Huxley, I. Sheikin, D. Braithwaite, J. Flouquet, Nature 406 (2000) 587
[2] D. Aoki, A. D. Huxley, E. Ressouche, D. Braithwaite, J. Flouquet, J. P. Brison, E. Lhotel and C. Paulsen, Nature 413 (2001) 613
[3] N. T. Huy, A. Gasparini, D. E. de Nijs, Y. Huang, J. C. P. Klaasse, T. Gortenmulder, A. de Visser, A. Hamann, T. Görlach and H. v. Löhneysen, Phys. Rev. Lett. 99 (2007) 067006
[4] M. Dias, P.A. Carvalho, O. Sologub, O.Tougait, H. Noël, C. Godart, E. Leroy, A.P. Gonçalves, Intermetallics 15 (2007) 413.
[5] A.P. Gonçalves, H. Noël, Intermetallics 13 (2005) 580.
[6] D. Berthebaud, O.Tougait, A.P. Gonçalves, H. Noël, Intermetallics 16 (2008) 373.
[7] A.P. Gonçalves, H. Noël, Intermetallics 9 (2001) 473.
[8]. A.P. Gonçalves, H. Noël, O. Tougait, A. Zelinskiy, Proceedings of the 38 JDA, Wroclaw, Poland, 2008, P06.

Atomistic Studies of Dislocation Structure and Motion

Guy Makov[1]

[1] *Department of Materials Engineering, Ben-Gurion University of the Negev, Beer Sheva 8404, Israel*
e-mail: makovg@bgu.ac.il

A quantitative, predictive theory of plastic deformation is a grand challenge of material physics. Dislocation motion is the fundamental mechanism underlying plastic deformation in metals. The study of dislocation structure, kinematics and dynamics is the focus of extensive experimental and theoretical studies. However, due to the multiple length and time scales involved, many fundamental issues remain unresolved. Atomistic simulations are ideally suited to analyzing phenomena at short time and length scales, below those easily accessible by experimental means. Thus, atomistic studies provide a unique insight into aspects of dislocation motion, such as how dislocations move in crystals and how they interact with other dislocations as well as with crystal defects. Molecular dynamics simulations have been applied to study dislocation motion in selected f.c.c. and b.c.c. metals, focusing on both kinematic and dynamic aspects. These studies expose both universal and differentiating properties of dislocation dynamics in metals. The linking of the insights obtained from atomistic studies into large-scale models and experimental observations is considered. Finally, the validity of these atomistic studies depends on both physical and computational assumptions, which will be reviewed.

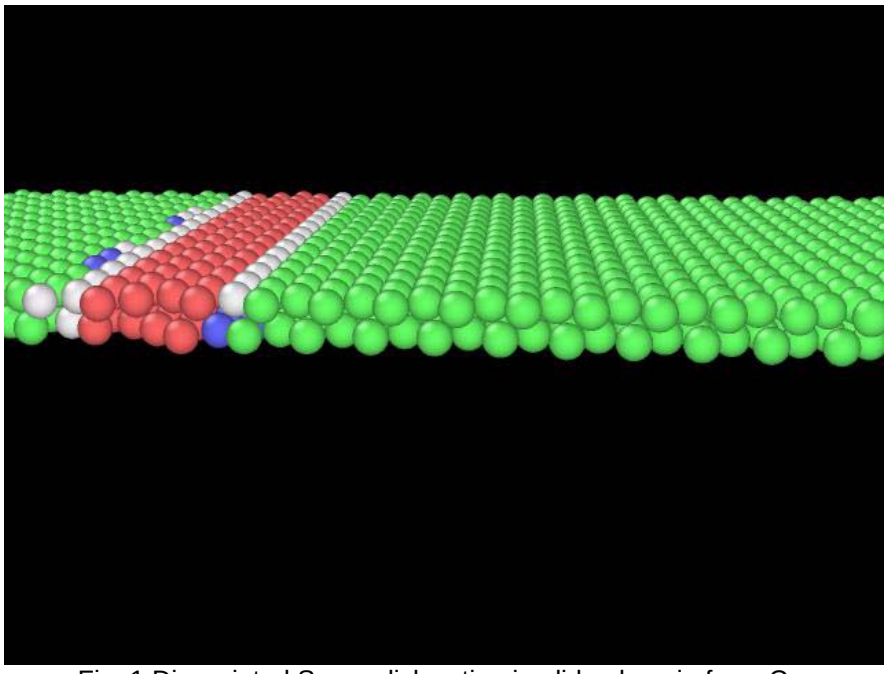

Fig. 1.Dissociated Screw dislocation in glide plane in f.c.c. Cu.

References

[1] D. Mordehai, Y. Ashkenazy, I. Kelson and G. Makov, “Dynamic properties of dislocations – a molecular dynamics study” Phys Rev. B 67, 024112 (2003).
[2]D. Mordehai, I. Kelson and G. Makov "Cross-slip and annihilation of screw dislocations in Cu: A molecular dynamics study" Mat. Sci. Eng. A 400-401, 37 (2005).
[3]D. Mordehai, I. Kelson and G. Makov "Nonplanar core and dynamical behaviour of screw dislocations in copper at high velocities" Phys. Rev. B74, 184115(2006).
[4]G. Makov, C. Gattinoni and A. de Vita, “Ab initio based multiscale modelling for materials science” Modelling Simul. Mater. Sci. Eng. 17 084008 (2009).

[5] R. Choudhury, C. Gattinoni, G. Makov and A. De Vita “Molecular dynamics studies of the dissociated screw dislocation in silicon” J. Phys. Cond. Matt. 22, 074210 (2010).
[6]P. Landau, G. Makov, R.Z. Shneck and A. Venkert “Universal strain–temperature dependence of dislocation structure evolution in face-centered-cubic metals” Acta Mat. 59, 5342 (2011).
[7]P. Landau, D. Mordehai, A. Venkert and G. Makov “Universal Strain - Temperature Dependence of Dislocation Structures at the Nano-Scale” Scripta Materialia 66, 135-138 (2012).

The SARAF the proton and deuteron 40 MeV accelerator and applications

Dan Berkovits for the SARAF team[1]

[1] *Soreq NRC, Yavne 81800, Israel*
e-mail: berkova@soreq.gov.il

The Soreq Applied Research Accelerator Facility (SARAF) is built as a user facility. An intense fast neutrons source, a thermal neutrons source and apparatuses for production of isotopes for basic and applied research will be available at the end of construction, foreseen in several years. SARAF is based on a high intensity CW proton / deuteron RF superconducting linear accelerator. Several novel technologies are used in order to build this demanding linac. To reduce technological risks, the construction was divided in two Phases. Phase-I was constructed in order to test and characterize the novel technologies and is in routine operation since 2010. SARAF phase-I, with its single 6 half-wave resonators separated vacuum cryomodule, is the first high current, superconducting low-beta linac in operation and it is presently delivering CW mA proton beams for target developments. Phase-II of this linac will allow acceleration up to 40 MeV and 5 mA CW proton and deuteron beams. Phase-II is now under conceptual redesign.

SARAF System Requirements

The goals SARAF are: 1) to enlarge the experimental nuclear science infrastructure and promote research in Israel, 2) to develop and produce radioisotopes for bio- medical applications and 3) to modernize the source of neutrons at Soreq and extend neutron based research and applications [1]. SARAF, when it fulfils its goals, is intended to replace the aging research reactor in Soreq. These goals define the requirements from the accelerator. The requirements were optimized to fulfil all of the above goals, within domestic cost constraints. Production of isotopes for radiopharmaceuticals is mainly done by tens of MeV protons, so this is a basic requirement. Variable energy protons allow optimizing the production yield, while minimizing parasitic isotopes production. Deuterons have two main advantages in isotopes production; the production yield in the (d,2n) reaction is significantly higher than the (p,n) reaction for several targets. In addition, at tens of MeV, the neutron yield of deuterons is significantly higher than of protons bombarding the same target. Although linac based neutrons sources are usually based on high energy proton based spallation reactions, for tens of MeVs projectiles the neutron yield of deuterons on light element targets is higher by more than a factor of 3 with respect to spallation. For example, while using a beryllium target, deuterons of 2 mA at 40 MeV, or 5 mA at 25 MeV, are enough to generate a thermal neutron flux that is equivalent to the flux available at the image plane of the neutron radiography apparatus at the Soreq IRR1 5 MW reactor. Tens of MeV deuterons on light element targets generate fast neutrons with a forward flux and neutron energy peaked around the beam energy divided by 2.5. Such a spectrum is ideal to produce isotopes using (n,2n), (n,p), (n,D) and (n,f) reactions and therefore open new and interesting opportunities for basic and applied research. These reactions are the basis for niche intense

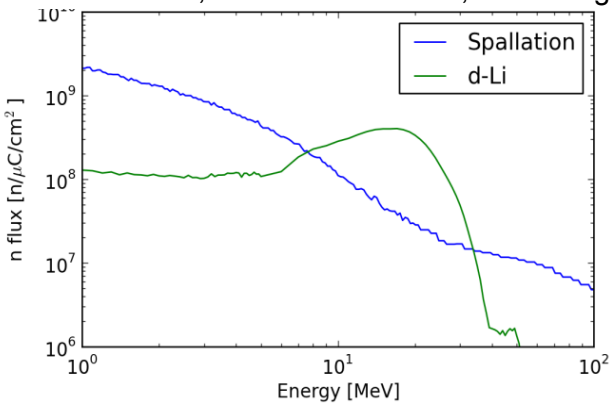

Figure 1: Forward neutron spectra comparison between 40 MeV deuterons on lithium (SARAF/IFMIF like) and spallation 1400 MeV protons on tungsten (ISOLDE). The spectra were measured and simulated 8 cm downstream the targets at zero degrees [1].

radioactive beams at SARAF Phase-II. For these reactions, the total amount of fast neutrons is two orders of magnitudes lower than in the spallation reaction. However, the neutron flux in the relevant range for these reactions (5-25 MeV) is higher by an order of magnitude (Fig. 1). The sources of this advantage are the low energy deuteron range in the target, which is shorter than spallation protons by an order of magnitude and the forward peaked structure of the stripping reaction.

The range of tens of MeVs protons or deuterons in matter is several millimeters, so the power density developed in a tens-of-kW irradiation target is significantly higher than in a MW spallation target. This requires development of new types of targets, based on both solid and liquid metal [2], and force the linac to deliver CW beams in order to avoid a high thermal load in the targets. It also requires developing special beam and target diagnostics and a procedure to slowly ramp the beam intensity on the targets.

System Specifications

The beam specifications that cover all the above requirements are summarized in Table 1.

Parameter	Value	Comment
Ion Species	Protons/Deuterons	$M/q \leq 2$
Energy Range	5 – 40 MeV	Variable energy
Current Range	0.04 – 5 mA	CW (and pulsed)
Operation	6000 hours/year	
Maintenance	Hands-On	Low beam loss

Table 1: SARAF Linac Top-level-requirements

The demands for variable energy, proton and deuteron currents in the mA range and low beam loss that meets the definition of a hands-on maintenance are met only by a superconducting RF linear accelerator. Independently phased cavities are needed in order to allow variable energy at the exit of the linac and efficient acceleration of more than one ion species. Superconducting cavities are needed for large beam apertures that moderate beam loss.

Phase-I status

Phase-I of the SARAF linac (Fig. 2) is composed of a 20 keV/u, 7 mA, 0.2 π mm mrad norm. rms emittance ECR ion source + LEBT, a 176 MHz, 4 m long, 250 kW, 4-rod RFQ, a 65 cm long MEBT and a 4.5 K 2.5 m long superconducting module housing 6 E_0=0.09 bulk Nb HWRs, 0.85 MV each and 3 6T solenoids in separated vacuum. The Phase-I linac routinely accelerates 1-2 mA CW protons up to 4 MeV and 10% duty factor deuterons up to 5.6 MeV. The design and commissioning of the acceleration components and the operation of the entire machine and the 13 m long HEBT line were published in recent years. The next section describes in detail additional beam tuning issues and technical challenges**.**

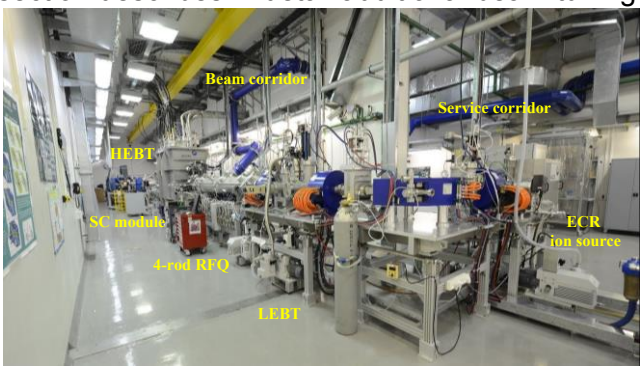

Figure 2: Phase-I 4 MeV protons and 5.6 MeV deuterons linac in the 4.5 m W, 5 m H and 25 m long beam corridor.

Figure 2: Phase-I 4 MeV protons and 5 MeV deuterons linac in the 4.5 m W, 5 m H and 25 m long beam corridor.

References

[1] D. Berkovits et al., "Operational Experience and Future Goals of the SARAF Proton / Deuteron Linac", Proceedings of LINAC 2012, Tel-Aviv (2012)100-105.

[2] S. Halfon et al., "High-power liquid-lithium jet target for neutron production", Review of Scientific Instruments 84 (2013) 123507-11.

A Novel Fireball Analysis for an Explosive Aerosolization Study

A. Sharon[*1], I. Halevy[1], D. Sattinger[1], L. Krantz[2], M. Pinhas[2], P. Banaim[1], I. Yaar[1]

[1]Nuclear Research Center Negev (NRCN), P.O.Box 9001, Beer- Sheva, Israel
[2]IAEC, Tel-Aviv, Israel

The final consequent risk following an explosion of radiological dispersal device (RDD) is highly depends on final radioactive particles' size distribution creates by detonation shock wave. Respirable, aerosols contribute to risk in a different way when compare it to non respirable aerosols or to ballistic, inertial, particles or even larger fragments. While aerosols (both, respirable and non respirable) are moving downwind with the cloud, heavier, inertial particles escape the initial fireball and deposited on the ground at a short distances from the ground zero (GZ) point. Respirable aerosols are risky when inhaled into the body (internal radiation) while non respirable have risk as an external exposure on the skin and from a distance. Hence, knowing the size distribution of the radioactive particles will, thus, enable more realistic risk assessment predictions.
We show here that detonation fireball fast multispectral radiometrycan be a novel tool that can be indicative to the final particles size distribution.

During Green Field[1] experimental project, ColoRad C7, fast multispectral radiometer (FMR) of IARD-Israel[2]was used. This unique tool was aimed to detect the fast temporal evolution of the fireball in time scales of micro seconds (sampling frequency of 250 kHz).
Fireball average radiant intensity was measured each four microseconds in four different spectral bands. The aim of using it is to be able to quantify the contribution of the different particles and detonation products to the total energy released following high explosive detonation. The measurement of the radiant intensity of the aerosols and other particles involved (detonation products, soot, carbon monoxide, carbon dioxide and dirt entrained into the fireball) and a comparison between clean and dirty shots enable to study the effect of agglomeration processes occur when dirt entrained into the fireball due to the vortices created following the detonation. Further analysis can yield the temporal variation of the radiant temperature and the effective radiant area.
Since most high explosives are under balanced to Oxygen we expect two radiate peaks following detonation: **the first one** is due to oxidation of explosive atoms and molecules (mainly H_2, C, CO and other metals, if exit (Al, Mg, etc.)) and **the second** is the late oxidation of detonation products with ambient Oxygen.
The conditions for the existence of the late energy pulse (called afterburn) are: free available ambient oxygen, material to be oxidized ("fuel") and "high enough" temperatures.
During the afterburn process, the C atoms of the explosive oxidize and become CO molecules and then CO_2 molecules if there is still available oxygen and high temperatures of more than 1750^oK degrees. At this stage entrained ambient dirt can agglomerate with the radioactive particles and thus to change the initial size of the particles and the all distribution.
Enhanced amount of dirt entrained into the fireball reduce its temperature and suppress the afterburn process. In such a case the 2^{nd} peak will be lower than the in case of a clean detonation where no dirt entrained. TNT is an example of explosive which isextremelyunder balanced to Oxygen (-74%). This means that in the case of clean detonation the first energy peak (detonation energy[3])yields only about one third of the total available energy (combustion energy).The rest two third might release during the afterburn stage (if exist!).
We have used the ColoRad C7 of IARD during different explosive atmospheric dispersion tests of RA material[1].
The spectral bands (all in the SWIR and MWIR range) were chosen in order to collect the molecular emission of the detonation products and the CO_2which we use as an afterburn indicator.

Figure 1: The ColoRad C7 (left) and high speed fireball snapshot 10 ms following TNT detonation (right).

2. Experimental results: radiant intensity and temperatures

A comparison between two shots of the same explosive charge (25 kg of TNT), one is at 0.55 m height above clean steel surface (on the left) and the other is on packed soil, dirt surface, is presented on figure 2.
The fireball radiant intensity of each of the four spectral bands is presented for each of the two shots.
One can easily recognize the two peaks of the energy pulses: the first one (around 1 ms) is related to the detonation energy and the second (around 30-50 ms) is the after burn contribution of later oxidation, mainly due to the emission of the CO_2.

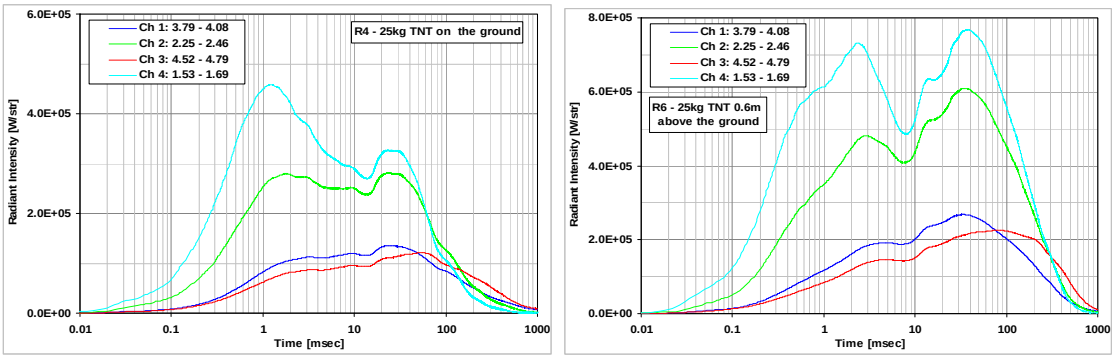

Figure 2: Fireball radiant intensity of clean (right) and dirt (left) of 25 kg of TNT charges.

The 1st and the 2ndpeaksratiofor each fireball is different when comparing the clean and the dirt shots. In the case of the clean shot, much lower amount of ambient dirt was entrained into the fireball and thus high temperatures were exist to support higher afterburn process. On the other hand, the dirt shot involves higher amount of soil that entrained by the fireball strong vortices, reduce the temperature and suppress the oxidation of the C atoms into CO_2, thus resulting in a lower after burn peak.
RA particle size distribution will be different for the two shots, even though the charges were similar! We can, thus, use the CO_2 radiant intensity (or power) as indicator for the fireball cleanness for certain explosive type. In the next stage it will be related to the reduction of the fraction of fine aerosols due to agglomeration with ambient dirt.

3. Summary

Fast multispectral radiometry of detonation fire balls is using for the study of the dynamic physical and chemical processes in the fireball. The after burn intensity, mainly due to

CO_2emission can used as an indicator for the fireball cleanness which effect the final size distribution of RA particles disperse by high explosive charges.

References

1.A. Sharon et al. Ground deposition pattern of an explosive RDD, Israel Nuclear Society conference, February 2014, Dead sea, Israel.
2. IARD – Sensing solutions Ltd., Yagur, 30065, Israel.
3. P. A. Cooper, Explosive Engineering, WILEY-VCH, ISBN-0-471-18636-8 1996.

Radioactive Contamination Estimation from micro-copters or helicopter Airborne survey: Simulation and real measurements

I. Halevy, M. Ghelman, Y. Yehuda-Zada, A. Manor, S. Dadon A. Sharon and I. Yaar

Nuclear Research Center – Negev, P. O. Box 9001, Beer-Sheva 84190, Israel

One of the main advantages of acquiring aero-radiometric measurements lies in the high collection rate of data over large areas and rough terrain. Typical aero-radiometric system records and saves gamma ray spectrum, correlated with the GPS derived location information in regular time intervals of one to two seconds. Such data can be used to locate radiation anomalies on the ground, map ground contamination or track a radioactive airborne plume. Acquiring spectral data of this type allows separation of natural radioactivity from that of man-made sources and identification of specific isotopes, natural or man-made.

The data acquisition can be done by helicopter or micro-copters at wide range of heights from few meters to few kilometers.

Usually the flight altitude will be kept constant to make the data analysis easier. Rough terrain will jeopardize that assumption. The radioactive particles are not always on the ground, they can be in a cloud above the ground or on roofs or trees. Speed of survey with a helicopter is in the range from hovering to ~120 Knots, while the speed of micro-copters is much lower, from hovering to ~30 Knots. Both, the helicopter and the micro-copters are suffering from limited abilities while severe weather conditions.

The main advantages of micro-copters are the ability to fly even indoor and without exposing the measuring team to radiation or extra flight risks.

When the survey is done or even during the survey, the main challenge is to estimate the radiation field and the contamination in the scene.

An iterative algorithm was suggested to estimate the radioactive contamination for analyzing an airborne survey [1].

In that work this algorithm will be tested on real scenario while spreading radioactive material, ^{99m}Tc, simulating an RDD events by explosion [2, 3].

In those simulations it is clear that a lower-height survey can improve the space resolution. Slow flight will improve the detection sensitivity but will take much more time.

This survey can be for detection only or it can bring also isotope identification by energy resolution. In our software, four energies windows can be set as our PDS-1000 flying detector.

We simulated a spread of radioactive sources on a radioactive background. A radioactive field at a survey height was calculated. From that data we found the spread of radioactive sources by our iterative algorithm.

There is no clear proof that the results are unique. The highest background we have the less significant map of spread radioactive sources can be achieved.

Few new results of simulation and real surveys are depicted in the next figures.

Figure 1: Mikro-Kopter / multi-rotor (upper)
Airborne radiation survey of ^{99m}Tc from "Green field" (Open field) test compared with ground survey (lower) [2].

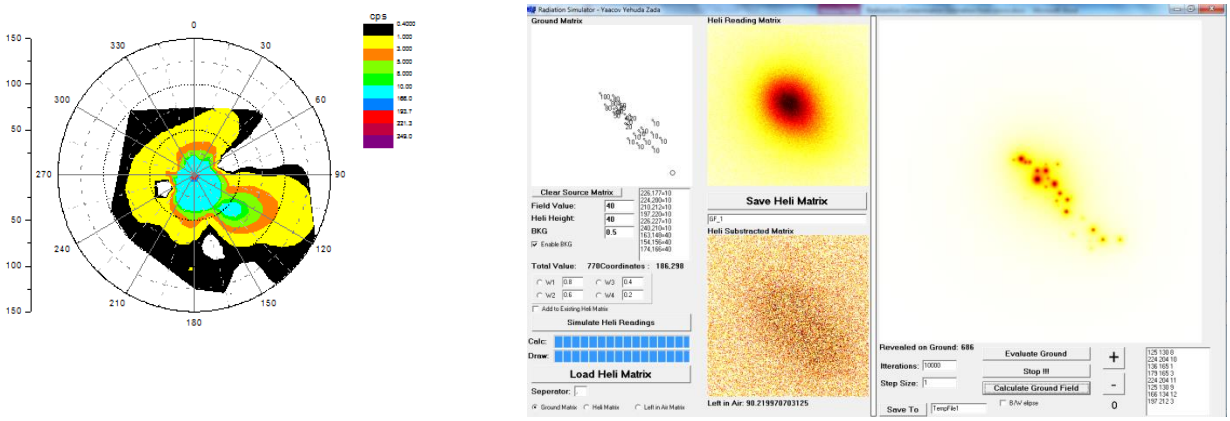

Figure 2: Airborne radiation survey analysis of ^{99m}Tc from "Green field" (Open field) test compared with ground survey [2].

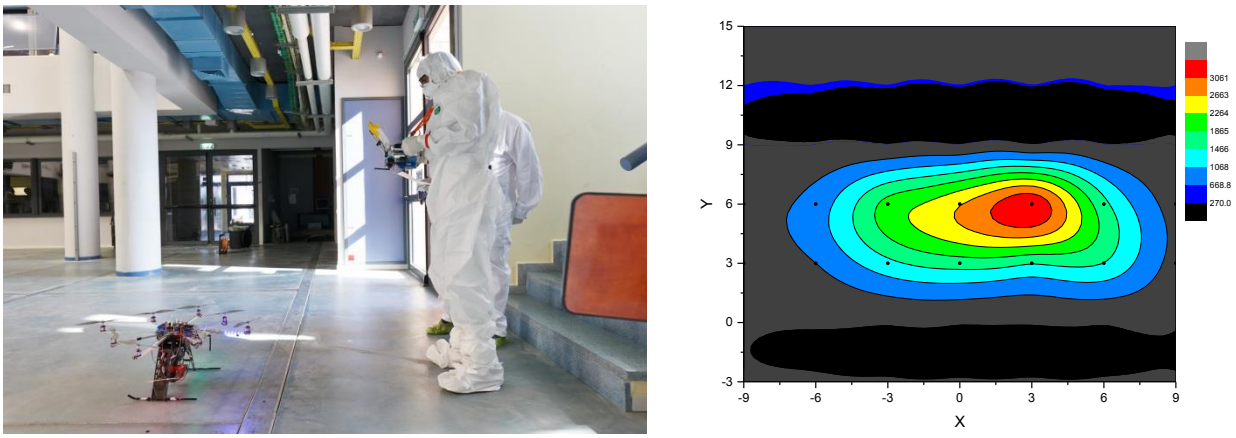

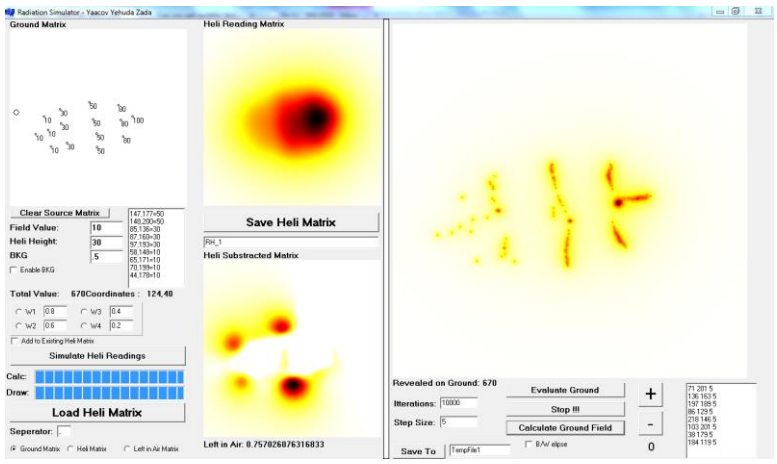

Figure 3: Airborne radiation survey of ^{99m}Tc from "Red-House" (Indoor) test compared with ground survey [3].

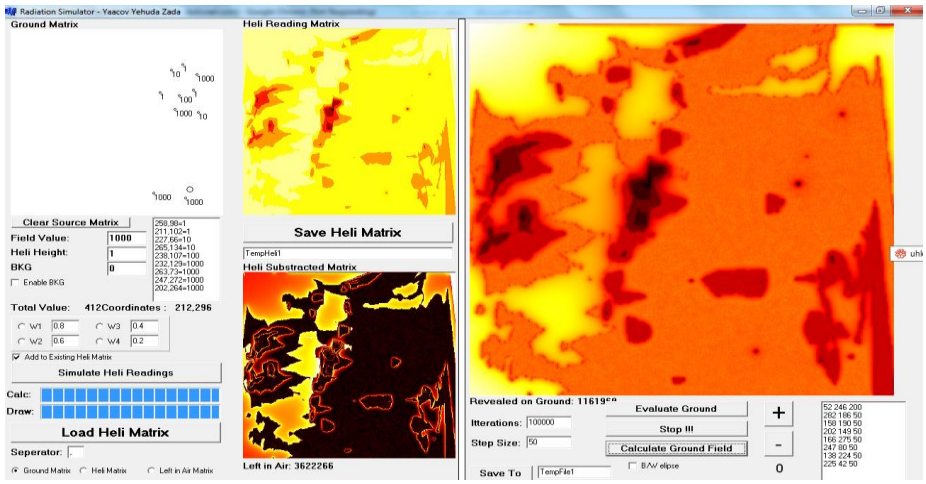

Figure 4: Airborne radiation survey of natural background from Air RAM 2000 measurements at the Government Wash area [4].

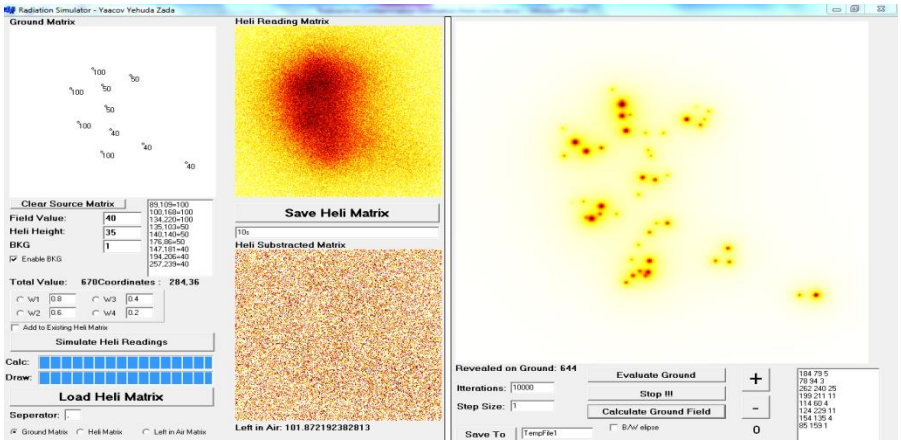

Figure 5: Airborne radiation simulation of natural background with ten spread sealed sources.

REFERENCES

[1] M. Ghelman, M. Sheinfeld, A. Manor, E. Vax, Y. Kadmon and D. Tirosh
The 25th Conference of the Nuclear Societies in Israel
16-18 February 2010, Crown Plaza Hotel, Dead Sea, Ein Bokek, ISRAEL

[2] A. Sharon, D. Sattinger, I. Halevy, R. Neuman, A. Ashkenazi and I. Yaar
Cloud Rise Model for a "Dirty Bomb" Event
The 25th Conference of the Nuclear Societies in Israel
16-18 February 2010, Crown Plaza Hotel, Dead Sea, Ein Bokek, ISRAEL

[3] Cloud Rise Model for an Explosion Inside a Building
A. Sharon, D. Sattinger, I. Halevy, R. Neuman, A. Ashkenazi and I. Yaar
The 25th Conference of the Nuclear Societies in Israel
16-18 February 2010, Crown Plaza Hotel, Dead Sea, Ein Bokek, ISRAEL

[4] Aerial Measuring System (AMS) / Israel Atomic Energy Commission (IAEC) Joint Comparison Study Report
Piotr Wasiolek and Itzhak Halevy: DOE/NV/25946-1941

Metallic Inert matrix fuel concept for minor actinides transmutation to achieve ultra-high burn-up

K.Lipkina, A.Savchenko, M.Skupov, A.Vatulin, A.Glushenkov, G.Kulakov, S.Ershov, V.Sorokin

A.A. Bochvar Institute of Inorganic Materials (VNIINM), P.O.Box 369, Rogova Street 5A, 123060, Moscow, Russia
e-mail : Ksenia.lipkina@gmail.com

Inert Matrix Fuel (IMF) is considered as one of the options for the incineration of excess Pu and minor actinides (MA) in fast or thermal reactors [1]. It can potentially provide higher burn-up than current fuel form, making it a promising alterative for future generation of nuclear power reactors.
Presently there are numerous concepts and versions of IMF element designs for burning civil and weapon grade plutonium. The most currently studied versions compromise pellet type fuel elements with an inert matrix based on zirconia or spinel. The disadvantages inherent in those versions of IMF, i.e. low thermal conductivity and the absence of metallurgical bond between cladding and fuel pellets reduce their serviceability during transients [2].
The goal of investigations is to propose the concept of IMF achieving high burn-ups that can be produced by simple technology and comply with requirement for “Rock-fuel”.
This can be achieved by replacing ceramics inert matrix on metallic inert matrix and additionally, we propose to change the pelletized design for a design where metallic inert matrix forms a metallurgical bond between the fuel and cladding. This bond provides high thermal conductivity while serving to protect against fuel-cladding interactions.
The proposed IMF has a heat conducting metal matrix and an isolated arrangement of PuO_2 in a fuel minielement. The fuel minielement is a thin-walled stainless steel tube, 1.4-2.5 mm in the diameter. It is filled with PuO_2 powder or granules (60-70 % vol.), sealed and placed within a fuel element. Aside from PuO_2, also oxides of other actinides may be loaded into a fuel minielement. Actinide oxides can be produced by pyrochemical method, $(Er,Y,Pu,Zr)O_{2-x}$ microspheres, prepared by internal gelation process (such as at ITU and PSI) can be also implemented (Fig.1).

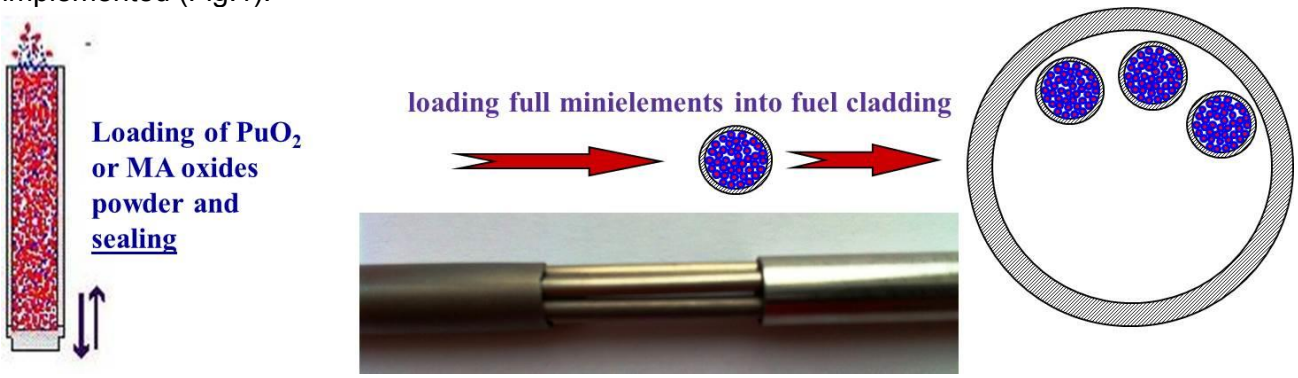

Fig.1 Scheme of loading of PuO2 or MA oxides powder and minielements into fuel cladding.

A fuel mini-element has the following functions:
1. To prevent fuel from interaction with the matrix and cladding as well as providing protection against corrosion.
2. As a barrier against fission products release.
3. To accommodate fuel swelling.
We undertook experiment-calculated studies of fuel quantity in IMF element depending on a fuel element design, quantity of fuel minielements (4 or 6) and their sizes (Table 1).The purpose of experiments is to evaluate the maximum quantity of fuel to be inserted into novel IMF design for thermal and fast reactors.
For thermal reactors with zirconium cladding, 9.1×0.7 mm, we implemented four zirconium minielements, 2.5×0.15 mm, or six zirconium minielements, 2.2×0.15 mm. For fast reactors with steel cladding, 6.9×0.4 mm, we implemented four steel minielements, 2.1×0.12 mm, or six steel

minielements, 1.8×0.12 mm (Fig. 2). For the fuel kernel itself we used UO_2 powder instead of PuO_2, 40-70 μm sized produced by UO_2 pellets grinding. The average volume fraction of UO_2 powder inside fuel minielement was 65% [3].

Table 1.Volume fraction of fuel (UO_2) under the cladding in various designs of fuel elements.

Reactor type	Volume fraction of fuel (UO_2), (%)	
	4 mini-elements	6 mini-elements
Thermal reactors with zirconium cladding, 9.1×0.7mm	21	23
Fast reactors with steel cladding, 6.9×0.4 mm	24	26

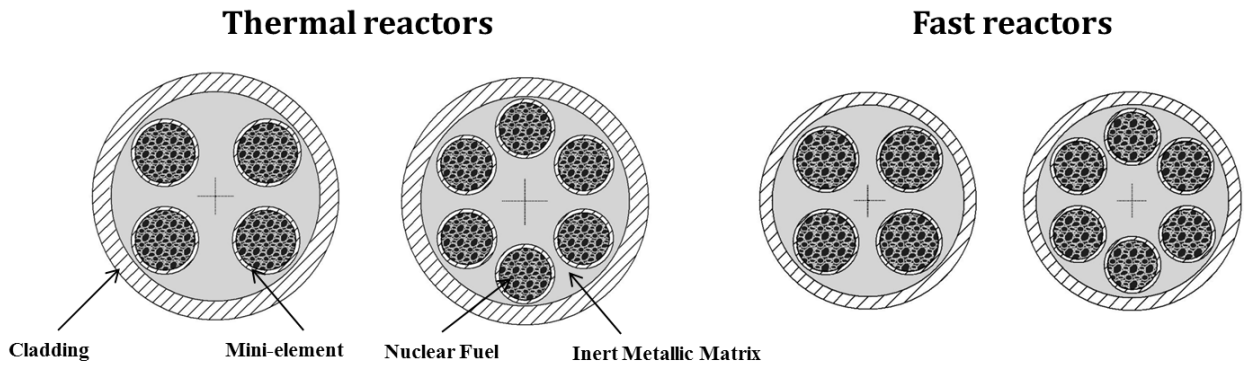

Fig. 2. Schematic cross-section of IMF with four and six minielements.

The total volume fraction of PuO_2 in a fuel element may be varied in average from 5 to 25 %, which is enough for thermal and fast reactor cores. Variations (diminishing volume fraction) can be made by changing the fuel-element diameter, implementation of mixture of PuO_2 and inert material as well as implementation of $(Er,Y,Pu,Zr)O_{2-x}$ microspheres.
Peculiarities of involving novel IMF design into nuclear fuel cycle are considered. Pu of poor quality with MA from spent PWR fuel, particularly spent MOX fuel, after pyrochemical reprocessing can be used as a fissile material. Then it would be delivered to fast or thermal reactors with the achievement of very high burn–up, followed by direct geological disposal as the “Rock- fuel”. The other option – to use fertile Pu+MA from FR after mechanical separation in case of application composite U-PuO_2 fuel in FRs [4].

References

[1] C. Degueldre, J.M. Paratte Concepts for an inert matrix fuel, an overview J. Nucl. Mater. **1-6**, **274** (1999).
[2] C. Degueldre “Inert Matrix Fuel has the potential to produce electricity while burning up more plutonium” Actinide Research Quarterly. Nuclear Materials Technology/ Los Alamos National Laboratory, 1st/2nd quarter **23-30,** (2003).
[3] A.M. Savchenko, A.V. Vatulin, A.V. Morozov, O.I. Uferov, S.A. Ershov, A.V. Laushkin, S.V. Maranchak, Y.V. Konovalov, Z.N. Petrova, E.K. Malamanova, Main results of the development of dispersion type IMF at A.A. Bochvar institute, J. Nucl. Mater. **26-31**, 396 (2010).
[4] A. Savchenko, A. Vatulin, K. Lipkina, G. Kulakov, et all, Prog. Nucl. Energy in press, **1-7** (2013), http://www.sciencedirect.com/science/article/pii/S014919701300200X

Effects of Helium Implantation on the Mechanical Behavior of 100nm-diameter Iron Nano-pillars

Peri Landau[1,2], Qiang Guo[2,3], Peter Hosemann[4], Yongqiang Wang[5], Julia R. Greer[2,6]

[1] *Department of Physics, NRCN, P.O.B 9001, Beer Sheva, Israel*
[2] *Department of Materials Science and Applied Physics, California Institute of Technology, 1200 East California Boulevard, Pasadena, CA, USA, 91125.*
[3] *State Key Laboratory of Metal Matrix Composites, Shanghai Jiao Tong University, 800 Dongchuan Road, Shanghai, P.R. China, 200240*
[4] *Department of Nuclear Engineering, University of California at Berkeley, Berkeley, CA, USA, 94720.*
[5] *Ion Beam Materials Laboratory, Los Alamos National Laboratories, Los Alamos, NM, USA, 87545*
[6] *The Kavli Nanoscience Institute, California Institute of Technology*

Ferritic and ferritic-martensitic steels are being considered for cladding in the next generation nuclear reactors as well as fusion applications and spallation source materials. For these applications, helium (He) accumulation due to the high appmHe/dpa ratio, represent a matter of concern rooted in the detrimental effects of irradiation on the mechanical performance. The investigations of the effects of ion beam irradiation on mechanical properties of iron represent a useful way to simplify the complexity of irradiation process. This study is focused on the effects of mostly He bubbles on the mechanical behavior and deformation mechanisms.

<101>-oriented cylindrical single crystalline Fe samples with diameters of 100nm and heights of 1μm were implanted with 0.36±0.06 at. % helium throughout their gauge sections to produce 1.5nm-diameter He bubbles (Figure 1). Uniaxial deformation experiments revealed a 40% higher yield and ultimate strengths in tension and a 25% higher yield strength and flow stress at 10% plastic strain in compression for implanted samples compared with as-fabricated ones due to He bubbles and radiation-induced defects. Observed tension-compression asymmetry in implanted pillars was attributed to the non-planarity of screw dislocation cores and to twinning-antitwinning deformation typical of bcc metals and the interaction between dislocations and He bubbles. Compressive stress-strain data in both sets of samples had three distinct regimes: (1) elastic loading followed by (2) discrete strain bursts during plastic flow with significant hardening up to strains of 5%, and (3) “steady state” discrete plasticity characterized by nearly-constant average flow stress. Each regime is discussed and explained in terms of competition in the rates of dislocation multiplication and dislocation annihilation.

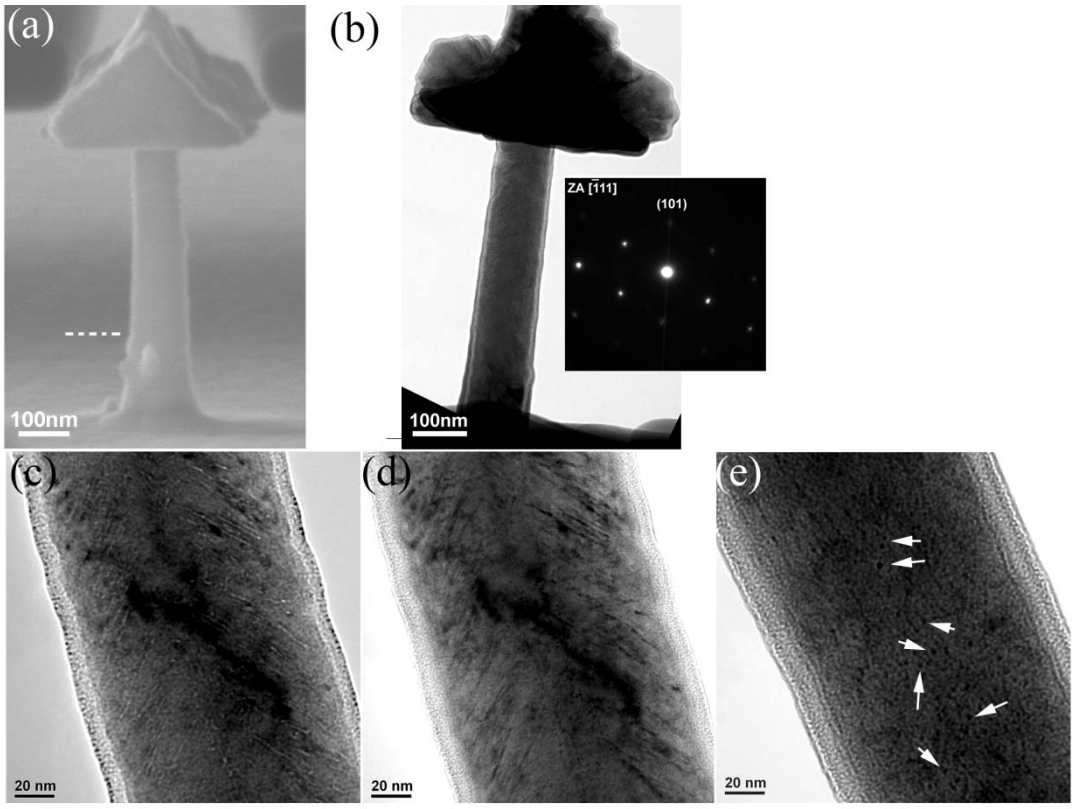

Figure 1: (a) A SEM image of a typical over-plated 100nm-diameter Fe nano-pillar at an orientation that shows the shape and contour of the pillar's triangular-prismatic top. The facets in the top prism are inclined at ~45º to the pillar axis. (b) Bright field TEM image of a Fe nano-pillar with the corresponding diffraction pattern. The pillar axis is close to the [101] direction. (c) Under-focus image of He bubbles that appear as bright dots with a dark fringe. (d) Over-focus image of He bubbles that appear as dark dots with a bright fringe. The He bubbles form a herring-bone-like arrangement parallel to {110} planes throughout the pillar height. (e) Over-focus image of He bubbles at an orientation ~90º away from the orientation in (d) where the rectangular facet of the prism-shaped head is perpendicular to the electron beam, showing a uniform distribution of bubbles throughout the pillar height. A few bubbles are pointed to by the arrows in the image.

Prospects for a NPP in Israel

IlanYaar

Ministry of National Infrastructures, Energy & Water Resources
Office of the Chief Scientist, 14 Hartom St., Jerusalem, 9136002, e-mail: ilany@energy.gov.il

The 2050 energy master plan for Israel[i] predict a shortage of up to 30% in the electrical producing resources of Israel by the year 2050. The plan also reviewed potential energy sources capable of closing this gap, including nuclear energy. Nuclear energy was found to be highly beneficial, considering environmental and economic considerations, although the writers of the master plain have recognised that there are major gaps that should be overcome before this option can be considered as a concrete alternative.
In order to close these gaps, the Ministry of National Infrastructures, Energy and Water Resources has recently initiated together with the Israel Atomic Energy Commission (IAEC) and the Prime Minister's Office, a prefeasibility study of a Nuclear Power Plant (NPP) in Israel. The main Goal of this study was to determine and analyze the major obstacles in the way to constructing and operating an NPP in Israel. This study was carried out by a team composed of experts from the Ministry, IAEC, Israel Electric Company (IEC) and the Academy.
The team of exports identified several "stumbling blocks" that have to be resolved in the way to construct the first a NPP in Israel; and recommended to continue the NPP pre-feasibility study in order to resolve them while closing or minimizing the major knowledge gaps in this subject in Israel[ii].
Israel is a small and highly populated country. Therefore, allocating a site suitable for the constructing of a NPP according to the IAECLicensing & Safety Division, Seismological, Geological and Geotechnical Siting Criteria and Guidelines[iii] is not a simple task. The only area that was found suitable for this purpose so far is a small area (0.75 square km) located at the south part of Israel.
One of the main stumbling blocks identified during the pre-feasibility study was the need to preserve this site from one hand, while trying to find more sites with the same potential on the other. Others stumbling blocks are the special security considerations that have to be taken into consideration for a NPP in Israel, the need to cool a large NPP far away from a large water resource.
In this work, the incentive for building a NPP in Israel will be presented together with the major stumbling blocks that have to be resolved in order to shorten the time needed for the construction of the first NPP.

---

[i] The Ministry of Energy and Water Resources and TAHAL Group, Master plan for energy economy in Israel, 147420-ד13-307 (Dec 2013) Draft (Original document was published in Hebrew).

[ii] Y. Levanon et al., Final summary of the work conducted by the team of exports in the pre-feasibility study for the construction of the first NPP in Israel, The Ministry of National Infrastructures, Energy and Water Resources (Feb 2013) Draft (Original document was published in Hebrew).

[iii] IAEC, Licensing & Safety Division, Seismological, Geological and Geotechnical Siting Criteria and Guidelines, (March 1985).

Non-magnetic ground state of PuO_2

A. B. Shick,[1] J. Kolorenc,[1] L. Havela,[2] T. Gouder,[3] R. Caciuffo[3]

[1] *Institute of Physics, ASCR, Na Slovance 2, 182 21, Prague, Czech Republic, e-mail: shick@fzu.cz*

[2] *Charles University, Ke Karlovu 5, CZ-12116, Prague, Czech Republic*

[3] *European Commission, JRC, Institute for Transuranium Elements, Postfach 2340, 76125 Karlsruhe, Germany*

In order to fully utilize the potential of nuclear power, maintaining at the minimum level the risks associated with the deployment of this technology, it is necessary to solve the problems of characterization, treatment, and disposal of high-level nuclear waste. On the time scale of several hundred years, the waste from the open fuel cycle will predominantly contain Pu and minor actinides. Their geological disposal requires a waste handling technology of exceptional durability, with highly reduced risk of accidental events. That is why the comprehensive knowledge of the physical and chemical properties of actinide-based oxides (AnO_2, An = Th, U, Np, Pu, Am, Cm), which constitute the main part of the long-lived nuclear waste, remains a key topic of condensed matter theory.

PuO_2 crystalises in the well-known CaF_2 fluorite structure, with eight-coordinated Pu, and four-coordinated O. For the divalent oxygen, the stoichiometry implies $5f^4$ configuration for Pu^{4+}. It is an insulator with a band gap of 1.8 eV and a temperature independent magnetic susceptibility. Whilst experimentally the absence of magnetism is clear, its theoretical understanding remains controversial. The crystal-field (CF) theory [1] explains this non-magnetic behaviour in terms of a Γ_1 nonmagnetic singlet ground state, which results from the CF splitting of the J=4 $^5\mathbf{I}_4$ manifold, in agreement with the inelastic neutron scattering spectra. However, the experimental value of the magnetic susceptibility is only 50% of what one would expect from the CF model, and its temperature dependence is weaker than the one predicted by the CF model.

The conventional density functional theory (DFT) in the local spin density (LSDA) and generalized gradient (GGA) approximations falls short to explain the insulating character of PuO_2 as well as other actinide oxides [2]. The hybrid exchange-correlation functionals [2], as well as LDA+U [3] yield the anti-ferromagnetic ground state in disagreement with experiments.

Here, we make use of a combination of LDA with the exact diagonalization of the Anderson impurity model (ED) and show that the LDA+ED calculations with the Coulomb U=6.5 eV and the exchange J=0.5 eV yield a non-magnetic singlet ground state with f-shell occupation of 4.5 at the Pu atoms. The non-integer filling of the f-shell is a consequence of a hybridization with the p-states of oxygen [4].

The LDA+ED electronic structure is shown in Fig.1. PuO_2 is calculated as an insulator with a band gap of 1.8 eV and the calculated density of states (DOS) is consistent with the experimental results of photoelectron spectroscopy (PES). The ground state is a singlet formed by the Pu-f and O-p states. Since it is a singlet, any magnetic or multipolar degree of freedom is frozen when the temperature is well below the gap between the ground state and excited states. The calculated energy difference between the ground state and the first excited states (triplet) is 126 meV in agreement with the experiment. Neither the ground state nor the excited states are exact crystal-field states since they involve the O-p ligand states.

Analogously to the CF theory, the LDA+ED can be used to estimate the magnetic susceptibility χ and its temperature dependence by adding the action of an external magnetic field. The susceptibility calculated for U=6.5 eV and J=0.5 eV is shown in Fig. 2 in comparison with the CF model. The hybridization of the ***f*** orbitals with the ligand states reduces the magnitude of χ as well as its temperature dependence and hence brings the theory closer to the experimental findings. With an increase of the exchange-J the

temperature dependence is further suppressed, and the magnitude of χ is only about 35 % larger than the experiment.

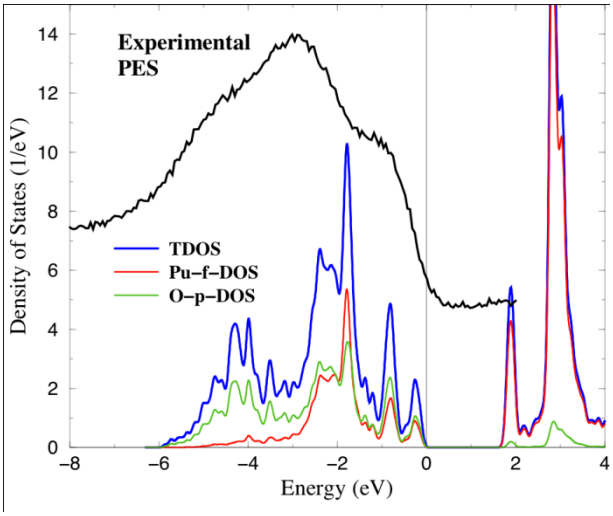

Fig. 1. The total, O-p and Pu-f-projected DOS from LDA+ED calculations, together with the experimental PES He-II spectrum. Note that the PES spectrum s adjusted to match the upper edge with the zero energy.

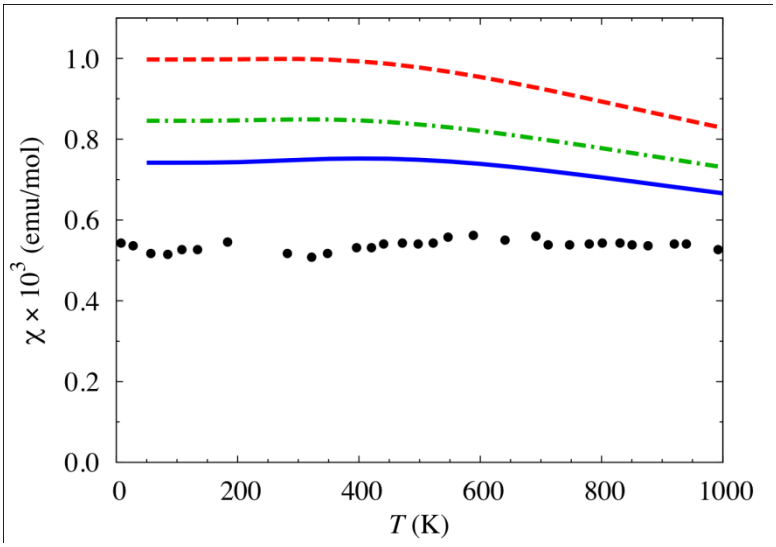

Fig. 2. Temperature dependence of the molar magnetic susceptibility calculated in the CF theory (red dashed line) and in the LDA+ED for *U*=6.5 eV and *J*=0.5 eV (green dot-dashed line), and *J*=0.6 eV (blue solid line). Black dots are the experimental data.

In summary, making use of the LDA+ED calculations we obtain a non-magnetic, insulating ground state with 4.5 electrons. This singlet ground state and the consequent non-magnetic behavior have a lot in common with the outcome of the CF theory. Significant improvement is that LDA+ED achieves these features for a realistic non-integer occupation of the Pu *f* orbitals.

References

[1] P. Santini et al., Rev. Mod. Phys. **81**, 807 (2009).
[2] X.-D. Wen et al., Chemical Review **113**, 1063 (2013).
[3] M.-T. Suzuki, N. Magnani, and P. M. Oppeneer, Phys. Rev. **B 88**, 195146 (2013).
[4] A. B. Shick, J. Kolorenc, L. Havela, T. Gouder, and R. Caciuffo, Phys. Rev. **B 89**, 041109 (2014).

Ab Initio Investigation of the Uranium-Oxygen System

N. A. Brincat[1], S.C. Parker[1], M. Molinari[1], G. C. Allen[2], M. T. Storr[3]

[1] *Department of Chemistry, University of Bath, Bath, BA2 7AY, United Kingdom*
e-mail: n.brincat@bath.ac.uk

[2] *Interface Analysis Centre, University of Bristol, Bristol, BS2 8BS, United Kingdom*

[3] *AWE, Aldermaston, Reading, Berkshire, RG7 4PR, United Kingdom*

UO_2, the most commonly used nuclear fuel globally, is regularly exposed to oxidising conditions during handling, storage and reactor operation. A number of stable higher oxides exist that also play a role in the nuclear fuel cycle; although they have not been researched as rigorously as UO_2[1]. The uranium oxides can be split into two broad categories: the fluorite based phases (UO_2, U_4O_9, U_3O_7 and U_2O_5) and the layered type structures (U_2O_5, U_3O_8 and UO_3), with the transformation occurring between the *γ*- and *δ*-U_2O_5 polymorphs. Fluorite based phases consist of UO_2 supercells (4 x 4 x 4) housing arrangements of oxygen point interstitials or oxygen defect clusters[2] whilst the layered oxides comprise alternating UO and O layers, often with species resembling the uranyl (UO_2^{2+}) ion[3].

In the present work we employ DFT (GGA, meta-GGA and HSE) simulations to reproduce the experimentally observed structure of UO_2, accounting for 3*k* non-collinear antiferromagnetic ordering, and calculate the elastic and electronic properties to a high degree of accuracy. These calculations are extended to the layered uranium oxides, making predictions of their fundamental properties, identifying their preferred charge configurations and assessing their order of stability. Furthermore we examine fluorite based phases of U_4O_9, U_3O_7 and U_2O_5 stoichiometry using UO_2 supercells (12, 24 and 48 atoms) containing additional oxygen point interstitials or defect clusters as a model for the larger (850 atom) unit cells reported experimentally. These models provide valuable insight into the properties of the fluorite based oxides and a useful comparison of stability against the layered type phases.

References

[1] G.C. Allen and N.R. Holmes, *J. Nuc. Mat.,* **231-237**, 223 (1995)

[2] D.A. Andersson *et al*, *Inorg. Chem.,* **2769-2778**, 52 (2013)

[3] P.C. Burns, *Canadian Mineralogist,* **1839-1894**, 43 (2005)

Origin of the exceptional Ising behavior of quasiparticles in the hidden-order material URu_2Si_2

Miroslaw Werwinski[1], Jan Rusz[1], John A. Mydosh[2], Peter M. Oppeneer[1]

[1] *Department of Physics and Astronomy, Uppsala University, Box 516, S-75120 Uppsala, Sweden*
[2]*Kamerlingh Onnes Laboratory, Leiden University, NL-2300 RA Leiden, The Netherlands*
e-mail: peter.oppeneer@physics.uu.se

The hidden order (HO) phase emerging below 17.5K in the heavy-fermion compound URu_2Si_2 has drawn considerable attention. In spite of intensive experimental and theoretical investigations the origin of the arising electronic order could not be unambiguously explained. Multifarious theories have been proposed to explain the intriguing appearance of the HO phase [1]. Since the actinide 5f electrons can adopt localized or itinerant character, theories based on localized 5f behavior have been proposed as well as competing theories based on the assumption of itinerant 5f behavior; in the latter the existence of a Fermi surface instability is central [2-4].

Experimental evidence in favor of either localized or itinerant 5f behavior is crucial. Recent experiments drew attention to a previously unrecognized aspect of the HO quasiparticles (QPs) in URu_2Si_2. A g-factor anisotropy exceeding 30 was estimated, implying that HO emerges out of QPs with giant Ising anisotropy [5]. The Ising behavior of the near Fermi-energy QPs was reported to support the picture of localized 5f states, possibly having a small hybridization with conduction electrons [5]. This extreme magnetic anisotropy is central to the hastatic order theory in which a local $5f^2$ crystal field doublet induces the Ising character [6]. For bandlike electrons, in general a g-factor of 2 with little anisotropy is expected which would definitely exclude delocalized 5f behavior [5,6].

We show on the basis of relativistic DFT-based electronic structure calculations that the bandlike 5f electrons in URu_2Si_2 exhibit surprisingly a colossal Ising behavior, a property which is truly exceptional for itinerant electrons. The calculated anisotropy of the total moment on one of the U atoms in URu_2Si_2 is shown in Fig. 1b; the moment vanishes steeply for directions away from the tetragonal c-axis, i.e. the moment displays a huge Ising anisotropy. The origin of the unique Ising anisotropy is found to be due to a combination of the peculiar nesting of Fermi surface states and the strong spin-orbit interaction. Our results have important consequences for models applicable to unveil the nature of the HO.

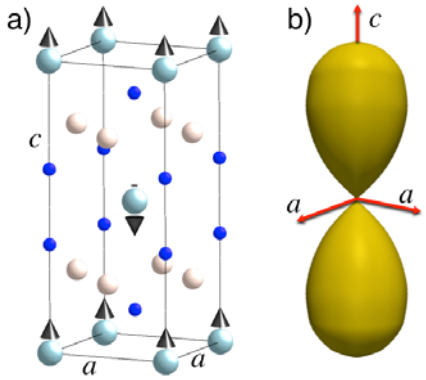

Fig. 1. a) The simple tetragonal unit cell of URu_2Si_2 that was employed in the calculations with equilibrium directions of uranium moments indicated. Large spheres depict U atoms, medium large spheres Ru, and small spheres Si atoms. b), Three- dimensional plot of the magnitude of the total U moment calculated as function of the direction in the unit cell.

References

[1] J.A. Mydosh and P.M. Oppeneer, Rev. Mod. Phys. **83**, 1301 (2011).
[2] S. Elgazzar et al., Nat. Mater. **8**, 337 (2009).
[3] P.S. Riseborough, B. Coqblin, and S.G. Magalhaes, Phys. Rev. B **85**, 165116 (2012).
[4] T. Das, Sci. Rep. **2**, 596 (2012).
[5] M.M. Altarawneh et al., Phys. Rev. Lett. **108**, 066407 (2012).
[6] P. Chandra, P. Coleman, and R. Flint, Nature **493**, 621 (2013).

Vibrational properties of the light actinides

Johann Bouchet,[1]

[1] *CEA, DAM, DIF, F-91297 Arpajon, France*
e-mail: johann.bouchet@cea.fr

Despite general interest in f-electron elements, details about their phonon-dispersion relationships are very limited. Experimentally, this fact is due to the great difficulty of realizing such experiments. The usual technique for the study of phonons, based on neutrons scattering, needs crystals large enough and isotopes with a small neutron absorption cross section. Lanthanides and actinides hardly fulfil these two conditions, not to mention the radioactivity of some of them. But recently, a new hope has emerged with several works, using inelastic x-ray scattering, mostly on U[1,2] and Pu[3]. Nevertheless all this experimental issues show that theoretical works are needed to tackle the f electrons systems elastic properties. Unfortunately these calculations are far from being straightforward [4]. Theoretically, the most important problem comes from the difficulty to treat correctly the f-electrons and the relativistic effects needed in such heavy materials.

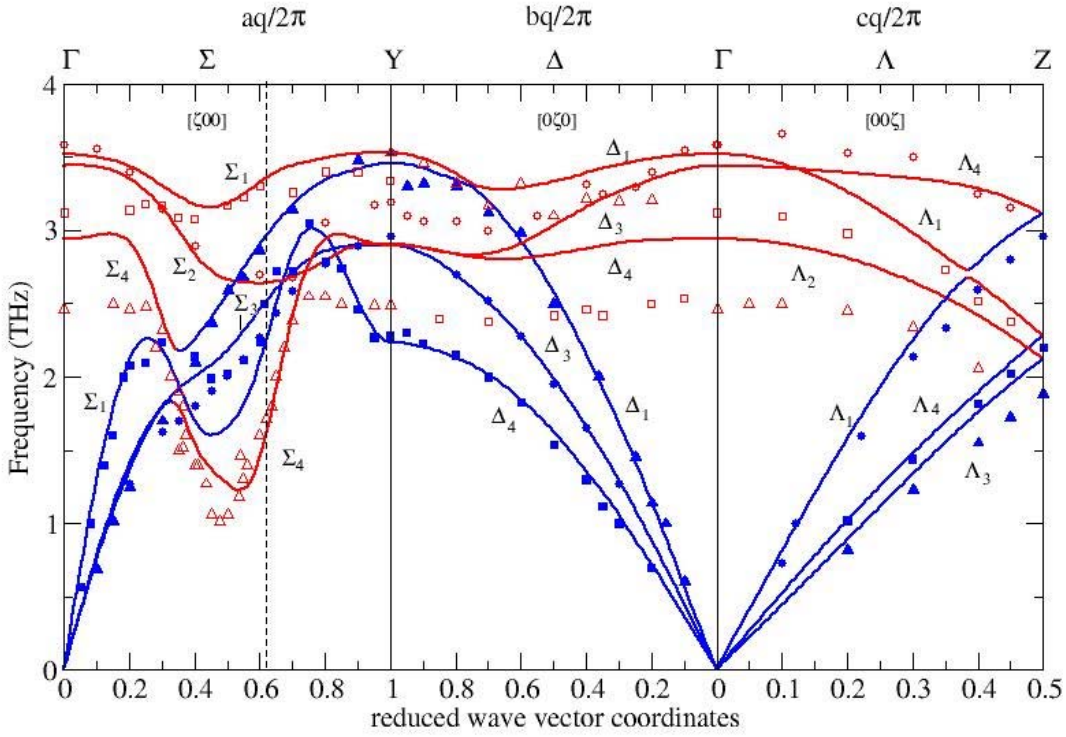

Fig. 1.Calculated phonon-dispersion curves for α-U at the lattice parameter corresponding to static equilibrium. Experimental neutron-scattering data are denoted by symbols.

Here we apply the Density functional Perturbation Theory (DFPT) implemented in the ABINIT package to study the phonon spectrum of Th[5], Pa and U [6]. We have also investigated the effect of pressure on the elastic constants of Th, Pa, U and Np. We show how several of the Born stability criteria are violated at the phase transitions occurring in light actinides.
In the α-U phase there are remarkable phonon anomalies in the [100] direction [7], see figure 1. At low temperature (T_0 = 43 K) a phase transition takes place to a new complicated structure (α_1-U), which is described as a charge-density wave (CDW). Uranium is the only element discovered so far to exhibit such a phase transition at ambient pressure. As a function of pressure the CDW disappears at ~ 1.5 GPa, and, at the same pressure, the

superconducting temperature reaches a maximum of ~ 2 K, and then decreases with further pressure. Using DFPT we calculate the electron-phonon coupling, the phonon linewidth and their evolution in pressure to discuss the interplay of charge-density waves and superconductivity in uranium [8]. The CDW has a strong impact on the elastic properties of uranium[9]. Here we have measured the equation of state of uranium compressed in a DAC up to 60 GPa, with X-ray diffraction, at 298K and 20K (below the CDW transition)[10]. The most hydrostatic pressure transmitting medium in this conditions, helium, has been used for these experiments in order to obtain reference EoS parameters (in particular, bulk modulus) suitable for comparison with ab initio calculations.
In addition, elastic constants have been calculated for the α_1-U structure at 0K. Using the quasi-harmonic approximation, the temperature effect on α-U lattice parameters and bulk modulus, see figure 2, have been calculated in order to generate an ab initio based 298 K P − V compression curve. The predictive character of DFT-GGA for the physical properties of uranium is discussed.

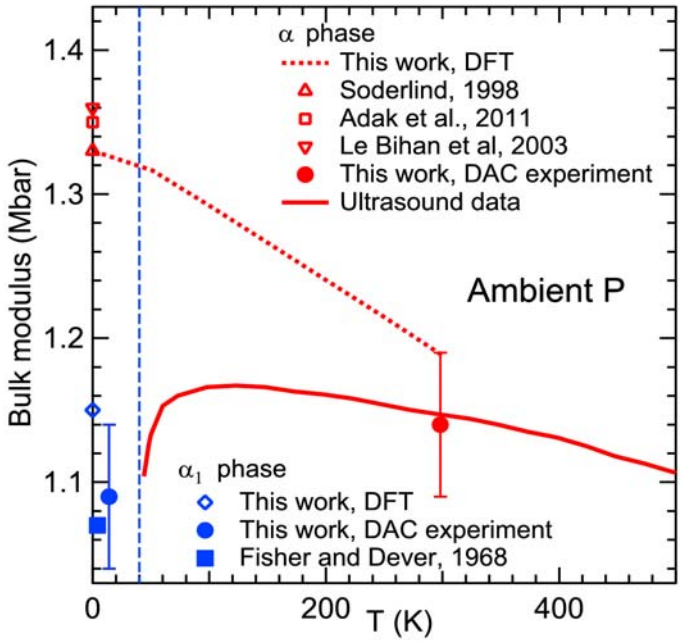

Fig 2. Variation of the bulk modulus of α-U and α1 -U with temperature at ambient pressure. Closed symbols and solid lines correspond to experimental data; open symbols and dashed line correspond to theoretical predictions. Ultrasound data for α-U are from Ref. 9. The vertical dashed line delimits the stability domains of α-U and α1 -U.
Oral presentation in Theory, electronic structure.

References

[1] M.E Manley et al. Phys. Rev. Lett. **86**, 3076 (2001).
[2] M.E Manley et al.Phys. Rev. B **67**, 052302 (2002).
[3] J. Wong et al. Science **301**, 1078 (2003).
[4] X. Dai et al. Science **300**, 953 (2003).
[5] J. Bouchet, F. Jollet and G. Zerah Phys Rev B, **74** (2006).
[6] J. Bouchet Phys Rev B, **77** (2008)
[7] W. P. Crummett, H. G. Smith, R. M. Nicklow, and N. Wakabayashi, Phys. Rev. B **19**, 6028 (1979)
[8] S. Raymond, J. Bouchet, G.H Lander et al., Phys. Rev. Letter, **107**, 136401 (2011)
[9] E. S. Fisher and D. Dever, Phys. Rev. **170**, 607 (1968).
[10] A. Dewaele, J. Bouchet, F. Occelli, M. Hanfland and G. Garbarino, Phys. Rev. B **88**, 134202 (2013)

Passive neutron interrogation in systems with a poorly characterized detection efficiency

Chen Dubi,[1] Elad Oster[1], Aharon Ocherashvilli, Bent Pedersen, Janus Hutszy[2]

[1] *Dep. Of Physics, Nuclear Research Center of the Negev (NRCN). POB 9001, Beer Sheva, Israel*
e-mail: chendb331@gmail.com.
[2] *JRC laboratory, Ispra, Italy*

Passive neutron interrogation for fissile mass estimation, relying on neutrons coming from spontaneous fission events, is considered a standard NDT procedure in the nuclear safeguard and safety community. Since most structure materials are (relatively) transparent to neutron radiation, passive neutron interrogation is considered highly effective in the analysis of dirty, poorly characterized samples. On the other hand, since a typical passive interrogation assembly is based on ^{3}He detectors, neutrons from additional neutron sources (mainly (α,n) reactions and induced fissions in the tested sample) cannot be separated from the main spontaneous fission source through energetic spectral analysis.
There for, applying the passive interrogation methods the implementation of Neutron Multiplicity Counting (NMC) methods for separation between the main fission source and the additional sources. Applying NMC methods requires a well characterized system, in the sense that both system die away time and detection efficiency must be well known (and in particular, independent of the tested sample).

Thinking of typical measurement in a typical assembly, it is safe to assume that the system parameters are well known, since they may be calibrated using well defined samples. However, in certain cases this might not be true: for instance, following the Fukushima Daiichi accident, the decommissioning process would require applying NMC on samples which might contain neutron absorbents in an unknown amount, creating a configuration in which the detection efficiency- which is assumed to be a system parameter in all traditional NMC methods- depends on the tested sample itself [1].
In addition, in recent years there is an academic and technological effort to extend the capabilities of neutrons interrogations to new settings. In particular, the problem of fissile mass estimation and detection in large containers is of utmost importance. Is such a setting, the system efficiency cannot be defined due to the spatial uncertainty on the location of the sample with respect to the detector ring. It should be mentioned that even in the most standard passive interrogation facility, a spatial uncertainty is expect, since the sample is often located in a sealed container.
In the present study, we introduce a new method, based on the SVM neutron multiplicity counting formalism [2], in which a prior knowledge of the system efficiency is not needed.
The method will be demonstrated on a set of measurement taken at the JRC laboratory, covering a large range of masses, detection systems and measurement time.
From a technical point of view, the interrogation facility itself is exactly the same as used in standard measurements, such as a standard coincidence counter, but with one restriction: data acquisition must be carried out in a LIST mode data acquisition machinery [3], recording the entire detection train digitally, rather than a single channel analyzer (SCA), which produces a train of TTL pulses, which are then fed into a neutron analyzer, based on the shift-register principle [4].
While at this point it is still hard to claim that the method is fully operational (mainly due to the limited data set at hand), we feel that it is safe to state that the results so form a good proof of feasibility of the method.

References

[1] T. Nagatani, S. Nakajima, T. Asano: Feasibility Study on Passive Neutron Technique Applied to Fuel Debris Measurement at Fukushima Daiichi Nuclear Power Plants, *proceedings of the 54th Institute of Nuclear Materials Management annual meeting, (2013).*

[2] C. Dubi, T. Ridnik, I. Israelashvili, J. Bagi, J. Huszti: A method for the estimation of fissile mass by measuring the number of neutron signals within a specific time interval, *Nuclear Instruments and methods A (NIMA)* **186-187**, 1658 (1989).
[3] J. Bagi, et al, Neutron coincidence counting with digital signal processing, *NIMA* **316 - 327** 608 (2009).
[4] N. Ensslin, W. Harker, M. Krick, D. Langner, M. Pickvell: Application guide to neutron multiplicity counting*, Los-Alamos manual*, LA-13422-M (1998).

Uranium(IV) Imidazolin-2-iminato Complexes: Synthesis, Structure and Catalytic Activity.

Isabell-Sarah R. Karmel,[1] Mark Botoshansky[1], Matthias Tamm*[2], Moris S. Eisen*[1].

[1] *Schulich Faculty of Chemistry, Technion – Israel Institute of Technology, Haifa 32000, Israel*
e-mail: karmel@techunix.technion.ac.il

[2] *Institut für Anorganische und Analytische Chemie, Technische Universität Braunschweig, Hagenring 30, Braunschweig 38106, Germany.*

The coordination chemistry of imidazolin-2-iminato ligands has been explored with various transition metals and lanthanides, exhibiting interesting structures with short M-N bonds and reactivities towards various organic substrates.[1] Herein, we present a new family of uranium(IV) complexes, bearing imidazolin-2-iminato moieties as ancillary ligands. The complexes $[U(Im^{tBu})_4]$ (**1**), $[U(Im^{Mes})_3(NMeEt)]$ (**2**) and $[U(Im^{Dipp})_2(NMeEt)_2]$ (**3**) were obtained by an acid-base reaction between the homoleptic $U(NMeEt)_4$ and respective neutral imidazolin-2-imine (Im^RNH), depending on the steric demand of the R substituent on the 1 and 3 position of the imidazoline backbone (Scheme 1). [2]

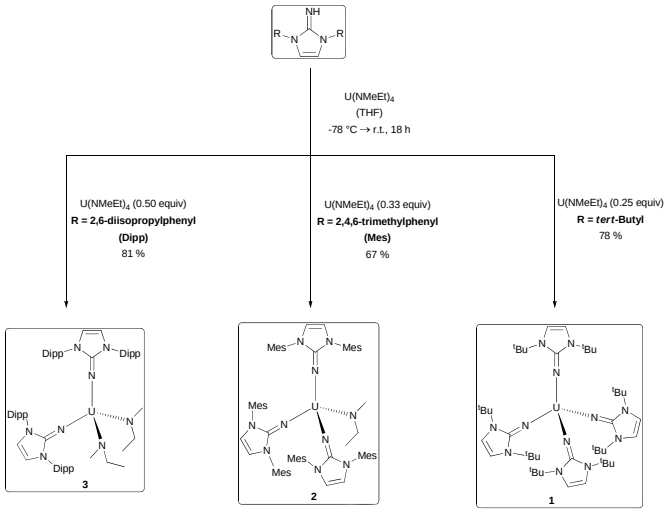

Scheme 1: Synthesis of complexes **1**-**3**.

Interestingly, the number of imidazolin-2-iminato ligands could not be varied by adjusting the reaction conditions, or the stoichiometry of the starting materials. The uranium complexes 1-3 display short U-N bonds, and large, almost linear U-N-C linkages, suggesting a substantial π-character of the U-N bond. Complexes **1**-**3** were investigated in the ring opening polymerization (ROP) of the cyclic ester, ε-caprolactone. While complexes **1** and **2** showed moderate activities at elevated temperatures, complex 3 displayed an extraordinary high activity ($7\cdot10^6$ $g(PCL)\cdot mol^{-1}\cdot h^{-1}$) at room temperature. In order to shed light on the mechanism of the ROP mediated by complex **3**, kinetic experiments were performed, revealing a first order dependence on catalyst and substrate. The mechanism of polymerization was compared with the two isolobal cyclopentadienyl uranium complexes **4**[3] and **5**[4] (Figure 1), revealing large differences in the polymerization rates and mechanisms. We will present the synthetic methods for the synthesis and structural details for the imidazolin-2-iminato complexes **1**-**3**, provide mechanistic and kinetic the details for the ROP of ε-caprolactone mediated by complexes **3**-**5**.

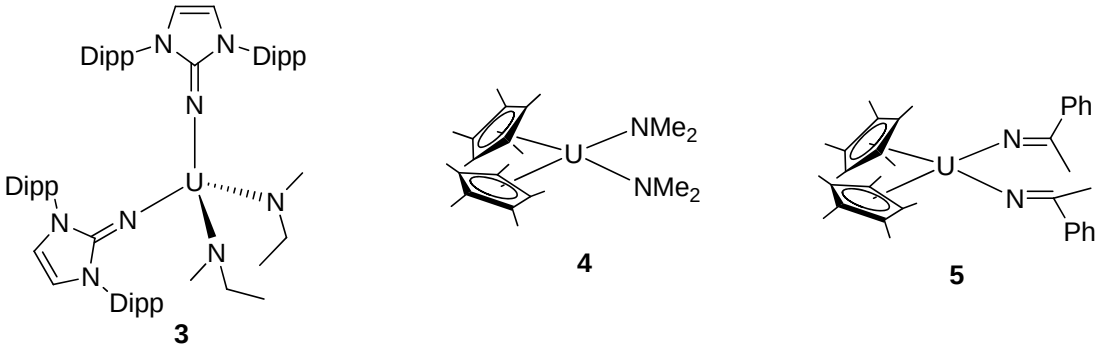

Figure 1: Isolobal uranium(IV) complexes **3**-**5**.

1. X. Wu, M. Tamm, *Coord. Chem. Rev*. **260**, 116 (2014) and references therein.
2. I. S. R. Karmel, M. Botoshansky, M. Tamm, M. S. Eisen, *Inorg. Chem*. (2014), Article in press: http://pubs.acs.org/doi/abs/10.1021/ic402806x
3. P. J. Fagan, J. M. Manriquez, S. H. Vollmer, C. S. Day, T. J. Marks, *J. Am. Chem. Soc.***103**, 2206 (1981).
4. K. C. Jantunen, C. J. Burns, I. Castro-Rodriguez, R. E. Da Re, J. T.Golden, D. E. Morris, B. L. Scott, F. L. Taw, J. L. Kiplinger, *Organometallics* **23**, 4682 (2004).

Coolant-fuel interaction in Sodium-cooled Fast Reactors:

Structural investigations of the Na-An-O (An = U, Np, Pu) systems

A.L. Smith[1,2], P.E. Raison[1], D.M. Bykov[1], R.J. Konings[1], A.K. Cheetham[2], R. Caciuffo[1]

[1] *European Commission, JRC-Institute for Transuranium Elements, 76125 Karlsruhe, Germany*
e-mail: Philippe.raison@ec.europa.eu

[2] *Department of Materials Science and Metallurgy, University of Cambridge, 27 Charles Babbage, Cambridge, CB3 0FS, United Kingdom*

Nuclear energy has the potential to provide Europe with a secure and sustainable electricity supply at a competitive price and to make a significant contribution to the reduction of greenhouse gases emissions. The interest for Sodium-cooled-Fast-spectrum Reactors (SFRs), when compared to Pressurized Water Reactors (PWRs), lies in their more efficient management of plutonium and other actinides as well as their ability to use almost all of the energy in the natural uranium versus 1% utilized in thermal spectrum systems. The high fuel efficiency of fast reactors could greatly dampen concerns about fuel supply. But these reactors have also several drawbacks when compared to PWRs (i.e sodium fire, Na reaction with O_2 and H_2O, interaction of sodium with oxide fuels). Their development at an industrial scale needs therefore an exhaustive safety assessment that comprises both experimental work and development of sophisticated modelling tools able to describe the reactor behaviour in normal or incidental conditions.

In SFRs various types of fuels can be envisaged (e.g. nitrides, carbides, metals) but mixed oxide fuels $(U,Pu)O_2$, with Pu/(U+Pu) concentration ratio comprised between 20 and 30 %, are still considered as a reference since substantial experience has already been gained in terms of fabrication, reactor operation, reprocessing and risk assessment. However one significant safety concern regarding this type of fuel comes from its potential interaction with the sodium in case of a breach in the stainless steel cladding. Indeed, in case of a defective cladding the metallic coolant will enter the pin and react with the fuel to form compounds of lower density and thermal conductivity leading to local swelling and development of hot spots that could damage further the cladding up to a pin failure. This will also involve the contamination of the primary circuit with fission products and transuranium elements. Thus it is crucial to have a complete understanding of the phenomena involved during a fuel-sodium interaction.

In the present work the Na-An-O systems with An = (U, Np, Pu) have been explored. Numerous ternary compounds have been identified and their crystallographic structure investigated, primarily using X-ray diffraction but also by neutron diffraction for some uranium-bearing compounds. In those systems it has been found that the oxidation states of the actinide can vary from +4 to +7 depending of the (Na+An)/O ratio, oxygen potential and temperature. As an example the Na-Np-O system is shown in Figure 1.

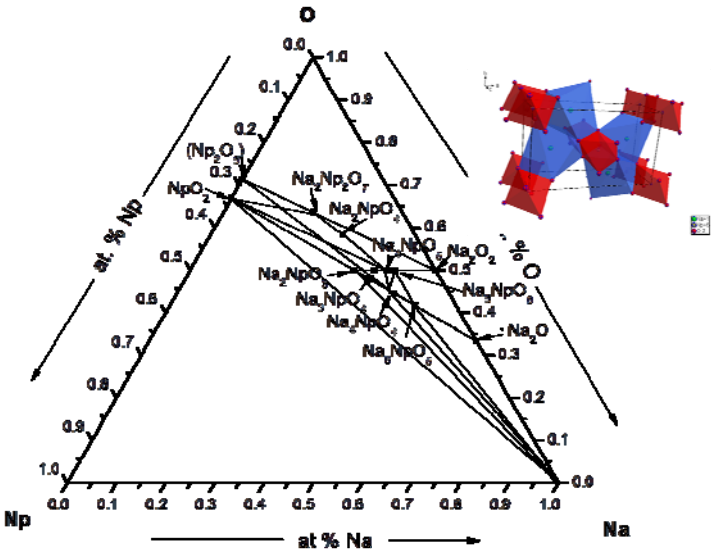

***Fig. 1**: Sketch of the Na-Np-O phase diagram between 673-1273 K, covering a large range of oxidation potential, (from [1]). An example of structure is given: α-Na_2NpO_4*

For each compound, once the crystallographic structure was solved, systematic studies have been performed to investigate potential phase transitions at high temperatures and to determine thermo-mechanical properties such as the thermal expansion coefficient along the different crystallographic axes [2].

Al last, in some of the studied compounds, namely $NaUO_3$, Na_3UO_4, Na_4NpO_5, Na_2NpO_4 and Na_5PuO_6, the valence state V, VI, VII for the uranium, neptunium and the plutonium, respectively. In those particular compounds the actinide cations are in the $[Rn]5f^1$ electronic configuration. It is planned to investigate their magnetic behavior at low temperature as reported for the $NaUO_3$ compound [3] which shows an antiferromagnetic ordering at 32 K.

In our presentation we will show our latest experimental results.

References

[1] A.L. Smith, P.E. Raison, R.J.M. Konings - "Synthesis and crystal structure characterisation of sodium neptunate compounds", J. Nucl. Mat. 413,114–121 (2011)

[2] A.L. Smith, P.E. Raison, L. Martel, T. Charpentier, I. Farnan, D. Prieur, Y C. Hennig, Y A. Scheinost, R.J.M. Konings, A.K. Cheetham - "A ^{23}Na Magic Angle Spinning Nuclear Magnetic Resonance, XANES and High Temperature X-Ray Diffraction Study of $NaUO_3$, Na_4UO_5, and $Na_2U_2O_7$. *Inorg. Chem. 53, 375-382 (2014)*

[3] *S. Van den Berghe, A. Leenaers, C. Ritter – " Antiferromagnetism in MUO_3 (M= Na, K, Rb) studied by neutron diffraction. J. Sol. State. Chem 177, 2231-2236 (2004)*

New catalytic processes promoted by organoactinides

Moris S. Eisen

Schulich Faculty of Chemistry, Technion-Israel Institute of Technology, Haifa 32000, Israel
e-mail: chmoris@tx.technion.ac.il

Neutral organoactinide complexes have been extensively studied in the last decade as catalysts for several organic transformations. Interestingly, in all these catalytic processes, the most widely used organoactinide complexes contain the cyclopentadienyl $(C5R5)^-$ ancillary ligand. More challenging is the synthetic chemistry of organoactinide complexes containing heteroatom ligands, and among these ligands, the amidinates, [RC(NR')(NR'')] are very attractive due to their straightforward synthesis from simple starting materials, and the facile modification of both their steric bulk and electronic properties through the choice of proper backbone substituents

The high coordinative unsaturation of the amidinate organoactinide complexes raises conceptual questions as to the possibility of their use as catalysts.1 Here we will present new highlights on the synthesis of amidinate organometallic complexes and their reactivity in the polymerization of lactones, the formation of a cationic amidinate actinide complex and the unexpected reactivity in the polymerization of ethylene.

1. E. Rabinovich, S. Aharonovich, M. Botoshansky and M. S. Eisen, *Dalton Trans.*, **2010**, *39*, 6667.
2. E. Domeshek, R. J. Batrice, S. Aharonovich, B. Tumanskii, M. Botoshansky and M. S. Eisen, *Dalton Trans*., **2013**, *42*, 9069

Uranium-Mediated Small Molecule Activation & a New Oxidation State in Uranium Chemistry

Karsten Meyer and Henry Storms LaPierre
Department of Chemistry and Pharmacy
Friedrich-Alexander University Erlangen – Nürnberg (FAU)
D-91058 Erlangen, Bavaria, Germany

In our efforts to activate small molecules of industrial and biological concern, we have turned our attention to coordinatively unsaturated, reactive uranium coordination complexes. For example, the chelating triazacyclononane-, single N-, and arene-anchored tris(aryloxide) ligands, $(ArO)_3tacn^{3-}$, $(ArO)_3N^{3-}$, and $(ArO)_3mes^{3-}$ have provided access to reactive coordination compounds of uranium in oxidation states II, III, IV, V, and VI with tailorable steric profiles. These complexes display a pronounced selectivity and reactivity in reactions with carbon dioxide, related small heteroallene molecules, and even the elemental chalcogens S, Se, and Te. As a result, they provide unique reaction pathways inaccessible to transition metal chemistry.

Here, we briefly summarize our work on CO_2 activation, including a previously unknown coordination mode, stoichiometric reductive cleavage, insertion reactions, and CO_2 functionalization chemistry *via* multiple bond metathesis. Most recently, we reported the stoichiometric and catalytic "disproportionation" of CO_2 to CO and CO_3^{2-} *via* reductive cleavage of CO_2, yielding a μ-oxo bridged complex, followed by the insertion of another molecule CO_2. In a similar strategy, we were able to isolate oxalates, thiooxalates, and several mixed carbonate complexes U–CO_2E–U, U–CS_2E–U, and even U–OC(S)Se–U by reacting bridged chalcogenide complexes U–E–U (E = S, Se) with CO_2, CS_2, and COS. Even more remarkable, the U–E–U species react with elemental sulfur, selenium, and tellurium to form polychalcogenides. These chalcogenido and mixed-carbonate complexes represent the first of their kind.

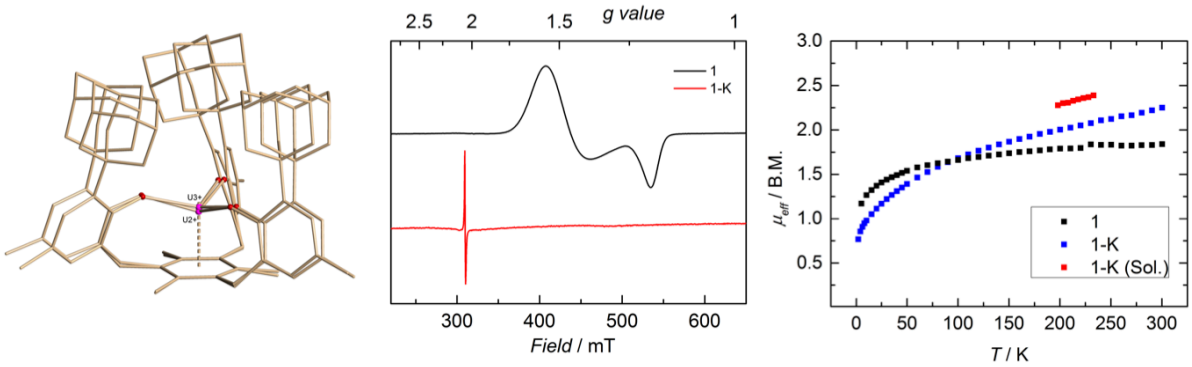

Molecular and electronic structure (XRD, EPR, SQUID) of U(III) 1 and U(II) 1-K in comparison

Finally, the molecular and electronic structure of a new oxidation state in U coordination chemistry is reported, namely U(II), with a $5f^4$ quintet ground state is reported. In K(2.2.2-crypt)[((^{Ad,Me}ArO)$_3$mes)U] (**1-K**), the U(II) center is supported by δ backbonding, which was established experimentally by single crystal X-ray diffraction, VT ^{1}H NMR, X-band EPR, solution (Evans' method) and solid-state (SQUID) magnetism studies, and optical absorption spectroscopy. The complex's electronic structure was further investigated by DFT calculations. In addition, prelimiary reactivity studies are reported.

Experiments on thin films of uranium and UO_2 – an overview

Ross Springell[1], Roger Ward[2], and Gerry Lander[3]

[1] *Royal Commission for the Exhibition of 1851 Research Fellow, Interface Analysis Centre, School of Physics, University of Bristol, Bristol BS2 8BS, United Kingdom*
[2]*Clarendon Laboratory, University of Oxford, Oxford, Oxon OX1 3PU, United Kingdom*
[3]*European Commission, JRC, Institute for Transuranium Elements, D-76125 Karlsruhe, Germany and Institut Laue Langevin, Grenoble, France*
e-mail: lander@ill.fr

For a number of years, we have produced by magnetron sputtering initially multilayers of uranium with the ferromagnets Fe, Co, Ni [1–3], and Gd [4], and then developed the technology to produce epitaxial films of uranium [5, 6] and uranium dioxide [7]. The sputtering machine was developed at Oxford University, and is now at Bristol.

This talk will outline some of the recent highlights of this project. We have recently shown:

(1) How the charge-density wave (CDW) in epitaxial α-U films deposited on Nb and W are quite different, and are related to whether the *a*-axis of α-U is in compression (U/Nb) or in tensile strain (U/W). The results support the theoretical understanding of the CDW in the bulk material advanced by Johann Bouchet [8].

(2) How the use of epitaxial UO_2 films can advance our understanding of antiferromagnetism at the surface [7], and show that what is observed at the surface of a thin film may be different from that observed on the surface of a bulk sample [9].

(3) How the use of UO_2 films can be used to study the *dissolution* of UO_2. U(IV), as in UO_2, is insoluble in H_2O, but U(VI) forms the uranyl ion and is soluble. When H_2O is placed on the surface of UO_2 nothing happens; however, if the water is then exposed to x-rays, the latter radiolyses the water, producing OH^- radicals. These convert U(IV) ions to U(VI) and they dissolve, thus simulating what happens in a underground depository when water enters. In this case the radiolysis is caused by the radioactivity at the surface of the fuel. [S. Rennie PhD project, University of Bristol]

References

[1] F. Wilhelm *et al.,* Phys. Rev. B **76**, 024425 **(**2007**)**
[2] R. Springell *et al.,* J. Phys. Cond. Mat. **20** 215229 (2008); *ibid* 215230 (2008)
[3] R. Springell *et al.,* Phys. Rev. B **77**, 064423 (2008)
[4] R. Springell *et al.,* Phys. Rev. B **81**, 134434 (2010)
[5] R. C. C. Ward *et al.,* J. Phys. Cond. Matt. **20**, 135003 (2008)
[6] R. Springell *et al.,* Phys. Rev. B **78**, 193403 (2008)
[7] Z. Bao *et al.* Phys. Rev. B **88**, 134426 (2013)
[8] J. Bouchet, Phys. Rev. B **77**, 024113 (2008)
[9] S. Langridge *et al.* arXiv:1312.3136v1 (2013)

XANES and RXES investigation of uranium aluminides

M. Pasturel,[1] C. Prestipino[1], N. Brisset[1], K. Kvashnina[2], M. Samsel-Czekała[3], O. Tougait[1], R. Troć[3]

[1] *Institut des Sciences Chimiques de Rennes, Chimie du Solide et Matériaux,UMR CNRS 6226, Université de Rennes 1, Campus de Beaulieu, bât. 10A, 35042 Rennes Cedex, France*
e-mail: mathieu.pasturel@univ-rennes1.fr
[2] *European Synchrotron Radiation Facility, 6 rue Jules Horowitz, 38042 Grenoble cedex 9, France*
[3] *Institute of Low Temperature and Structure Research, Polish Academy of Sciences, ul. Okólna 2, 50–422 Wrocław, Poland*

Despite the large difference in their crystal structures and uranium-uranium or uranium-ligand interatomic distances, the UAl_2, URuAl and UT_2Al_{10} (T = Fe, Ru) aluminides present similar magnetic and transport features. The thermal dependence of their magnetic susceptibility is dominated by the presence of a broad shoulder below 100 K [1-4] while their electrical resistivity exhibits a pronounced S-shape curve [2,4-6]. These features are well explained in UAl_2 and URuAl by the occurrence of spin fluctuations at low temperature, while the discussion is open on URu_2Al_{10} where an important positive magnetoresistivity rather suggests valence fluctuations [4].

Evidencing valence fluctuations using X-ray absorption techniques has been shown to be efficient in many rare earth based intermetallics such as recently reported for $YbRh_2Si_2$ [7] or $CeRhSi_2$ [8]. In the case of uranium intermetallics, the outer character of the *5f*-orbitals induces a stronger hybridization with the ligands and thus a broadening of the bands, resulting in a superimposition of the X-ray absorption peaks for each electronic configuration and a poor resolution of the spectra. Nevertheless, a recent paper reports on the possibility to deduce the valence of uranium in intermetallics using Resonant X-ray Emission Spectroscopy (RXES) [9].

In order to evidence the occurrence of hypothetical valence fluctuations in URu_2Al_{10}, XANES at U-L_3 edge as well as RXES have been performed on the ID26 beamline at ESRF (Grenoble, France) on poly- and single crystals of this phase and isostructural UFe_2Al_{10} (exhibiting common magnetic features), from room temperature down to 12 K. The spin fluctuators UAl_2 and URuAl have also been probed for comparison of the different results. In this presentation, the results will be discussed in terms of temperature and crystallographic dependence of the uranium configuration in these aluminides.

References

[1] A.C. Gossard et al., *Phys. Rev*. **128**, 1038 (1962)
[2] V. Sechovský et al., *J. Less-Common Met.,* **121**, 169 (1986).
[3] T. Sugai et al., *J. Phys.:Conf. Ser.* **273**, 012122 (2011).
[4] R. Troć et al., *Intermetallics* **19**, 913 (2011).
[5] A.J. Arko et al., *Phys. Rev. B* **5**, 4564 (1972).
[6] R. Troć et al., *Submitted to Phys. Rev. B.*
[7] H. Nakai et al., *J. Phys. Soc. Jpn*. **82**, 124712 (2013).
[8] D. Kaczorowski et al., *J. Phys. :Cond Matter* **22**, 215601 (2010).
[9] C.H. Booth et al., *PNAS* **109**, 10205 (2012).

XRD, ellipsometry and Raman spectroscopy examination of uranium coupons exposed to low pressures of H_2 at ~ 80°C

Robert M. Harker, Afiya H. Chohollo, Michael Parsley, Richard Gover, Peter Morrall and Imran Khan

AWE Aldermaston, Aldermaston, Reading, RG7-4PR,United Kingdom
e-mail : robert.harker@awe.co.uk

Samples of uranium coupons exposed to H_2 were prepared which were identical in every respect in so far as is possible, but which differ only in their hydrogen exposure time (where this time is significantly less than a classically understood 'induction time'). As-received oxide was removed on all surfaces and two faces (~12x12 mm) were polished to a sub-micron standard. Samples were individually taken through a Vacuum Thermal Pre-Treatment cycle from room temperature to 200°C to the reaction temperature (80°C) over 40 hrs and subsequently exposed to 10 mbar O_2 for 24 hours. After O_2 was removed, the samples were exposed to 10 mbar H_2 for pre-determined times of up to 48 minutes. Examination of the samples by SEM has, as expected, identified small features protruding from the surface believed to have been caused by sub-surface precipitation of UH_3. Initial observations of these samples by SEM are reported elsewhere [1], while the current paper outlines the XRD, ellipsometry and Raman investigation of said samples.

XRD and ellipsometry data show that the oxide overlayer thickness generated in these experiments were 310-575Å except for the 46 second sample (640-690Å) which experienced an additional air leak during the oxidation step. XRD measurements on the samples showed an increase in the amount of β-UH_3 detected as a function of H_2-exposure time (Figure 1); this increase was concomitant with an increase in the coverage by surface protrusions observed by SEM. The sample that experienced the air leak in the oxidation step exhibited a value for $\%UH_3$ which was much higher than all other samples. However, it should be noted that the calculated amount of β-UH_3 was found to be very sensitive to the fitting procedure used.

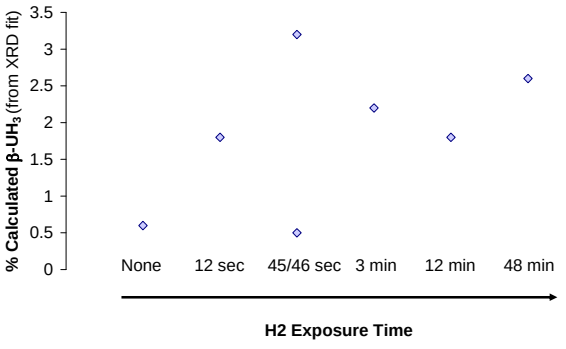

Figure 1. Variation of calculated % β-UH_3 (from XRD fit) with H_2-exposure.

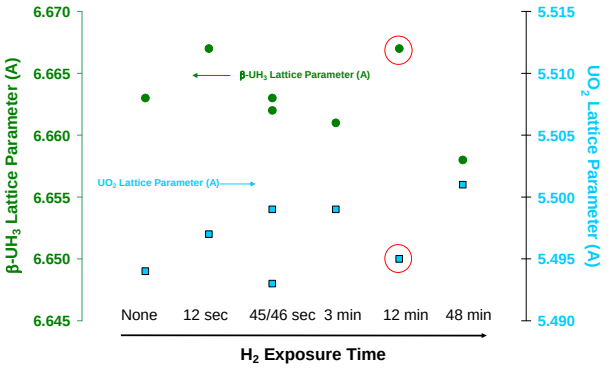

Figure 2. Variation of β-UH_3 and UO_2 lattice parameters, with H_2-exposure.

XRD measurements yielded lattice parameters of uranium that were found to be comparable to literature values whereas the lattice parameters for both UO_2 and β-UH_3 were found to be higher than literature values by around 0.5% and 2%+, respectively. We had anticipated that the β-UH_3 lattice parameter would be both less than unconstrained β-UH_3 (6.643+/-0.001Å [2]; 6.6310+/-0.0008Å [3]) and perhaps reducing as a function of H_2-exposure due to increased hydrostatic stress imparted by surrounding metal. No definitive relationship is evident (Figure 2) although the general trend appears to be of a reduction in

β-UH_3 lattice parameter with H_2 exposure and this interpretation is given confidence if the 12 minute sample (considerably worse quality fit as compared to remaining samples) is omitted (red-ringed). Conversely the trend for UO_2 lattice parameter appears to be increasing with hydrogen exposure time, and again this interpretation is given confidence if the 12 minute sample is omitted (red-ringed). The reason for the UO_2 trend is unclear and a number of possibilities will be discussed.

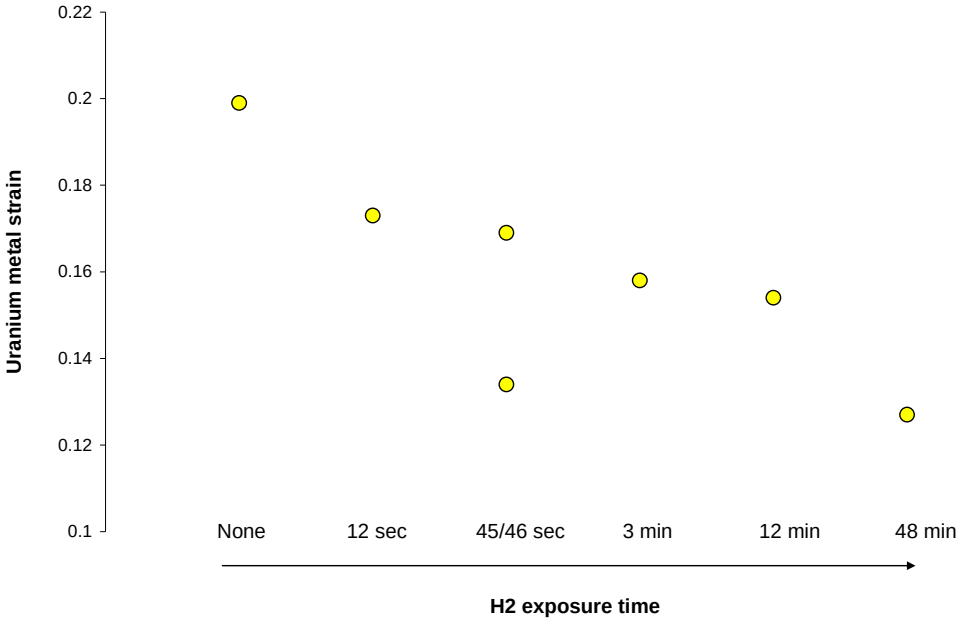

Figure 3. Uranium metal strain, as output from XRD model fit, with H_2-exposure

Finally the strain in the U metal (as given as an output from the XRD model fit) was shown to progressively decrease with the same hydrogen exposure (Figure 3). A number of explanations could be presented to explain this trend. Firstly, dissolved hydrogen in the metal could have promoted dislocation, grain boundary or defect migration in the metal at the hydriding temperature of 80°C. Secondly, growing hydrides could deform the surrounding metal and allow for a relaxation of regions of high stress. Thirdly, hydrides could be precipitating at points of high stress in the metal thereby removing them from the system.

Despite extensive efforts, Raman investigations of one of these samples showed no evidence of a UH_3 signature. There are two possibilities to explain this result. Firstly, it could be that the UH_3 signal is of a small enough relative size in comparison to the oxide signal that it cannot be observed. Secondly, this lack of a UH_3 signature could be due to a metal layer existing between the UH_3 precipitates and the oxide overlayer.

(1) R. M. Harker, A. H. Chohollo, *MRS Proceedings* **1444**, 189-195 (2012).
(2) W. Bartscher et al., *Solid State Communications* **53** (4), 423-426 (1985).
(3) R. E. Rundle, *J. Am. Chem. Soc*. **69**, 1719-1723 (1947).

Superconductivity : Is there a problem in transuranics?

Eric Colineau, Jean-Christophe Griveau, Rachel Eloirdi, Amir Hen, Roberto Caciuffo

[1] *European Commission, Joint Research Centre, Institute for Transuranium Elements, Postfach 2340, 76125 Karlsruhe, Germany*
e-mail: eric.colineau@ec.europa.eu

Superconductivity was first reported in 1942 for uranium metal (α-U) [1] and in 1958 for U compounds [2]: UCo, U_6Mn, U_6Fe, and U_6Co, with critical temperatures T_c, of 1.7, 2.3, 3.9, and 2.3K, respectively. A new class of U superconductors emerged in the early 1980's with the discovery of U heavy fermion superconductors : UBe_{13} (T_c = 0.85K) [3], UPt_3 (T_c = 0.53K) [4], URu_2Si_2 (T_c = 1.5K) [5], UPd_2Al_3 (T_c = 1.9K) [6]… Furthermore, in most of these systems, the superconducting phases coexist with antiferromagnetic (AF) correlations which have characteristic temperatures, usually the Néel temperature T_N, that are typically one order of magnitude greater than the corresponding superconducting critical temperatures T_c. Superconductivity was even shown to co-exist with ferromagnetism in e.g. UGe_2 ($T_c \approx$ 0.8K, $T_C \approx$ 30K at p $\approx$ 1.2GPa) [7] and URhGe (T_c = 0.25K, T_C = 9.5K) [8]. Heavy fermion superconductors still remain a major challenge for condensed matter physics. The existence of heavy fermion superconductivity and its coexistence or proximity with magnetic order suggests that the conventional mechanism of phonon-mediated superconductivity is inappropriate and that alternative mechanisms, like spin fluctuations, should be considered for Cooper pairing.

Beside the large number of U superconductors, it is worth noticing the lack of transuranium superconductors : neither Np nor Pu metals are superconductors and, until the beginning of the century, no Np or Pu-based superconductor had ever been reported (with the exception of Np Chevrel phases $NpI+xMo_6Se_8$ (T_c=5.6K) [9], where 5f electrons are thought not to contribute to superconductivity). However, in the recent years, several transuranium superconductors have been discovered : $PuCoGa_5$ ($T_c \approx$ 18.5 K) [10], $PuRhGa_5$ ($T_c \approx$ 8.7 K) [11], $NpPd_5Al_2$ ($T_c \approx$ 4.9K) [12], $PuCoIn_5$ ($T_c \approx$ 2.5K) [13] and $PuRhIn_5$ ($T_c \approx$ 1.6K) [14]. Rare exceptions or top of the iceberg?

In this contribution, we will review the transuranium analogues of the main uranium superconductors, as well as the transuranium superconductors and discuss the problems that might prevent us from observing more of them.

References

[1] G. Aschermann and E. Justi, *Phys. Z*., **43**, 207 (1942)
[2] B.S. Chandrasekhar and J.K. Hulm , *J. Phys. Chem. Solids* **7**, 259 (1958)
[3] H.R. Ott et al., *Phys. Rev. Lett*. **50**, 1595 (1983)
[4] G.R. Stewart et al., *Phys. Rev. Lett*. **52** , 679 (1984)
[5] W. Schlabitz et al., *Z. Phys*. **B 62**, 177 (1986)
[6] C. Geibel et al., *Z. Phys*. **B 84**, 1 (1991)
[7] S.S. Saxena et al., *Nature* **406**, 587 (2000)
[8] D. Aoki et al., *Nature* **413**, 613 (2001)
[9] D. Damien et al., *Solid State Communications* **38**, 437 (1981)
[10] J.L. Sarrao et al., *Nature* **420**, 297 (2002)
[11] F. Wastin et al., *J. Phys.: Condens. Matter* **15**, S2279 (2003)
[12] D. Aoki et al., *J. Phys. Soc. Jpn*. **76**, 063701 (2007)
[13] E D Bauer et al., J*. Phys.: Condens. Matter* **24**, 052206 (2012)
[14] E.D. Bauer et al., abstract K8-03, M2S Materials and Mechanisms of Superconductivity Conference, July 29- August 3, 2012, Washington. See also E.D. Bauer et al., National High Magnetic Field Laboratory 2012 MagLab Research Report, P01970-E002-PF.

Correlation of prompt fission neutron emission with fission fragment properties in ^{252}Cf(SF)

F.-J. Hambsch, A. Göök, S. Oberstedt, M. Vidali

[2]*European Commission, Joint Research Centre, Institute for Reference Materials and Measurements, Retieseweg 111, 2440 Geel, Belgium*
e-mail: franz-josef.hambsch@ec.europa.eu

The prompt fission neutron spectrum has been recognized recently as being of large importance in neutronics calculations for reactor design. To improve the knowledge and to come up with a new evaluation the IAEA has initiated a Coordinated Research Project (CRP) on "Prompt Fission Neutron Spectra of Actinides". The prompt fission neutron emission is also of particular importance for the understanding of the fission process. Neutron multiplicities and energy distributions could give answers to questions related not only to the neutron emission itself, but also questions relevant to the formation of the fission fragments. In addition, the sharing of excitation energy among the fragments and the time scale of the process is of paramount importance for nuclear fission modelling.
Nuclear modelling has also become so sophisticated that fluctuations of the prompt neutron multiplicity in resonances need to be included. Fluctuations of the mass and total kinetic energy (TKE) [1,2] as well as independently in the neutron multiplicity [3] in both isotopes have been observed in resonance-neutron induced fission. To verify possible correlations a new instrument has been designed at JRC-IRMM to measure fission neutron multiplicities of ^{235}U and ^{239}Pu as a function of resonance-neutron energy. To pave the road for the implementation of the to be build SCINTIA neutron detector array an experimental investigation of ^{252}Cf(sf) prompt neutron multiplicity in correlation with fission fragments has been undertaken.
The present report will highlight results of the correlation of fission fragment properties like mass and TKE with prompt neutron emission. The experimental investigation was completely based on digital data acquisition and signal processing. As fission fragment detector a twin Frisch-grid ionization chamber (TFGIC) was used. A thin layer of ^{252}Cf (~700 fission/s) on a thin Ni-backing placed on the common cathode allowed simultaneous detection of both fission fragments. As neutron detector a NE-213 type liquid scintillator was placed along the TFGIC axis. A coincidence between the neutron detector and the cathode of the TFGIC triggered the acquisition system. In addition the acquisition was made to accept triggers from the TFGIC without requiring coincidences with a neutron detector. This allowed intrinsic calibration using the non-coincident events as well as monitoring electronic stability. In a previous experiment [4] this electronic stability had been identified as a large source of systematic errors in the correlation between e.g. the TKE of the fragment pairand the prompt neutron multiplicity.
Digital signal processing made possible to clean fission fragment events from piled-up alpha particles and fission-fission pile-up. In addition, it was possible to reach a time-of-flight resolution for the prompt fission gamma-rays of 0.9 ns FWHM. Further treatment of the fission fragment correlations with neutrons yielded very good agreement with earlier measurements of the same quantities [5]. The recent question [6] on the dependence of the prompt neutron multiplicity as a function of TKE was also solved. The angular distribution in the centre-of-mass system was found to deviate slightly from isotropy. Presently we are investigating whether this is significant and points to either neutron emission at the scission point (so-called scission neutrons) or during acceleration of the fission fragments.
This is again a question which is as old as the first measurements of prompt neutron–fission fragment correlations and which has consequences for the understanding of the fission process.

References

[1] F.-J. Hambsch, H. H. Knitter, C. Budtz-Jorgensen, J. P. Theobald, Nuclear Physics A 491 (1989) 56.

[2] F.-J. Hambsch, I. Ruskov, L. Dematte, in: Proc. Scientific Workshop on Nuclear Fission Dynamics and the Emission of Prompt Neutrons and Gamma Rays (Theory- 1), EUR 24802, Sinaia, Romania, 2011, p. 41.

[3] R. E. Howe, T. W. Phillips, C. D. Bowman, Phys. Rev. C 13 (1976) 195.

[4] C. Matei, Neutron and fission fragment coincidence measurements with a ^{252}Cf(sf) source, EC-JRC IRMM Progress Report 15.10.2011-15.10.2012 (2012).

[5] C. Budtz-Jorgensen, H.-H.Knitter, Nucl.Phys. A490 (1988) 307.

[6] A. Tudora, Ann. Nucl. Ener.53 (2013), 507.

New Reactivity of the Uranyl Ion

Robert J. Baker,[1] Aurora Walshe[1], Emtithal Hashem[1]

[1] *School of Chemistry, Trinity College Dublin, Dublin 2, Ireland*
e-mail: bakerrj@tcd.ie

Recent research has shown that thorium and uranium compounds in their +4 oxidation state are active catalysts for a number of C-C bond forming reactions. [1] However, as the high oxophilicty of the actinide ion would predict that low activities would be observed for oxygen containing substrates, these have not been explored to a great extent. The ring opening polymerisation of ε-caprolactone and *rac*-lactide by $[Cp^*_2MMe_2]$ (M = Th, U) suggest that this may not be the case. [2,3]

Herein, we report on the use of uranyl aryloxide **1** in the ring opening polymerisation of epoxides, [4] lactides and caprolactones [5]. This is the first example of a high oxidation state actinide complex that acts as a catalyst for this reaction. A comprehensive NMR spectroscopic study has allowed for the mechanism to be determined and theoretical calculations have also been performed and will be discussed.

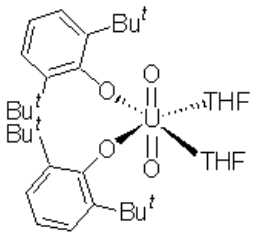

1

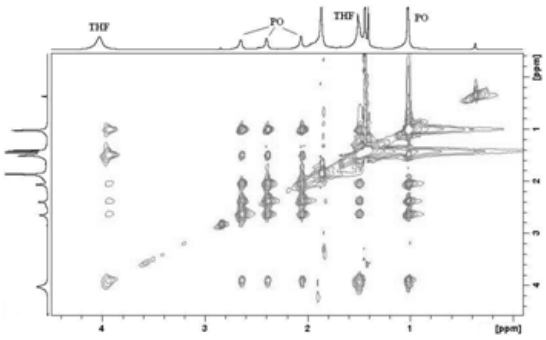

References

[1] A.R. Fox, S.C. Bart, K. Meyer, C.C. Cummins, *Nature*, **455**, 341 (2008).
[2] E. Rabinovich, S. Aharonovich, M. Botoshansky, M.S. Eisen, *Dalton Trans.*, **39** 6667 (2010).
[3] E. Barnea, D. Moradove, J.‑C. Berthet, M. Ephritikhine, M.S. Eisen, *Organometallics*, **25** 320 (2006).
[4] R.J. Baker, A. Walshe, *Chem. Commun.*, **48** 985 (2012); J. Fang, A. Walshe, L. Maron and R.J. Baker, *Inorg. Chem.*, **51** 9132 (2012).
[5] A. Walshe, J. Fang, L. Maron and R.J. Baker, *Inorg. Chem.*, **52** 9077 (2013).

Novel bi-metallic uranyl complexes - Redox chemistry in aqueous solutions

I. ZILBERMANN[1], G. YARDENI[1], A. MIZRAHI[1], E. MAIMON[1] ,A.Z. ZEHAVI-COHEN[3] and D. MEYERSTEIN[2]

[1] Chemistry Department, NRCN, Beer-Sheva, Israel
[2] Chem. Dept., Ben-Gurion Univ. of the Negev, Beer-Sheva and Biological Chem. Dept. Ariel Univ., Ariel, Israel
[3] Chemistry Department, Tel-Aviv University, Tel-Aviv, Israel.

The synthesis of organic ligands which can accommodate two uranium atoms at different oxidation states, mixed valency being then achieved by redox chemistry at room temperature is definitely a challenge in coordination chemistry. The following complexes were synthesized and characterized by elemental analysis, NMR, MS, IR and UV-vis.

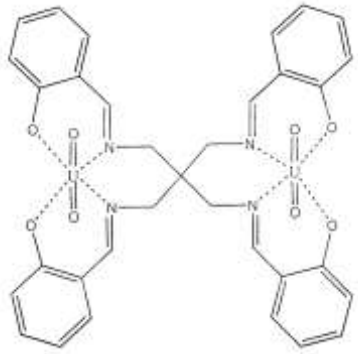

$(UO_2)_2L^1$

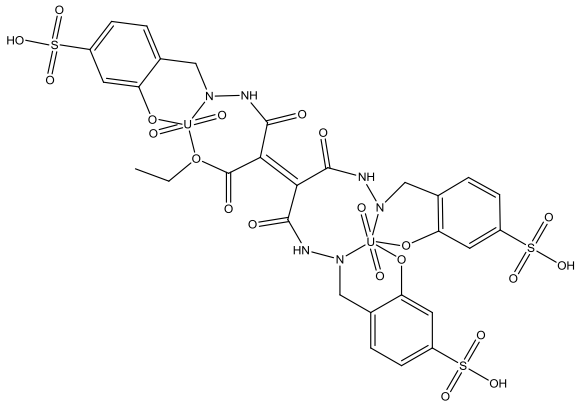

$(UO_2)_2L^2$

L^1 forms a bimetallic complex with two uranyl centres which dissolves in organic solvents, but the complex (and not the ligand) dissolves in 90:10 v/v H_2O/CH_3OH . From the Job-plot the binding constant of the new complex may be approximated as $K \sim 8 \times 10^{17}$ M^{-2}. **$(UO_2)_2L^1$** is reduced radiolytically by $^{\bullet}CH_2O^-$ (at pH 10) but not by $^{\bullet}CH_2OH$ with $k = 3.6 \times 10^9$ $M^{-1}s^{-1}$. The ligand, **L^1** , is not reduced by $^{\bullet}CH_2OH$ and precipitates in the presence of water or base. Preliminary electrochemical results in methanol show two irreversible reduction waves at -1.05 and at -1.73 V vs. SCE.

L^2 forms a bimetallic complexes with both two uranyl and two U(IV) centres which are

water soluble. From the Job-plot in water at pH 5, the binding constants of the new complexes, uranyl and U(IV), may be approximated as K ~ 4 x 10^{10} M^{-2} and K ~ 2 x 10^{9} M^{-2} respectively.

Preliminary electrochemical results at pH 5, for $(UO_2^{2+})_2\mathbf{L^2}$ show two irreversible reduction waves at -0.30 and -0.93 V vs. SCE.

Pulse radiolytic results for the same complex, $(UO_2^{2+})_2\mathbf{L^2}$, in water at pH 5, show that both e^-_{aq} and $CO_2^{\bullet -}$ reduce both the complex and the ligand on similar time scales, 200 μs and 6 ms in two reactions in which the first reaction obeys first order kinetics while the second one obeys second order kinetics.

Detailed data will be presented.

E-mail for corresponding author: israelz2003@gmail.com

Electronic structure of cage-like compound UFe_2Al_{10} – Theory and XPS experiment

M. Samsel-Czekała[1], E. Talik [2], M. Pasturel [3], R. Troć [1]

[1] *W. Trzebiatowski Institute of Low Temperature and Structure Research of PAS, P.0.Box 1410, 50-950 Wrocław 2, Poland, e-mail: M.Samsel@int.pan.wroc.pl*
[2] *A. Chełkowski Institute of Physics, University of Silesia, Uniwersytecka 4, 40-007 Katowice, Poland*
[3] *Institut des Sciences Chimiques de Rennes, Chimie du Solide et Matériaux, UMR CNRS 6226, Université de Rennes 1, Campus de Beaulieu, bât. 10A, 35042 Rennes Cedex, France*

The U-Fe-Al system exhibits several ternary phases [1]. Among the most intensively investigated phases are those with a generalized formula of UFe_xAl_{12-x}, possessing a wide Fe-content range for $3<x<6$. In this composition range four magnetic phase regions have been identified [2]. All these phases crystallize in the tetragonal $ThMn_{12}$-type structure. Interestingly that the considered here true stoichiometric phase, UFe_2Al_{10}, adopts a different structure of the orthorhombic $YbFe_2Al_{10}$-type [3] with the *Cmcm* symmetry that is closely related to the ternary ordered-variant of the $CeMn_4Al_8$-type (*I4/mmm* symmetry). In the $YbFe_2Al_{10}$-type structure [4], the uranium atom has a coordination number (CN) of 20 (4Fe + 16 Al) while the iron atom forms in its coordination a distorted icosahedral having the 2 U and 10 Al atoms. Zenou et al. [5], based on the total energy calculations, using the full potential band structure method with linearized augmented plane waves (FP-LAPW) with the spin-orbit (SO) coupling correction, explained why the UFe_2Al_{10} compound has rather the $YbFe_2Al_{10}$-type than $ThMn_{12}$-type structure. In turn, as many as five different sites are occupied in the UFe_2Al_{10} structure by the Al atoms. They coordinate in the irregular polyhedron of the U, Fe or Al atoms with CN ranging from 12 to 14.

The investigated here uranium aluminide, despite showing the modified Curie-Weiss behaviour, appeared to be a magnetically non-ordered compound, as indicated by magnetization, magnetic susceptibility, and neutron-diffraction measurements [6-8]. Among all the family of isostructural rare-earth ternaries, RFe_2Al_{10}, the similar magnetic properties were found for *R* = Ce, Pr and Nd, while for *R* = Y and La, the iron-containing compounds occurred to be the Pauli-paramagnets [9]. This fact proves that Fe in the latter systems like also in other *R*- and U- isotypic compounds, is non-magnetic. Interestingly, such compounds but based on Ce were classified as mixed-valent. All the remaining representatives with *R* = Sm and Gd-Tm have been reported to be magnetically ordered with the fairly high transition temperatures reaching even 20 K [4].

For the considered here UFe_2Al_{10} the crystallographic structure and scalar relativistic densities of states (DOS), calculated by FP-LAPW method, were studied for the first time (also under applied pressure) by Halevy et al. [10]. No pressure-induced change in the structure (up to 23.6 GPa) was reported. In turn, the calculated DOS corresponding to both ambient and the maximum applied pressure showed that the major part of the U 5f peak is located above the Fermi level (E_F) and the peak is slightly shifted above E_F and simultaneously lowered by applying pressure.

Here we present results of band structure calculations for UFe_2Al_{10}, employing the fully relativistic full-potential local-orbital (FPLO) code [11] within the local density approximation (LDA). As a result the DOS and Fermi surface have been computed. The calculated total and partial DOS are presented in the inset to Fig. 1. Next, we calculated the corresponding valence-band X-ray photoemission spectrum (XPS) and compared it in Fig. 1 with the XPS measured using Al Kα radiation. As seen from this figure, the densities originating from the U 5f states are split by the SO interaction into two narrow peaks, distant at about 0.75 eV from each other. One peak is cut by the Fermi level and the other one is located above E_F. The main contribution of the Fe 3d electrons is centred at around 1.5 eV below E_F while the Al 3sp electron contribution is spread in the whole energy region of valence bands. Hence, one can deduce that in the vicinity of E_F, the 5f electrons hybridize strongly with the Fe 3d and Al 3sp electrons.

As further Fig. 1 indicates, the calculated XPS is dominated by the U 5f peak crossing E_F (no. 1) and by the Fe 3d peak (no. 2) of much smaller intensity, while the wide Al 3sp feature (no. 3) is usually diminished substantially (compared to pure DOS) by the photoionization cross-sections. In consequence, the overall calculated and measured valence-band XPS are in good agreement. Nevertheless, it appears that the location of the maximum of the experimental U 5f peak (shifted by about 0.5 eV from E_F) points to more localized 5f electrons in UFe_2Al_{10} than suggested by the LDA calculation results. This difference probably is due to electron-electron correlation effects beyond LDA. Interestingly, such an effect of some localization is also evidenced by the presence of a small 7 eV satellite in the measured 4f core-level XPS (not displayed).
Finally, we have found that the calculated Fermi surface of UFe_2Al_{10} contains not too large closed anisotropic pieces of both hole-like and electron-like character, originating from two Kramers double-degenerate bands.

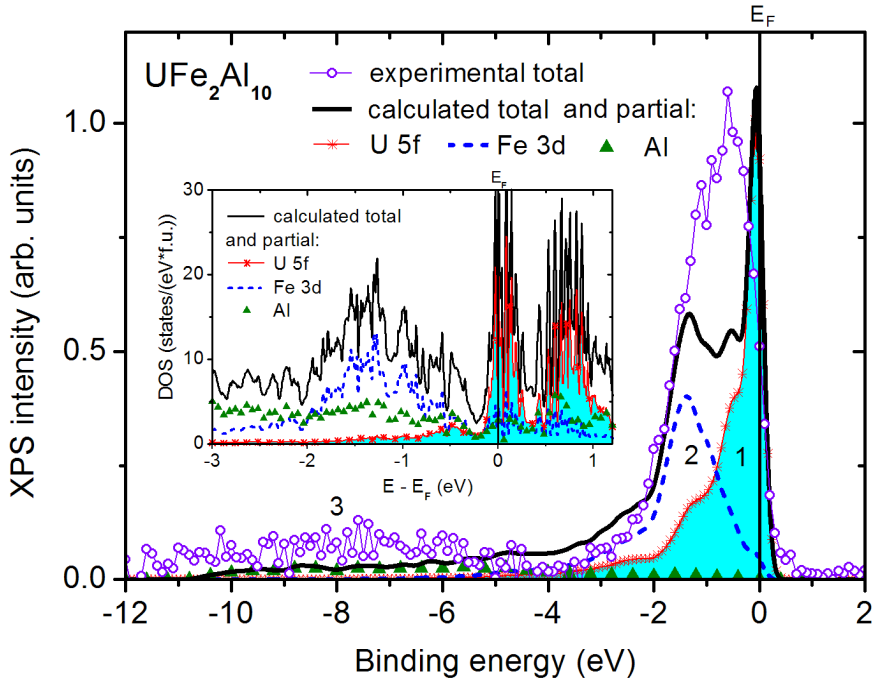

Fig. 1. Experimental and calculated valence-band XPS and the corresponding calculated DOS (inset).

References

[1]. A.P. Gonçalves and H. Noël, *Intermetallics* **13**, 580 (2005).
[2]. M. Kuznietz et al., *Phys. Rev. B* **60**, 9494 (1999).
[3]. L. Meshi et al., *J. Alloys Compd.* **347**, 178 (2002).
[4]. S. Niemann and W. Jeitschko, Z. Kristallogr. **210**, 338 (1995).
[5]. V.Y. Zenou, L. Meshi, and D. Fuks, *Intermetallics* **19**, 713 (2011).
[6]. H. Noël, A.P. Gonçalves, and J.C. Waerenborgh, *Intermetallics* **12**, 189 (2004).
[7]. L. Meshi, M. Talianker, and A. Munitz, *J. Alloys Compd.* **370**, 206 (2004).
[8]. T. Sugai et al., *J. Phys.: Conf. Series* **273**, 012122 (2010).
[9]. V.M.T. Thiede, T. Ebel, and W. Jeitschko, *J. Mater. Chem.* **8**, 125 (1998).
[10] L. Halevy et al., *J. Alloys Compd.* **419**, 21 (2006).
[11] FPLO5.00-18 version (http://www.FPLO.de).

Presented for an oral communication within the topic „Theory, electronic structure“.

Molecular nanomagnetism in actinide-based coordination complexes

R. Caciuffo,[1] G. Amoretti,[2] S. Carretta,[2] L. Chatelain,[3] Colineau,[1] A. Degeyer,[4] S. Gambarelli,[3] J. Hermle,[3] N. Magnani,[1] M. Mazzanti,[3] V. Mougel,[3] J. Pécaut,[3] P. Santini,[2] E. F. Tuna.[5]

[1] *European Commission, JRC, Institute for Transuranium Elements, Karlsruhe, Germany*
e-mail: roberto.caciuffo@ec.europa.eu
[2]*Dipartimento di Fisica e Scienze della Terra, Università di Parma, Italy*
[3]*CEA, SCIB, INAC, Lab. de Reconnaissance Ionique et Chimie de Coordination, Grenoble, France*
[4]*CEA, Service Général des Rayons X, SP2M, INAC, Grenoble, France*
[5]*School of Chemistry and Photon Science Institute, The University of Manchester, UK*

We present very recent results obtained for a hetero-metallic U(V)-Mn(II) one-dimensional chain assembled through cation-cation interactions [1], and for a triangular molecule containing three $U(V)O_2^+$ ($5f^1$) ions [2]. The former is the first example of an actinide-containing single-chain magnet (SCM), with a relaxation barrier of 134 K, a blocking temperature of 6 K, and an impressive coercive field B_c = 3.4 tesla at 2 K. The latter is characterized by a non-magnetic ground doublet corresponding to two oppositely twisted chiral arrangements of the U moments, and (in presence of a magnetic field orthogonal to the triangle plane) by quantum tunnelling of the noncollinear magnetization accompanied by oscillations of the anapole (toroidal) moment.

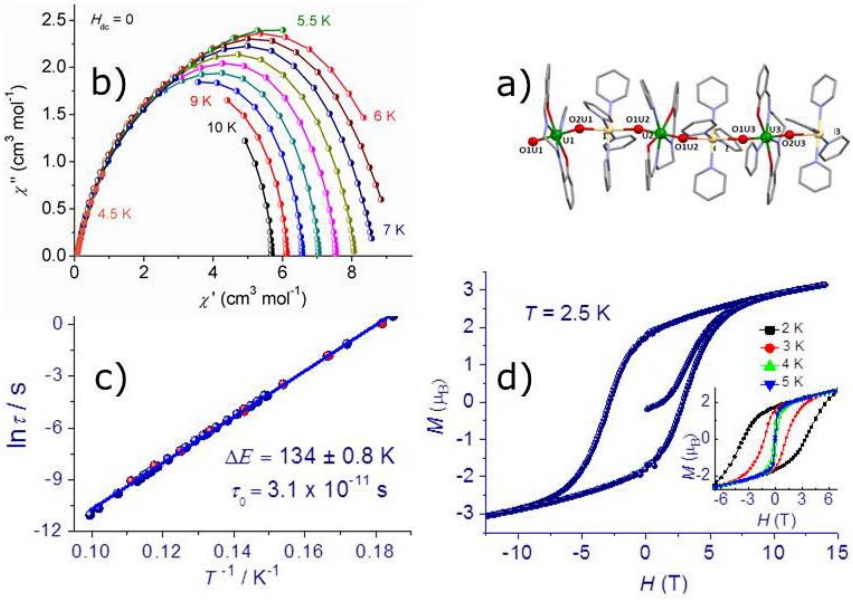

Fig. 1. (a) Mercury view of the structure of **1**; ligands were represented in pipes, H and co-crystallised solvent molecules were omitted for clarity, C are represented in grey, O in red, Mn in cream, N in light blue and U in green.(b) Cole-Cole plot of ac magnetic susceptibility components at different temperatures. (c) Arrhenius plot displaying T-dependence of the relaxation times. (d) Field dependence of the magnetisation measured at 2.5 K. Inset: hysteresis loops recorded at four different temperatures.

The reaction of the monomeric uranyl(V) complex $[UO_2(salen)py][Cp^*_2Co]$ with $Mn(NO_3)_2$ in pyridine in a 1:1 ratio affords the $[\{[UO_2(salen)(py)][Mn(py)_4](NO_3)\}]_n$ coordination polymer (**1**) in 65% yield (Fig. 1). Magnetic susceptibility and isothermal magnetization versus field data were recorded in the temperature range 2–300 K with a Quantum Design MPMS-XL 7T and a Quantum Design MPMS-XL 5.0 SQUID. Measurements were carried out on finely ground polycrystalline samples restrained in eicosane to prevent sample torquing. Magnetization loops have been measured while sweeping the magnetic field at a constant rate, from 7 to -7

T and back, with the sample kept at different temperatures from 2 to 10 K. The real and imaginary components, χ' and χ'', of the complex a.c. magnetic susceptibility were measured at zero-dc field as a function of temperature and frequency with a Quantum Design PPMS-14T platform using the mutual- inductance technique and a MPMS XL7 SQUID magnetometer. The results obtained show that the Mn-UO_2-Mn coordination polymer exhibits slow relaxation of the magnetization with a high relaxation barrier (ΔE = 134 K) and shows an open hysteresis, thus providing the first example of actinide based SCM (Fig. 1). The high magnetic anisotropy of the pentavalent uranyl complex and the high spin of Mn(II) associated to a significant intrachain magnetic communication and long interchain intermetallic distances are probably at the origin of the SCM behavior. The convenient route to uranium based 1D heterodimetallic chains associated to the wide range of possible Schiff base available create an entry into the development of actinide based SCM.

The second compound that will be discussed here is a triangular molecule (**2**) containing three $U^{V}O_2^{+}$ ($5f^1$) ions, $[UO_2L]_3$ (L = 2-(4-tolyl)-1,3-bis(quinolyl)malondiiminate) [2] (Fig. 2). We have investigated its properties through electron paramagnetic resonance (EPR) spectroscopy, magnetic susceptibility and high-field magnetization measurements. The analysis of the results shows that **2** is characterized by a non-magnetic ground doublet corresponding to two oppositely twisted chiral arrangements of the uranium moments. EPR spectroscopy has evidenced the presence of sizable non-axial terms in the local crystal fields experienced by U ions. This leads to a significant splitting of the ground doublet in the presence of a magnetic field orthogonal to the triangle plane. Hence, the low-frequency dynamics of **2** is characterized by quantum tunneling of the noncollinear magnetization accompanied by oscillations of the expectation value of the toroidal moment. The frequency of this phenomenon strongly depends on the applied magnetic field.

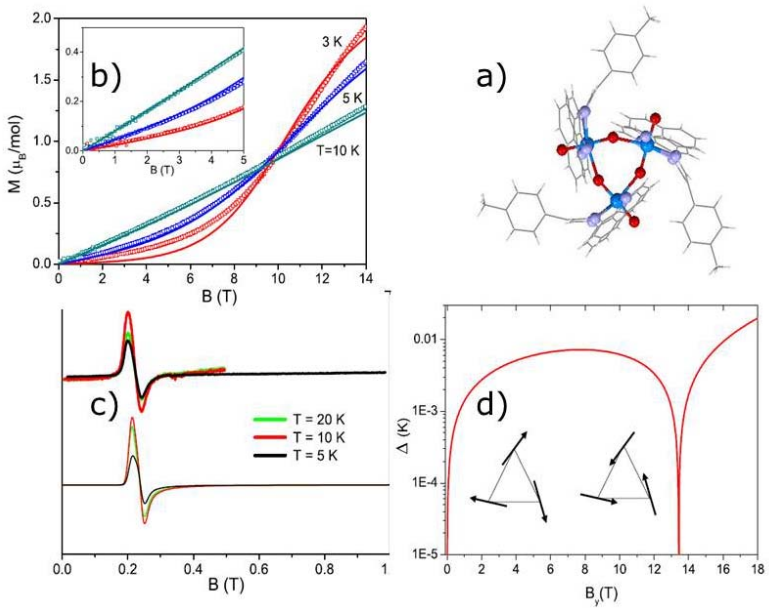

Fig. 2. (a) The structure of **2**; large magenta spheres: U, small red (dark gray in print) spheres: O, small blue (light gray in print) spheres: N, C and H are shown as wireframe.(b) Measured (points) and calculated (lines) field dependence of the molecular magnetization of **2**. The inset shows the effect of a small amount of paramagnetic impurities. (c) Measured (thick lines) and calculated (thin lines) EPR spectra of 2 for T = 5, 20 and 10 K in order of increasing height. (d) Calculated magnetic field dependence of the tunnel splitting Δ. The field is applied perpendicularly to the triangle plane. The inset contains a sketch of the two moment configurations involved in the tunneling process.

References

[1] V. Mougel et al., Angew. Chem. Int. Ed. **53**, 819 (2014)
[2] S. Carretta et al., J. Phys. Condens. Matter **25**, 486001 (2013)

^{235}U prompt fission neutron spectrum measurement via activation technique with the DONA detector at SARAF

M. Friedman,[1] N. Jovancevic,[2] L. Daraban,[2] F.-J. Hambsch,[2] M. Hult,[2] S. Oberstedt,[2] M. Paul,[1] G. Ron[1], A. Shor[3]

[1]*Racah Institue of Physics, Hebrew University of Jerusalem, Jerusalem 91904, Israel*
e-mail: moshe.friedman@mail.huji.ac.il
[2]*European Commission, Joint Research Centre, Institute for Reference Materials and Measurements, Retieseweg 111, 2440 Geel, Belgium*
[3]*Nuclear Physics and Engineering Division, Soreq Nuclear Research Center, Yavne 81800, Israel*

The understanding of neutron emission in fission and the mechanism of the fission process are essential for safe and economic use of nuclear power, and for further development of GEN IV reactors. The energy distribution of fission neutrons has a very strong influence on nuclear reactor parameters, such as k_{eff}, and accurate measurements of the prompt fission neutron spectra (PFNS) are therefore very important. PFNS measurements are made primarily using two types of experimental methods. The first method is based on the counted neutrons at specific energies, thus yielding spectra of prompt neutrons. The second method involves performing integral measurements which rely primarily on the measurement of the average cross section directly. The differential data is then used for calculating the average cross section for a given reaction, and compare to the integral data. An overview of such experiments performed at research centers worldwide, shows that a discrepancy between the integral and differential measured data still exists today [1]. More specifically, for ^{235}U, one of the most important isotopes for fission applications, such discrepancy exists for incident neutron energies above ~10 MeV, as demonstrated in Fig. 1.

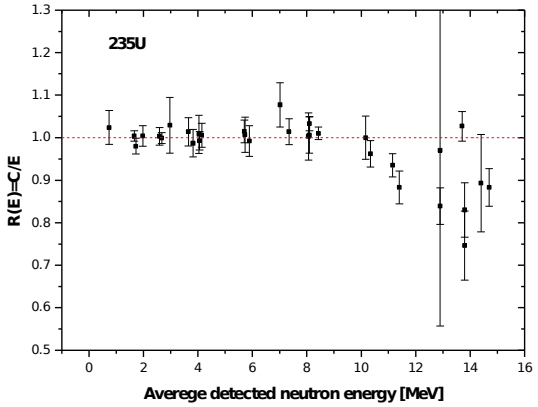

Fig. 1. Ratio of calculated (differential) to experimental (integral) average cross section for ^{235}U. Calculated data are based on ENDF-B/VII. Data are plotted for average energy of detected neutrons.

The DONA detector (DOsimetry and spectrometry using Neutron Activation), developed at IRMM Geel [2,3], is an assembly of 11 activation samples, arranged in a circular disk (see Fig 2.). The activity at secular equilibrium for reaction *k* is proportional to:

$$A_k \propto \sum_i \sigma_{ki} \Phi_i \qquad (1)$$

where σ_{ki} is the corresponding activation excitation function and Φ_i is the neutron fluence in energy bin *i*. From Eq. (1), the neutron fluence Φ_i can be determined by the unfolding procedure. Advantages of the DONA detector are that it is practically only sensitive for the neutron radiation and requires no electrical power at the measurement site.

A measurement of the PNFS of ^{235}U is planned at the SARAF accelerator [4], with the LiLiT target as a neutron source [5]. SARAF is a high current proton/deuteron RF accelerator being developed at Soreq, where phase I has been commissioned, and the experimental programs have begun. LiLiT is a liquid lithium target developed at Soreq to handle the high power densities from the high current beam, also recently commissioned.

As a preparation experiment, the above technique was tested with the well defined neutron spectrum of ^{252}Cf. Monte Carlo calculations were performed in order to estimate the effects of neutron scattering, and the sensitivity of the unfolding procedure to the initial neutron energy spectrum. Such calculations are crucial for the analysis of the data expected to be acquired with LiLiT in SARAF. We will update about the results of the preparation experiment, and the plans of the collaboration for the near future.

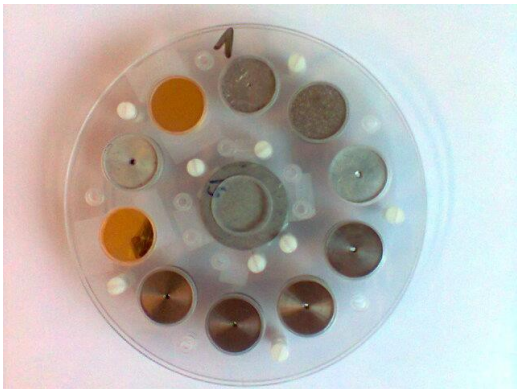

Fig. 2. Dona assembly, made from 11 different samples in a circular arrangement.

References

[1] R. Capote, K. I. Zolotarev, V. G. Pronyaev, and A. Trkov, Validation the ENDF-B/VII 235U(nth,f) prompt fission neutron spectrum updated dosimetry cross section (IRDFF), PHYSOR 2012 – Advances in Reactor Physics – Linking Research, Industry, and Education, Knoxville, Tennessee, USA, April 15-20, 2012.

[2] J.S.E. Wieslander, G. Lövestam, M. Hult, A. Fessler, J. Gasparro, and P. Kockerols, Radiat. Prot. Dosimetry **138** (2010).

[3] G. Lövestam, M. Hult, A. Fessler, J. Gasparro, P. Kockerols, K. Okkinga, H.Tagziria, F. Vanhavere, J.S.E. Wieslander, Neutron fluence spectrum using disk activation, Radiat. Meas. 44 (2009) 72-79.

[4] D. Berkovits *et al.,* Operational Experience and Future Goals of the SARAF Proton / Deuteron Linac, in: Proceedings of LINAC2012, Tel-Aviv, (2012) 100-104.

[5] S. Halfon, A. Arenshtam, D. Kijel, M. Paul, D. Berkovits, I. Eliyahu, G. Feinberg, M. Friedman, N. Hazenshprung, I. Mardor, A. Nagler, G. Shimel, M. Tessler and I. Silverman, Rev. Sci. Instrum. **84** (2013).

Exchange bias in UO_2/Py thin films

Evgeniya A. Tereshina,[1] Ross Springell[2], Ladislav Havela[3], Roberto Caciuffo[4]

[1] *Institute of Physics ASCR, Na Slovance 2, 18221 Prague, Czech Republic*
e-mail: teresh@fzu.cz

[2] *Royal Commission for the Exhibition of 1851 Research Fellow, Interface Analysis Centre, School of Physics, University of Bristol, UK, BS2 8BS, UK*

[3] *Faculty of Mathematics and Physics, Charles University, Ke Karlovu 5, 12116 Prague, Czech Republic*

[4] *European Commission, Joint Research Centre, Institute for Transuranium Elements, Postfach 2340, D-76125 Karlsruhe, Germany*

Exchange bias (EB) [1] manifests as a shift of a magnetic hysteresis loop along the magnetic field axis with a simultaneous enhancement of coercivity due to interfacial interactions of dissimilarly ordered materials (e.g. an antiferromagnet (AF) in contact with a ferro- or ferrimagnet (F)). It is an effect of fundamental importance for novel hard magnets, recording media, spin-valve and tunneling devices. In recent decades, extensive studies and attempts to describe the EB effect have been made. They have resulted in the development of a number of theoretical models for different AF-F systems (see e.g. review article by Nogués et al. [2]). However, there is still no generally accepted theory that predicts the EB behavior for an apt pair of materials brought together. The latter is partly due to the huge variety of samples studied and surface and interface effects within them. Intuitively, a default condition for observing exchange bias (with the field H_{EB} as the measure of the effect) should be an anisotropy of the antiferromagnet being large enough to "pin" the magnetization of the ferromagnet along a particular direction [1]. Recent progress in the studies of exchange-biased thin films of UO_2 combined with magnetite [3], made it of interest to test whether the exchange coupling mechanism operating in oxides is present in 3*d* alloys.

Bulk magnetism of UO_2 has been largely investigated [4]. The U^{4+} magnetic moments of UO_2 are localized and the compound orders antiferromagnetically below the Néel temperature T_N = 30.8 K. Permalloy (Py) $Ni_{80}Fe_{20}$ (Curie temperature T_C = 853 K) was chosen as the ferromagnetic component of the bilayer. UO_2 films with variable thickness of the covering $Ni_{80}Fe_{20}$ layer have been grown by reactive sputter deposition. The sputtering system is equipped with in-situ RHEED that allowed the characterization of the surface structure of each deposited layer. This, combined with standard XRD, showed epitaxial growth of the UO_2 layer on CaF_2 substrates ([100] growth direction) and a polycrystalline permalloy layer on top of it. Each sample was also covered with a 300 A thick Nb capping layer to avoid oxidation.

Magnetic properties of UO_2/Py thin films were studied in Prague using a VSM magnetometer and a SQUID with the Reciprocating Sample Option (RSO) installed to improve the sensitivity. The majority of the samples measured with field in the film plane direction showed a hysteresis of 20-50 Oe and no bias after field cooling. The temperature dependence of magnetization of UO_2/Py showed a well-defined Néel anomaly at about 31 K, being characteristic of antiferromagnetic ordering of the UO_2 layer. An attempt to measure the samples with field in the direction perpendicular to the film has brought a different result - an order of magnitude larger hysteresis and exchange bias of up to 220 Oe (see Fig. 1). In contrast to the large values of exchange-bias field found in oxide bilayers UO_2/Fe_3O_4 (e.g. a maximum effect of 2600 Oe in UO_2(300 Å)/Fe_3O_4(90 Å) [3]), these values belong to rather conventional magnitude of EB found in various metallic systems. The effect requires more studies as the increase of the hysteresis width can be due to the shape anisotropy and the

demagnetization factor. This however, would not explain the presence of exchange bias in the latter measurement geometry.

An order of magnitude difference in EB values of UO_2/Py and UO_2/Fe_3O_4 could potentially result from a much weaker exchange interaction in the former, compared to that of an oxide system UO_2/Fe_3O_4. The use of CaF_2 substrates for the UO_2/Py films could have had an impact on compensated/uncompensated [5] antiferromagnetic surface layer of UO_2. Furthermore, in the case of Fe_3O_4 there was epitaxy relationship between UO_2 and Fe_3O_4 [3], whereas the interface is rougher for polycrystalline Py. The exchange interaction is vital in both imprinting the interface spin structure of the ferromagnet into the adjacent AF material when cooling in field and then in pinning the ferromagnet by AF spins (held by AF exchange and anisotropy), which gives the off-set of the hysteresis loop. Permalloy itself exhibits only weak magnetocrystalline anisotropy.

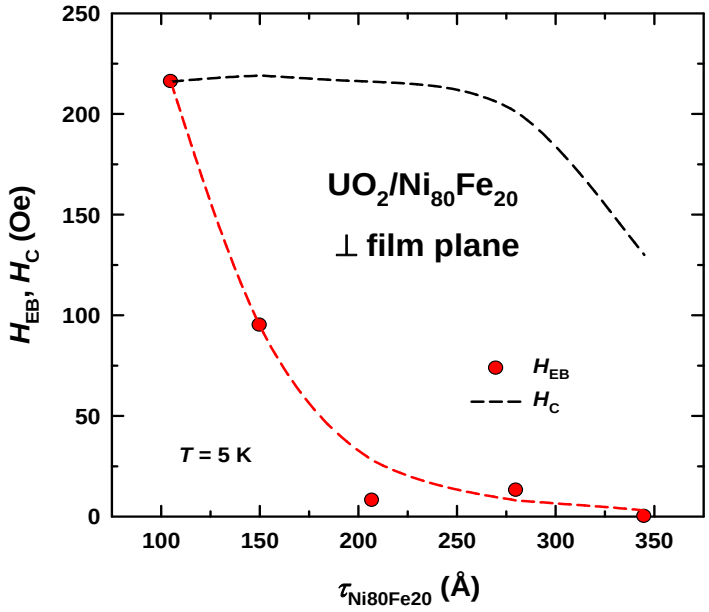

Fig. 1. Dependence of exchange bias and coercive field on the Py layer thickness in UO_2/Py bilayers measured at T = 5 K after field cooling in a 1 T field. Such decrease is typical for the EB effect.

This work has been supported by the Czech Science Foundation under the grant No. 13-25866P.

References

[1] W. H. Meiklejohn and C. P. Bean, *Phys. Rev. B* **102**, 1413 (1956).

[2] J. Nogués, J. Sort, V. Langlais, V. Skumryev, S. Surinach, J. S. Muñoz, and M. D. Baró, *Phys. Rep.* **422**, 65 (2005).

[3] Z. Bao, E. Tereshina, C. Kübel, L. Havela, T. Gouder, R. Caciuffo, Exchange bias in UO_2/Fe_3O_4 thin films (unpublished).

[4] P. Santini, S. Carretta, G. Amoretti, R. Caciuffo, N. Magnani, and G. H. Lander, *Rev. Mod. Phys.* **81**, 807 (2009).

[5] A.P. Malozemoff, *Phys. Rev. B* **35**, 3679 (1987).

Growth and characterization of uranium-alloy thin films

A M Adamska, T B Scott, R Springell, A D Warren, L Pico, O Payton

[1]*Interface Analysis Centre, School of Physics, HH Wills Physics Laboratory, University of Bristol, Tyndall Avenue, Bristol, BS8 1TL, United Kingdom*
e-mail: am.adamska@bristol.ac.uk

As world populations continue to grow and supplies of fossil fuels dwindle, there is an increasing need for alternative low-cost, carbon neutral and secure supplies of electricity. Nuclear energy is just one solution to this problem, which has become increasingly feasible as the technology matures, yielding improvements in safety, size and efficiency. The proclaimed target for the next generation of nuclear fission reactors is to become still safer and at the same time more efficient. In the wake of the Fukishima Daiichi nuclear power plant incident there is an increased emphasis on developing improved and inherently safe materials for fuels, cladding and structural materials. The preferred choice of nuclear fuel materials is limited not only by the characteristics of the reactor cores in which they are deployed but also by their subsequent behaviour as a waste-form. The key risk posed by spent nuclear fuel involves a release of radiation that could harm human health or the environment. To date, the fuel materials that have been developed for use in power reactors include uranium and thorium metals, their alloys, oxides, carbides, nitrides and hydrides, with oxide (UO_2) emerging as the fuel type predominant.

In the present study we concentrated on the growth and characterization of U-alloy thin films, which may be used as a useful low activity experimental surrogate for bulk alloy systems, significantly reducing experimental risk and limitations. In addition, they provide a simplified model surfaces for oxidation and corrosion studies that may be subsequently used to predict material changes in their bulk counterparts. More fundamentally, a thin film approach to the study of actinide compounds may lead to better understanding of 5*f* electron systems.

Pure uranium has three crystalline phases below its melting point. The room temperature (RT) α-U phase is base-centered orthorhombic structure [1]. In fuels this phase shows very poor operational stability [2], related to highly anisotropic thermal expansion [3]. It also exhibits poor dimensional stability during irradiation, making it undesirable as a fuel. The high-temperature (T > 775°C) body-centered cubic (*bcc*) γ-U phase is more resistant to irradiation effects than the α-phase and exhibits isotropic thermal expansion properties. Unfortunately, in pure U this phase cannot be preserved to RT, which presents a significant technical limitation. Conceptually, a solution to this problem is to stabilise the γ-phase down to RT by U alloying with Nb, Zr, or Mo in bulk form [4]. It has been already shown that the γ-phase U-Mo poly- and single-crystal alloys can be synthesised in thin film form [5]. Subsequently, we explored the binary alloy phase diagrams of both poly- and single-crystal U-Ta and U-Zr thin films synthesised using UHV *dc* magnetron sputter deposition. For the U-Ta system, the γ-phase U-alloy could not be formed indicating significant immiscibility. Instead separate α-U and Ta were formed containing only trace amounts of the partnering element. By comparison, successful alloying was observed for the U-Zr system. The coexistence of α- and γ-phase of U were detected for polycrystalline U-Zr system with the prevailing crystal structure controlled by composition. Epitaxial U-Zr samples were determined to have formed bi-layered structure of single-crystal γ-U, α-U phases or γ-U, α-U and δUZr_2 phases depending on the concentration of alloying element (Fig. 1.).

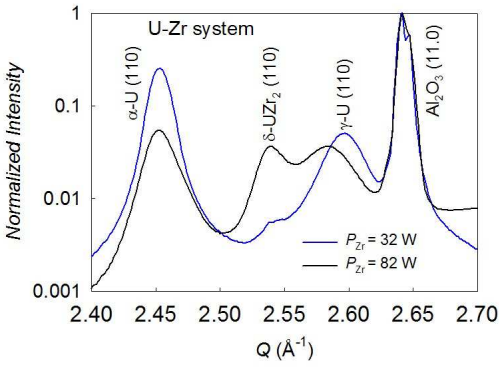

Fig. 1. Comparison of the XRD patterns close to the sapphire (11.0) peak for single-crystal U-Zr alloy thin films deposited at T = 800°C using different Zr powers.

EBSD maps recorded from the surface of the double U-Zr single-crystal sample indicated an α-U single-crystal located at the top of the film, see Fig. 2.

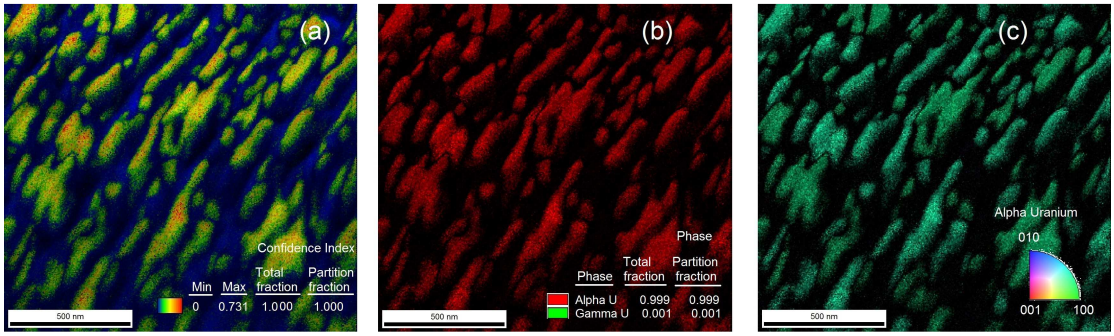

Fig. 2. EBSD maps of the double U-Zr single crystal showing (a) confidence index for the recognized phase, (b) phase fractions and (c) the inverse pole figure showing the orientation of the single crystal.

The surface topography of U-Zr single crystal shown in Fig. 3-4. exhibits a surface morphology of sharply stepped ridges. Secondary electron images of the surface reveals small square or rectangular holes ascribed as gaps or windows in the upper 'defective' layer revealing the underling 'perfect' film (Fig. 4).

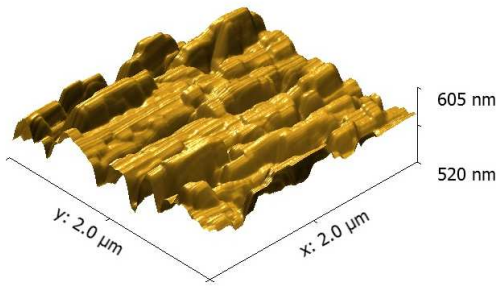

Fig. 3. AFM topography of the double U-Zr single-crystal thin film.

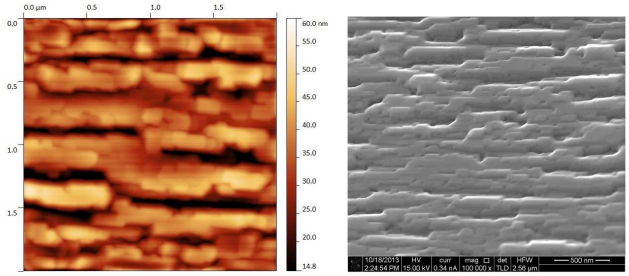

Fig. 4. Comparison between (a) AFM micrograph and (b) SE image of the surface of the double U-Zr single-crystal thin film.

References

[1] G. H. Lander et al., *Acta Cryst.* **B26**, 129 (1970)
[2] G. Ostberg et al., *J. Nucl. Mater.* **10**, 329 (1963)
[3] L.T. Lloyd, *J. Nucl. Mater.* **3**, 67 (1961)
[4] V.P. Sinha et al., *J. Alloys and Compds.* **506**, 253 (2010)
[5] A M Adamska et al.,*Thin Solid Films* **550**, 319 (2014)

Crystal structure and physical properties of $\{Th,U\}_3Ir_4Ge_{13}$

Roman Gumeniuk, Walter Schnelle, Horst Borrmann, Ulrich Burkhardt, Andreas Leithe-Jasper, Yuri Grin

Max Planck Institute for Chemical Physics of Solids, Nöthnitzer Str. 40, 01187 Dresden, Germany
e-mail: gumeniuk@cpfs.mpg.de

$Th_3Ir_4Ge_{13}$ and $U_3Ir_4Ge_{13}$ have been synthesized by arc-melting of the initial components by the followed annealing of the obtained samples at 900° C for 7 days. $Th_3Ir_4Ge_{13}$ (space group $Pm\bar{3}n$, a = 9.0586(3) Å) crystallizes with $Tm_3Co_4Ge_{13}$ type of structure, which adopts the same structure arrangement as $Yb_3Rh_4Sn_{13}$ prototype [1] with the only difference, that the 24(*k*) crystallographic site occupied by Ge atoms is split [2]. Possible modulation of the structure of $Th_3Ir_4Ge_{13}$ has been discussed. $U_3Ir_4Ge_{13}$ (space group *R3c*, a = 12.6329(1) Å, c = 15.5505(1) Å) crystallizes with non-centrosymmetric rhombohedral HT-$Y_3Pt_4Ge_{13}$ type [3]. The rhombohedral unit cell parameters are related to the initial cubic of $Yb_3Rh_4Sn_{13}$ prototype as following: $a_{rhom} \approx a_{cub}\sqrt{2}$, $c_{rhom} \approx a_{cub}\sqrt{3}$. This corroborates a close structural relationship between both type of structures.

$Th_3Ir_4Ge_{13}$ is diamagnetic in the whole measured temperature range with a molar susceptibility $\chi = -372\times10^{-6}$ emu mol^{-1} at T = 300 K. A kink in the susceptibility observed at T_k = 210 K could indicate first order structural phase transition, charge density wave or opening of a gap at the Fermi surface. A kink at ~ 240-250 K is also observed in the specific heat of $Th_3Ir_4Ge_{13}$ (γ_{el} = 4.7 mJ mol^{-1} K^{-2})

The inverse magnetic susceptibility of $U_3Ir_4Ge_{13}$ is described by a Curie-Weiss law in the temperature range 40-400 K. The effective magnetic moment μ_{eff} and the Weiss temperature θ_P determined from a linear fit to χ^{-1} are 4.06 μ_B/f.u. and +7.3(1) K, respectively. $U_3Ir_4Ge_{13}$ orders ferromagnetically at T_C = 12 K in good agreement with data reported in [4]. The observed Sommerfeld coefficient of the electronic specific heat γ_{el} = 372 mJ mol^{-1} K^{-2} for $U_3Ir_4Ge_{13}$ is large, which could suggest heavy fermion behavior. The estimated magnetic entropy reaches the value $S_{mag} \approx 0.32R\ln2$.

References

[1] J.P. Remeika et al., *Solid State Commun.* **34**, 923 (1980).
[2] L.G. Akselrud et al., *Visnyk Lviv. Univ. Ser. Khim.*, **39**, 112 (2001).
[3] R. Gumeniuk et al., *Phys. Rev. B*, **87**, 224502 (2013).
[4] B. Lloret et al., *J. de Phys.*, **49**, C8-487 (1988).

New Calculation Method for Electron Inelastic Mean Free Path in Thin Films: Measurements and Monte Carlo Transport

Eitan Tiferet[1], Mordechai Geller[1,2], Alon Givon[2*], Itzhak Orion[2]

[1] *Department of Materials, Nuclear Research Center-Negev, Israel*
e-mail: iorion@bgu.ac.il
[2] *Department of Nuclear Engineering, Ben-Gurion University of the Negev, Israel*
[*] *Present address: The Weizmann Institute of Science, Rehovot, Israel*

The advanced in third generation synchrotrons, such as ESRF, and new x-ray sources enable the use of photoelectrons with higher kinetic energy than before. This created a void in the IMFP (Inelastic Mean Free Path) data, which was filled recently with the publication of calculated IMFP values over the 50 eV to 30 keV energy range [1]. Yet, the indispensible experimental data for the validation of calculated IMFP values is lacking in energies above 5 keV.
For the lower energy range, below 2000 eV, the IMFP measurements methods were based on detecting the backward elastic scattered electrons, and from that extracting the inelastic MFP, eventually..
This study was aimed to establish new methods for low Z materials in the 5 to 15 keV energy range for measuring the electron IMFP. Full description of both the wide energy spectrum approach and the total current measurement approach are presented. The wide energy spectrum approach relies on the multiple inelastic scattering effect that predicts electron kinetic energy decrease by 15% in average, and thus requires experimental spectroscopy measurements.
We show experimental results, performed at the Spanish CRG BM25 beam-line (SpLine) in ESRF [2], that substantiate our wide energy spectrum approach. The spectral results, as shown in Fig. 1, demonstrate the distinct characteristics of the electron multiple inelastic scatterings. These characteristics match the theoretical calculations and give IMFP values that agree with the published IMFP calculated data.

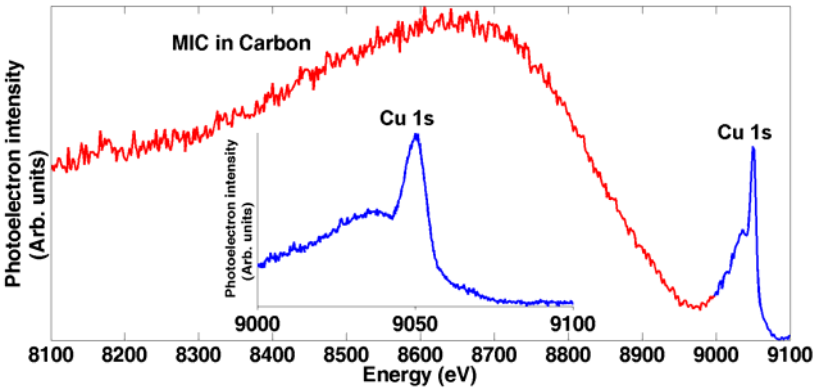

Fig. 1.The multiple inelastic collisions electrons peak (MIC) in a Carbon film over a Cu bulk.

The new methods were shown to accurately describe the transport of electrons in the 5 to 15 keV energy range. Our wide energy spectrum measurements approach was confirmed in synchrotron experiments, and the IMFP of carbon graphite was measured in various energies [3]. The measured electron IMFP at energies of 8860 eV and 7854 eV compared to the IMFP reported in the literature showed a difference of 1.9% and 1.7%, respectively. These innovative methods and the novel Monte Carlo simulation program opened new possibilities for the study of electron IMFPs at energies between 5 and 15 keV that previously were not available.
The inelastic scattered electrons peak was experimentally revealed, for the first time, in our spectral results at ESRF. The advancement in the study of electron IMFP measurements at

energies above 5 keV was achieved by applying the electron multiple inelastic scattering theory on new concepts that integrates experimental measurements and Monte Carlo simulations. For the simulations, a new Monte Carlo code that meets the methods demands is in progress. The code can provide different electron track images, due to detection angular opening, and to score multiple inelastic collisions compared to the elastic electrons tally.

References

[1] W. S. M. Werner, Differential surface and volume excitation probability of medium-energy electrons in solids, Physical Review B **74**, 075421 (2006).
[2] The Spanish CRG Beamline for Absorption and Diffraction
http://www.esrf.eu/UsersAndScience/Experiments/CRG/BM25.
[3] A. Givon et al., Hard X-ray Photoelectron Spectroscopy Study of Electron Spectral Structure beyond the Known Signal Electron Peak, J. Chem. Eng. 7 601-605 (2013).

High Explosive Radiological Dispersion Device: Time and Distance Multiscale Study

A. Sharon[*1], I. Halevy[1], L. Krantz[2], D. Sattinger[1], P. Banaim[1],I. Yaar[1]

[1]Nuclear Research Center Negev (NRCN), P.O.Box 9001, Beer- Sheva, Israel
[2]IAEC, Tel-Aviv, Israel

A wide range of explosion tests imitates different explosive RDD scenarios were conducted and aimed at increasing the preparedness for possible terrorism events, where radioactive (RA) materials disperse via an explosive charge. About 20 atmospheric dispersion tests were conducted using6-8 Ci of ^{99m}Tc which were coupled to TNT charges within the range of 0.25-25 kg. Tests performed above different typical urban ground surfaces (in order to study the surface effect on the activity ground deposition pattern due to different in particles size distribution). We have used an efficient aerosolizing devices, means that most of the RA particles were initially created within the size of fine aerosols, mostly respirable. Ground activity measurements were performed both, around the dispersion point and up to few hundred meters downwind. Micrometeorology parameters (wind intensity and direction, potential temperature, relative humidity, solar radiation and atmospheric stability) were collected allowing comparisons topredictions of existing atmospheric dispersion models'[1]. Based on the experimental results, new model parameterizations were performed. Improvements in the models' predictions were achieved and a set of thumb rules for first responders was formulated. This paper describes the project objectives, some of the experimental setups and results obtained. Post detonation nuclear forensic considerations can be made based upon results achieved.

1. Introduction

Health and environmental consequences of an explosive RDD event depend on many parameters. Among them: type and amount of high explosive (HE), type of RA material, device geometry, surface type below the detonation and local meteorology conditions. A given set of these parameters will define the severity of the event by means of the total dose levels that people might be exposed to (both externally and internally) and the level (and size) of the contaminated area. The dispersion of fine respirable size (<10 micron)is mainly a risk via inhalation while the dispersion of large size particles and aerosols is a hazardous via external exposure. The final RA particle size distribution following such an event is the key question for a reliable risk assessment calculations and preparedness for explosive RDD events.

The project includes three phases (I, II and III) with different aims for each one. GFI included a wide set of detonation tests where simulant material were dispersed and the explosion cloud were detected up to the effective height, before its downwind motion. One of the important achievements of this phase is the formulation of a model[2] for the elevation of the explosion cloud up to the effective height as a function of: time elapsed, horizontal wind speed, atmospheric stability class and HE amount up to 100 kg (equivalent to TNT).

The other two phases included atmospheric dispersion of an explosive RDD devices using a short live RA material (^{99m}Tc with $T_{1/2}$=6.02 hr. and gamma photon on 141 kev). The device used was such that, initially, most of the RA particles created were within the range of fine aerosols. The HE amount used was up to 25 kg of TNT.

Data collecting done during and after the tests included different time and length scales. From micro-seconds (follow the detonation fireball evolution) to minutes (follow the downwind motion of the contaminated cloud)and from the immediate area around the detonation point to 100's m downwind direction.

The main project objectives were:

- Measuring the surface activity concentrations around ground zero(GZ), were meteorology is not yet influence, and up to a few hundred meters downwind. Existing models are weak in very near area predictions.
- Study the fireball–ground interaction by means of the amount of activity deposited on the ground in the close vicinity where the fireball “kisses” the ground.
- Measuring the aerial distribution of the activity around the detonation point.
- Measuring the effect of different HE amounts and different surfaces on the ground activity deposition pattern.
- Comparison between predictions of atmospheric and health physics dispersion codes (Hotspot, ERAD, LODI, RODOS, ARGOS) and field results.
- New models’ parameterizations based on the experimental results and comprehensive calculations.

2. Experimental setup

Phases II and III of the project included 20 tests where6-8 Ci of ^{99m}Tc dispersed by 0.25-20 kg of TNT charges. Shots were done above clean or dirt surfaces in order to study the effect of the different amount of dirt entrained into the fireball. While clean (steel) surface do not involve much of dirt entrainment into the fireball, dirtier surfaces (packed sand soil, concrete, asphalt) involve dirt in the fireball and hence reduce the amount of fine RA particles, due to agglomeration-condensation processes.
We study the effect of different heights of detonation above ground level and compare it to ground detonation.
High resolution radiation detection (about 40 points collected) was done in order to get an accurate 2D radiation fields. Special attention was given to few meters circle around the detonation point, called "Ground Zero" (GZ).
RA concentrations in the air were measured by high volume air samplers around the detonation point.
Particles were collected by stubs from the GZ area and were analyzed by SEMand EDS for the sake of size distribution, morphology and chemical composition. Agglomerates of dirt and RA material were detected.
Tests were documented and recorded by three video cameras (from 3 different locations), high speed camera, thermal camera (part of the shots), fast multispectral radiometer (in some of the tests) and stills camera.
Radiation detection was done by $LnBr_3$, personal detection system PDS (CsI crystal), HPGE, NaI (different volumes) and beta surface detectors. Each point were measured shielded (by Lead plates) and unshielded for local and integrated (including the GZ “hot zone”) radiation levels, respectively.

3. Results and discussions

A comparison between the 2D ground contamination raw data (cps) and analyzed data (real surface activity) for 0.25 kg of TNT shot is shown in figure 1.

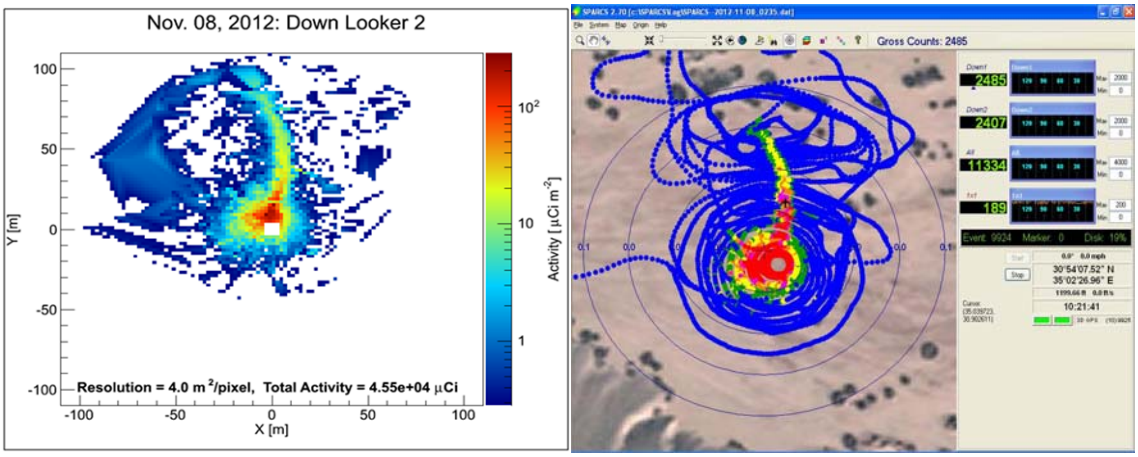

Figure1: Raw (right)vs. analyzed (left) data of activity ground deposition following detonation of 0.25 kg of TNT combined to RA source of 6.6 Ci of ^{99m}Tc.
Note that the 2D maps in figure 1 do not include the contribution of the "hot" area, few meters around the detonation point, where most the activity was deposited. It was found out that 3-20% of the total activity was deposited in area radios of 3-4 fireball radii. Since most of the RA particles dispersed were fine, respirable size, just 2% of the total activity was found on the ground up to 300 m downwind. That means that most of the activity, initially dispersed, was not found. The "hot zone" activity is shown in figure 2.

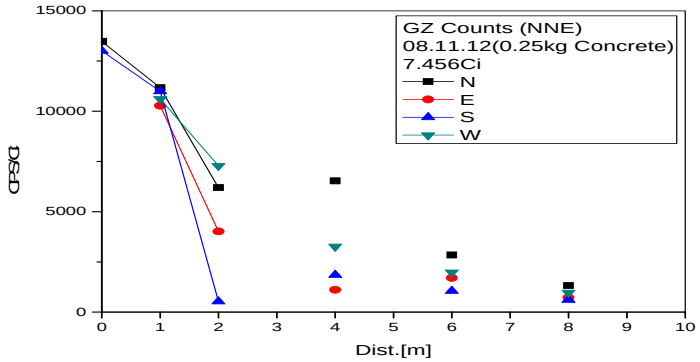

Fig. 2: The "hot zone" activity [cps/Ci] distribution along four directions away from the detonation point (North, South, East and West).

3. Summary

The final activity ground deposition pattern following the detonation of an RDD involves time and distance multiscale phenomena. The initial radiactive particle's size defined at 10's-100's micro-seconds time scale while agglomeration to ambient dirt occur 10's-100's ms after the detonation.

The area few meters around the detonation point contains much more activity then the wide area of few hundreds of meters downwind. We have shown an example of results from a real RA material atmospheric dispersion test performed during this study.

References

1. Hotspot 2.07.2, Health physics and atmospheric dispersion code, LLNL-USA, Sep. 2011.
2. A. Sharon, I. Halevy, D. Sattinger, I. Yaar, Cloud rise model for RDD events, Atmospheric Environment 54 (2012) 603-610.

Fast Multispectral Radiometry for Particles Analysis

A. Sharon[*1], I. Halevy[1], D. Sattinger[1], L. Krantz[2], M. Pinhas[2], I. Yaar[1]

[1]Nuclear Research Center Negev (NRCN), P.O.Box 9001, Beer- Sheva, Israel
[2]IAEC, Tel-Aviv, Israel

The radiological risk following detonation of radiological dispersal device (RDD) is highly depends the final particles' size distribution remains after the detonation. In order to produce a realistic source term for the atmospheric dispersion model we should be able to predict the total fraction of aerosols created after the detonation as well as the respirable part of this fraction. The rest of the particles will not be dispersed downwind and hence them concentration will be calculated using much simpler models.
The radiological risk out of radioactive (RA) material is highly depends on the particle size. Respirable size (<10 microns) of Alfa, Beta and Gamma emitters are all dangerous when inhaled into the body while larger aerosolos might be risky from a distance (Gamma emitters) or in an external body contact (Alfa, Beta and Gamma). Larger particles (which are not aerosols) are dangerous as fragments when penetrating the body (Alfa, Beta and Gamma) or when depositing on the ground as Gamma emitters. We show here that by using a fast multispectral radiometryfor the detonation fireball analysis it is possible to quantify the reduction of total amount of aerosols due to particles agglomeration with dirt.

1. Introduction

Sets of detonation tests were done using 0.25-25 kg of TNT charges above different surface types. The ColoRad C7, (fast multispectral radiometer (FMR)) of IARD-Israel[2]was used. This unique tool was aimed to detect the fast temporal (radiant intensity and radiant temperature) evolution of the fireball in time scales of micro seconds (samplingrate of 250 kHz).
Fireball average radiant intensity was measured each four microseconds in four different spectral bands. The aim of using this tool was to be able to quantify the contribution of the different particles and detonation products to the total energy released following a high explosive detonation. The measurement of the radiant intensity of the aerosols and the other particles involved (detonation products, soot, carbon monoxide, carbon dioxide and dirt entrained into the fireball) and a comparison between clean and dirt shots enable to study the effect of agglomeration processes occur when dirt entrained into the fireball due to the vortices created following the detonation. Further analysis can yield the temporal variation of the radiant temperature and the effective radiant area.
Since most high explosives are under balanced to Oxygen we expect two radiate peaks following detonation: **the first one** is due to oxidation of explosive atoms and molecules (mainly H_2, C, CO and other metals, if exit (Al, Mg, etc.))and **the second** is the late oxidation of detonation products with ambient Oxygen.
There are three necessary conditions for the occurrence of the late energy pulse (called afterburn): 1. free available ambient oxygen, 2.material to be oxidized ("fuel") and 3. "high enough" temperatures.
During the afterburn process, the C atoms of the explosive oxidize into CO molecules and then into CO_2 molecules, if there is still available oxygen and high temperatures (> 1750^oK). Entrained ambient dirt (into the fireball) can be agglomerated to the radioactive particles and to change the initial size of the particles.
Enhanced amount of dirt entrained into the fireball reduce its temperature and suppress the afterburn process. In such a case the 2^{nd} peak will be lower than the in case of clean detonation where no dirt entrained into the fireball. TNT is an example of explosive which is extremely under balanced to Oxygen (-74%). This means that in the case of clean detonation the first energy peak (called the detonation energy[3])yields only about one third of the total available energy (combustion energy).The rest two third might release during the afterburn stage (if exist!).

The spectral bands (all in the SWIR and MWIR range) were chosen in order to cover the molecular emission of the detonation products and the CO_2which can be used as an “afterburn indicator”.
Figure 1 showa TNT fireball during the afterburn stage (right) and the radiometer used during GF tests.

Figure 1: Fireball snapshot of 0.25 kg (TNT) during the afterburn stage at t=28.3 ms.

2. Experimental results: radiant intensity and temperatures

A comparison between two shots of the same explosive charge (25 kg of TNT), one is at 0.55 m height above clean steel surface (on the left) and the other is on packed soil, dirt surface, is presented on figure 2.
The aerosol and the CO_2power [kw] for the two shots are compared.
One can recognize the two peaks of the energy pulses: the first one (around 1ms) is related to the detonation energy and the second (around 30-50 ms) is the after burn contribution of the later oxidation, mainly due to the emission of the CO_2.

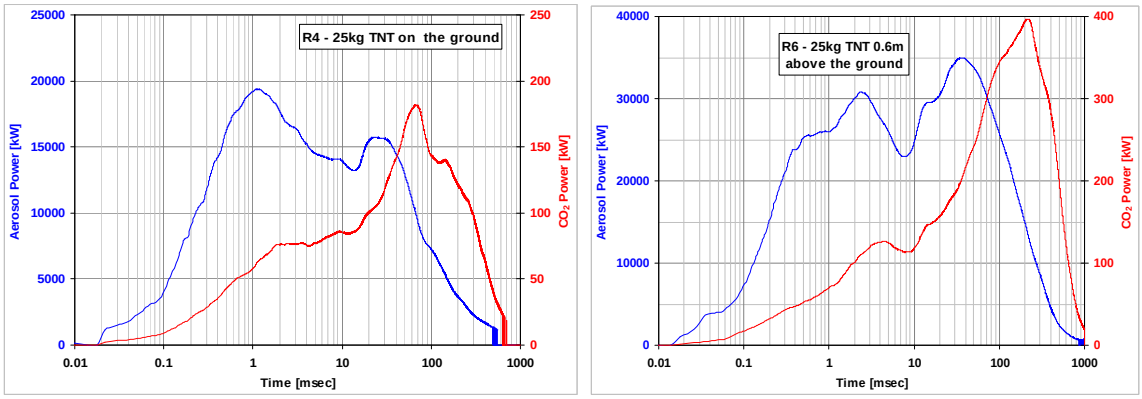

Figure 2: Fireball radiant intensity of clean (right) and dirt (left) of 25 kg of TNT charges.

The afterburn peak of the CO_2 power is more than two times higher in the case of the cleaner shot much lower amount of ambient dirt was entrained into the fireball and thus higher temperatures were exist to support longer afterburn process. On the other hand, the dirt shot involves high amount of soil that entrained by the fireball strong vortices, reduced the radiant temperature and suppressed the oxidation of the C atoms and the CO molecules into CO_2.
RA particle size distribution will be different for the two shots, even though the charges were similar! We can, thus, use the CO_2 radiant intensity (or power) as an indicator for the fireball cleanness for certain explosive type. In the next stage it will be related to the reduction of the fraction of fine aerosols due to agglomeration with ambient dirt.

3. Summary

Fast multispectral radiometry of detonation fire balls is using for the study of the dynamic physical and chemical processes in the fireball. The afterburn intensity, mainly due to CO_2emission can be used as an indicator for the fireball cleanness which effect the final size distribution of RA particles disperse by high explosive charges.

References

1.A. Sharon et al. Ground deposition pattern of an explosive RDD, Israel Nuclear Society conference, February 2014, Dead sea, Israel.
2. IARD – Sensing solutions Ltd., Yagur, 30065, Israel.
3. P. A. Cooper, Explosive Engineering, WILEY-VCH, ISBN-0-471-18636-8 1996.

Aerial Measuring System (AMS)/ Israel Atomic Energy Commission (IAEC) Joint Comparison Study

I. Halevy [1], P. Wasiolek [2], S. Dadon[1], M. Sheinfeld[1], A. Broide[1], S. Rofe[1] and I.Yaar[1]

1. Israel Atomic Energy Commission, Israel

2. U.S. Department of Energy National Nuclear Security Administration Remote Sensing Laboratory, USA

Israeli Team: I. Halevy, S. Dadon, M. Sheinfeld, A. Broide, S. Rofe and I.Yaar
American Team: AMS team – RSL LV
Piotr Wasiolek, Rusty Malchow, Carson Riland, Manuel Avaro, Ray Arsenault
Ed Zachman, Mike Lukens, Joe Keller, Jaz Stampahar and John Gelsthorpe

In support of the U.S. Department of Energy (DOE) International Emergency Management and Cooperation (IEMC/NA-46) Program, the comparison of the U.S. and Israeli Aerial Measuring Systems (AMS) study was proposed and accepted. The study, organized by the DOE/National Nuclear Security Administration (NNSA) Remote Sensing Laboratory (RSL), involved the DOE/NNSA Aerial Measuring System Project based at the RSL and operated under a contractor agreement by National Security Technologies, LLC (NSTec), and the Israel Atomic Energy Commission (IAEC) Aerial Measuring System. The operational comparison was conducted at RSL-Nellis in Las Vegas, Nevada, during week of June 24–27, 2013. The Israeli system, Air RAM 2000 (figure 1, down), was shipped to RSL-Nellis and mounted together with the DOE Spectral Advanced Radiological Computer System, Model A (SPARCS-A, figure 1 up) on U.S. DOE Bell-412 helicopter for a series of aerial comparison measurements at local test ranges, including the Desert Rock Airport and Area 3 at the Nevada National Security Site (NNSS). A four-person Israeli team from the IAEC, Nuclear Research Center – Negev (NRCN) supported the activity.
The main objective of this joint comparison was use the DOE/RSL Bell-412 helicopter aerial platform, perform the comparison study of measuring techniques and radiation acquisition systems utilized for emergency response by IEAC and NNSA AMS [1].

MEASURING SYSTEMS

One advantage of acquiring aero-radiometric measurements lies in the high collection rate of data over large areas and rough terrain. Typical aero-radiometric systems record and save gamma-ray spectra, correlated with the Global Positioning System (GPS) derived location information (latitude, longitude, elevation over GPS ellipsoid=GPS altitude) in regular time intervals of 1 to 2 seconds. Such data can be used to locate radiation anomalies on the ground, map ground contamination, or track a radioactive airborne plume. Acquiring spectral data of this type allows separation of natural radioactivity from that of man-made sources and identification of specific isotopes, whether natural or man-made.
During the acquisition the flight altitude is kept constant, with typical values recorded between 50 and 985 feet (ft) (15 and 100 meters [m]) above ground level (AGL). The helicopter ground speed is maintained constant, in the case of DOE Bell-412, 70 knots (130 km/h).
For the comparison study, AMS and IAEC used their emergency response radiation detection systems, Israel's Air RAM 2000, and the DOE's SPARCS. For altitude measurements the AirRAM 2000 system uses a barometric altimeter with the range of 0–8000 ft, which is calibrated at 1000 ft by a radar altimeter. The SPARCS system uses radar altimeters for vertical positioning (altitude over the ground) and Differential GPS for location.

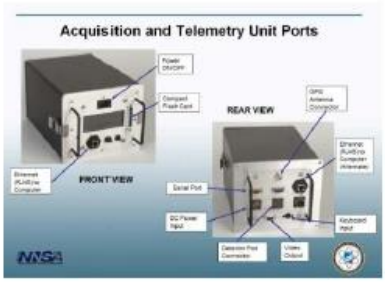

Figure 1. Interior of the SPARCS-A pod and The SPARCS ATU connections, up.
The Air ram2000, down.

Survey Aircraft

The DOE Bell-412 helicopter was used as the airborne platform to carry out the comparison study (figure 2). The Bell-412 is a twin engine utility helicopter that has been manufactured by Bell Helicopter since 1981. With a standard fuel capacity of 330 gallons, it is capable of flying for up to 3.7 hours, with a maximum range of 356 nautical miles and a cruising speed of 122 knots. However, with the AMS radiation survey configuration of 12 detectors, four crew members (two pilots, a mission scientist, and an equipment operator), with a survey speed of 70 knots (120 ft/sec) at survey altitude of 300 ft AGL, the Bell-412 was capable of 2.5 hours of flight time.

Figure 2. DOE Bell-412 helicopter during survey

RESULTS
Attenuation and Sensitivity
Lake Mohave Calibration Line

The altitude spiral flight over the Lake Mohave Calibration Line was used to derive the local effective air attenuation coefficient, obtain the sensitivity of both acquisition systems, and estimate their inherent background. The altitude spiral consists of passes between two waypoints programmed into helicopter navigation system over the land calibration line and water line at several different altitudes. During the exchange, the altitudes were 50, 100, 200, 300, 750, 1500, and 3000 ft AGL. The path plots of the altitude spiral flight plotted independently by both groups are presented in Figure 3.

Figure 3. The AirRAM 2000 inside the DOE Bell-412 helicopter

The count rate ratio of the SPARCS single 2″ × 4″ ×16″ NaI detector to the AirRAM 2000 two 2″ × 2″ inch detectors of about 18 (Table 1) compares very well with the ratio of volumes between systems of 16 [128 $inch^3$ (2″ × 4″ × 16″)/8 $inch^3$ (2″ × 2″ × 2″)]. From the altitude spiral, the effective air attenuation coefficient and sensitivity of the detectors can be derived by plotting each altitude flight's net gross counts versus altitude on a semi-log plot (Figure 4) and exponentially fitting the gross counts expression:

$$Calt = CGC \times e\exp[\mu air \times (H - Havg)]$$

Where:
Calt = gross counts normalized to the averaged survey altitude, (cps).
CGC = total terrestrial count rate or gross counts, (cps).
μair = gamma ray air attenuation coefficient, ft^{-1}.
H,Havg = average radar altitude, ft AGL.
The difference in sensitivity between the SPARCS single 2″ × 4″ ×16″ NaI detector to the AirRAM 2000 two 2″ × 2″ inch detectors is remarkable, ~18 times.

Table 1. Average count rate from different detectors at the calibration line

Altitude (ft)	Count rate (cps)					
	Land Line			Water Line		
	SPARCS NaI 2″×4″×16	AirRAM two NaI 2″×2″	Count Ratio	SPARCS NaI 2″×4″×16	AirRAM two NaI 2″×2″	Count Ratio
50	2620	151	17	159	11	14
100	2450	141	17	155	10	16
200	2139	118	18	165	11	15
300	1887	102	18	172	10	17
750	993	53	19	190	12	16
1500	405	22	18	173	11	16
3000	223	13	17	196	12	16

The slope in figure 4 is the gamma ray air attenuation coefficient (0.00186 ft^{-1}).
From the graph it is clear that the heights altitude for detecting 8.5 μR/hr is ~1950 ft.

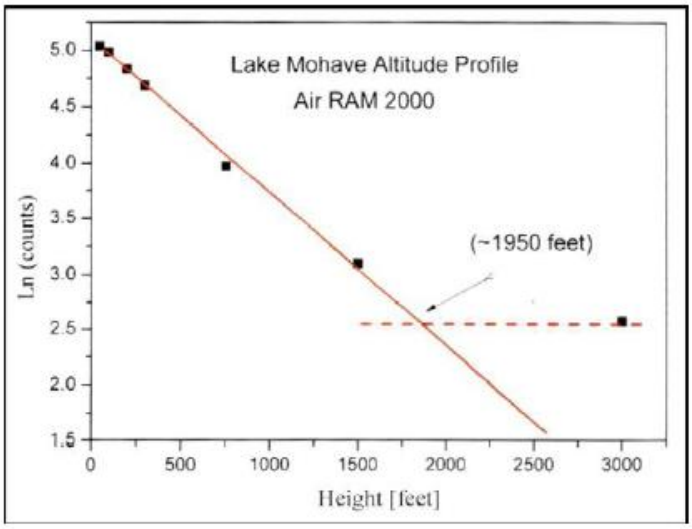

Figure 4. Results of the curve fit of the altitude spiral data collected with AirRAM and analyzed by IAEC

Desert Rock Airport Sources Overfly

Three radioactive sources listed in Table 2 were placed approximately 1500 ft (450 m) apart along the runway at the Desert Rock Airport (Figure 5). Using the visual flight rules, several passes directly over the sources (marked with orange cones) were executed. To study the response of the SPARCS and AirRAM, the flight altitude and speed were varied from 50 to 150 ft AGL and from 35 to 150 knots. The results of the source flyover are presented in Figure. The SPARCS data (gross counts from the 2″ × 4″ × 16″ NaI crystal) show an elevated count rate at any combination of flight altitude and speed tested, from 50 ft AGL at 50 knots to 150 ft AGL at 100 knots. The AirRAM, due to much lower detector volume, failed to detect the smaller 60Co source at 100 ft and both 60Co sources at 150 ft AGL. A higher flight speed of 100 knots, combined with lower sampling frequency (sample every 2 seconds) affected the AirRAM capability to spatially locate the sources.

Table 2. Activity and location of the radioactive sources used in the study

	Activity (mCi)	Longitude	Latitude
^{137}Cs	20.6	−116.028505	36.624740
^{60}Co	3.6	−116.031402	36.621293
^{60}Co	1.7	−116.034129	36.617998

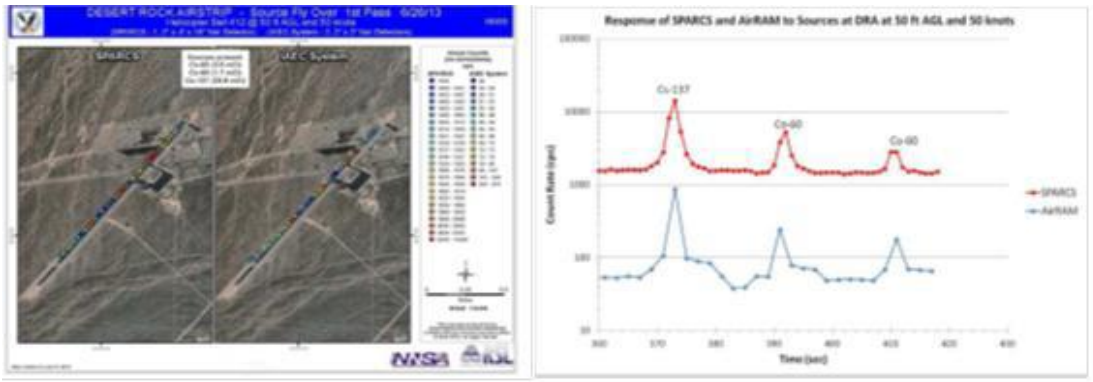

Figure 5. Source flyover at Desert Rock Airport at 50 ft AGL altitude at 50 knots ground speed presented spatially (left) and as time series (right)

Contours
Natural Background

To compare responses of the SPARCS and AirRAM to variable natural radiation background, the AMS test/evaluation area (Government Wash) was surveyed using standard AMS techniques of flying uniformly spaced parallel lines over survey area. The actual flight lines flown during the exchange are shown in Figure 6.

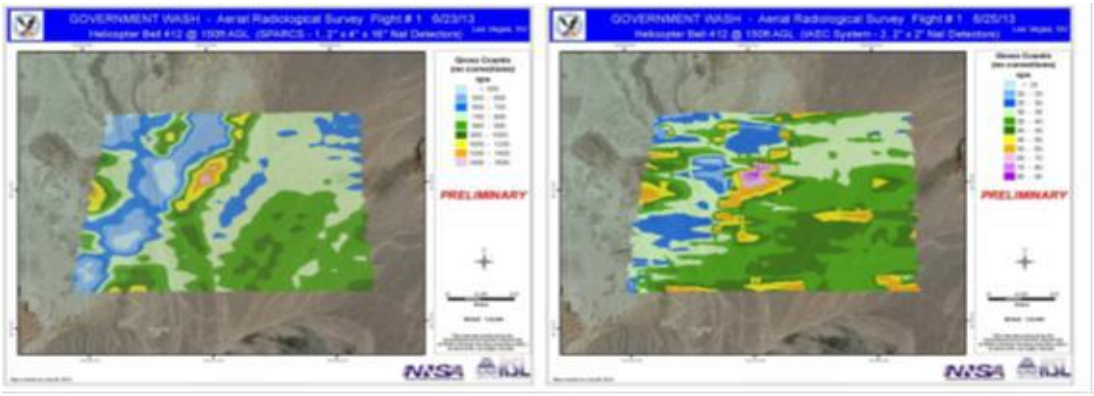

Figure 6. Gross-count contour of the natural background area (Government Wash) created using IAEC AirRAM detection system and AMS data processing techniques

[1] PIOTR WASIOLEK and ITZHAK HALEVY, AERIAL MEASURING SYSTEM (AMS)/ ISRAEL ATOMIC ENERGY COMMISSION (IAEC) JOINT COMPARISON STUDY REPORT, Nevada National Security Site June 24–27, 2013 , DOE/NV/25946--1941

On the search for a Lifshitz point in UPd_2Si2

Tomasz Plackowski, Dariusz Kaczorowski, Maria Szlawska and Józef Sznajd

Institute of Low Temperature and Structure Research, Polish Academy of Sciences,
P.O.Box 1410, 50-950 Wrocław, Poland
e-mail: D.Kaczorowski@int.pan.wroc.pl

In striking dissonance with quite extensive theoretical development of the concept of the Lifshitz point (LP) instability, made since the seminal paper by Hornreich, Luban, and Shtrikman [1], experimentally, LP as “a multicritical point whose critical behavior is strikingly different from any other,” has so far been unambigously identified in one magnetic system only, namely in MnP. Here, we suggest that a good candidate for the occurrence of the Lifshitz-type singularity might be the ternary uranium silicide UPd_2Si_2. The *H-T* phase diagram of this compound, determined with the magnetic field applied parallel to the easy magnetization direction (tetragonal axis), comprises three ordered phases, characterized by the incommensurate longitudinal spin wave (ICLSW), commensurate ferrimagnetic-like (FiM), and simple antiferromagnetic (AFM) structures, respectively. From the combined heat capacity, isothermal magnetocaloric effect, and magnetization data [2], we argue that the observed tricritical point of merging the paramagnetic, ICLSW and FiM phases exhibits the fingerprints of the conventional LP scenario, as hitherto established for MnP. This tempting conjecture appears supported by the results of some theoretical analyses performed in the framework of the mean field approximation (MFA) and the linear perturbation renormalization group (LPRG) approach to the extended axial-next-nearest-neighbor-Ising (ANNNI) model [2,3], which both indicate that the triple point in UPd_2Si_2 can be at least a Landau isolated critical point.

References

[1] R.M. Hornreich, M. Luban, and S. Shtrikman, Phys. Rev. Lett. **35**, 1678 (1975).
[2] T. Plackowski, D. Kaczorowski, and J. Sznajd, Phys. Rev. B **83**, 174443 (2011).
[3] J. Sznajd, J. Phys.: Condens. Matter 24, 436006 (2012).

High-pressure effects on the itinerant 5*f* ferromagnet U_2Fe_3Ge

D.I. Gorbunov[1,2], M.S. Henriques[3], A.V. Andreev[1], Z. Arnold[1], S. Surblé[4], S. Heathman[4], J.-C. Griveau[4], E.B. Lopes[3], J. Prchal[2], L. Havela[2], A.P. Gonçalves[3]

[1]Institute of Physics, Academy of Sciences of the Czech Republic, Na Slovance 2, 182 21 Prague, Czech Republic
e-mail: gorbunov@fzu.cz
[2]Department of Condensed Matter Physics, Faculty of Mathematics and Physics, Charles University, Ke Karlovu 5, 121 16 Prague, Czech Republic
[3]Nuclear and Technological Campus, IST/CFMC, University of Lisbon, Estrada Nacional 10, 2695-066 Bobadela LRS, Portugal
[4]European Commission, Joint Research Centre, Institute for Transuranium Elements, Postfach 2340, 76125 Karlsruhe, Germany

Magnetic properties of intermetallic compounds based on uranium and 3*d* metals are to a great extent determined by the 5*f*-3*d* hybridization. It substantially delocalizes the 5*f* electrons preventing the formation of ordered uranium magnetic moments, as in UFeAl and UFeGe (the 3*d* magnetic moment disappears as well) [1,2]. On the other hand, there exist compounds, such as UFe_2, where both sublattices, U and Fe, are magnetic [3].

Compounds having an ordered magnetic moment only within the uranium sublattice provide the focus on the nature of the 5*f* states. U_2Fe_3Ge is such a compound. It crystallizes in the hexagonal Mg_2Cu_3Si type structure (space group $P6_3/mmc$), an ordered variant of the $MgZn_2$ Laves structure (C14) [4]. U_2Fe_3Ge is a particularly interesting system since its magnetic order comes from the U sublattice only in spite of the short U-U spacing $d_{U\text{-}U} \leq 3.2$ Å, far below the Hill limit 3.4 Å for U. U_2Fe_3Ge is an itinerant ferromagnet (Curie temperature $T_C = 55$ K) having an easy-plane anisotropy.

The itinerant nature of the magnetism in U_2Fe_3Ge makes the compound sensitive to applied pressure. In general, the elastic anisotropy reflects the U-U bonding anisotropy. The direction of the shortest U-U links is the most compressible, while the U moments tend to orient perpendicular to it. The softest lattice direction seems to be the most direct parameter tuning the magnetic properties rather than the overall volume itself.

The goal of the present work is to establish the connection between structural and electronic properties of U_2Fe_3Ge, studied on a single crystal under high pressures. The stability of the crystal structure was probed by X-ray diffraction, the pressure response of the electronic properties was studied by magnetization and electrical resistivity measurements.

The structural behavior of U_2Fe_3Ge was studied by X-ray diffraction up to $p = 27$ GPa. On an unloaded sample mounted in the pressure cell the following lattice parameters were obtained: $a = 5.140$ Å and $c = 7.786$ Å. There is no obvious sign of a structural transition in the pressure range studied, in agreement with the high stability of the Laves phase structure. The relative changes of the lattice parameters $\Delta a/a$, $\Delta c/c$ and volume $\Delta V/V$ are shown in Fig. 1. Both unit cell parameters, and thus the relative cell volume decrease in a similar manner, but the compression along the *c* axis is slightly higher. The linear compressibility along each lattice direction *i* (k_i) was calculated by fitting the data to the following quadratic equation

$$G_i(p) = g_i(0) - k_i\, g_i(0)\, p + k_i'\, g_i(0)\, p^2. \quad (1)$$

It was found that $k_a = 3.0\times10^{-3}$ GPa^{-1} and $k_c = 3.7\times10^{-3}$ GPa^{-1}. The volume compressibility $k_V = 2k_a + k_c$ is related to the bulk modulus $B_0 = 1/k_V$. For U_2Fe_3Ge $k_V = 0.0097$ GPa^{-1} and $B_0 = 104$ GPa. B_0 was also obtained by fitting $\Delta V/V$ to the Birch-Murnaghan equation of state [5,6]. It yielded $B_0 = 89$ GPa, in reasonable agreement with the previous result.

Figure 2 demonstrates the effect of pressure on the magnetization along the easy *a* axis of the U_2Fe_3Ge single crystal at $T = 2$ K. A monotonous reduction of the spontaneous magnetic moment M_s is observed from 1.0 μ_B/f.u. at ambient pressure to 0.75 μ_B/f.u. at $p = 0.74$ GPa. The inset in Fig. 2 shows that M_s at $T = 2$ K and T_C decrease linearly with pressure. Both parameters display rather high relative decrease rates, $d(\ln M_s)/dp = -0.33$

GPa^{-1} and d(ln T_C)/dp = - 0.27 GPa^{-1}. A linear extrapolation of the $T_C(p)$ and $M_s(p)$ functions to zero indicates that the magnetic order in U_2Fe_3Ge will be completely suppressed between 3 and 4 GPa, which corresponds to V = 171 Å^3 (V/V_0 = 0.96 for T_C and V/V_0 = 0.97 for M_s).

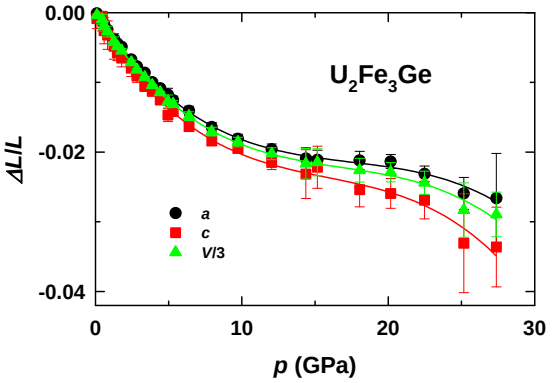

Fig 1. Pressure dependence of the relative lattice parameters and cell volume of U_2Fe_3Ge.

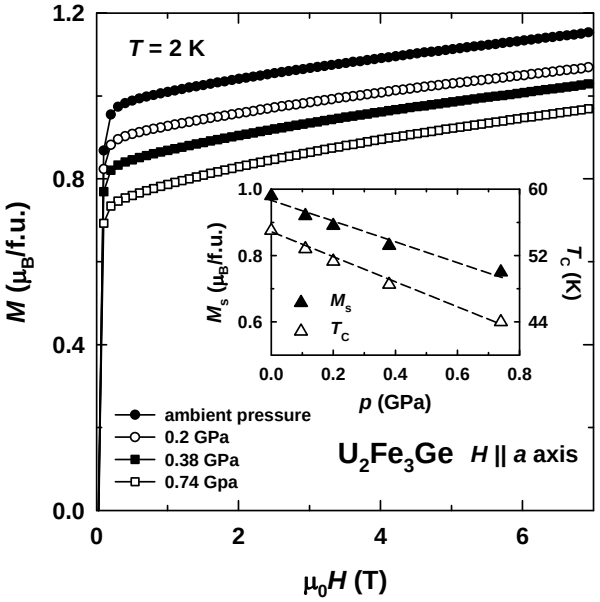

Fig. 2. Magnetization curves along the *a* axis of the U_2Fe_3Ge single crystal at T = 2 K at various pressures. The inset shows the spontaneous magnetic moment at T = 2 K and Curie temperature as functions of pressure.

Figure 3 shows the temperature dependence of the electrical resistivity ρ of U_2Fe_3Ge measured at various applied pressures with the current flowing along the *a* axis. All the data were normalized at T = 150 K since the contacts can shift between successive pressure steps. At ambient pressure, a distinct change in the slope coincides with the onset of the ferromagnetic transition, and in the low temperature region (1.5-15 K) $\rho \sim T^2$. With increasing pressure, there is an overall flattening of the resistivity curves, which is most likely to be due to a decrease in the resistivity at high temperatures. Indeed, the absolute values of ρ (not shown) at T = 300 K were found to decrease, probably as a result of the spin-disorder scattering caused by reduced magnetic moments.

In the low-T limit at elevated pressures the resistivity obeys the law $\rho \sim T^2\exp(-\Delta/T)$, pointing to the scattering of conduction electrons on spin-wave excitations with a gap Δ in the spin-wave spectrum. The energy gap is 1 K at 0.71 GPa and grows to 20 K at 3.51 GPa. The T_C values obtained from the magnetization and resistivity measurements are in good agreement.

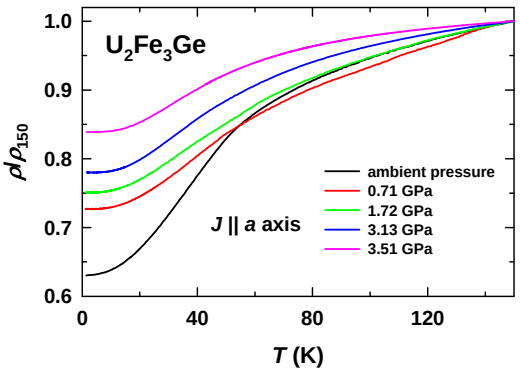

Fig. 3. Temperature dependence of the normalized electrical resistivity of the U_2Fe_3Ge single crystal at various

References

[1] A.V. Andreev, M.I. Bartashevich, Phys. Met. Metallogr. **62**, N2 50 (1986).
[2] L. Havela *et al*., J. Magn. Magn. Mater. **177–181**, 47 (1998).
[3] Y. Hamaguchi *et al*., J. Phys. Soc. Japan **17**, 398 (1962).
[4] M.S. Henriques *et al*., J. Phys.: Condens. Matter **25**, 066010 (2013).
[5] F. Birch, Phys. Rev. **71**, 809 (1947).
[6] F. Murnaghan, Am. J. Math. **49**, 235 (1937).

Pressure induced Amorphization of $Ln_{1/3}(Nb,Ta)O_3$

A. Melchior,[1] O. Noked[1,2], R. Shuker[2], E. Sterer[1]

[1] Physics Department, Nuclear Research Centre, Negev,
PO Box 9001, 84109 Beer Sheva, Israel
e-mail: avimel@gmail.com
[2] Physics Department, Ben-Gurion University,
84105 Beer Sheva, Israel

The research focuses on the phenomenon of pressure induced amorphization (PIA) in $Ln_{1/3}MO_3$, Ln - La,Pr,Nd and M-Nb,Ta. In most pressure induced phase transitions the material changes from a crystalline phase to another crystalline phase. However, if this transition is kinetically hindered, the increased free energy due to the applied pressure will result in a structural collapse to an amorphous intermediate phase. This phenomenon is known as pressure induced amorphization.
The studied materials have double perovskite structure with orthorhombic symmetry. Due to stoichiometry, the A-site lanthanide cations occupy every other 001 plane and only 2/3 of the sites in the partially occupied planes. To the best of our knowledge this is the largest group of materials exhibiting PIA.
The materials were measured using X-ray diffraction and Raman spectroscopy. Complementary measurements included TEM, resistive heating, CO_2 laser heating and X-ray absorbance (EXAFS). It was found that all niobates ($Ln_{1/3}NbO_3$) undergo PIA around 14.5 GPa, while all tantalates ($Ln_{1/3}TaO_3$) undergo PIA around 18.5GPa. This difference will be discussed in the talk.
Linear pressure-volume response was found in all the materials studied. This is a unique behavior, since in most materials applying pressure reduces interatomic distances and increases repulsion forces, thus making the material less compressible. The mechanism found to explain this behavior is the existence of ever growing tilting of the MO_6 (M-Nb,Ta) octahedral building blocks as a function of pressure. This tilting weakens the M-O-M pi-bonding found between the transition metal B-cations (M) and the oxygen anions (O) between them. While in other materials with perovskite structure this tilt is compensated and opposed by the repulsion forces of the A-site cations, the 2/3 A-site unoccupancy in $Ln_{1/3}MO_3$ significantly reduces compensation, which results in a growing compressibility with pressure until a structural collapse occurs.

Melting curves under high pressure of some light actinide metals

J. Gal

Ilse Katz Institute for Nanoscale Science and Technology Ben-Gurion University of the Negev

The prediction of the high pressure dependence of the melting temperatures of metals is traditionally based on Lindemann-Gilvarry scaling law[1] and the Debye model. The Born[2] approach assumes that melting occurs if one of the shear elastic moduli vanishes. Lindeman's approach is based on the assumption that melting occurs when the displacement of the atoms $<u^2>$ reaches a critical fraction of the nearest spacing[1]. The M. Born criterion of melting is based on analysis of stability of crystal lattice against shear stress. Predicting the crystal will melt if one of its shear elastic moduli vanishes ($1/2(C_{11}-C_{12}) = 0$ or $C_{44}(T_m) = 0$), meaning that the solid lost its rigidity and no long or short range crystallographic order exist.

In the present contribution it is shown that by combining these two approaches the melting temperature Tm(P) up to ultra high pressures can be predicted just from the low pressure experiments. This is done by deriving the ambient temperature isothermal bulk modulus B_o and the pressure derivative B' from the equation of state in the P-V plane at ambient pressures and Tm_o - the ambient pressure melting temperature. The experimental data at low pressures are fitted by utilizing combined Lindemann-Gilvarry law with Murnaghan equation of state:

$$T_m(P) = T_{mo}\,[\{B'/B_o \cdot P + 1\}^{1/B'}]^{2/3}\ \exp\{2\,\gamma_o[1-(B'/B_o \cdot P+1)^{1/B'}]\}$$

It is shown that only one free parameter γ_o is needed to predict the pressure dependency melting curves of many metals. γ_o is assigned as an effective Grüneisen parameter. The melting curves of Ar, Al, Fe, Ni, Cu, Pb ,U at ultra high pressures can be predicted by extrapolation utilizing this combined approach.

We conclude that the behavior of elemental metals melting curves up to ultra high pressures is driven by the bulk modulus B_o and its pressure derivative B' as determined from the equation of state. However, we show that the effective Grüneisen parameter γ_o for metals exhibiting pressure dependent volume collapse associated with anomalous melting behavior, like Bi and α-Pu, becomes negative, demonstrating the universality of Lindemann-Gilvarry criterion.

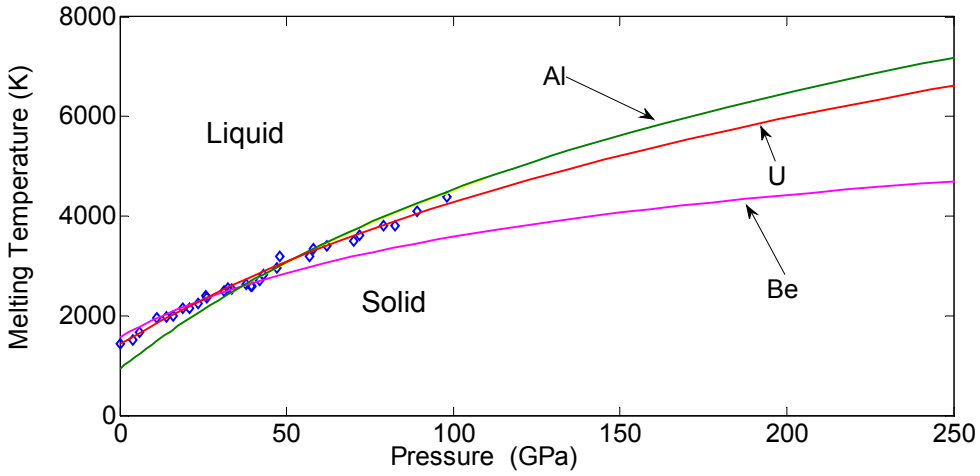

Fig 1. Melting curve of uranium under pressure, determined by combined Lindemann-Gilvarry law with Murnaghan equation of state.

The diamond dots are the experimental data of Yoo et al [3]. The red solid curve is the Lindemann-Murnghan best fit with B_o=138 GPa, B'=3.8 as derived from the EOS and γ_o = 2.25. The fits were done by fixing all parameters except the Grüneisen parameter γ_o. The present approach best fits to the experimental data of Be (magenta),U(red) and Al(green) are depicted. More examples will be shown in the presentation.

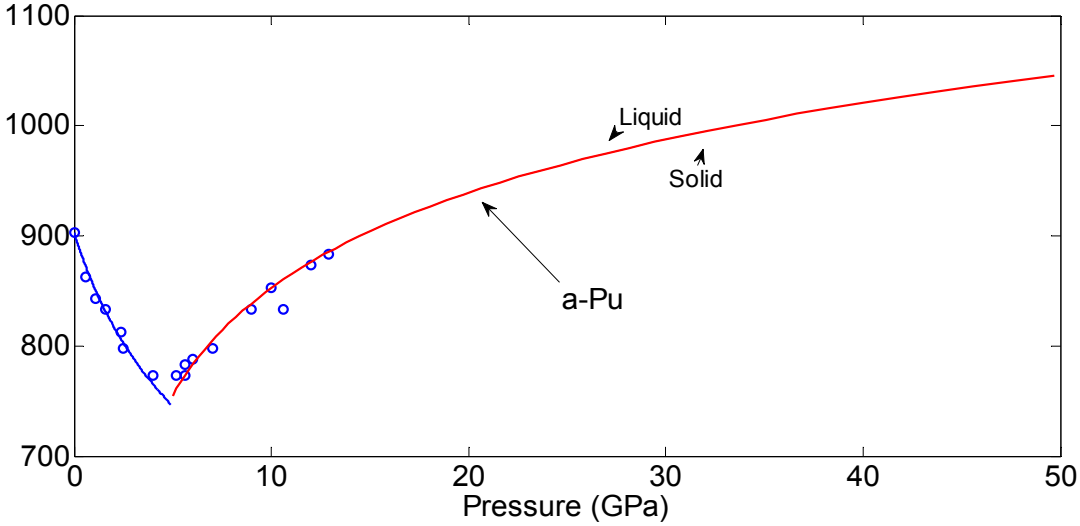

Fig 2. Melting curve of α-Pu. The experimental[4] data at low pressures are fitted by utilizing combined Lindemann-Gilvarry law with Murnaghan equation of state. For P< 4 GPa γ_o =-1.1 (negative), for P> 5GPa γ_o = 1.1. B_o=42 GPa, B'=12 are derived from the EOS.

References

1. F.A. Lindemann Z.Physik **11** 609 (1910).
2. Max Born J.Chem.Phys. 7 591 (1939).
3. C-S Yoo, J.AkellA and J.A. Moriarty PRB 48, 15 529 (1993**).**
4. C. Roux and P. del Roux, Nuc.Mat. 40,305(1971)**.**

Recent progress in the investigation of the electronic and magnetic properties of $NpNi_5$

A. Hen,[1,2] E. Colineau,[1] R. Eloirdi,[1] J.-C. Griveau,[1] J.-P. Sanchez,[5] F. Wilhelm,[6] A. Rogalev,[6] A. B. Shick,[7] I. Halevy,[2,3,4] I. Orion,[2] and R. Caciuffo[1]

[1]European Commission, Joint Research Centre, Institute for Transuranium Elements, Postfach 2340, D-76125 Karlsruhe, Germany
E-mail: amir.hen@mail.huji.ac.il
[2]Nuclear Engineering Department, Ben Gurion University, IL84105 Beer-Sheva, Israel
[3]Physics Department, Nuclear Research Center Negev, P.O. Box 9001, IL84190 Beer-Sheva, Israel
[4]California Institute of Technology, W. M. Keck Laboratory 138-78, Pasadena, California 91125, USA
[5]SPSMS, UMR-E CEA/UJF-Grenoble 1, INAC, FR-38054 Grenoble, France
[6]European Synchrotron Radiation Facility (ESRF), B.P.220, F-38043 Grenoble, France
[7]Institute of Physics, Academy of Sciences of the Czech Republic, Na Slovance 2, CZ-182 21 Prague, Czech Republic

ReT_5 (Re = rare earth, T = Transition metal) compounds have been studied in the past in the frame of its magnetic properties (small Re to T stoichiometric ratio, large spontaneous magnetization and high Curie temperature) [1-2]. Extending these investigations to actinide analogues is interesting, as the wider radial extension of the *5f* electronic shell compared to the *4f* one should result in a larger inter-sublattice exchange interaction, and in non-negligible An-An exchange coupling. The spin-orbit interaction in the *5f* configuration for the actinide atoms is also larger than the *4f* spin-orbit interaction. For these reasons, a magnetic behaviour even richer than the one observed in the rare earth compounds is expected.

$NpNi_5$ [3] was synthesized by arc-melting and X-Ray powder diffraction enabled to confirm a $CaCu_5$ (D_{6h}) P6/mmm hexagonal crystallographic structure having one Np atom per unit cell, with room-temperature lattice parameters a = 4.8501 (5) Å and c = 3.9841 (5) Å. Physical properties were measured by the means of Superconducting – Quantum – Interference – Device (SQUID) magnetometry, ^{237}Np Mössbauer spectroscopy (Fig. 1), specific heat measurements (Fig. 2) and X-Ray magnetic circular dichroism (XMCD) (Fig. 3).

$NpNi_5$ is a ferromagnetic binary system, where the Np *5f* electrons seem to be essentially localized. Magnetization curves (not shown) indicate that $NpNi_5$ is a soft ferromagnet with a T_C ~16 K with a clear Curie–Weiss behaviour above T_C (μ_{eff} ~ 3.7 μ_B, θ_P ~ 14.6 K).
Mössbauer spectroscopy data (Fig. 1) suggests a Np^{3+} oxidation state ($5f^4$ electronic configuration), The hyperfine field inferred from the spectrum at 4.2 K (~439 T) yields an ordered moment at the Np site μ_{Np} ~ 2 μ_B. Comparison with saturated magnetization suggests an average moment of only 0.04 μ_B on the Ni sites.
The specific heat (Fig. 2) shows a clear and narrow anomaly at ~16 K corresponding to the onset of magnetic order. In applied magnetic fields the peak is shifted towards higher temperature and broadened (not shown), as expected for a ferromagnet. The magnetic transition can be extracted form the total specific heat by subtracting the phonons, electron, and nuclear contributions. Inset shows the low temperature part indicating the presence of the nuclear Schottky contribution.

In this communication we will present the results obtained (including preliminary data from XMCD) and discuss them in the light of theoretical considerations.

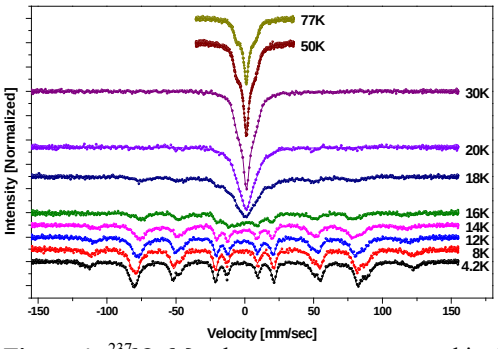

Figure 1: ^{237}Np Mössbauer spectra measured in the temperature range 4.2 - 77 K.

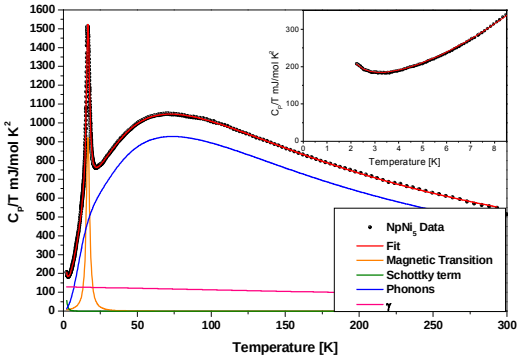

Figure 2: Normalized specific heat as a function of temperature, Solid lines – theoretical fit and its components. Insert – low temperature specific heat.

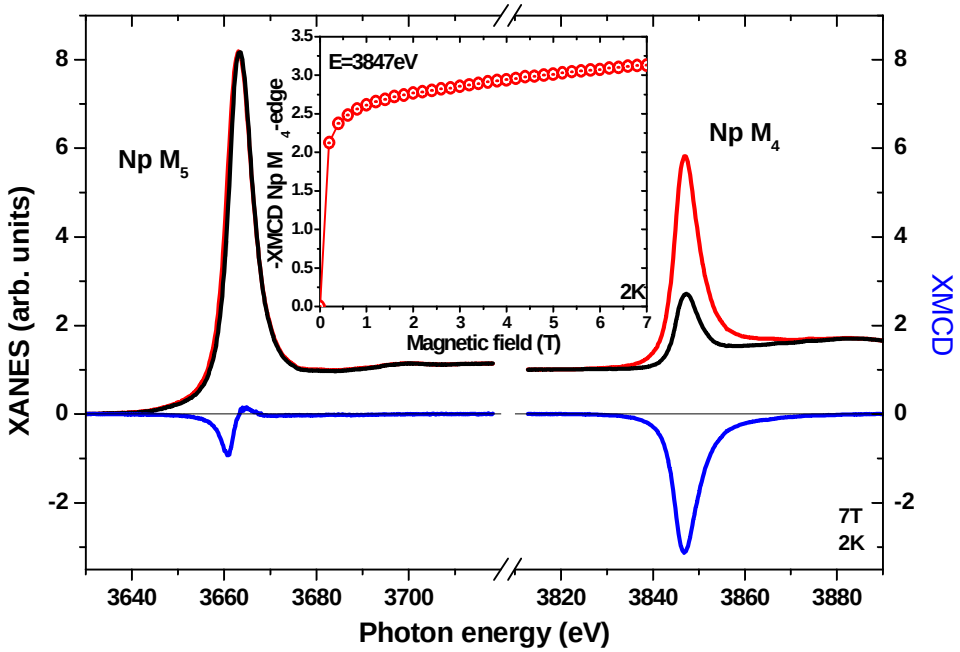

Figure 3: X-ray absorption spectra μ^+ (red line), μ^- (black line) measured at 2 K and H_{ext}=7 T at the $M_{4,5}$ Np absorption edges; Blue line – XMCD signal, inset – field dependence of the XMCD signal at the M_4 edge.

Acknowledgements

The high purity Np metals required for the fabrication of the compound were made available through a loan agreement between Lawrence Livermore National Laboratory and ITU, in the frame of a collaboration involving LLNL, Los Alamos National Laboratory and the US Department of Energy.

References

[1] S. Nasu *et al.,* Journal of Physics and Chemistry of Solids, **32**, 2779 (1971).
[2] R. M. Gale´ra *and* A. Rogalev, Journal of Applied Physics **85**, 4889 (1999).
[3] M. Akabori *et al.*, Journal of Alloys and Compounds **257** 268 (1997).

Materials research using Positron Annihilation Spectroscopy (PAS)

Sharon May-Tal Beck,[1] D Cohen[2], O Hen[3], J Dumas[2], A Ocherashvili[1], E Piasetzky[3], N Pilip[3], G Ron[2], I Sabo-Napadensky[4] and R Weiss-Babai[4]

[1] *Physics department, NRCN, P.O.Box 9001, Beer-Sheva , 84190, Israel*
e-mail: smtbeck@gmail.com
[2] *Racah Institute of Physics, Hebrew University of Jerusalem, Jerusalem, 91904, Israel*
[3] *School of Physics and Astronomy, Tel-Aviv University, Tel-Aviv, 69978, Israel*
[4] *Soreq NRC, Yavne, 81800, Israel*

Positron Annihilation Spectroscopy (PAS) is a well-established method used in the fields of condensed matter physics, nuclear physics, chemistry, materials science and materials engineering [1]. In PAS, positrons are typically injected into the bulk of a material where they rapidly thermalize and are likely to be trapped in neutral or negatively charged crystallographic defects. After a time interval that can vary from ~100ps to few ns, depending on the material's type and its defects, the positrons annihilate with that material electrons, each such process results in the emission of two almost back to back photons carrying each approximately 511 keV. Due to momentum and energy conservation, the momentum distribution of the annihilating electrons reflects in angular distribution around the 180° between the two emitted photons (ACAR – Angular Correlation of Annihilation Radiation) and in the broadening of their energy distribution (DB – Doppler broadening). The electron density in the positron proximity before annihilation defines the lifetime of positron in the material [2], with measurable differences between mean lifetimes in the bulk region and in defect traps.
The relatively high energy photons emitted from annihilation events penetrate the material under study, allowing non-destructive measurements.
The distinguishable differences between the electron characteristics at point defects as opposed to the undamaged bulk region, and the high affinity of positrons to the defects, make them useful as a probe for point defects, the smallest of which are single atoms vacant from their lattice sites (mono-vacancies), down to very low concentrations, of ~10^{-6} a^{-1} and up [3]. Comparison to sensitivity regions of other research methods is shown in Fig. 1, taken from [4]. The very good resolution of ACAR measurements allow detailed exploration of Fermi surfaces in single-crystal materials.

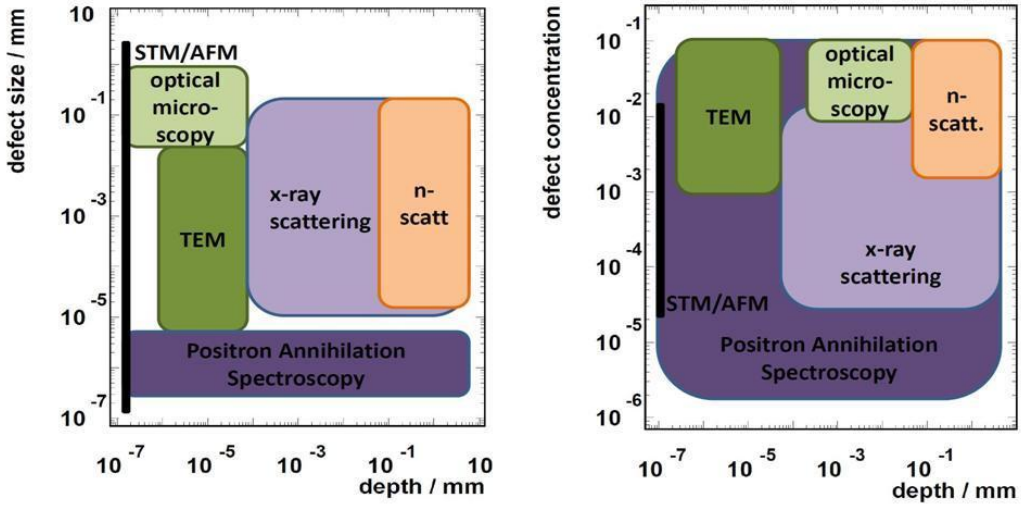

Fig. 1 Sensitivity regions accessible to various standard techniques: optical microscopy, neutron scattering (n-scatt), transmission electron microscopy (TEM), scanning tunnelling microscopy (STM) / atomic force microscopy (AFM), x-ray scattering, and positron annihilation.

The two most common PAS measurement systems are based on table-top gamma spectrometers, and slow positron beams. In table top measurements, positrons from a ^{22}Na

source (mean energy ~200 keV) [5] probe materials to depths of hundreds of microns, giving integrative information on their interior. In slow positron beams the source positrons are moderated, low energy positrons are selected and accelerated to create a mono-energetic beam with energy varying from tens of eV to ~25-50 keV. It is possible to scan the material from its surface to a depth of few microns and profile damage or thin layer characteristics [6].

The positron group at NRCN has built a table-top positron lifetime spectrometer [7], which with a unique data analysis method gets to a state of the art time resolution, of ~140ps. An Israeli collaboration, including researches, students and technicians from the Hebrew University, Tel-Aviv University, NRCN and Soreq NRC, is currently building the first slow positron beam in Israel [8]. The beam will be the center of the newly formed **S**low **PO**sitron facili**T**y (SPOT) at the Hebrew University. This beam, together with the PAL spectrometer of NRCN, will bring new material research capabilities to the Israeli community. The SPOT positron beam will serve as a tool for both fundamental and industry-oriented applied materials research.

PAS measuring methods and their applications will be discussed in more detail and the positron beam design concepts and challenges will be described.

References

[1] A. Dupasquier, A.P. Mills, Jr . (Eds.), *Positron Spectroscopy of Solids*, IOS, Amsterdam, (1995).
[2] M. J. Puska et al*. Journal of Physics F: Metal Physics* **13**, 1091 (1983).
[3] R. H. Howell et al. *Applied Surface Science* **116**, 7-12 (1997).
[4] S. May-Tal Beck, et al., *Defect and Diffusion Forum* **331** (Ed. B.N Ganguly and G. Brauer), 95-112 (2012).
[5] P.J. Foster et al.,*Journal of Applied Physics* **101**, 043702 (2007).
[6] W. Anwand et al., *Defects and diffusion forum* **331**, 25 (2012).
[7] S. May-Tal Beck et al., *Material Science Forum* **445-446**, 495-497 (2004).
[8] S. May-Tal Beck et al., to be published in *Journal of Physics: Conference Series* (2014).

Detection of SNM by Pulsed Neutron Interrogation

Bent Pedersen[1], Aharon Ocherashvili[2], Valeriy Mayorov[1], Arie Beck[2], Eric Roesgen[1], Hanania Ettedgui[2], Marita Mosconi[1], Jean-Michel Crochemore[1]

[1] *Nuclear Security Unit, Institute for Transuranium Elements, Joint Research Centre, Via E. Fermi 2749, Ispra 21020 (VA), Italy*
e-mail: bent.pedersen@jrc.ec.europa.eu
[2] *Physics Department, Nuclear Research Center Negev P. O. Box 9001, 84190 Beer-Sheva, Israel*

A method for the detection of special nuclear materials (SNM) in shielded containers which is both sensitive and easily applicable under field conditions is presented. The method applies neutron induced fission in SNM by means of an external pulsed neutron source with subsequent detection of the fast prompt fission neutrons. Liquid scintillation detectors surrounding the container under investigation are able to discriminate gamma rays from fast neutrons by the so-called pulse shape discrimination technique (PSD).
The presentation explains laboratory tests performed with an array of eight detectors at the Pulsed Neutron Interrogation Test Assembly (PUNITA) for the purpose of investigating the method. Both single neutron detections, and coincident multiple neutron detections, from induced fission events are used as signatures for the presence of fissile materials. We discuss the sensitivity observed in both methods.
By proper time gating of the pulsed neutron source and the detection system, the interrogation can be done by either epi-thermal or thermal neutrons. Epi-thermal neutrons interrogation is particularly interesting as these neutrons are very penetrating and difficult to shield against. The results of such experimental investigations are demonstrated and discussed.
The experimental configuration in the PUNITA facility has been modeled with MCNP. Based on these simulations a scaled-up facility intended for inspection of air cargo containers (ULDs) has been modeled. This facility will fit a standard 20-foot ISO transport container, employ a single standard neutron generator, a large graphite moderator and a large array of liquid scintillation detectors. The objective is the detection of few hundred grams of ^{235}U embedded in a standard five cubic metre container. The results of these simulations are also discussed.

Fissile Mass Estimation by Pulsed Neutron Source

I. Israelashvili[1], C. Dubi[1], H. Ettedgui[1], A. Ocherashvili[1], B. Pedersen[2], A. Beck[1], E. Roesgen[2], J.M. Crochmore[2], T. Ridnik[1], I. Yaar[1]

[1]Nuclear Research Center of the Negev, P.O.B 9001, Beer Sheva, 84190, Israel

[2]Nuclear Security Unit, Institute for Transuranium Elements, Joint Research Centre, Via E. Fermi, 2749, 21027 Ispra, Italy

Passive methods for detecting correlative neutrons from spontaneous fissions (e.g. multiplicity and SVM) are widely used for fissile mass estimations. These methods are feasible for materials that emit a significant amount of fission neutrons (like plutonium). Active interrogation, in which fissions are induced on the tested material by an external continues or pulsed neutron source, has the potential advantages of fast measurement alongside independency of the spontaneous fissions rate of the tested material (enables uranium measurement).

Until recent, using the multiplicity method, for uranium mass estimation, was possible only for active interrogation made with continues neutron source. Pulsed active neutron interrogation measurements were analyzed with techniques, e.g. differential die away analysis (DDA), which ignore the multiplicity effect (self-induced fission chains).

Recently, both, the multiplicity and the SVM techniques, were theoretically extended for analyzing active fissile mass measurements, made by a pulsed neutron source. In this study we experimentally examined, for the first time, the SVM technique for pulsed neutron source. The measurements were conducted at the PUNITA facility of the Joint Research Centre in Ispra, Italy. Promising, but still preliminary, results of mass estimation by the SVM technique for pulsed neutron source are presented.

Studies on the $UFeSb_2$ uranium antimonide

A.P. Gonçalves,[1] M.S. Henriques[1], J.C. Waerenborgh[1], I. Curlik[2], S. Ilʹkovič[2], M. Reiffers[2]

[1] *Campus Tecnológico e Nuclear, Instituto Superior Técnico/CFMC, Universidade de Lisboa, Estrada Nacional 10, 2695-066 Bobadela LRS, Portugal*
e-mail: apg@ctn.ist.utl.pt
[2] *Faculty of Humanities and Natural Sciences, Presov University, 081 16 Presov, Slovakia*

$UFe_{1-x}Sb_2$ is a ternary uranium phase that crystallizes in the tetragonal $HfCuSi_2$-type structure (SG. P4/nmm) [1], the U and Fe atoms being located in one position (2c and 2b, respectively), while Sb occupies two sites (2a and 2c). This phase is closely related to the USb_2 binary compound (Cu_2Sb-type structure, SG. P4/nmm), which is a layered structure with Sb(I), U and Sb(II) sheets stacked along the *c* axis: $UFe_{1-x}Sb_2$ can be seen as formed from USb_2 by inserting an additional Fe layer between the planes that compose the Sb(II) sheets. $UFeSb_2$ is the limit compound in of this homogeneity range. Its crystal structure ($HfCuSi_2$-type), unit cell parameters and electrical resistivity as a function of temperature were already reported [2].
The binary antimonide USb_2 orders antiferromagnetically below T_N = 206K, the refinement of its magnetic structure from neutron diffraction data [3] showing a sequence of alternating (↑↓↓↑) U ferromagnetic layers and a magnetic moment of ~1.9μB/U. In $UFeSb_2$ the shortest U-U distance (4.327 Å, corresponding to the *a* cell parameter) is well above the Hill limit, pointing to a strong chance of magnetic ordering for the U sublattice, similarly to the USb_2 case. However, the possibility of a Fe magnetic contribution is not excluded, which leads to the existence of two potential magnetic sublattices in $UFeSb_2$. Indeed, the reported resistivity data shows a maximum at ~40K [2] that can be related to a magnetic transition. Here we present the synthesis and a detailed study on the $UFeSb_2$ compound, by powder X-ray diffraction, electrical resistivity, magnetoresistance, magnetization, specific heat and Mössbauer spectroscopy measurements.

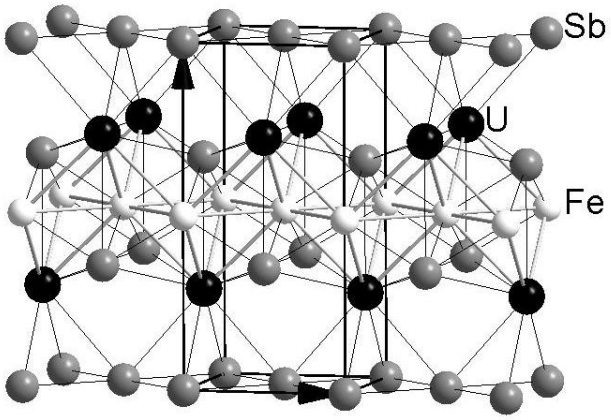

Fig. 1. $UFeSb_2$ unit cell, emphasizing the layered-type structure.

A $UFeSb_2$ polycrystalline sample was prepared by arc-melting, followed by annealing at 750ºC for one week. The Rietveld refinement confirms that $UFeSb_2$ crystallizes in the $HfCuSi_2$-type structure and indicates that the majority of the sample consists of $UFeSb_2$ (98.2 w%) and only minor amounts of $FeSb_{1+x}$ and α-Fe (1.7 and 0.1 w%, respectively) exist. All the nearest neighbor atoms of U are at distances close to or higher than the sum of the metallic radii, pointing to the possibility of a non negligible U magnetic moment. However, the very short Fe-Sb1 distances indicate strong interactions between these atoms and a probable collapse of the Fe magnetic moments.
The low temperature electrical resistivity versus temperature results are similar to those previous reported [3], showing a maximum at ~40K under zero applied magnetic field. At

higher fields the maximum broadens and shifts to higher temperatures, as expected for a ferromagnetic-type transition.

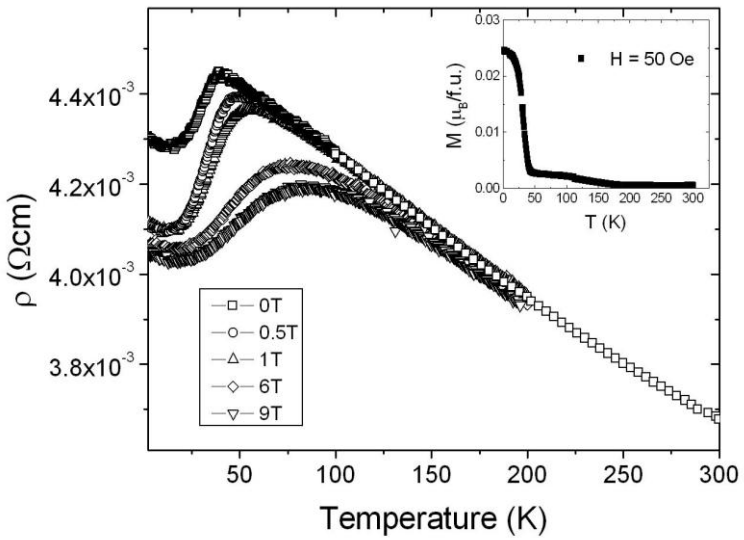

Fig. 2. $UFeSb_2$ electrical resistivity versus temperature results, under different applied magnetic fields. The inset shows the low field magnetization as a function of temperature.

Low field magnetization measurements show a ferromagnetic-type transition at T_C=31(1)K, in agreement with the electrical resistivity results. However, the spontaneous magnetic moment is only ~0.2μ_B/f.u., indicating a complex magnetic structure and/or strong hybridization in the U and Fe atoms, with the consequent decreasing of their magnetic moments (as, for example, in the UFe_4Al_8 case [4]). The temperature dependence of the $UFeSb_2$ specific heat shows only a very small anomaly at T_C, pointing to itinerant magnetism. At low temperatures the specific heat follows $C_P=\gamma T + \beta T^3$, with γ=51(1) mJ/mol.K^2 and β=0.55(1) mJ/mol.K^4 (θ_D=152K). The γ value points to a relatively high density of electronic states at the Fermi level and classifies this compound as a moderately enhanced correlated system.

^{57}Fe Mossbauer spectroscopy measurements at 4K, below the magnetic transition temperature, show no magnetic splitting. This means that no strong magnetic exchange interactions involving Fe are existent and neither long-range magnetic ordering nor standard spin-glass behavior of the iron sub-lattice is associated with the magnetic anomaly detected by the magnetization measurements. This suggests that the magnetic transition observed at ~30K originates exclusively from the U atoms. As referred above, the Fe-Sb distances are very short, which may be related to a strong hybridization between Fe and Sb, shifting the 4s electron density in Fe towards the more electronegative Sb atom. This would explain the significantly lower electron density at the Fe nuclei in $UFeSb_2$, when compared to metallic α–Fe.

Acknowledgments: this work was partially supported by the the Slovak Research and Development Agency, under the contract No. SK-PT-0011-12; slovak VEGA Nos. 2/0070/12, and by the FCT-APVV bilateral collaboration Portugal/Slovakia

References

[1] M.S. Henriques, T. Malnoe, O. Tougait, R. Vilar, A.P. Gonçalves, *Solid State Phenom*. **194**, 21 (2013).

[2] D. Kaczorowski, R. Kruk, J. P. Sanchez, B. Malaman, F. Wastin, *Phys. Rev. B* **58**, 9227 (1998).

[3] J. Leciejewicz, R. Troc, A. Murasik, A. Zygmunt, *Phys. Status Solidi* **22**, 517 (1967); *Phys. Status Solidi* **24**, 763 (1967) (erratum).

[4] J.A. Paixão, B. Lebech, A.P. Gonçalves, P.J. Brown, G.H. Lander, P. Burlet, A. Delapalme, J.C. Spirlet, *Phys. Rev. B* **55**, 14370 (1997).

Correlating the effects of temperature and pressure on Raman scattering in UO_2

Tsachi Livneh,[1] Eran Sterer[1]

[1] *Department of Physics, Nuclear Research Center, Negev, P.O. Box 9001, Beer Sheva, 84190, Israel*
e-mail: T.Livneh@nrcn.org.il

Due to its technological and scientific significance uranium dioxide is one of the most extensively studied actinide compounds. Optical spectroscopy was shown to be highly valuable in revealing the role played by the $5f^2$ band at ambient conditions [1, 2]. Furthermore, the complexity of the absorption spectra is reflecting the importance in the electronic *5f* system of crystal-field effects in the eV energy range.

As an extension of our study of the effect of pressure on the Raman spectrum of UO_2 [3, 4] we investigated the effect of temperature on the energy of the crystal-field transitions and the frequency of phonons, ν_i, and correlate it with the former. The combined effect on the phonon frequency is described by $\left(\frac{\partial \nu_i}{\partial T}\right)_P = \left(\frac{\partial \nu_i}{\partial T}\right)_V - \frac{\chi}{\beta}\left(\frac{\partial \nu_i}{\partial P}\right)_T$. The temperature dependent shift is constructed from the combination of the *implicit* term $\frac{\chi}{\beta}\left(\frac{\partial \nu_i}{\partial P}\right)_T$, which reflects the effect of temperature through the thermal expansion coefficient, β, (χ being the compressibility) and an *explicit* term, $\left(\frac{\partial \nu_i}{\partial T}\right)_V$, which reflects the phononic thermal population change under "freezed" (constant volume) equilibrium conditions [6].

The case of dominant implicit term is well described under the approximation that the temperature dependence of the frequency is exclusively due to volume effects. Hence, the relative motions of two entities that have no electronic overlap (as in the case of ions). In contrary, dominant explicit term points to more significant covalent nature of the bonding in the solid.

In our presentation we will employ the formulation shown above and compare the measured pressure and temperature Gruneisen parameters in UO_2 with those of ionic CaF_2. We will then qualitatively discuss the correlation of our results with the expected differences between the two solids.

References

[1] J. Schoenes *Phys. Rep.* **63** 301 (1980)
[2] J. Schoenes *J. Chem. Soc. Faraday Trans. II* **83** 1205 (1987)
[3] T. Livneh and E. Sterer *Phys. Rev. B* **73** 085118 (2006)
[4] T. Livneh *J. Phys. Condens. Matter.* **20** 085202 (2008)
[5] T. Livneh , in prepapration
[6] G. Lucazeau , *J. Raman Spectrosc.* **34** 478 (2003)

Recent progress in the investigation of the electronic and magnetic properties of $NpNi_5$

A. Hen,[1,2] E. Colineau,[1] R. Eloirdi,[1] J.-C. Griveau,[1] J.-P. Sanchez,[5] F. Wilhelm,[6] A. Rogalev,[6] A. B. Shick,[7] I. Halevy,[2,3,4] I. Orion,[2] and R. Caciuffo[1]

[1]European Commission, Joint Research Centre, Institute for Transuranium Elements, Postfach 2340, D-76125 Karlsruhe, Germany
E-mail: amir.hen@mail.huji.ac.il
[2]Nuclear Engineering Department, Ben Gurion University, IL84105 Beer-Sheva, Israel
[3]Physics Department, Nuclear Research Center Negev, P.O. Box 9001, IL84190 Beer-Sheva, Israel
[4]California Institute of Technology, W. M. Keck Laboratory 138-78, Pasadena, California 91125, USA
[5]SPSMS, UMR-E CEA/UJF-Grenoble 1, INAC, FR-38054 Grenoble, France
[6]European Synchrotron Radiation Facility (ESRF), B.P.220, F-38043 Grenoble, France
[7]Institute of Physics, Academy of Sciences of the Czech Republic, Na Slovance 2, CZ-182 21 Prague, Czech Republic

ReT_5 (Re = rare earth, T = Transition metal) compounds have been studied in the past in the frame of its magnetic properties (small Re to T stoichiometric ratio, large spontaneous magnetization and high Curie temperature) [1-2]. Extending these investigations to actinide analogues is interesting, as the wider radial extension of the *5f* electronic shell compared to the *4f* one should result in a larger inter-sublattice exchange interaction, and in non-negligible An-An exchange coupling. The spin-orbit interaction in the *5f* configuration for the actinide atoms is also larger than the *4f* spin-orbit interaction. For these reasons, a magnetic behaviour even richer than the one observed in the rare earth compounds is expected.

$NpNi_5$ [3] was synthesized by arc-melting and X-Ray powder diffraction enabled to confirm a $CaCu_5$ (D_{6h}) P6/mmm hexagonal crystallographic structure having one Np atom per unit cell, with room-temperature lattice parameters a = 4.8501 (5) Å and c = 3.9841 (5) Å. Physical properties were measured by the means of Superconducting – Quantum – Interference – Device (SQUID) magnetometry, ^{237}Np Mössbauer spectroscopy (Fig. 1), specific heat measurements (Fig. 2) and X-Ray magnetic circular dichroism (XMCD) (Fig. 3).

$NpNi_5$ is a ferromagnetic binary system, where the Np *5f* electrons seem to be essentially localized. Magnetization curves (not shown) indicate that $NpNi_5$ is a soft ferromagnet with a T_C ~16 K with a clear Curie–Weiss behaviour above T_C (μ_{eff} ~ 3.7 μ_B, θ_P ~ 14.6 K).
Mössbauer spectroscopy data (Fig. 1) suggests a Np^{3+} oxidation state ($5f^4$ electronic configuration), The hyperfine field inferred from the spectrum at 4.2 K (~439 T) yields an ordered moment at the Np site μ_{Np} ~ 2 μ_B. Comparison with saturated magnetization suggests an average moment of only 0.04 μ_B on the Ni sites.
The specific heat (Fig. 2) shows a clear and narrow anomaly at ~16 K corresponding to the onset of magnetic order. In applied magnetic fields the peak is shifted towards higher temperature and broadened (not shown), as expected for a ferromagnet. The magnetic transition can be extracted form the total specific heat by subtracting the phonons, electron, and nuclear contributions. Inset shows the low temperature part indicating the presence of the nuclear Schottky contribution.

In this communication we will present the results obtained (including preliminary data from XMCD) and discuss them in the light of theoretical considerations.

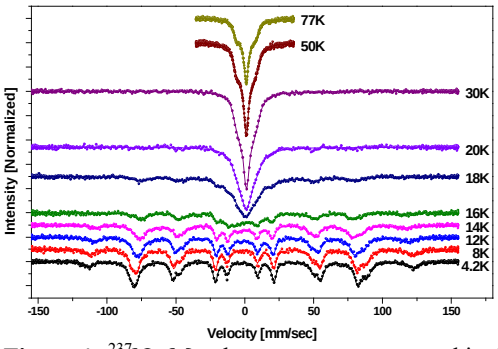

Figure 1: ^{237}Np Mössbauer spectra measured in the temperature range 4.2 - 77 K.

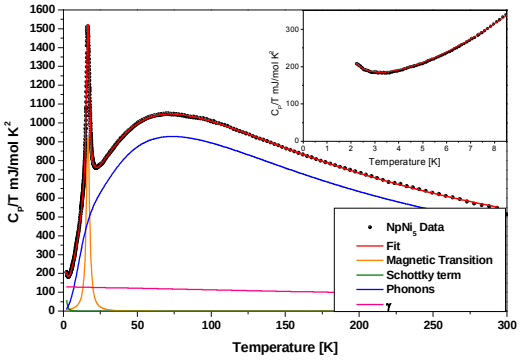

Figure 2: Normalized specific heat as a function of temperature, Solid lines – theoretical fit and its components. Insert – low temperature specific heat.

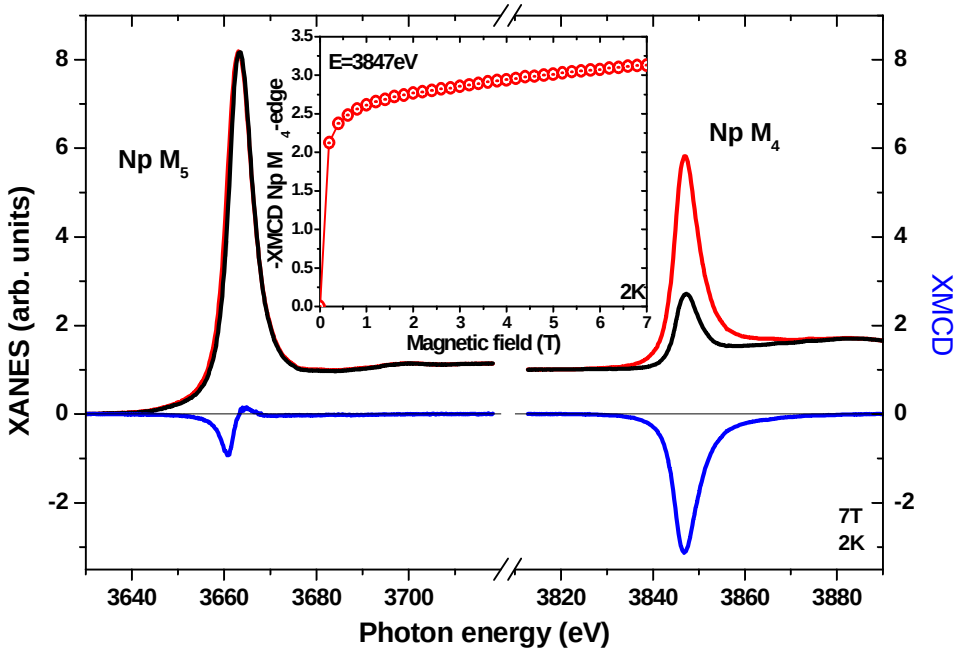

Figure 3: X-ray absorption spectra μ^+ (red line), μ^- (black line) measured at 2 K and H_{ext}=7 T at the $M_{4,5}$ Np absorption edges; Blue line – XMCD signal, inset – field dependence of the XMCD signal at the M_4 edge.

Acknowledgements

The high purity Np metals required for the fabrication of the compound were made available through a loan agreement between Lawrence Livermore National Laboratory and ITU, in the frame of a collaboration involving LLNL, Los Alamos National Laboratory and the US Department of Energy.

References

[1] S. Nasu *et al.,* Journal of Physics and Chemistry of Solids, **32**, 2779 (1971).
[2] R. M. Gale´ra *and* A. Rogalev, Journal of Applied Physics **85**, 4889 (1999).
[3] M. Akabori *et al.*, Journal of Alloys and Compounds **257** 268 (1997).

Multi-Step Excitation Schemes in Laser Spectroscopy of Actinides and Lanthanides in Solutions

I.N. Izosimov,[1] N.G. Firsin[2], N.G. Gorshkov[2], S.N. Nekhoroshkov[2]

[1]*Joint Institute for Nuclear Research, Joliot Curie 6, Dubna, 141980, Russia,*
[2] *Khlopin Radium Institute, 2nd Murinski avn. 28, St. Petersburg, 194021, Russia*
e-mail: izig@mail.ru

Development of laser spectroscopy with tunable lasers gives rise to new procedures for detection of trace amounts of various substances in various media. A possibility to tune a wavelength of laser radiation allows selective action on certain atoms and molecules and, hence, selective detection of these species [1]. The practical application of laser spectroscopy to analysis of different samples is confronted with one essential difficulty, namely the element to be detected must be permanently located in the area of interaction with laser radiation. Therefore the use of solutions of the substances to be analyzed is the most attractive from the practical standpoint. When the pulse (1ns) UV radiation produced by nitrogen laser is used for lanthanide and actinide excitation in solutions the UV radiation is absorbed with different molecules and as a consequence the background radiation is increased. Using short laser pulses for excitation of molecules and ions in liquids and time resolution for registration of luminescence and chemiluminescence produced by actinide and lanthanide ions we can efficiently separate target signals from short-lived background luminescence [1]. Selective excitation of detectable molecules can additionally decrease the intensity of background radiation. In addition, UV radiation is absorbed with chemiluminogen (luminol in our experiments) molecules, which makes difficult interpretation of the results of chemiluminescence registration. Therefore a key problem of chemiluminescence application to detection of lanthanides and actinides in solutions is an increase in the selectivity of detection. Appropriate selectivity of lanthanide or actinide molecules excitation can be reached by initiation of transitions within 4f- or 5f-electron shell, which correspond to visible spectral range of absorbed laser radiation. Since the energy of one-quantum excitation in visible range may be insufficient for initiation of chemiluminescence it was proposed to excite lanthanide or actinide ion by multi-quantum absorption of visible light [1-3]. The use of laser radiation with tunable wavelength allows selective excitation of actinide or lanthanide species with subsequent registration of luminescence or chemiluminescence. The details of multi-step excitation of luminescence/chemiluminescence excitation in solutions are considered. It is shown that a multi-step scheme of luminescence/chemiluminescence excitation increase both the sensitivity and selectivity of detection of substances.

The experiments were performed on an installation involving a pulse nitrogen laser OBB-1010 with a pulse length of 1 ns and a pulse power of approximately 1.4 MW per a pulse and two tunable dye lasers OBB-1011 and OBB-1012 with a pulse length of 1 ns and 800 ps respectively. The pulse power 300 kW was reached for dye lasers. A delay time for luminescence registration was 2 μs. The scheme [1] *two step-one color*, i.e. in irradiation of actinide-containing solution by one laser (two photons absorbed from one laser pulse) and the scheme *two step-two color*, when a solution is irradiated by two lasers operating at different wavelengths (two photons absorbed from two synchronized laser pulses) were used for excitation of actinide ions in the range of 5f electron transitions.

Initiation of chemiluminescence as a result of excitation of Pu(IV) with two dye lasers was demonstrated for a solution containing CsF, luminol, and Pu(IV). A choice of solution composition was made based on an attempt to provide favorable conditions for observation of luminol chemiluminescence and to avoid formation of colloidal species of hydrolyzed Pu(IV). The spectrum of chemiluminescence excitation in both two step-one color (Fig.1) and two step-two color (Fig.2) schemes correlated with absorption spectrum of Pu(IV). In both schemes we realized selective excitation of chemiluminescence and this selectivity is caused by the features of absorption spectra of Pu(IV) solutions. The selectivity of Pu(IV) detection is similar to selectivity of absorption spectroscopy but the sensitivity is higher. A two-step

scheme of chemiluminescence excitation makes this procedure not only highly sensitive but also highly selective procedure of detection of substances.

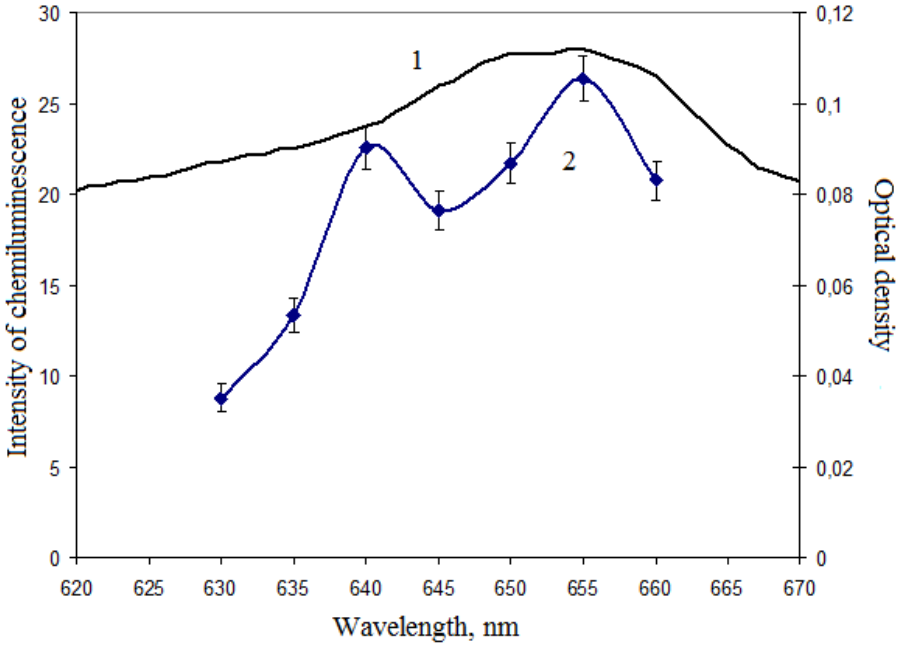

Fig.1. Spectrum of chemiluminescence excitation by the scheme two step-one color in solution containing CsF, luminol, and Pu(IV) (*2*). Absorption spectrum of Pu(IV) (*1*).

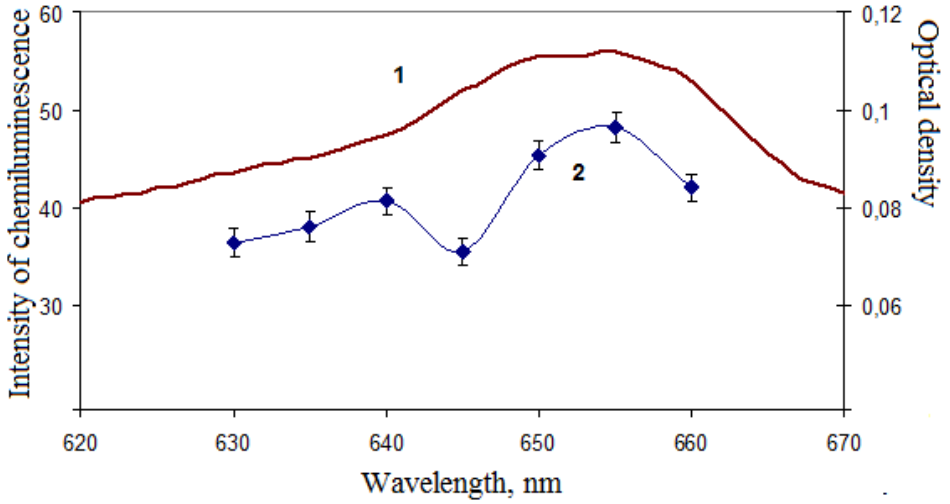

Fig.2. Spectrum of chemiluminescence excitation in CsF+luminol+Pu(IV) solution by the scheme two step-two color (*2*). Wavelength of laser radiation at the first excitation step was varied (*2*), the wavelength at the second step was fixed at 490 nm. Absorption spectrum of Pu(IV) (*1*).

References

[1] I.N. Izosimov, *Phys. Part. Nucl.* **38**, 177 (2007).
[2] N.G. Gorshkov, I.N. Izosimov, V.A. Mikhalev et al., *Radiochemistry* **6**, 525 (2012).
[3] I.N. Izosimov, N.G. Firsin, N.G. Gorshkov et al., *Joint Institute for Nuclear Research Preprint* E6-2012-62, Dubna (2012).

Physical Properties and XPS spectra of cage-like compound UB_{12}

R. Troć[1], M. Samsel-Czekała[1], R. Wawryk[1], A. Pikul[1], H. Misiorek[1], E. Talik[2], N. Shitsevalova[1,3]

[1] *W. Trzebiatowski Institute of Low Temperature and Structure Research of PAS, P.0.Box 1410, 50-950 Wrocław 2, Poland, e-mail: R.Troc@int.pan.wroc.pl*
[2] *A. Chełkowski Institute of Physics, University of Silesia, 4 Uniwersytecka Street, 40-007 Katowice, Poland*
[3] *I. Frantsevich Institute for Problems of Materials Science of NASU, 3 Krzhyzhanovsky Street, 03680 Kiev, Ukraine*

Boron with uranium form three metallic borides having chemical formula: UB_2, UB_4 and UB_{12}. Here we present temperature variations of magnetic susceptibility, electrical resistivity (performed in zero and in magnetic fields up to 9 T), thermoelectric power, thermal conductivity and specific heat measured for UB_{12} bulk sample. Moreover, we have also measured for this sample a valence-band X-ray photoemission spectrum (XPS) and compared it with the calculated one using the fully relativistic and full-potential local-orbital (FPLO) method within the local density approximation (LDA).

The dodecaboride UB_{12} crystallizes in the face-centered cubic (fcc) UB_{12}-type structure (space group *Fm3m*) in which the boron atoms form the B_{24} cages accommodating the metal atoms. The atomic diameter of the latter atoms may occur to be distinctly smaller than the existing voids able for such an accommodation. As a result, the enclosed metal atom undergoes large vibrations reflected in existing soft Einstein phonons giving rise e.g. to superconductivity found for ZrB_{12}, ScB_{12} and LuB_{12}. Alternatively, this structure has the NaCl-type arrangement comprising two substructures, i.e. the usually weakly bonded metal atoms in the fcc-lattice (at the Na sites) and the very rigid B_{12} cubooctahedral networks (at the Cl sites). The latter boron-framework is formed by strong covalent bonds, but its stabilization requires two valence-electrons taken from each metallic atom.

The UB_{12} bulk sample was prepared according to the procedure proposed by Paderno and co-workers [1], i.e. by borothermic reduction of uranium dioxide at about 1500 ^{0}C. The first obtained powders were then compacted by casting into rods followed by vacuum sintering.

As it was reported many years ago [2], also the UB_{12} sample obtained in different manner as described above, showed only weakly temperature dependent paramagnetism. The measured isothermal magnetization up to 5 T exhibits a curvature at low temperatures which changes to a linear behaviour starting at 14 K. Although the U–U distances in UB_{12} are of about 0.52 nm, some magnetic correlations at low temperatures occur, which may lead to the observed deviation in magnetization from linearity. It is not surprising, because the rare-earth borides RB_{12} (where R = Tb-Tm) having the similar metal-metal atomic distances as those in UB_{12} are all antiferromagnets at low temperatures [3].

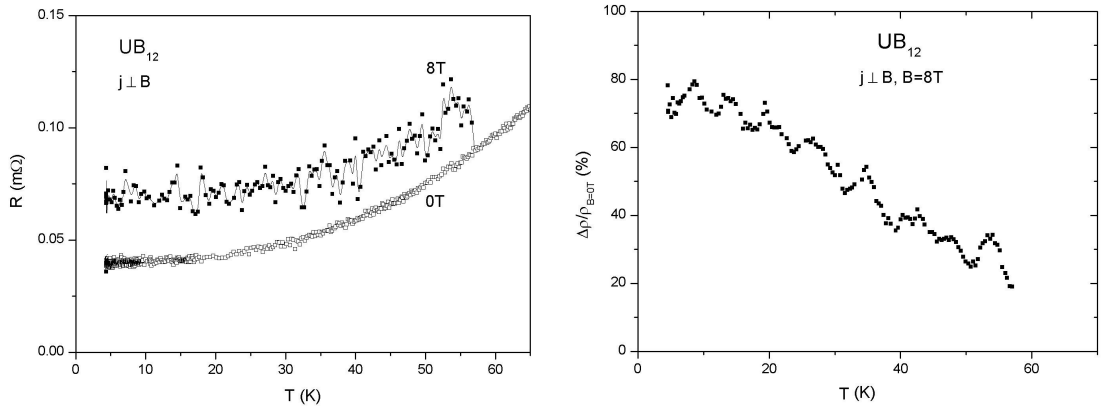

Fig. 1. Thermal dependencies of the resistivity and magnetoresistivity.

The temperature dependence of the electrical resistivity of our UB_{12} polycrystalline sample coincides well with that reported by Kasaya et al. [4] which was made on a single crystal (RRR value of 77). Both measurements point to a typical metallic behaviour of this dodecaboride. In turn, such a dependence of the magnetoresistivity (MR), taken at 8 T, as shown in Fig. 1, is quite unusual. The observed non-smoothed temperature variation of highly positive MR in magnetic field, may be connected with the special cage-type of the UB_{12}-type crystal structure, where the uranium atom is rather weakly bonded with B_{24} atoms.
The thermoelectric power S(T) of UB_{12} (measured for the first time) shows two negative minima at 35 and 212 K and a small sharp positive maximum at 5 K, however, no signal of the presence of superconductivity down to 0.3 K. The minimum in S(T) at 35 K is also reflected by a very enhanced maximum in the thermal conductivity, $\kappa(T)$, occurring at the same temperature. Then, $\kappa(T)$ above 100 K becomes practically temperature independent.
The specific heat (C_p) of UB_{12} exhibits a typical temperature behaviour as that of other metallic RB_{12} non-magnetic compounds, e.g. as LuB_{12} does [5].This similarity in $C_p(T)$ is a consequence of nearly non-interacting, freely oscillating metal atoms (Einstein oscillators) located in cavities of a simple cubic rigid Debye lattice formed by B_{12} clusters. The existing Einstein modes for both cases indicate e.g. an enhanced peak present in the C_p/T^3 vs T function. Hence, it is highly probable that the enhanced peaks observed in the S(T) and $\kappa(T)$ functions are phonon drags induced by Einstein modes. Only the large difference exists for these two dodecaborides between their values of electronic specific heat coefficients, $\gamma(0)$, being equal to 20 vs. 4 mJ/mol K^2, respectively. Our $\gamma(0)$ value for UB_{12} agrees exactly with that given in Ref. 4.
Finally, we present in Fig. 2 the experimental and calculated valence-band XPS for UB_{12}.
As seen, the agreement between these two kinds of spectra is very good. This fact is not surprising because of the highly metallic character of uranium dodecaboride. Interestingly, the 4f core-level XPS (not displayed) shows the presence of two satellites, called 1 eV and 7 eV.

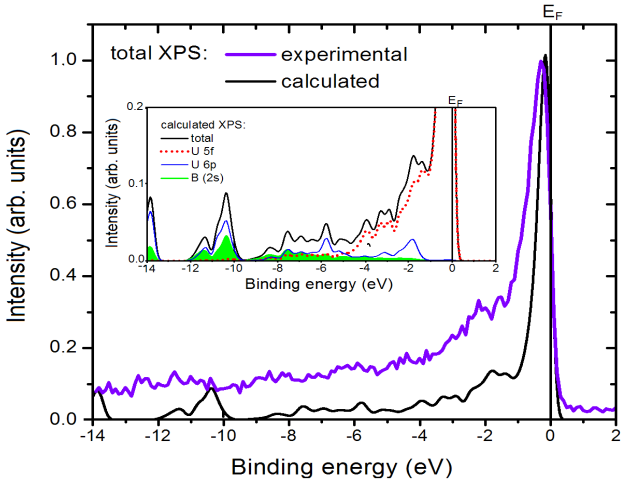

Fig. 2. Experimental and calculated valence-band XPS of UB_{12}.

References

[1] Y. Paderno, V. Filippov, N. Shitsevalova et al., *JJAP Series* **10**, 154 (1994).
[2] R. Troć, W. Trzebiatowski, K. Piprek, *Bull. Acad. Polon. sc*, *ser. de sc. chim*. **19**, 6 (1971).
[3] A. Czopnik, N. Shitsevalova, A. Krivchikov et al., *J. Solid State Chem.* **177**, 507 (2004).
[4] M. Kasaya, F. Iga, K. Katoh et al., *J. Magn. Magn. Mater.* **90-91**, 521 (1990).
[5] A. Czopnik, N. Shitsevalova, V. Pluznhnikov et al.,*J. Phys.: Cond. Matter* **17**, 5971 (2005).

Presented for an oral communication within the topic “Strongly correlated behaviours, superconductivity and quantum criticality”.

Self-induced radiation damage in thin metallic films

Eyal Yahel[1], Rafael Hevroni[2] and Itzhak Kelson[2]

[1] Physics Department, Nuclear Research Center-Negev, Beer Sheva, Israel
[2] School of Physics, Tel Aviv University, POB 39040 Tel Aviv 6997801, Israel

A novel method for the study of radiation damage in thin films is introduced[1]. It utilizes a high flux surface source of alpha emitters which implant their daughters - themselves alpha emitters - in the sample, using the recoil obtained during the decay process. The effect of the damage is measured through changes in the electric resistivity of the sample. Thin films of gold and platinum served as test cases for the method, demonstrating the fundamental difference between this newly presented irradiation method and conventional, external irradiation experiments. The different behavior of these metals during isochronous annealing of the damage, compared to literature data, serves as an example for that difference.

1. Hevroni, R., Schmidt, M., Yahel, E. & Kelson, I. Radiation damage studies by a novel alpha emitter technique. *Nucl. Instruments Methods Phys. Res. Sect. B Beam Interact. with Mater. Atoms* **313,** 45–49 (2013).

XMCD study on $AnFe_2$ Laves-phase compounds

F. Wilhelm[1], R. Eloridi[2], J-C. Griveau[2], N. Magnani[2], A. Rogalev[1], R. Caciuffo[2], and G. H. Lander[2]

[1] *European Synchrotron Radiation Facility (ESRF), B. P. 220, F-38043 Grenoble, France*
e-mail: wilhelm@esrf.eu
[2]*European Commission, JRC, Institute for Transuranium Elements, D-76125 Karlsruhe, Germany*

X-ray Magnetic Circular Dichroism (XMCD) is a powerful spectroscopic technique that offers a possibility to determine quantitatively element and shell specific spin and orbital magnetic moments in ferro-, ferri- or even paramagnetic samples. At the third generation synchrotron radiation facilities, small x-ray beam with flexible polarization sized down to few microns can be routinely achieved. This technique is thus perfectly suited for studying minute samples (a few micrograms) of transuranium materials.

We report here on XMCD experiments at the An $M_{4,5}$-edges and at the Fe *K*-edge on UFe_2, $NpFe_2$, $PuFe_2$, and $AmFe_2$. All experiments have been carried out at the ID12 beamline of the ESRF. All materials are anisotropic cubic Laves-phase ferromagnets. Results for UFe_2 are published in [1] whereas results for $NpFe_2$ and $PuFe_2$ are published in [2]. The $AmFe_2$ work is new.

As it is well known, in UFe_2 the uranium moment is small, and consists of almost cancelling spin and orbital contributions [3]. This cancellation is caused by hybridization between the U 5*f* electrons and the 3*d* states of Fe, which *reduces* both the orbital and the spin magnetic moments to ~ 0.2 μ_B . The 5*f* spin and orbital moments are much larger on the actinide atoms in $NpFe_2$ and $PuFe_2$, and the XMCD results confirm those published for $PuFe_2$ from neutron studies [4]. In addition, the XMCD studies show the importance of the <Tz> term [2], which describes anisotropy of the spin magnetic moment and its experimental value was not available for transuranium ions. The 5*f* electrons are itinerant in all these materials, despite the large magnetic anisotropy present.

In $AmFe_2$ the Am – if it is assumed to have six 5*f* electrons – should be nonmagnetic with a filled j = 5/2 shell. Experimentally, this is not the case, the hybridization and strong internal field from the Fe atoms, induces a small moment (~ 0.1 μ_B) on the Am site, and it has both a spin and orbital contribution. Surprisingly, the Am M_4 XMCD signal is very narrow (~ 5 eV FWHM), whereas in all other studied Laves phase materials the actinide M_4 XMCD signal is found to be ~ 10 eV FWHM. This finding suggests a narrow (i.e. localized) j = 5/2 empty state of Am above E_F in $AmFe_2$.

We also report the systematics of the Fe *K*-edge XMCD, which provide more information on the magnetic interactions between the 5f states of actinide and the 3*d* states of Fe atoms.

References

[1] M. Finazzi *et al.,* Phys. Rev. B **55**, 3010 (1997).
[2] F. Wilhelm, R. Eloirdi, J. Rusz, R. Springell, E. Colineau, J–C. Griveau, P. M. Oppeneer, R. Caciuffo, and G. H. Lander, Phys. Rev. B **88**, 024424 **(**2013**).**
[3] M. Wulff *et al.,* Phys. Rev. B **39**, 4719 (1989); B. Lebech *et al.,* J. Phys. Cond. Mat. **1**, 10229 (1989).
[4] M. Wulff *et al.,* Phys. Rev. B **37**, 5577 (1988).

Separation factors of U and Pr or Nd in LiCl-KCl-CsCl melt – liquid gallium, indium or gallium-indium eutectic alloy system

Stanislav Yu. Melchakov,[1] Dmitry S. Maltsev,[1] Vladimir A. Volkovich,[1] Leonid F. Yamshchikov,[1] Alexandr G. Osipenko,[2] Mikhail V. Kormilitsyn[2]

[1] *Department of Rare Metals and Nanomaterials, Ural Federal University, Ekaterinburg, 620002, Russia*
[2] *Research Institute of Atomic Reactors, Dimitrovgrad, 433510, Russia*
e-mail: s.yu.melchakov@gmail.com

Metals of the third group of the periodic table and their alloys are promising systems for separating components of spent nuclear fuel (SNF) during its pyrochemical reprocessing. Radiation stability of this metals allow reprocessing a high burn-up fuel of fast neutron reactors after a relatively short cooling time, while low melting points (29.77 °C for Ga, 156.78 °C for In and 15.3 °C for the Ga-In eutectic) allow working in a wide temperature range.

Efficiency of separation of SNF's components in a 'molten salt – liquid metal' system can be estimated from the values of separation factor (Θ):

$$\Theta_{Me1/Me2} = (c_1 \cdot x_2)/(c_2 \cdot x_1), \quad (1)$$

where c_1, c_2, x_1, x_2 – mole fractions of separated metals in the salt electrolyte and liquid alloy, respectively.

In the present work the separation factors, Θ, of Ln/U couples were calculated. In chloride melts uranium and lanthanides form ions containing the metals in the oxidation state +3. Therefore the following equation was employed to calculate Θ [1]:

$$\lg \Theta_{Me1/Me2} = nF\bullet(E^*_2 - E^*_1)/(2.303RT) + \lg \gamma_1 - \lg \gamma_2, \quad (2)$$

where E* denotes formal standard electrode potentials of the metals in the salt phase and γ – activity coefficients of the same metals in the liquid alloy phase, and the number of exchanged electrons, n, equals to 3. The salt phase was based on the ternary low melting LiCl-KCl-CsCl eutectic (m.p. 263 °C) and the formal electrode potentials of uranium, neodymium and praseodymium in this melt were determined experimentally.

Temperature dependencies of activity coefficients of *f*-elements were calculated using experimental data on activity (a) and solubility (X) of Pr, Nd and U in liquid Ga, In and Ga-In eutectic alloy obtained in the present work and taken from the literature [2]. The relation between a, γ and X is expressed by the following equation:

$$\lg a = \lg \gamma + \lg X \quad (3)$$

The effect of temperature on activity coefficients of Pr, Nd and U in alloys with Ga, In and Ga-In eutectic is shown in Figure 1 and the calculated separation factors of Pr/U and Nd/U couples at 723, 773 and 823 K are presented in Table 1.

Data presented in Table 1 show that separation of lanthanides and actinides using gallium-indium alloys is possible. The largest separation factors of all studied here Ln/An couples are reached for gallium-containing liquid metal electrodes and by their magnitude they are virtually identical for Ga and Ga-In alloys. The reason for such behaviour is that at least one of the *f*-elements (uranium or a lanthanide) predominantly interacts with gallium, whilst indium in the eutectic alloy acts as an indifferent additive. As the temperature decreases the efficiency of Ln/An separation is increasing, as expected.

From eq. (1) and the results of Θ calculations it can be concluded that under the equilibrium conditions in the studied 'liquid metal – molten salt' system lanthanides should concentrate in the salt phase and actinides (in our case U) should concentrate in the liquid metal.

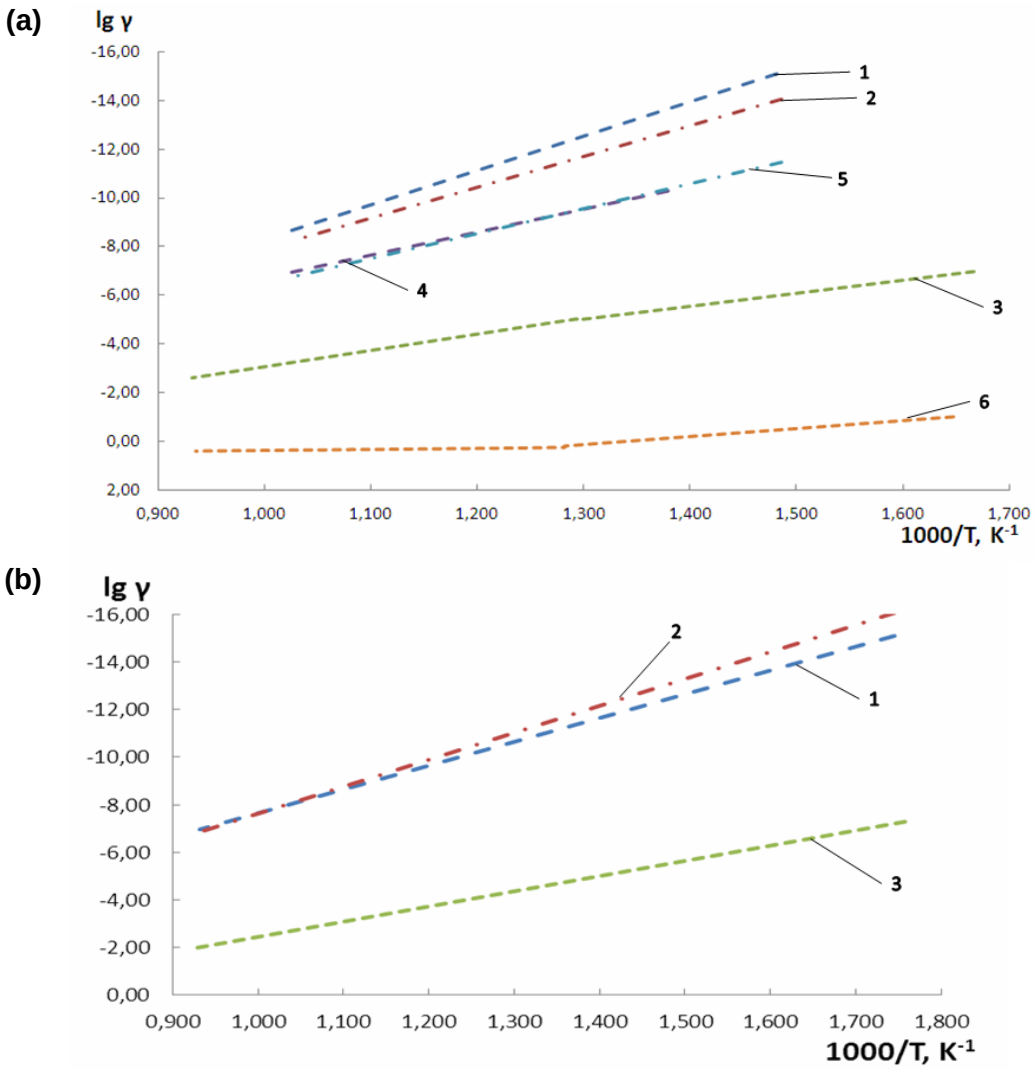

Fig. 1. – Temperature dependencies of activity coefficients of Pr, Nd and U in alloys with individual gallium and indium (a) and Ga-In eutectic (b).
(a): 1 - Pr(Ga), 2 - Nd(Ga), 3 - U(Ga), 4 - Pr(In), 5 - Nd(In), 6 - U(In); (b): 1 - Pr, 2 - Nd, 3 - U

Table 1 – Separation factors of Pr/U and Nd/U couples calculated at various temperatures

Alloy	Elements	Separation factor Θ		
		723 K	773 K	823 K
Ga	Pr / U	$1.6 \cdot 10^5$	$1.1 \cdot 10^5$	$0.6 \cdot 10^5$
	Nd / U	$14.9 \cdot 10^5$	$6.2 \cdot 10^5$	$2.0 \cdot 10^5$
In	Pr / U	1916	732	428
	Nd / U	1567	551	299
Ga-In	Pr / U	$75.4 \cdot 10^5$	$17.1 \cdot 10^5$	$4.6 \cdot 10^5$
	Nd / U	$24.6 \cdot 10^5$	$5.6 \cdot 10^5$	$1.6 \cdot 10^5$

References:

[1]. V.A. Lebedev, Selectivity of Liquid Metal Electrodes in Molten Halides. Chelyabinsk, Metallurgy (1993) (in Russian).
[2]. V.A. Lebedev et al., Thermochemistry of Alloys of Rare Earth Metals and Actinides, Chelyabinsk, Metallurgy (1989) (in Russian).

Magnetic properties of a $U_3Cu_4Ge_4$ single crystal

A.V. Andreev[1], D.I. Gorbunov[1,2], M.S. Henriques[3], Y. Skourski[4], L. Havela[2], A.P. Gonçalves[3]

[1] *Institute of Physics, Academy of Sciences, Na Slovance 2, 182 21 Prague, Czech Republic*
e-mail: a.andreev@seznam.cz
[2] *Department of Condensed Matter Physics, Faculty of Mathematics and Physics, Charles University, Ke Karlovu 5, 121 16 Prague, Czech Republic*
[3] *Nuclear and Technological Campus, IST/CFMC, University of Lisbon, Estrada Nacional 10, 2695-066 Bobadela LRS, Portugal*
[4] *Dresden High Magnetic Field Laboratory, Helmholtz-Zentrum Dresden-Rossendorf, D-01314 Dresden, Germany*

Magnetic and other electronic properties of uranium intermetallics are determined by state of 5f electrons. The degree of their localization/itinerancy can be modified by choosing the appropriate combination of ligands (*d* and *p* elements). It is known that the 5*f*-3*d* hybridization is the deciding factor in the magnetism of intermetallics containing both uranium and a 3*d* metal (*T*). It tends to delocalize the 5*f* electrons, which might reduce considerably the uranium magnetic moment or even cause it to disappear. The 3d magnetic moment might vanish as well. However, there exist 5*f*–3*d* intermetallic compounds having at least one sublattice ordered magnetically. An example is provided by the $U_3T_4Ge_4$ compound with *T* = Fe having the orthorhombic structure of the $Gd_3Cu_4Ge_4$ type (space group *Immm*). The compound is a ferromagnet (the Curie temperature T_C = 18 K) with the magnetism dominated by uranium, Fe does not carry a sizeable magnetic moment [1]. The low magnetic moment 0.4 μ_B per U atom at *T* = 2 K suggests the itinerant nature of the 5f-magnetism. $U_3Fe_4Ge_4$ displays strong magnetic anisotropy with the anisotropy field around 60 T.

In order to define the role of the *T* element in the formation of magnetic properties of the $U_3T_4Ge_4$ system, the degree of localization of the 5*f* electrons was modified by substituting Fe by Cu. The isostructural $U_3Cu_4Ge_4$ compound displays ferromagnetic order as found by powder neutron diffraction [2]. We grew for the first time a single crystal of $U_3Cu_4Ge_4$ and studied its electronic properties. The compound displays ferromagnetic order as follows from the temperature dependence of magnetization measured in a low field of 0.02 T along the *a* axis (upper panel in Fig. 1). The rapid decrease in the magnetization, the strong λ-type anomaly in the specific heat (middle panel in Fig. 1) and the weak anomaly in the electrical resistivity (lower panel in Fig. 1) indicate that the phase transition into paramagnetic state occurs at T_C = 73 K.

Magnetization curves of the $U_3Cu_4Ge_4$ single crystal were measured in static (up to 14 T) and pulsed (up to 60 T) magnetic fields at T = 2 K (Fig. 2). The compound displays uniaxial magnetic anisotropy, the easy magnetization direction is the *a* axis with the spontaneous magnetic moment M_s = 5 μ_B/f.u. which corresponds to 1.67 μ_B per U atom. In the crystal structure of $U_3Cu_4Ge_4$ the U atoms occupy two inequivalent sites for which equal magnetic moments of about the same magnitude were found by powder neutron diffraction [2]. There is no component of M_s along the *b* and *c* axes of $U_3Cu_4Ge_4$. Nevertheless, a strong magnetocrystalline anisotropy is observed within the (*bc*) plane. The *b* axis is the hardest magnetization direction. The anisotropy field between the *a* and *c* axes slightly exceeds the highest available field of 60 T, whereas it is substantially higher (at least 150 T) between the *a* and *b* axes. The magnetic anisotropy of $U_3Cu_4Ge_4$ is much stronger than that of $U_3Fe_4Ge_4$, where the strongest direction is the *c* axis with the anisotropy field of 60 T (and of 40 T along the *b* axis).

The $U_3Cu_4Ge_4$ compound exhibits complex behavior in a magnetic field. Figure 2 also indicates that the magnetization along the *a* axis is a featureless function of field up to 60 T. Along the *b* axis $U_3Cu_4Ge_4$ displays a field-induced phase transition at 25 T. Above the transition the magnetization is a linear function of field. The transition filed decreases with increasing temperature and above 50 K the transition can be also in steady fields up to 14 T

(Fig. 3) where it lost its first-order sharpness and looks as S-shape. The magnetization along the *c* axis exhibits a slight positive curvature up to about 20 T, which indicates the presence of a field-induced magnetic transition as well. In order to clarify the origin of the magnetization jumps, a study of sound propagation in high pulsed magnetic fields is planned.

In conclusion, the present study allowed us to determine the role of the T element in the formation of magnetic properties of the $U_3T_4Ge_4$ systems. Since the 3d electronic shell is partially filled for Fe and full for Cu, the replacement of Fe with Cu resulted in a significant reduction of the 5f–3d hybridization. As a result, the system tends towards a more robust ferromagnetic order originating exclusively from the uranium sublattice. The $U_3Cu_4Ge_4$ compound displays much higher values of the Curie temperature (T_C = 73 K) and spontaneous magnetic moment (M_s = 5 μ_B/f.u.) and stronger magnetocrystalline anisotropy as compared to those of $U_3Fe_4Ge_4$ (T_C = 18 K, M_s = 1.2 μ_B/f.u.). A more systematic study of the $U_3T_4Ge_4$ systems requires investigation of the compounds with *T* = Co and Ni which is in progress.

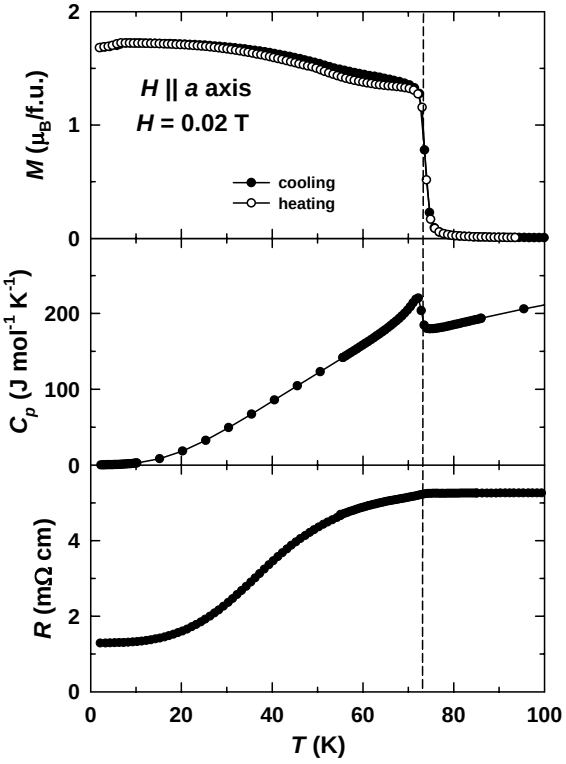

Fig. 1. Temperature dependence of the magnetization along the *a* axis in a field of 0.02 T (a), of the specific heat (b) and of the electrical resistivity (c) of the $U_3Cu_4Ge_4$ single crystal.

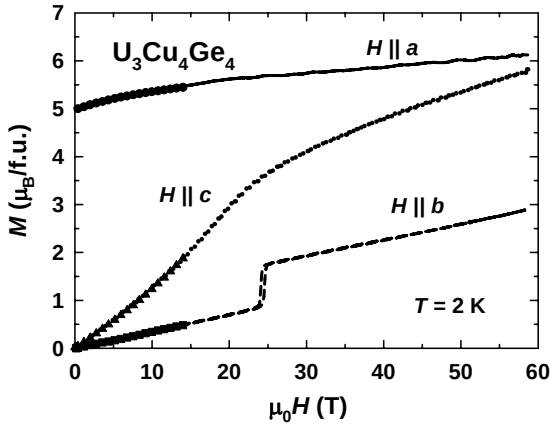

Fig. 2. Magnetization curves measured along the *a*, *b* and *c* axes of the $U_3Cu_4Ge_4$ single crystal at *T* = 2 K.

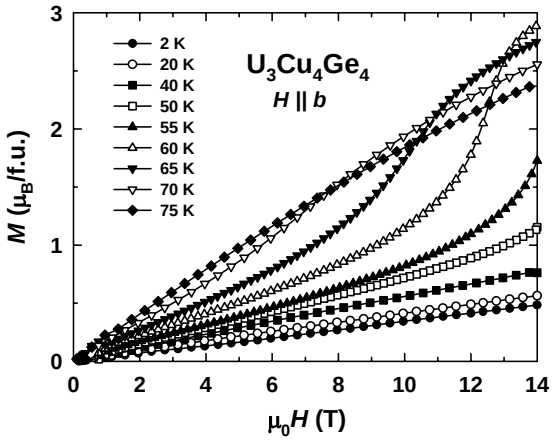

Fig. 3. Temperature evolution of the magnetization curve along the *b* axis.

References

[1] M.S. Henriques, D.I. Gorbunov, J.C. Waerenborgh, L. Havela, A.V. Andreev, Y. Skourski, A.P. Gonçalves, *J. Alloys Compd.* **555**, 304 (2013).

[2] S. Pechev, B. Chevalier, D. Laffargue, B. Darriet, J. Etourneau, *J. Alloys Compd.* **271–273**, 448 (1998).

The interaction of H_2O with strained uranium metal surfaces

E. Tiferet[1], M. H. Mintz[1,2], S. Zalkind[1], I. Jacob[2] and N. Shamir[3]

[1]*Nuclear Research Centre-Negev, POBox 9001, Beer Sheva 84190, Israel*

[2]*Ben Gurion University of the Negev, POBox 653, Beer Sheva 84104, Israel*

[3]*59 Rotem St., Omer 84965, Israel. noah.shamir@gmail.com*

The interaction of water vapor was studied on uranium metal surfaces, with various degrees of strain (relieved by different degrees of heating) [1]. The main features of dissociation, adsorption and initial oxidation for the studied surfaces will be presented. Common to all strained surfaces, on the metal surface a full dissociation occurs, while after oxidation only on most of them the water dissociation is full and on one of them, it is only partial. The oxygen dissociation product adsorbs (with sticking coefficient decreasing with strain relief), forming clusters, for all strains, while the hydrogen product clusters only on the strain relieved and recrystallized surface. The most interesting phenomenon, revealed for these surfaces, is the inhibition of hydrogen adsorption by traces of water vapor [2], changing from 10% for the mostly strained (defected) surface down to 1% for the strain relieved one. The suggested mechanism for this inhibition will be discussed.

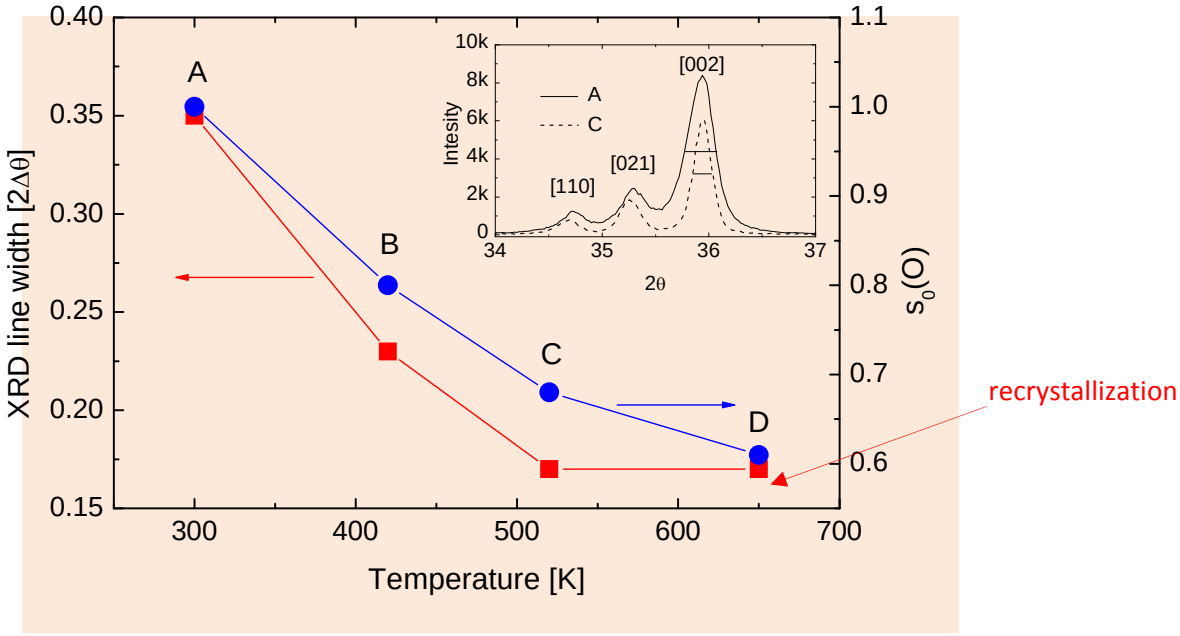

Fig. 1: The correlation between strain relief (heating temperature) and oxygen (product of water dissociation) sticking coefficient.

Table 1: Summary of results for the interaction of H_2O with strained uranium surfaces:

sample	Heating to, for 48+ h	Water dissociation		Clustering for H_2O adsorption		AES pressure depend-ence		Hydrogen adsorption inhibited by H_2O	Oxidation by H_2O - addition Of 1‰ O_2
		metal	oxide	O (s_0)	H (s_0)	H_2O	O_2	DRS	AES
A	No heating	Full	Full	Y (1)	N(0.5)	No	No	Yes (10%)	Enhance-ment
B	420 K	Full	Partial	Y(.80)	N (0.4)	Yes		Yes (1%)	No inhibition
C	520 K	Full	Full	Y(.68)	N (0.4)	No		Yes (2%)	No inhibition
D	~650 K	Full	Full	Y(.68)	Y(.17)	No		Yes (1‰)	No inhibition

References

[1] E. Tiferet, M.H. Mintz, S. Zalkind, I. Jacob, N. Shamir, *J. Alloys Comp.* **444–445**, 177 (2007).

[2] E. Tiferet, M.H. Mintz, I. Jacob, N. Shamir, *Surf. Sci.* **601**, 4925 (2007).

Inhibition of hydrogen adsorption on uranium surfaces by traces of water vapor

E. Tiferet[1], M. H. Mintz[1,2], S. Zalkind[1], I. Jacob[2] and N. Shamir[3]

[1]*Nuclear Research Centre-Negev, POBox 9001, Beer Sheva 84190, Israel*

[2]*Ben Gurion University of the Negev, POBox 653, Beer Sheva 84104, Israel*

[3]*59 Rotem St., Omer 84965, Israel. noah.shamir@gmail.com*

Direct–recoils-spectrometry (DRS) measurements of exposures of uranium surfaces to mixtures of hydrogen and water vapor [1], yielded that traces of about 1% water vapor are sufficient to inhibit hydrogen dissociation and chemisorption on uranium surfaces, at room temperature [2]. The efficiency of the inhibition increases with temperature in the range of 200 – 400 K. O_2, in contrast to H_2O, is not an inhibitor to surface adsorption and dissociation of hydrogen. Three types of mechanisms are discussed in order to account for the above inhibition effect of water. It is concluded that the most probable mechanism involves the reversible adsorption (physisorption) of water molecules on hydrogen dissociation sites causing their ‘‘blocking’’.

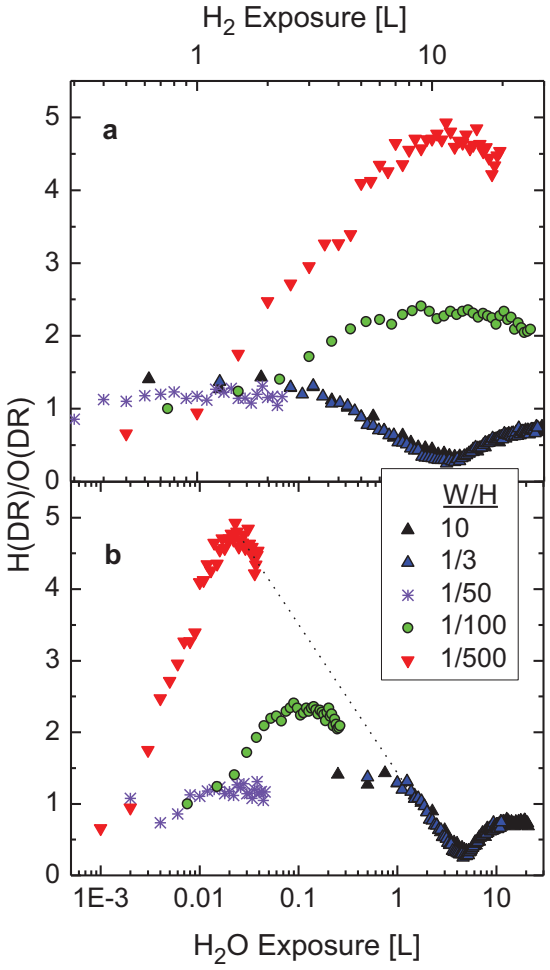

Fig. 1: Exposure curves performed at room temperature for different W/H mixture ratios, with a fixed partial pressure of H_2 ($2 \cdot 10^{-8}$ Torr). (a) H/O versus H_2 exposure dose. (b) H/O versus the corresponding H_2O exposure dose

Refernces:

[1] E. Tiferet, M.H. Mintz, S. Zalkind, I. Jacob, N. Shamir, *J. Alloys Comp.* **444–445**, 177 (2007).

[2] E. Tiferet, M.H. Mintz, I. Jacob, N. Shamir, *Surf. Sci.* **601**, 4925 (2007).

Integrated Surface Science Approach for Study of Spent Fuel Corrosion Processes

T. Gouder

European Commission, Joint Research Centre – Institute for Transuranium Elements (JRC-ITU), Herrmann-von-Helmholtz-Platz 1, 76344 Eggenstein-Leopoldshafen, Germany

Studying surface reactions of actinide oxides is important for the prediction of the long term stability of spent nuclear fuel. The oxides constitute the matrix of the spent fuel and their corrosion occurs via surface processes. One promising route for establishing the reaction mechanisms in the complex fuel is to replace it by simplified model systems. These allow addressing part-aspects of the overall process in so called single effect studies. In our approach, the fuel matrix is represented by sputter deposited thin films of actinide oxides (ThO_2, UO_2, PuO_2, mixed oxides, etc.) into which fission products, minor actinides, cladding or waste container materials are incorporated by co-deposition. The surface reactivity of these systems is studied in a two-step process. 1. Single surface-gas interactions are investigated by studying the gas adsorption under UHV. While being different from real world corrosion conditions, the reaction parameters can be closely controlled (gas dosage, mixing, temperature…). 2. Real world reactions are probed under atmospheric conditions, e.g. by performing electrochemistry studies.

We will first present the new surface science lab station (Fig. 1), which is now being assembled at ITU and is dedicated to these studies. It allows carrying out sample preparation, and reactivity studies under UHV and ambient pressure. The system will allow working with transuranium elements. Special emphasis is given to the combination of spectroscopy techniques (XPS, UPS, BIS, TPD, HREELS, Kelvin probe) probing the average surface, and mapping techniques probing local reactivity aspects. The use of AFM for studying local reactivity aspects under controlled atmosphere (combined with electrochemistry) will be presented. Another important aspect is the gap between ultra-high vacuum conditions, imposed by most surface spectroscopies, and the ambient reaction conditions (aqueous environment) of spent fuel during storage. To assess it, diagnostic techniques running under both conditions are being implemented (e.g. Kelvin probe measuring the surface potential under UHV and ambient pressure).

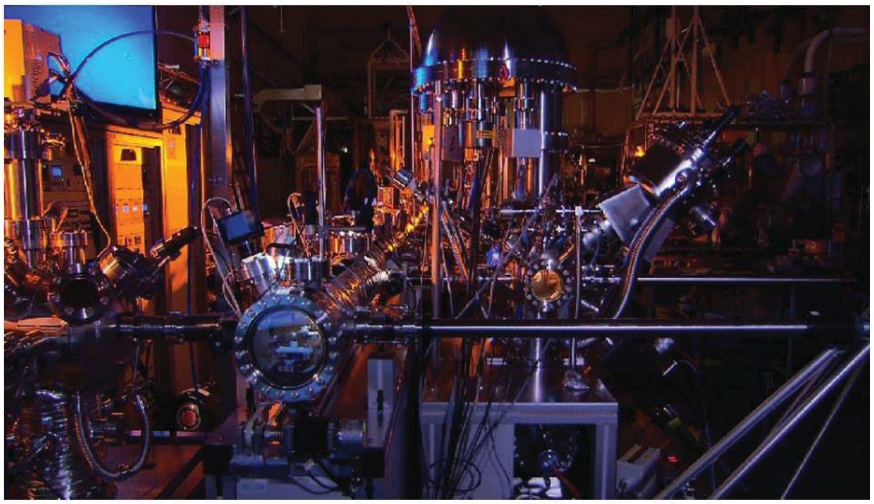

Fig. 1 Surface Science Lab Station

A modular setup has been chosen, where the various techniques are mounted in individual chambers, which can be connected to the station on demand. The machine is

designed for multiuser operation allowing carrying out various experiments simultaneously. It will be made available for outside users and projects.

In a second part we will briefly discuss the surprising surface reaction of early actinide dioxides (from ThO_2 to PuO_2) and mixed oxides ($Th_xU_{1-x}O_2$ and $U_xPu_{1-x}O_2$) with ice. Ice was chosen to fix water in high concentrations to the surface under ultrahigh vacuum conditions. The study was motivated by the possible role of water in promoting further oxidation of PuO_2 [1,2]. To our surprise we found that in presence of UV light and ice, PuO_2 undergoes a fast surface reduction to Pu_2O_3, while UO_{2+x} (x = 0 to1) is also reduced, but to a lesser extent [3]. Surface NpO_2 is reduced to Np_2O_3, which is known to be stable [4] only at the top surface (Fig. 2). In MOX, UO_{2+x} reduction is more pronounced, and this seems to be directly related to the presence of Pu. A similar observation is made for TOX, where U reduction is also faster than in pure UO_{2+x}. Surface reduction is shown to be a true interfacial process, where the solid absorbs light and undergoes a photochemical reaction. It is not a simple surface reaction of the oxides with ice photolysis products.

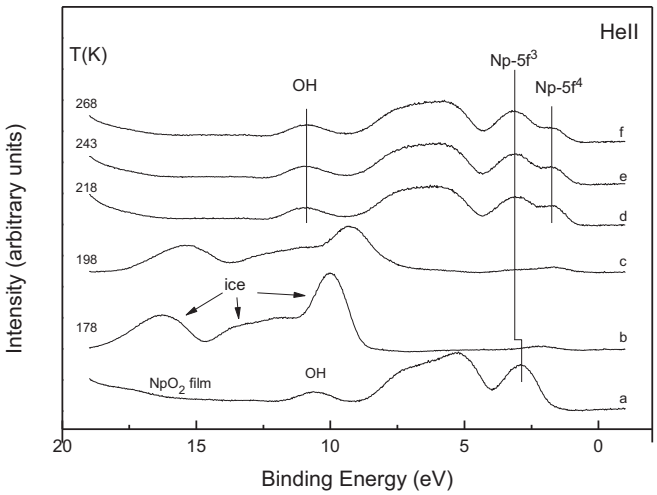

Fig. 2 Reduction of NpO_2 by ice/UV. a) initial NpO_2 with its $5f^3$ emission b) thick ice overlayer at 178K, c)-f) warming up: After ice desorption the Np_2O_3 appears with its $5f^4$ peak.

References

1 J.D. Farr, R.K. Schulze, M.P. Neu, J. Nucl. Mat. 328 (2004), 124.
2 T. Fanghänel, V. Neck, Pure Appl. Chem. 74 (2002), 1895.
3 T. Gouder, A. B. Shick, F. Huber, Topics Catal. 56 (2013), 1112.
4 R. Naegele, L.E. Cox, J.W. Ward, Inorg. Chim. Acta 139 (1987) 327.

Monitoring the *in- situ* oxide growth on uranium by UV-Visible reflectance spectroscopy

Danielle Schweke, Chen Maimon, Zelig Chernia and Tsachi Livneh

Nuclear Research Centre-Negev, P. O. Box 9001, Beer-Sheva 84190, Israel
Daniela.schweke@gmail.com

We demonstrate the *in-situ* monitoring of oxide growth on U-0.1%wtCr by means of UV-Visible reflectance spectroscopy (see Figure 1) in the thickness range of ~20-150 nm. Oxidation rates were deduced from fitting the kinetic data at different temperatures in the range 22-90^{o}C to the inverse logarithmic function. The upper bound of ~0.2µm for the thickness determination on U-0.1%wtCr samples is attributed to cracking and detachment processes in the formed oxide, which are due to the high mismatch between the oxide and metal.

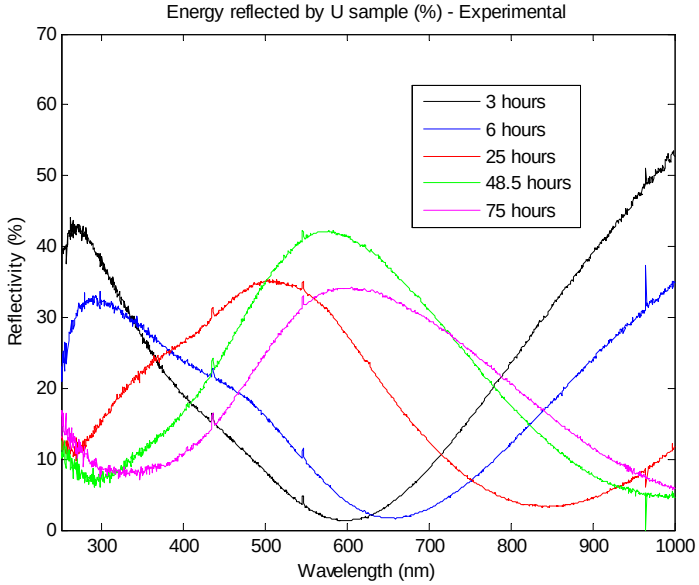

Figure 1: Reflectance spectra obtained from a U-0.1%wtCr sample oxidized at 70°C for different oxidation times

Two different approaches for deducing the oxide thickness from the reflectance spectra are presented: In the “modeling approach”, we employ a model for a metallic substrate covered by a dielectric layer, while taking into account the buildup of oxygen gradient and surface roughness. Then we fit the simulated spectra to the experimental one. In the “extrema analysis”, we derive an approximated analytical expression, which relates the oxide thickness to the position of the extrema in the reflectance spectra based on the condition for optical interference of the reflected light. Good agreement is found between the values extracted by the two procedures (see Figure 2).

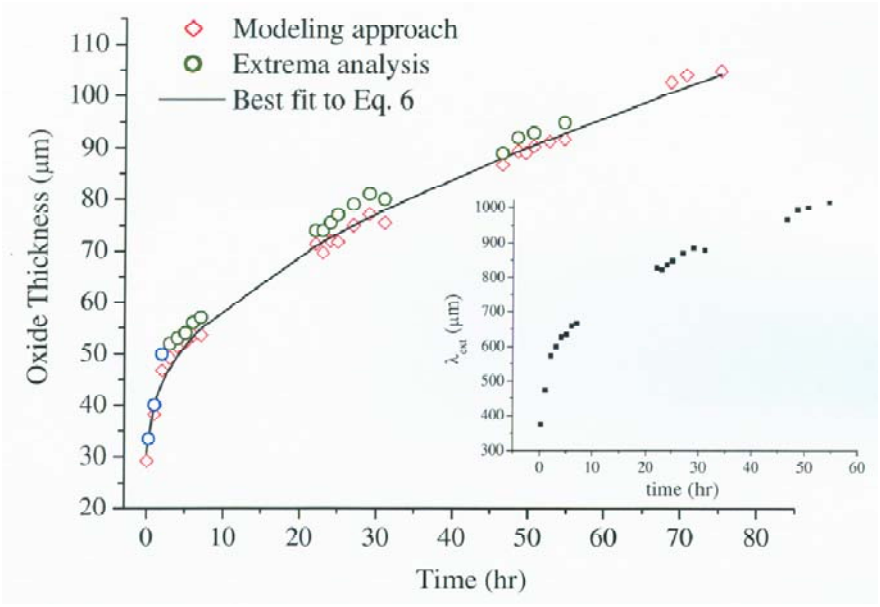

Figure 2: Time dependence of the dioxide thickness during oxidation at 70^{o}C obtained by using the "modeling approach" procedure (diamonds) and the "extrema analysis" (circles) and best fit to the inverse logarithmic function (solid line). In the inset: The time dependence of the 1st minimum.

Both procedures are general and may be used for a variety of metal-oxide systems, bearing in mind that their appropriate application involves a satisfactory knowledge of the metal-oxide dielectric functions. While the first provides some physical insight on the characteristics of the interfaces of the oxide with the metal (oxide composition gradient) and with the ambient (roughness), the second is rather empirical in nature and under the proper assumptions is more straightforward in its employment. Hence, the first procedure is advantageous in cases when deeper understanding of the physical/structural nature of the metal-oxide interface is required. The second is beneficial for “simple” systems where the interfaces are easily defined, or for cases where the signal to noise ratio in reflectance is low. This is due to the high sensitivity of finding the positions of the various extrema in the reflectance signal.

Amorphous carbon enhancement of hydrogen penetration into UO_2

S. Zalkind[1], N. Shamir[2], T. Gouder[3], R. Akhvlediani[4], A. Hoffman[4]

[1]*Physics Dept., Nuclear Research Centre-Negev, POB 9001, Beer-Sheva 84190, Israel*

[2]*59 Rotem St., Omer 84965, Israel*

[3] *European Commission – Joint Research Centre, Institute for Transuranium Elements, POB 2340, 76125 Karlsruhe, Germany*

[4] *Schulich Faculty of Chemistry, Technion, Israel Institute of Technology, Haifa 32000, Israel*

In a previous study [1,2], it was demonstrated that an amorphous carbon layer, deposited on a native oxide covered uranium surface, significantly enhances the interaction of hydrogen with the uranium metal. Fig. 1[2], demonstrates the preferential hydrogen attack (forming uranium hydride) on the carbon covered area of the naturally oxidized uranium metal.

The interaction of D_2 and H_2O (humidity) with amorphous carbon covered UO_2 vs. clean UO_2 was studied using Secondary Ion Mass Spectrometry (SIMS) and X-ray Photoelectron Spectroscopy (XPS). It was found that SIMS depth profiles of the carbon covered side vs. the bare oxide (Fig. 2), show significant higher intensities of H- and D- for the first, through the carbon layer and beneath it. The presence of a thin carbon layer on a UO_2 surface caused a significant buildup of hydroxyl, probably adsorbed on the carbon, but maybe also beneath the layer, in the presence of atmospheric humidity. Exposure of the carbon covered oxide to D_2 on a UHV annealed surface also caused a growth of the hydroxyl. It is concluded that the carbon surface strongly enhances the dissociation of water vapor as well as that of hydrogen and the penetration of the dissociation products to the oxide, as compared to the bare UO_2 surface. The contribution of the latter, beneath the carbon, should be verified or ruled out by further experiments.

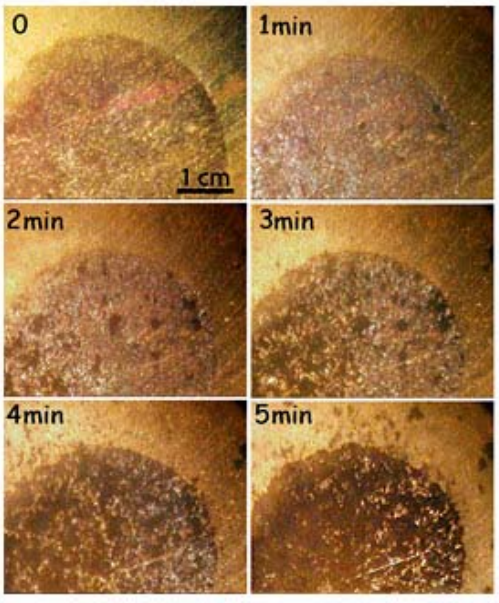

Fig. 1 [2]: HSM micrographs, taken during the exposure of native oxide covered uranium, to hydrogen, at 90°C and 14.6 PSI, presenting the preferential hydrogen reaction with the carbon covered area of the oxidized uranium surface.

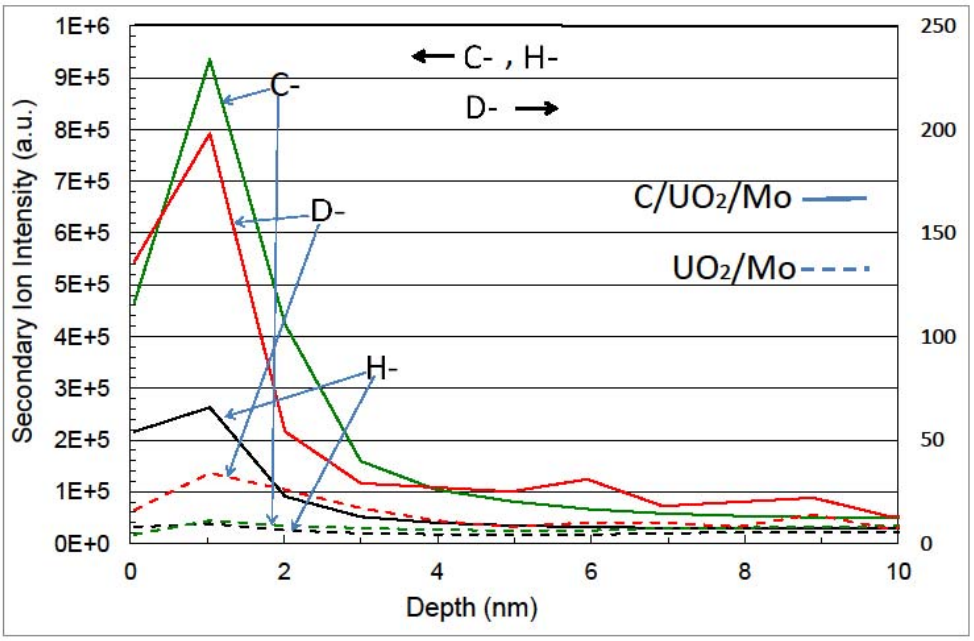

Fig. 2: SIMS depth profile of the sample, after extraction from the UHV surface study system.

References

[1] N. Shamir, Appl. Surf. Sci. **253**, 5957 (2007).

[2] N. Shamir, D. Schweke, A. Rubin, T. Livneh, S. Zalkind, Mater. Sci. Eng. **9**, 012037 (2010).

Selective Oligomerisation and [2+2+2] Cycloaddition of Terminal Alkynes from Simple Actinide Precatalysts

Rami J. Batrice,[1] Jamie McKinven,[2] Polly L. Arnold,[2,*] and Moris S. Eisen[1,*]

[1] *Schulich Faculty of Chemistry, Institute of Catalysis Science and Technology, Technion – Israel Institute of Technology, Technion City, 32000 Haifa, Israel*
[2] *EaStCHEM School of Chemistry, University of Edinburgh, Joseph Black Building, The King's Building, Edinburgh, EH9 3JJ, U.K.*

A simple class of uranium and thorium complexes (1-3) have been synthesized and used in the catalytic oligomerisation and cyclotrimerisation of terminal alkynes.

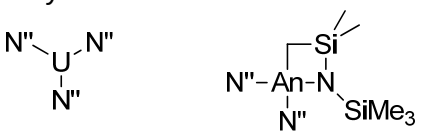

(**1**) An = U (**2**), Th (**3**)

N" = $N(SiMe_3)_2$

The catalytic reactions are quantitative and performed under facile conditions, (75°C in C6D6), and it has been determined that the catalyst loading is essential to the control of the product distribution; below a 10% loading, oligomers are preferentially formed ranging from dimers to pentamers depending on the substitution of the alkyne. However, at a 10% or greater loading, the [2+2+2] cycloaddition product toward tri-substituted benzenes is formed as the major product.

Activation of the precatalyst presumably generates an actinide-hydride species which undergoes migratory insertion by additional alkyne, followed by protolytic cleavage by another molecule of alkyne, generating the actinide-alkynyl moiety and substituted alkene. Further migratory insertions propagate the reaction toward the title products.

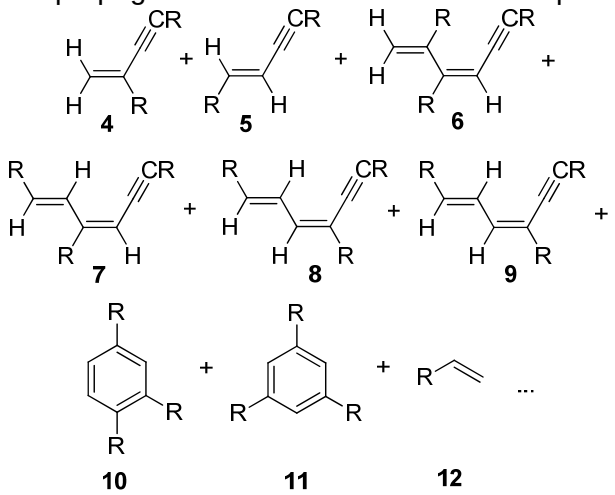

R = ^{n}Bu (**a**), ^{t}Bu (**b**), $SiMe_3$ (**c**), Ph (**d**)

This type of reactivity further expands the library of reactions the actinides are able to perform. The observed cyclotrimerisation marks the first example of an actinide catalyst and one of the few examples of homometallic systems capable of performing this type of transformation.

Electrochemistry of uranium in fused LiCl-KCl-CsCl eutectic

Dmitry Maltsev, Vladimir Volkovich, Evgeny Vladykin, Boris Vasin

Department of Rare metals and Nanomaterials, Ural Federal University, Mira Str., Ekaterinburg, 620002, Russia
e-mail: d.s.maltsev@gmail.com

Pyroelectrochemical methods are considered as prospective technique for reprocessing spent nuclear fuels (SNF). These methods have a number of obvious advantages in comparison with the existing aqueous extraction processes. The advantages include significantly lower volumes of liquid radioactive wastes, high radiation stability of alkali chlorides used as working media, absence of neutron moderators. The eutectic mixture of lithium, potassium and sodium chlorides is one of possible low melting solvents (T_f = 529 K) that can be employed for practical realization of the process. However, there is no information concerning uranium behavior and properties in this melt. In the present work we studied the behavior and determined main electrochemical and thermodynamic properties of uranium in LiCl-KCl-CsCl eutectic melt. The measurements were performed between 573–1073 K employing potentiometry, chronopotentiometry and cyclic voltammetry.

Uranium formal standard electrode potentials in LiCl-KCl-CsCl eutectic were determined using electromotive force method. E*U(III)/U(0) linearly increases with temperature and between 576-1067 K can be described by the following equation:

$$E^*_{U(III)/U(0)} = -2.901 + 6\cdot10^{-4} \cdot T\ (\pm\ 0.029)\ V \qquad (1)$$

From the results of the electrochemical measurements the Gibbs free energy change of the formation of uranium trichloride in LiCl-KCl-CsCl melt at 576-1067 K was calculated:

$$\Delta G^*_{UCl3} = -839.8 + 161.7\cdot10^{-3} \cdot T\ (\pm\ 2.6)\ (kJ/mol) \qquad (2)$$

The results ($E^*_{U(III)/U(0)}$, ΔG^*_{UCl3}) obtained in the present work for LiCl-KCl-CsCl melt are in a good agreement with the available literature data for the melts of other cationic composition, Fig. 1.

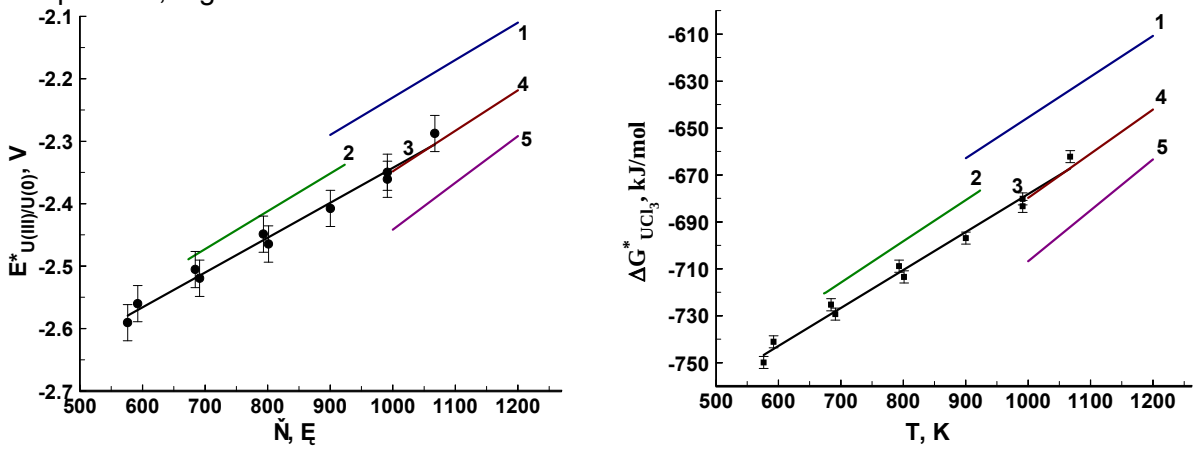

Fig. 1. – The effect of temperature of $E^*_{U(III)/U(0)}$ (left) and $\Delta G^*_{U(III)/U(0)}$ (right) in alkali chloride melts: 1, LiCl; 2, LiCl-KCl; 3, LiCl-KCl-CsCl; 4, NaCl; 5, CsCl. 1, 2, 4, 5 – literature, 3 – present work. Reference electrode – $2Cl^-/Cl_2$

Uranium (IV)/(III) electrochemical reduction was studied using cyclic voltammetry and chronopotentiometry. Examples of the experimental results are shown in Figs 2 and 3. Analysis of the cyclic voltammograms showed that U(IV) → U(III) reduction is a reversible one-electron diffusion controlled process, and this conclusion was confirmed by chronopotentiometric data. The diffusion coefficients of U(III) and U(IV) ions were obtained using both techniques, Fig.5-6, and they are satisfactorily described by the equations (3-6):

cyclic voltammetry:

$$\lg D_{U(III)} = -3268.47/T - 0.82\ (\pm 0.15)\ cm^2/s \quad (3)$$
$$\lg D_{U(IV)} = -2033.43/T - 2.26\ (\pm 0.13)\ cm^2/s \quad (4)$$

chronopotentiometry:

$$\lg D_{U(III)} = -2470.14/T - 0.79\ (\pm 0.17)\ cm^2/s \quad (5)$$
$$\lg D_{U(IV)} = -4331.02/T + 1.25\ (\pm 0.11)\ cm^2/s \quad (6)$$

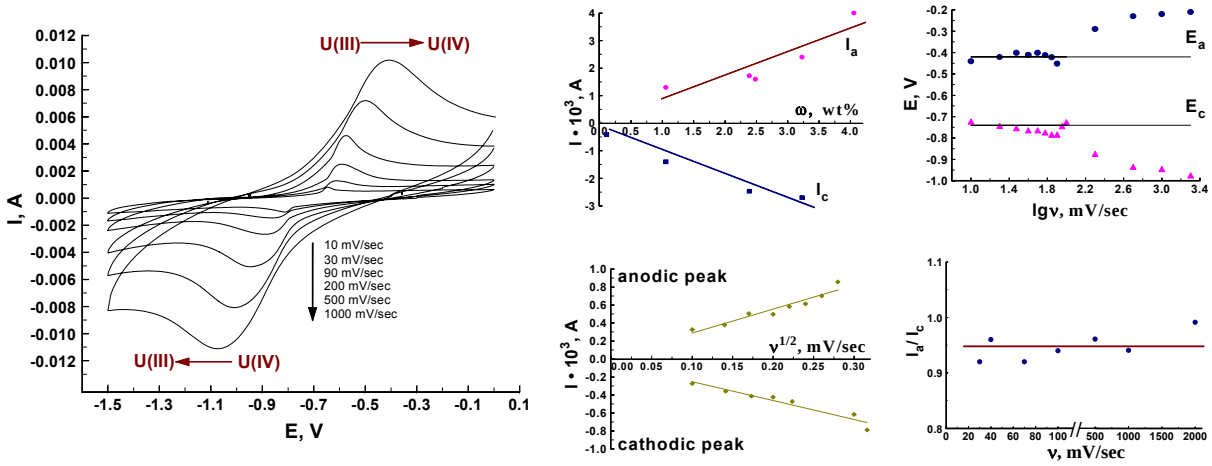

Fig. 2. – Cyclic voltammograms measured in the region of U(IV)/U(III) reduction/oxidation in LiCl-KCl-CsCl melt at 573 K, 0.5 wt.% U and their diagnostic criteria.

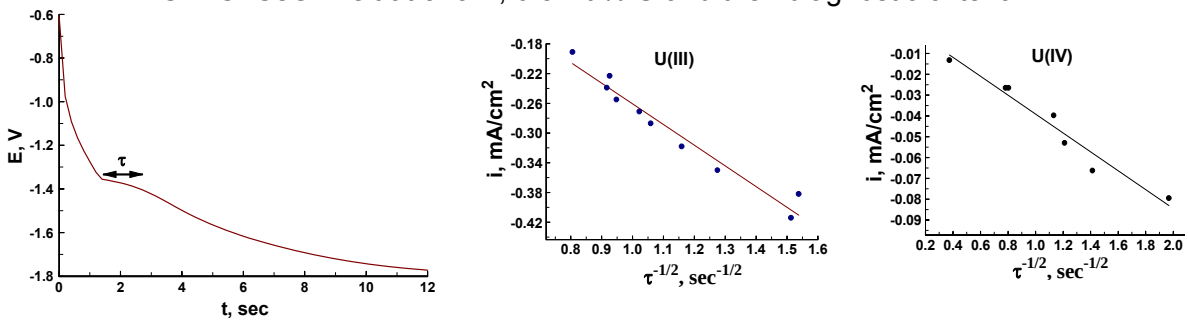

Fig. 3. – Typical chronopotentiogramm measured in LiCl-KCl-CsCl-UCl_3 melt at 573 K, 0.5 wt.% U and diagnostic criteria.

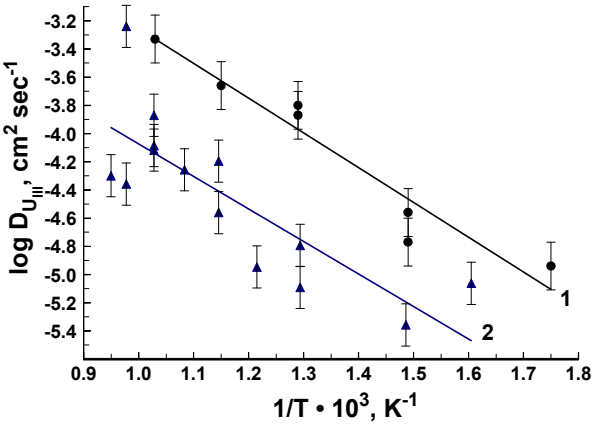

Fig. 5. U(III) chloro-species diffusion coefficients in LiCl-KCl-CsCl eutectic based melts. 1 – data from chronopotentiometry, 2 – data from CV

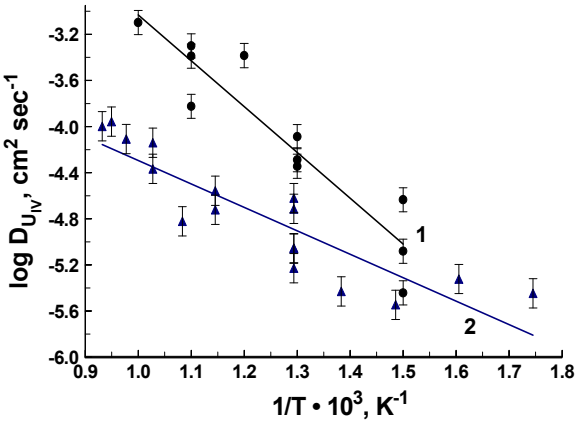

Fig. 6. U(IV) chloro-species diffusion coefficients in LiCl-KCl-CsCl eutectic based melts. 1 – data from chronopotentiometry, 2 – data from CV

Chemical aspects of the interactions occurred in the aqueous system U(VI)-zero valent iron nanoparticles - carboxy- methyl – cellulose-H_2O

Ioana-Carmen Popescu (Hoştuc)[1], Petru Filip[2], Doina Humelnicu[3] Ionel Humelnicu[3],

Thomas Bligh Scott[4] , Richard Andrew Crane [4]

[1]*R&D National Institute for Metals and Radioactive Resources – ICPMRR Bucharest 70 B-dul Carol I, Sector 2, 202917 Bucharest, Romania,*
e-mail : ioana.popescu@icpmrr.ro , janepopescu@gmail.com

[2]*C. D. Nenitescu Institute of Organic Chemistry, 202B Splaiul Independentei, Sector 6, 71141 Bucharest, Romania*

[3]*Al.I. Cuza University of Iasi, The Faculty of Chemistry, No. 11Bd. Carol-I, 700506 Iasi, Romania*

[4]*Interface Analysis Centre, University of Bristol, 121 St. Michael's Hill, Bristol BS2 8BS, United Kingdom*

Carboxy-methyl-cellulose (CMC), a common ''delivery vehicle'' for the subsurface deployment of iron nanoparticles (INP) has been tested in the current work for the removal of aqueous uranium from synthetic water samples. A comparison of the removal of aqueous uranium from solutions using carboxymethyl-cellulose with and without iron nanoparticles (CMC–INP and CMC, respectively) was tested over a 48 h reaction period. The tests were performed for pH ranging between 5 and 7.
Kinetic studies were performed as well. The correlation coefficients indicated that the experimental results obtained in the case of the adsorption on the studied adsorbents best fit to the Freundlich model.
The calculated values of E_S resulted from Dubinin– Radushkevich equation plot points out that the adsorption takes place mainly according to a physical mechanism. The positive values obtained for CMC (E_S = 1.34 kJ/mol) and CMC–INP (E_S = 1.24 kJ/mol) adsorbents shows that the adsorption is an endothermic process enhanced by the high temperature [1].
Scanning electron microscopy (SEM) and energy dispersive Xray spectroscopy (EDX) analysis was performed using a SEM VEGA II LSH scanning electronic microscope with an EDX QUANTAX QX2 detector.
Considering the carboxylic groups' affinity towards uranyl ions, the experimental results confirm the complex interaction within the investigated system. The redox conditions in the studied system are changed due to the oxidation of the nanoscale zero-valent iron particles (INP) and the reduction of U(VI) to U(IV) [2]. So that, the U(VI) is precipitated as uraninite (UO_2). In the same time, a part of the U(VI) is coordinately bonded to the carboxyl-methyl-cellulose conform the recorded IR spectra. The proposed chemical structure of the uranyl-CMC complex is presented in Fig. 1.
Analysis of liquid samples using spectrophotometry determined a maximum sorption capacity of uranium, Q_{max}, of 185.18 mg/g and 322.58 mg/g for CMC and CMC–INP respectively, providing strong evidence of an independent aqueous uranium removal ability exhibited by CMC. The results point out that CMC provides an additional capacity for aqueous uranium removal. Thus, the uranyl ions' adsorption on the CMC–INP material follows a complex mechanism involving the redox precipitation (UO_2), chemisorption (by the CMC) and physical adsorption (by the formed iron oxyhydroxides). Further tests are required to determine whether similar behaviour will be observed for other aqueous contaminant species and if the presence of CMC within INP slurry inhibits or aids the reactivity, reductive capacity and affinity of INP for aqueous contaminant removal.

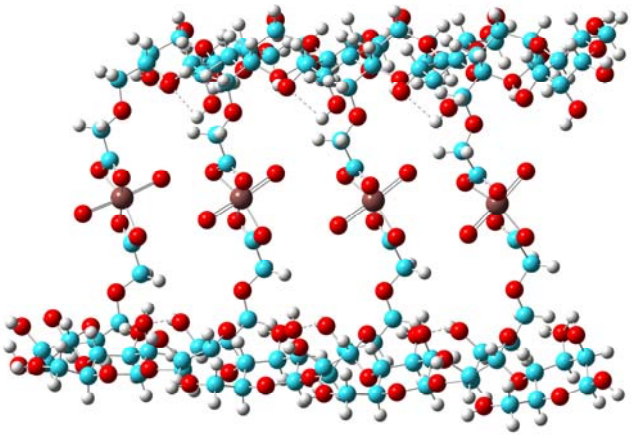

Figure 1. The proposed chemical structurure of CMC-Uranyl complex (red for O atoms, cyan for C atoms, white for H atoms and purple for U atoms).

References

[1] A.H. Chen, S.M. Chen, *J. Hazard. Mater.* **172**, 1111–1121 (2009).
[2] T.B. Scott, I.C. Popescu, R.A. Crane, C. Noubactep, *J. Hazard. Mater.* **186,** 280–287 (2010)

Reaction of uranium dioxide with copper-containing chloride melts

Andrey V. Shchetinskiy, Viktor A. Ivanov, Vladimir A. Volkovich

Department of Rare Metals and Nanomaterials, Ural Federal University, 19 Mira Str., Ekaterinburg, 620002, Russia
e-mail: volkovich@dpt.ustu.ru

Cermet composition materials consisting of metallic copper and uranium dioxide can be used for manufacturing fuel rods of nuclear power reactors. Reprocessing of such irradiated fuel of dispersive type can be done employing non-aqueous pyrochemical methods and developing such technology requires information on interaction of uranium dioxide with chloride melts containing copper ions.

Alkali chloride based melts containing cuprous chloride or pure copper(I) chloride can be used as working media for reprocessing of this type of cermet fuel. The irradiated fuel can be dissolved by reacting it with gaseous chlorine directly in the fused salt. During such dissolution copper(I) chloride will be oxidized to copper(II) chloride which is in turn a very effective chlorinating agent acting as the chlorine transfer species. The Red/Ox potential of the working medium is determined by the [Cu(II)]/[Cu(I)] ratio and is very high, being close to that of the chlorine electrode. Copper(II) ions act as oxidants not only towards copper but also to uranium dioxide and the following reactions are possible in the melt:

$$Cu + CuCl_2 \rightarrow 2\ CuCl \quad (1)$$

$$UO_2 + Cl_2 \rightarrow UO_2Cl_2 \quad (2)$$

At the same time metallic copper is thermodynamically incompatible with the melts containing UO_2^{2+} ions because the equilibrium of the following reaction:

$$2\ Cu + UO_2Cl_2 \rightarrow 2\ CuCl + UO_2 \quad (3)$$

is fully shifted to the right. This is confirmed by the values of the formal standard potentials of copper and uranium dioxide in alkali chloride melts, *e.g.*, in NaCl-KCl equimolar mixture.

A series of experiments on simulated copper-uranium dioxide fuel compositions was performed. Samples reacted with an alkali chloride melts containing Cu(II) and Cu(I) ions with simultaneous chlorine sparging. The experimental results confirmed the above assumptions.

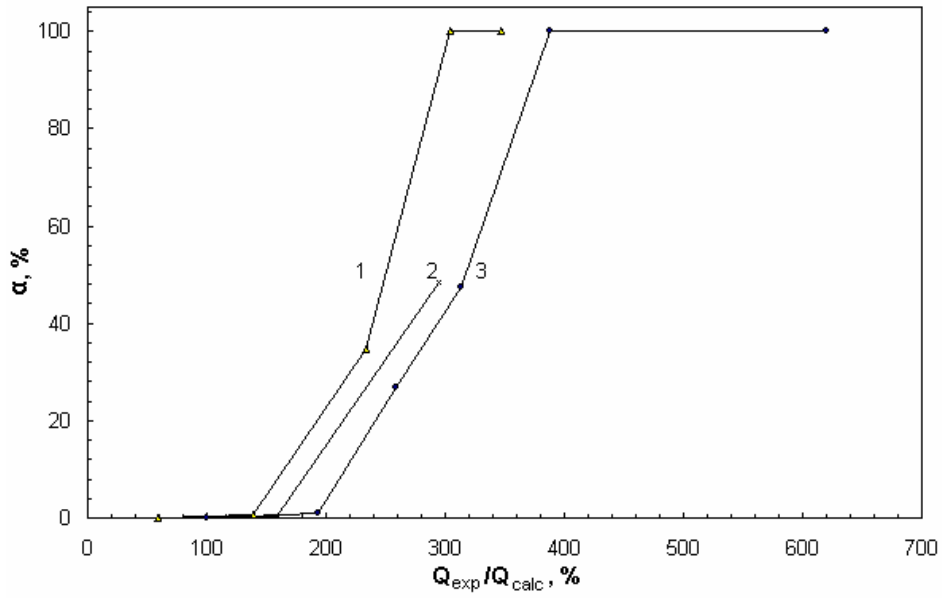

Fig. 1. Fraction of dissolved UO_2 during chlorination of Cu+UO_2 samples in CuCl (1, 2) and NaCl-2CsCl eutectic containing 10 wt.% Cu_2Cl_2 (3). Temperature, °C: 1 – 520; 2 – 620; 3 – 610.

Figure 1 shows that dissolution of uranium dioxide in the studied systems begins only after complete conversion of copper to the oxidation state +2. Therefore the suggested method can be recommended as a method for separating uranium dioxide from the construction materials of the fuel elements.

Uranium that was dissolved alongside with copper forming UO_2^{2+} ions in the salt phase can be essentially quantitatively reduced to UO_2 and precipitated from the melt. The process described by reaction (3) can be used for this purpose. In practice a copper plate (or a rod) should be submerged into the melt and kept in contact with the salt phase for a certain period of time. After completing reduction of uranium to UO_2 copper plate is removed from the melt.

Towards Prediction Of Crystal Structure Of Al-Rich Intermetallides Formed In Al-T-A Systems

Avraham I Bram[a,b], Arie Venkert[c], Louisa Meshi[a,b]

[a] *Department of Materials Engineering, Ben-Gurion University of the Negev, Beer-Sheva 84105, Israe e-mail: avrambram@gmail.com*

[b] *Ilse Katz institute for nanotechnology, Ben Gurion University of the Negev, Beer Sheva 84105, Israel*

[c] *Nuclear Research Center-Negev, POB 9001 , Beer-Sheva, Israel. e-mail: venkert@bgu.ac.il*

Crystal structure of the material has a significant contribution on its properties. However, there is no universal model that can predict precisely the crystallographic structure of a stable material at specific composition and temperature. Since the 1950's, various prediction approaches were developed and yielded many different methods of computer simulation and innovative theories which are summarized in the review of *Woodley et al.* [1]. These methods are based on complicated calculations of quantum sizes.

While reviewing former studies on Al-T-A system (where T=Transition metals and A=Actinides or Lanthanides), we found correlation between the aluminides formed at specific composition and their crystal structures. In this study we tried to develop a simple approach useful in prediction of the crystallographic structure of stable Al-rich intermetallides found in the Al-T-A system. This system is one of the most complicated systems to predict using the conventional methods, because it includes multiple atoms in the unit cell in general and specifically - heavy atoms with unique electronic structure (f-orbital). Present research contains our conclusions regarding Al-T-A systems where T are 3d transition metals and A – Th, as an example of actinides. The stoichiometry which was chosen for this purpose was $Al_{20}T_2Th$. To verify our prediction, we prepared and characterized five alloys containing different 3d transition metals. The alloys were prepared by arc melting in UHP Argon atmosphere followed by rapid cooling during molding into rod shape. Thermal treatment was performed in order to homogenize the alloys with the purpose to attain the equilibrium phases in each system. Scanning and transmission electron microscopy (SEM and TEM) and X-ray powder diffraction methods were used for characterization of the as-received and heat treated alloys. The experimental results were in good agreement with our prediction.

This research is a first step for development of a simplified crystal structure prediction method for the Al-rich intermetallics formed in Al-T-A system.

References:

[1] Woodly S.M and Catlow R., *Nature Materials* **7**, 937-946 (2008).

Growth and characterization of uranium-alloy thin films

A M Adamska, T B Scott, R Springell, A D Warren, L Pico, O Payton

[1]*Interface Analysis Centre, School of Physics, HH Wills Physics Laboratory, University of Bristol, Tyndall Avenue, Bristol, BS8 1TL, United Kingdom*
e-mail: am.adamska@bristol.ac.uk

As world populations continue to grow and supplies of fossil fuels dwindle, there is an increasing need for alternative low-cost, carbon neutral and secure supplies of electricity. Nuclear energy is just one solution to this problem, which has become increasingly feasible as the technology matures, yielding improvements in safety, size and efficiency. The proclaimed target for the next generation of nuclear fission reactors is to become still safer and at the same time more efficient. In the wake of the Fukishima Daiichi nuclear power plant incident there is an increased emphasis on developing improved and inherently safe materials for fuels, cladding and structural materials. The preferred choice of nuclear fuel materials is limited not only by the characteristics of the reactor cores in which they are deployed but also by their subsequent behaviour as a waste-form. The key risk posed by spent nuclear fuel involves a release of radiation that could harm human health or the environment. To date, the fuel materials that have been developed for use in power reactors include uranium and thorium metals, their alloys, oxides, carbides, nitrides and hydrides, with oxide (UO_2) emerging as the fuel type predominant.

In the present study we concentrated on the growth and characterization of U-alloy thin films, which may be used as a useful low activity experimental surrogate for bulk alloy systems, significantly reducing experimental risk and limitations. In addition, they provide a simplified model surfaces for oxidation and corrosion studies that may be subsequently used to predict material changes in their bulk counterparts. More fundamentally, a thin film approach to the study of actinide compounds may lead to better understanding of 5*f* electron systems.

Pure uranium has three crystalline phases below its melting point. The room temperature (RT) α-U phase is base-centered orthorhombic structure [1]. In fuels this phase shows very poor operational stability [2], related to highly anisotropic thermal expansion [3]. It also exhibits poor dimensional stability during irradiation, making it undesirable as a fuel. The high-temperature (T > 775°C) body-centered cubic (*bcc*) γ-U phase is more resistant to irradiation effects than the α-phase and exhibits isotropic thermal expansion properties. Unfortunately, in pure U this phase cannot be preserved to RT, which presents a significant technical limitation. Conceptually, a solution to this problem is to stabilise the γ-phase down to RT by U alloying with Nb, Zr, or Mo in bulk form [4]. It has been already shown that the γ-phase U-Mo poly- and single-crystal alloys can be synthesised in thin film form [5]. Subsequently, we explored the binary alloy phase diagrams of both poly- and single-crystal U-Ta and U-Zr thin films synthesised using UHV *dc* magnetron sputter deposition. For the U-Ta system, the γ-phase U-alloy could not be formed indicating significant immiscibility. Instead separate α-U and Ta were formed containing only trace amounts of the partnering element. By comparison, successful alloying was observed for the U-Zr system. The coexistence of α- and γ-phase of U were detected for polycrystalline U-Zr system with the prevailing crystal structure controlled by composition. Epitaxial U-Zr samples were determined to have formed bi-layered structure of single-crystal γ-U, α-U phases or γ-U, α-U and δUZr_2 phases depending on the concentration of alloying element (Fig. 1.).

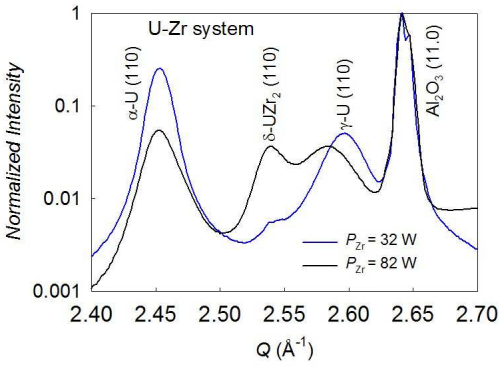

Fig. 1. Comparison of the XRD patterns close to the sapphire (11.0) peak for single-crystal U-Zr alloy thin films deposited at T = 800°C using different Zr powers.

EBSD maps recorded from the surface of the double U-Zr single-crystal sample indicated an α-U single-crystal located at the top of the film, see Fig. 2.

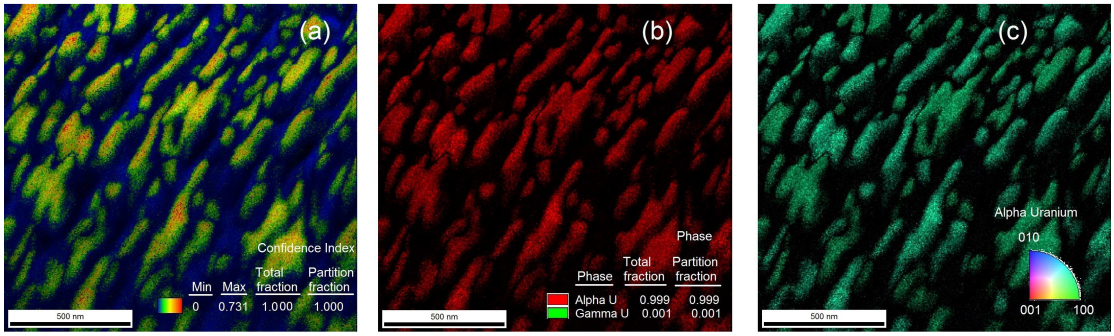

Fig. 2. EBSD maps of the double U-Zr single crystal showing (a) confidence index for the recognized phase, (b) phase fractions and (c) the inverse pole figure showing the orientation of the single crystal.

The surface topography of U-Zr single crystal shown in Fig. 3-4. exhibits a surface morphology of sharply stepped ridges. Secondary electron images of the surface reveals small square or rectangular holes ascribed as gaps or windows in the upper 'defective' layer revealing the underling 'perfect' film (Fig. 4).

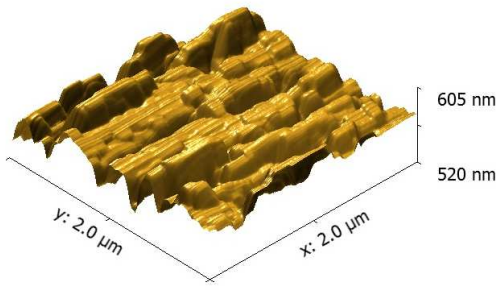

Fig. 3. AFM topography of the double U-Zr single-crystal thin film.

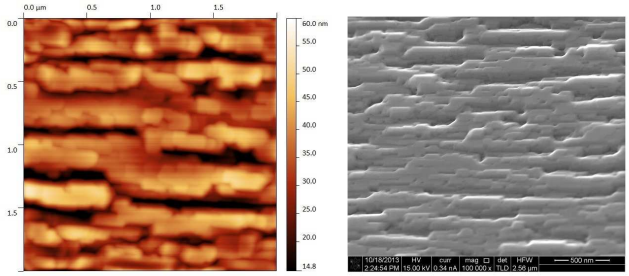

Fig. 4. Comparison between (a) AFM micrograph and (b) SE image of the surface of the double U-Zr single-crystal thin film.

References

[1] G. H. Lander et al., *Acta Cryst.* **B26**, 129 (1970)
[2] G. Ostberg et al., *J. Nucl. Mater.* **10**, 329 (1963)
[3] L.T. Lloyd, *J. Nucl. Mater.* **3**, 67 (1961)
[4] V.P. Sinha et al., *J. Alloys and Compds.* **506**, 253 (2010)
[5] A M Adamska et al.,*Thin Solid Films* **550**, 319 (2014)

X-ray Diffraction Analysis of High-Purity Cerium-Lanthanum Alloys

Dr Keith R Hallam[1], Dr Michael Ling[2]

[1] *University of Bristol, Interface Analysis Centre, School of Physics, HH Wills Physics Laboratory, Tyndall Avenue, Bristol, BS8 1TL, United Kingdom*
e-mail: k.r.hallam@bristol.ac.uk
[2] *AWE, Aldermaston, Reading, Berkshire, RG7 4PR, United Kingdom*

Introduction

Recent developments in hot-stage and electron microscopy technology allow for metals and alloys to be successfully examined at temperatures up to 1000°C. This has been achieved for a number of light metals and their alloys, yielding new insights into microstructural refinement arising from grain growth and phase transformations. The application of SEM, EBSD and XRD are considered to have provided the greatest amount of useful information previously and we believe that this approach will provide insights into the poorly understood mechanisms of phase transformation and microstructure development in the heavy f-block metals and alloys, including U and Pu. We are determining the feasibility of high-temperature materials analysis of a series Ce-La alloys, as a surrogate [1]. Four samples of high-purity Ce-La alloys (1%, 3%, 5% and 10% La), together with Ce metal, have been used for a feasibility study into the implementation of hot stage XRD analysis. One major obstacle in the way of surface analysis of f-block elements is their high electropositivity and thus rapid tarnishing in air, as they react readily with O_2 and H_2O vapour to form surface oxides.

A Philips Xpert Pro diffractometer (λ=1.5406Å CuKα source; generator voltage 40keV; emission current 30mA) was used with an Anton Parr HTK 1200 high temperature oven camera to take measurements at temperatures up to 870°C in a number of different environments (inert He or Ar; low vacuum or higher vacuum).

Results

0%La, 1%La, 3%La, 5%La and 10%La alloys; Room temperature; Low vacuum

Fig. 1 presents XRD patterns from the Ce-x%La alloys recorded at room temperature, under a low vacuum. As the La contribution to the alloy increases, the peaks shift towards lower 2θ, indicative of an increase in the lattice d-spacings - as might be expected due to the slightly larger metallic radius of La (1.8791Å) compared to Ce (1.8247Å) [2].

3%La alloy; Temperatures up to 870°C; High vacuum

Fig. 2 presents an example temperature cycling of a 3%La coupon under high, 10^{-6}mbar, vacuum. The coupon was taken from room temperature, 25°C, up to 870°C - well above the melting point of the alloy - and back down to room temperature. For the purposes of this present study, it is most important to note the rapid onset of oxidation at temperatures of 300°C and above. By the time 400°C is reached, the oxide peak dominates over the metallic. This particular coupon was taken well over the literature melting point of the alloy. However, once the experiment was concluded and the sample retrieved, it was still largely intact, though heavily oxidised, and had not undergone bulk melting.

3%La alloy; Temperatures up to 760°C; Argon flow

Room temperature signal intensities were found to drop by ~90% when Ar was flowing through the camera, in comparison to those count rates observed with either air or vacuum present. However, the Ar flow was not seen to prevent or significantly reduce sample oxidation (Fig. 3). The reaction of the metal/alloy was not simple, in that initially-formed oxide peaks at 300-400°C were then seen to shift towards lower 2θ as the temperature continued to rise towards the literature melting point.

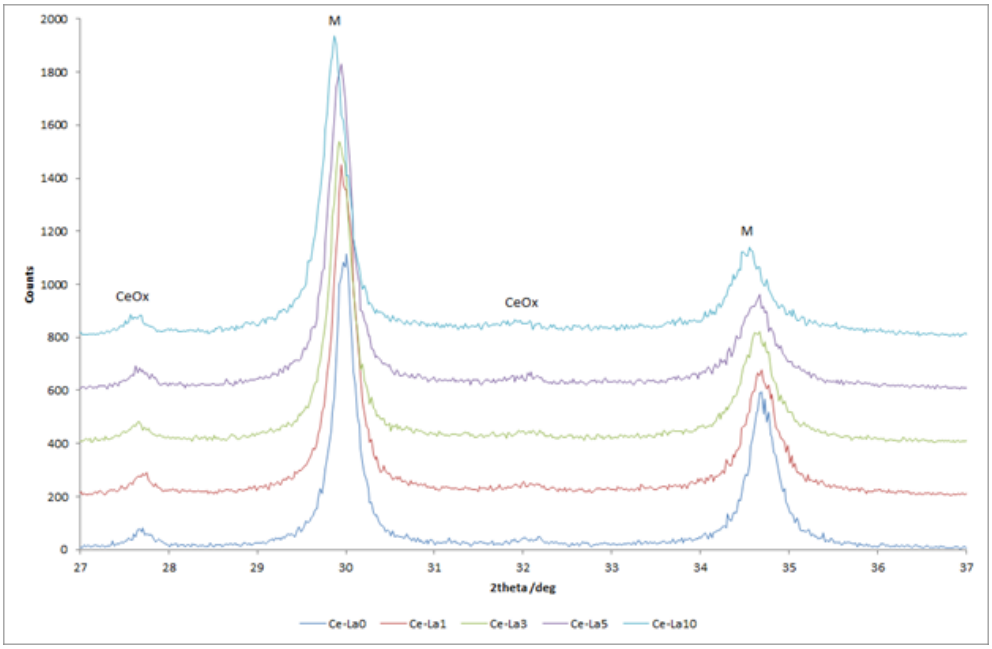

Fig. 1. Ce-x%La alloy; SiC-ground; Room temperature; Low vacuum.

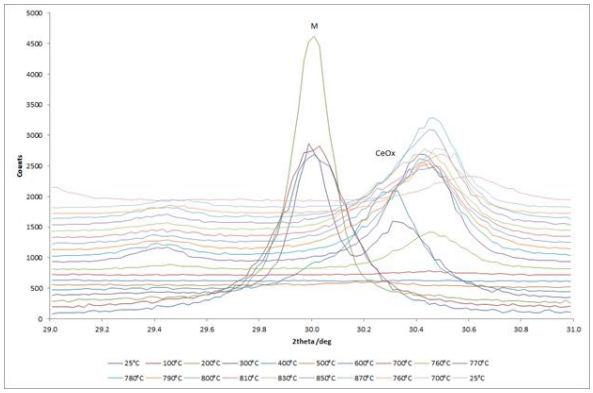

Fig. 2. Ce-3%La alloy; SiC-ground; High vacuum.

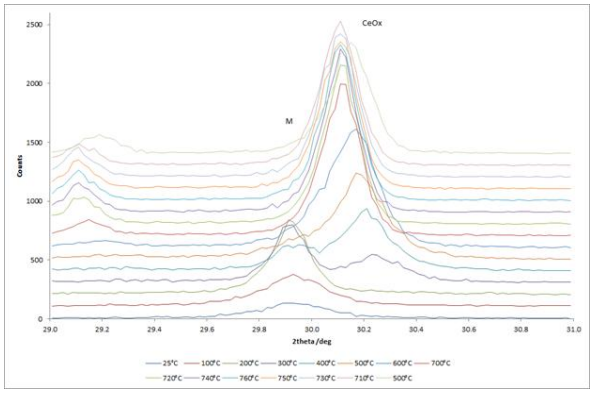

Fig. 3. Ce-3%La alloy; SiC-ground; Argon flow.

Conclusions

1. At 25°C, as the La contribution to the alloy increases, peaks shift towards lower 2θ, indicative of an increase in the lattice d-spacings.
2. At 25°C, additional metal/oxide peaks as well as the major metallic alloy signal were seen.
3. 400°C oxidation under low vacuum formed hexagonal and cubic oxide forms.
4. Oxidation was seen at temperatures of 300°C and above but coupons taken well above their nominal melting point were found to have retained their bulk form.
5. Samples taken up to 740 or 750°C, cooled and reground to remove surface oxide were found to resemble original room temperature coupons.
6. Flowing or static Ar was seen to reduce signal intensities sharply but neither was able to reduce surface oxidation of coupons.
7. It was not found possible to heat Ce metal and Ce-La alloy coupons to induce phase change without them undergoing substantial surface oxidation.

References

[1] M Ling “Development of Ce-La Alloys as Pu-Ga Surrogate Alloys” The 41èmes Journées des Actinides, Stará Lesná, Slovakia (9-12 April 2011).

[2] *Handbook of Chemistry and Physics*, http://www.hbcpnetbase.com, Section 4, Table 2, Crystallographic Data for the Rare Earth Metals at 24°C (297K) or Below (accessed 26 January 2013).

The influence of surface cleaning preparation on the initiation of uranium hydride sites

Antonios Banos[1], Camille Stitt[1], Dr. Tom Scott[1]

[1]University of Bristol, Interface Analysis Centre, School of Physics, HH Wills Physics Laboratory, Tyndall Avenue, Bristol, BS8 1TL, United Kingdom; e-mail: ab13306@bristol.ac.uk

The effect of various methods of surface cleaning preparation on the early stages of the uranium-hydrogen reaction have been identified and evaluated. There are numerous factors influencing the nucleation rate and density, growth and location of hydride initiation, such as metallurgy of the sample, pressure and temperature of the reaction, surface and gas impurities, microstructure, etc. The impact of the above mentioned parameters has been well investigated by others, though little attention has been given to the cleaning treatment preceding the reaction. This present work has concentrated on isolating this variable using five different surface cleaning techniques on five identical samples cut from the same lot. The samples have been react altogether on the same cell under high vacuum and constant volume conditions. Hydrogen uptake by the samples was followed by monitoring the pressure decrease in the system. Post-mortem examination and characterisation of the reacted surfaces was undertaken using focused ion beam (FIB) milling and secondary ion mass spectrometry (SIMS).

Study of the $U(Al,Si)_3$ vertex location in the 400ºC isothermal section of the U-Al-Si phase diagram

Gennady Rafailov[1,2] Gili Shalev[1], , Isaac Dahan[2], Louisa Meshi[1]

[1] *Department of Materials Engineering, Ben Gurion University of the Negev, Beer-Sheva 84105, Israel. e-mail: refelov@bgu.ac.il*
[2] *Materials Department, Nuclear Research Center of Negev (NRCN), P.O.Box 9001, Beer-Sheva 84190, Israel*

Ternary U-Al-Si system has been extensively investigated due to the high potential of Uranium alloyed with Silicon as low-enriched fuel. Another interest in the U-Al-Si ternary system originates from the use of Aluminum alloy, where Silicon is a major alloying element, as U-fuel cladding. Due to the high exploitation temperature, U-Al-Si interaction layer forms among the Uranium fuel and Al-Si-alloy cladding. Thus, investigation of the U-Al-Si system is of technological importance. In order to perform thermodynamic modeling (one of the options to study the ternary U-Al-SI phase diagram) the exact composition of invariant points and exact homogeneity ranges of intermetallides formed in this phase diagram have to be determined empirically. In the past, thermodynamic modeling of the U-Al-Si system was based on the isothermal section suggested by Dwight [1]. In this work the $U(Al,Si)_3$ ordered phase was not identified, whereas in a later research [2] it was found to be stable in a wide range of compositions. This emphasizes the need to verify his results. U(Al,Si)3 vertex is one of the critical locations required for thermodynamic calculations [3]. With an intention to either contradict or support previous results on the $U(Al,Si)_3$ vertex location, two alloys with different compositions existing within the Al-Si-$U(Al,Si)_3$ triangle were characterized. The alloys were heat treated in order to obtain equilibrium state. Phase characterization of the alloys was performed using scanning electron microscopy, transmission electron microscopy and X-ray diffraction. Rietveld method was applied on XRD data for quantitative analysis. Experimental results imply that the location of the $U(Al,Si)_3$ vertex should be at 25at.% U-13at.% Al-62at.%Si. This result contradicts previous results reported in [1].

References:

[1] A.E Dwight, "A Study of the Uranium-Aluminum-Silicon System", Argonne National Laboratory, 1982
[2] G. Rafailov, "Investigation of Ordered Phase (U,Fe)(Al,Si)3", M.Sc. Thesis, Ben Gurion University, 2009
[3] D. Rabin, E. Brosh, R.Z. Shneck, L. Shenhav, “Thermodynamic modeling of some Al-U-X ternary systems”, 42nd CALPHAD International Conference

Towards construction of quasi-binary UAl_3-USi_3 phase diagram

Gennady Rafailov[1,2] Asaf Uziel[1], Avner White[1], Itzhak Dahan[2], Louisa Meshi[1]

[1] *Department of Materials Engineering, Ben Gurion University of the Negev, Beer-Sheva 84105, Israel. e-mail: refelov@bgu.ac.il*

[2] *Materials Department, Nuclear Research Center of Negev (NRCN), P.O.Box 9001, Beer-Sheva 84190, Israel*

Ternary U-Al-Si system has been extensively investigated due to the high potential of Uranium alloyed with Silicon as low-enriched fuel. Another interest in the U-Al-Si ternary system originates from the use of Aluminum alloy, where Silicon is a major alloying element, as U-fuel cladding [1]. In this system, UAl3 and USi3 phases are of special importance. Since UAl3 and USi3 are isostructural and follow the Hume-Rothery rules closely, it would be expected that their quasi-binary phase diagram will be isomorphous. However, previous studies have shown that this system does not display complete liquid and solid solubility. Moreover, conflicting results were reported regarding the phases found [2-4]. In current work, several compositions were cast and then heat-treated in order to reach equilibrium for subsequent characterization of Si-rich part of the USi3-UAl3 quasi-binary phase diagram. The as-cast and heat-treated alloys were characterized by scanning and transmission electron microscopy and X-ray diffraction (XRD) methods. Quantitative results were obtained from Rietveld analysis performed on XRD data. The results show that the ordered U(Si,Al)3 phase, identified in an earlier study of the Al-rich region [3] is present also in the Si-rich region (studied in present research). Furthermore, ordered phase exhibited substantial stability over quite large range of compositions and temperature. Our results unambiguously point out that this quasi-binary system contains an order-disorder transformation and not a miscibility gap at low temperatures in the studied range of compositions.

References:

[1] Leenares A., Detavernier C., Van Den Berghe S. (2008). J. Nuclear Materials, 381. 242-248.

[2] Dwight A.E. (1982). Argonne National Library ANL-82-14.

[3] Rafailov G., (2009). M.Sc. Thesis, Ben Gurion University.

[4] Rogl P., Noel H. (2007). Non-ferrous metal systems (p.4), selected nuclear and engineering systems. Landolt-Bornstein – Group IV Phys. Chem., v.11C4, 56-73

Studies on the U-Fe-C ternary phase diagram

A.P. Gonçalves,[1] M.S. Henriques[1], L. Havela[2]

[1] *Campus Tecnológico e Nuclear, Instituto Superior Técnico/CFMC, Universidade de Lisboa, Estrada Nacional 10, 2695-066 Bobadela LRS, Portugal*
e-mail: apg@ctn.ist.utl.pt
[2] *Dept. Condensed Matter Physics, Faculty of Mathematics and Physics, Charles Univ., 121 16 Prague, the Czech Republic*

Nuclear fuel plays a key issue on the safety, sustainability, economics, reliability and proliferation resistance of Generation IV reactors. For its proper choice not only the nuclear properties should be considered, but also the fuel thermophysical characteristics and its compatibility with the core materials during the extreme fission conditions. Uranium binary carbides are possible candidates due to the inexistence of phase transformations at the operation temperatures, stability under irradiation and chemical inertness, coupled to their higher fissile metal density, melting point and thermal conductivity, when compared with UO_2. The interaction between uranium carbide fuels and steel canning materials have been studied in the sixties, which lead to the discovery of the $UFeC_2$ compound [1].Three other ternary phases, $U_{\sim 32}Fe_{\sim 17}C_{\sim 51}$, $U_{30.6}Fe_{8.6}C_{60.8}$ and $U_{11}Fe_{12}C_{18}$, were reported later, but only the last one was confirmed, with its crystal structure studied [2]. However, the existence of additional ternary phases can interfere with the binary materials stability. Therefore, we decided to perform studies on the U-Fe-C ternary phase diagram in order to identify the new phases and to investigate the U-Fe-C isothermal section at 1100ºC.

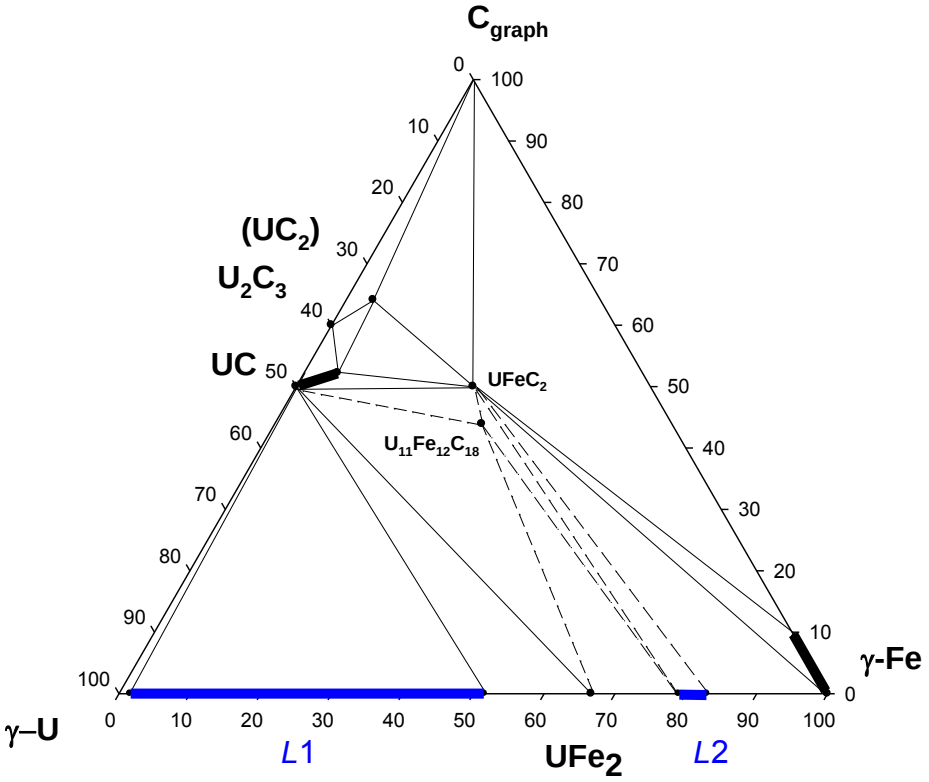

Fig. 1. Isothermal section of the U-Fe-C system at 1100ºC (thick lines: solid solutions; dash tie-lines: extrapolations; thick blue lines: liquid lines)..

Preliminary results indicated that the U-Fe-C system at 1100ºC is characterized by the formation of six binary and eleven ternary domains. $UFeC_2$ was confirmed to be stable at this temperature, together with the $U_{11}Fe_{12}C_{18}$ phase. An island phase field with the UxFeyCz

composition and crystallizing in the α-UC_2-type structure (or closely related), was also identified at 1100ºC. The compound announced as $U_{\sim 32}Fe_{\sim 17}C_{\sim 51}$, reported to be stable at 1050ºC [3], was not observed at this temperature.

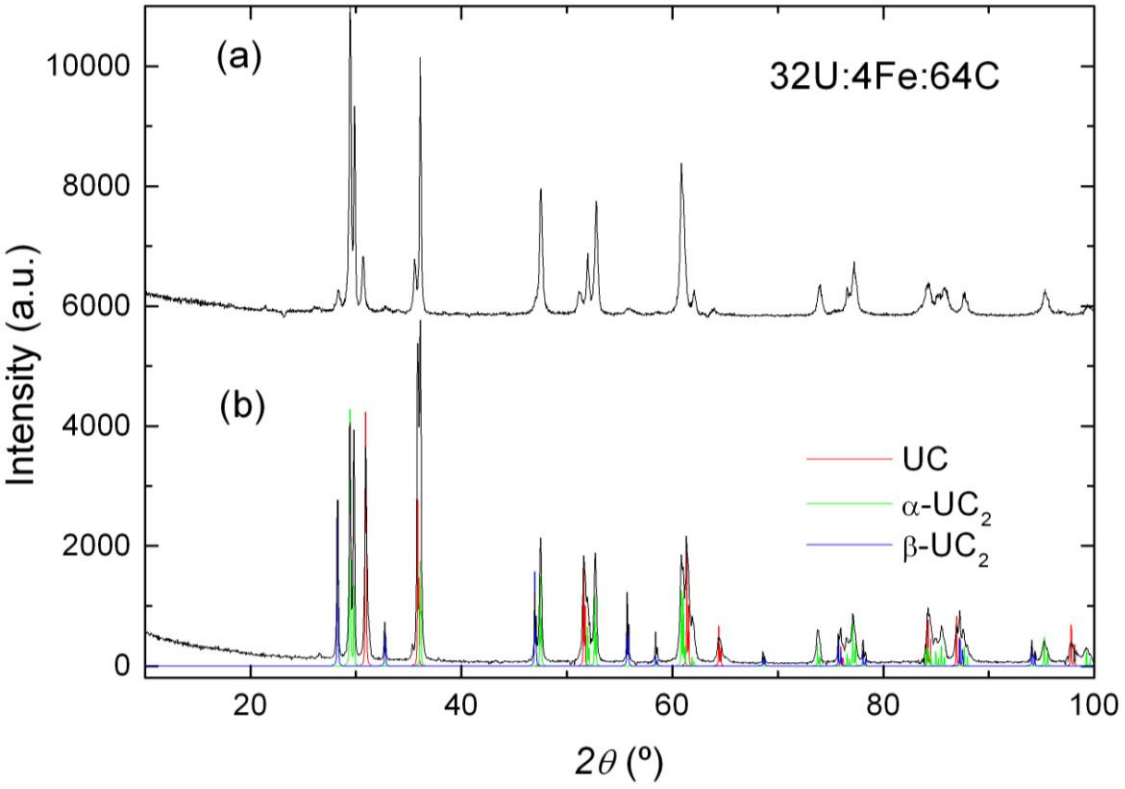

Fig. 2. X-ray powder diffractogram of a 32U:4Fe:64C nominal composition sample: (a) as-cast and (b) heat treated at 1300ºC; coloured lines represent simulations for three binary uranium carbides.

The study of ternary samples heat treated at 1300ºC allowed the clear identification of new phases and phase relations. Fig. 2 shows the X-ray powder diffractograms of (a) an as-cast and (b) a heat treated at 1300ºC for 15 hours 32U:4Fe:64C nominal composition sample. The β-UC_2 phase, crystallizing with the CaF_2-type structure, clearly exists at this temperature. At 1300ºC the CaF_2-type structure phase coexists with the cubic UC_{1+x} (NaCl-type) and tetragonal α-UC_2 (CaC_2-type). This contrasts with previous results on the U-C binary system, where the high-temperature β-UC_2 phase was reported to transform into the low-temperature α-UC_2 phase at 1820ºC [4]. Therefore, most probably small amounts of Fe stabilize the cubic CaF_2-type structure phase.

Acknowledgments
This work was partially supported by FCT, Portugal, under the contract No. CERN/FP/123588/2011. M.S.H. acknowledges FCT for the SFRH/BD/66161/2009 grant.

References
[1] P. Baldock, J.R. McLaren, H.J. Hedger, *J. Nucl. Mater*. **5**, 257 (1962).
[2] K.H. Wachtmann, M.A. Moss, R.-D. Hoffmann, W. Jeitschko, *J. Alloys Compd*. **219**, 279 (1995).
[3] Z.M. Alekseyeva, *Metally* **5**, 151 (1992) (in Russian).
[4] P.Y. Chevalier, E. Fischer, *J. Nucl. Mater*. **288**, 100 (2001).

Solubility of uranium in liquid gallium, indium and their alloys

Vladimir A. Volkovich,[1] Dmitry S. Maltsev,[1] Leonid F. Yamschikov,[1] Alexander G. Osipenko,[2] Mikhail V. Kormilitsyn[2]

[1] *Department of Rare Metals and Nanomaterials, Institute of Physics and Technology, Ural Federal University, Ekaterinburg, 620002, Russia*
[2] *State Scientific Center "Research Institute of Atomic Reactors", Dimitrovgrad, 433510, Russia*
e-mail: v.a.volkovich@urfu.ru

Pyrochemical reprocessing of spent nuclear fuels (SNF) employing molten salts and liquid metals as working media is considered as a possible alternative to the existing liquid extraction (PUREX) processes. Liquid salts and metals allow reprocessing highly irradiated high burn-up fuels with short cooling times, including the fuels of fast neutron reactors. Pyrochemical technology opens a way to practical realization of short closed fuel cycle.
Liquid low-melting metals are immiscible with molten salts and can be effectively used for separation (or selective extraction) of SNF components dissolved in fused salts. Binary or ternary alloys of eutectic compositions can be employed to lower the melting point of the metallic phase. However, the information on SNF components behaviour and properties in ternary liquid metal alloys is very scarce.
In the present study solubility of uranium (primary fissile material) were determined in liquid Ga, In and their alloys (containing 21.8, 40 and 70 wt. % In) over 800 degrees range. The alloy containing 21.8 % In represents the eutectic composition with the lowest melting point of 289 K (16 ^{o}C) in the binary Ga–In system. Solubility of uranium was determined using four different techniques: from the difference of activity and activity coefficients determined by electromotive force measurements; by filtering supersaturated alloys; by precipitation of intermetallic compounds from supersaturated alloys; and by centrifuging supersaturated alloys.
Solubility of uranium in individual liquid gallium and indium is presented in Fig. 1. The proposed liquidus line in the Ga-rich region of Ga-U binary phase diagram [1] gives considerably higher uranium solubility than was obtained from the results of experimental measurements in the present work. In-U binary phase diagram is not known and there is only a part of liquidus line from the indium side [1]. Fig. 1 shows that the proposed line agrees well with the results obtained in the present work. Solubility of uranium (in molar fractions) in Ga and In can be expressed by the following equations.
Gallium based alloys:

$$\lg X_{U(Ga)} = 0.4074 - 2954.2 / T \quad (600–1073\ K)$$
$$\lg X_{U(Ga)} = -2.5051 - 1218.4 / T \quad (296.5–600\ K)$$

Indium based alloys:

$$\lg X_{U(In)} = 3.2059 - 6445.7 / T \quad (780–1069\ K)$$
$$\lg X_{U(In)} = -0.3722 - 3610.7 / T \quad (607–780\ K)$$

Solubility of uranium in Ga-In alloys depends on the alloy composition, Fig. 2. Increase of indium content in the alloy results in lowering uranium solubility. Solubility of uranium in the studied alloys is described by the following equations.
Ga-21.8 wt.% In:

$$\lg X_U = -0.1693 - 2839.3 / T \quad (530–1076\ K)$$
$$\lg X_U = -3.8033 - 930.85 / T \quad (297–530\ K)$$

Ga-40 wt.% In:

$$\lg X_U = 2.1594 - 5253.8 / T \quad (710–985\ K)$$
$$\lg X_U = -3.3337 - 1380.3 / T \quad (446–710\ K)$$

Ga-70 wt.% In:

$$\lg X_U = -0.229 - 3793.9 / T \quad (680–1060\ K)$$
$$\lg X_U = -4.8354 - 635.8 / T \quad (470–608\ K)$$

X-ray diffraction analysis of the intermetallic compounds precipitated from the Ga-In alloys showed that all of them were isostructural with UGa_3 phase. Increasing indium content in the starting allow to 70 wt.% (58.6 at.%) resulted in a very minor change of the lattice parameter from 4.251 Å for the phase formed in Ga to 4.255 Å for the phase formed in Ga-70 wt.% In alloy. For comparison, the lattice parameter of UIn_3 phase (also isostructural with UGa_3) is 4.601 Å. This indicates that uranium in Ga-In alloys predominantly interacts with gallium.
To check this assumption activity of uranium was measured in liquid gallium, indium and Ga-In alloys. The results are presented in Fig. 3. Activity of uranium in liquid indium is considerably higher than in gallium and Ga-In alloys. Moreover, uranium activity in Ga-In alloys containing up to 40 wt.% indium is very close to that in pure gallium. Only in Ga-70 wt.% In alloy activity of uranium is somewhat higher at higher temperatures (above 670 K); on lowering the temperature this difference becomes smaller and below 600 K activity of uranium in Ga and studied Ga-In alloys becomes virtually identical. This again confirms predominant interaction of uranium with gallium.

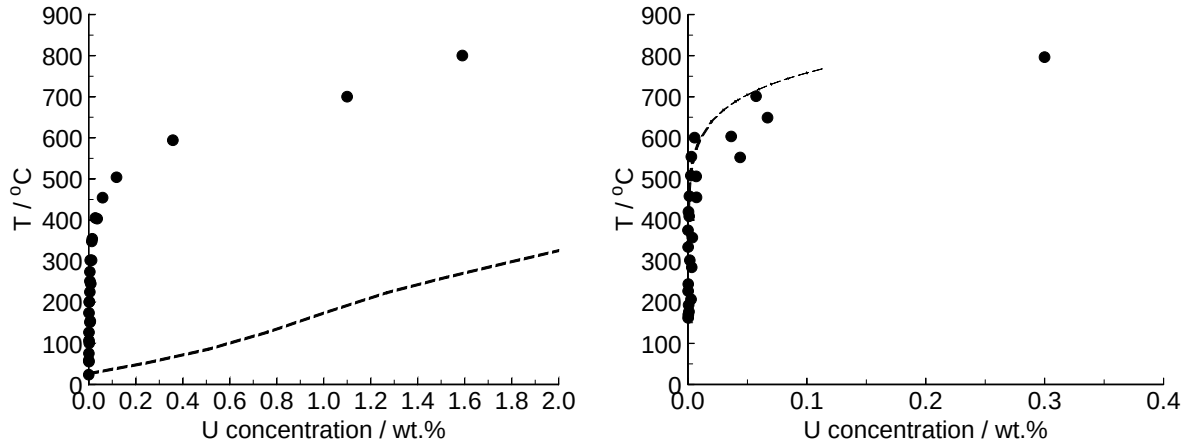

Fig. 1. Solubility of uranium in liquid gallium (left) and indium (right). Symbols show experimental data obtained in the present work, lines – proposed liquidus lines in U-Ga and U-In binary systems [1].

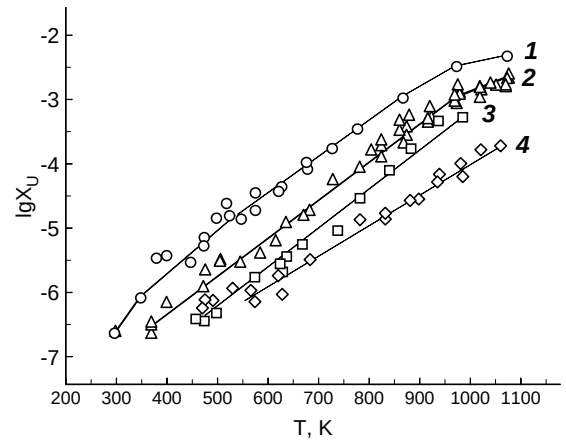

Fig. 2. Solubility of uranium in liquid gallium (1) and Ga-In alloys (2–4). Indium content of the alloys, wt.%: 21.8 (2), 40 (3), 70 (4).

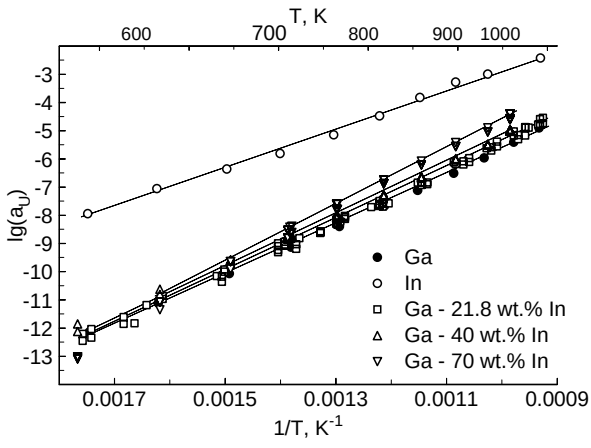

Fig. 3. Activity of uranium in liquid gallium, indium and Ga-In alloys (composition is shown for each set of data)

Acknowledgements
The work was partially supported by Russian Ministry of Education and Science (grant N976.42G.041/14).

References
[1] ASM Binary Phase Diagrams. ASM International (1996).

Conceptual study of multiphase structure of high uranium density alloys to reduce chemical interaction

A. Savchenko

A.A. Bochvar Institute of Inorganic Materials (VNIINM), P.O.Box 369, Rogova Street 5A, 123060, Moscow, Russia
e-mail : sav-alex111@mail.ru

The basic factor that limits the serviceability of fuel elements developing in the framework of RERTR Program (transition from HEU to LEU fuel of research reactors) is interaction between U10Mo fuel and aluminium matrix [1]. Interaction results in extra swelling of fuels, disappearance of a heat conducting matrix, a temperature rise in the fuel centre, penetration porosity, etc. Several methods exist to prevent fuel-matrix interaction. In terms of simplifying fuel element fabrication technology and reducing interaction, doping of fuel is the most optimal version.

We developed a concept of U-Mo fuel alloying that consists in producing an alloy of the two or multiphase structure, viz., basic γ(U-Mo) and intermetallic phases [2]. The alloys should be of eutectic type for strengthening interatomic bonds and stabilization of γ(U-Mo) phase. The intermetallic phase shall have the maximal density of uranium, low molybdenum content, be well compatible with aluminium, highly irradiation resistant and precipitate along grain boundaries. The latter condition allows fuel particle production via grinding. After grinding the weakly interacting with Al intermetallic phase is primarily available at the fuel particle surfaces, forming some kind of a protection barrier.

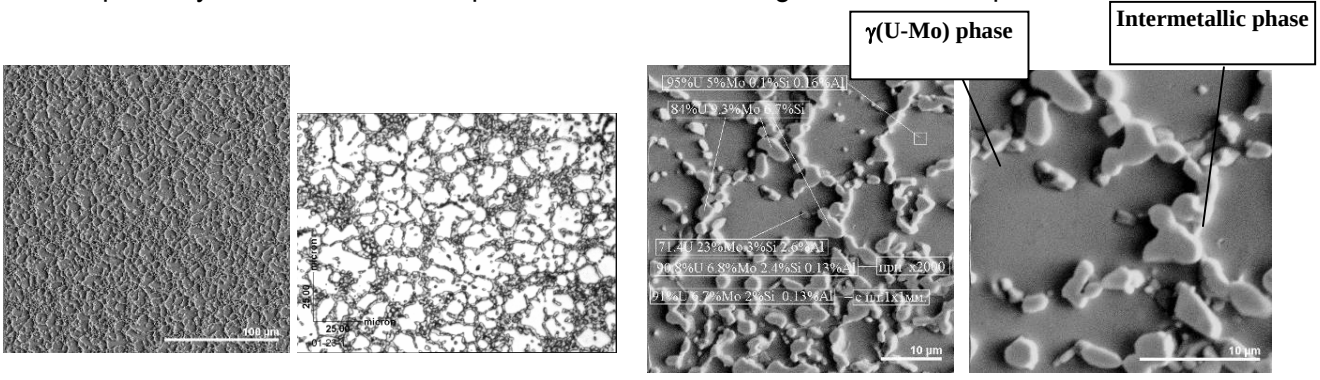

a) **b)**

Fig.1. Structures of alloyed UMo two-phase alloy; a – U + 5.7Mo + 0.9Si; b – U + 6.3Mo + 0.9Si + 0.15Al.

Using casting and powder metallurgy methods a group of alloys were fabricated with additives of Si (0.8-1.5%) as well as Si plus Al (1.2% in total) and various Mo content within 5 to 9%.

After casting some alloys were annealed at 500^0C for 4 hours to study stability of γ(U-Mo) phase. Microstructures of two alloys (U+5.7%Mo+1.04%Si – weight percent) as well as (U+6.3%Mo+0.9%Si+0.15%Al) are shown in the figure 1. It consist of mainly of 2 phases: γ(U-Mo) phase containing 5% of Mo and 0.1% of Si and intermetallic ternary phase U-9.3Mo-6.7Si, probably $(UMo)_3Si_2$. It should be mentioned that gamma phase did not decompose after annealing in spite of low Molybdenum content.

Under compatibility testing after anneal at 600^0C for 6 hours the intermetallic phase weakly interacting with aluminium strongly reduced interaction. The interaction was small in comparison with standard fuel – granules of U-10Mo alloy, and of a nodular mode. The acquired results indicate the feasibility of diminishing the interaction through this method.

Principally novel results were received for stabilizing γ-(U-Mo) phase with low uranium content in eutectic type alloys by the third neutral stabilizing element. It can be explained by additional stabilizing impact of Mo located not only in γ-(U-Mo) phase, but also in intermetallic phase.

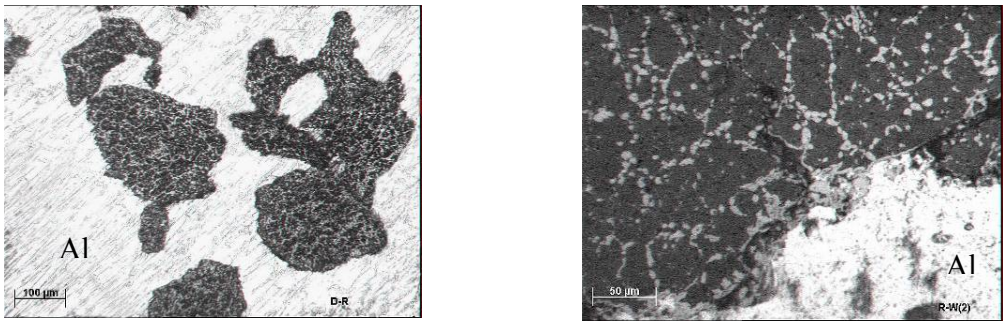

a) **b)**

Fig.2. Microstructure of fabricated fuel composition with UMo alloy, a – (U+5.7Mo+1.04Si) + Al as fabricated; b – (U+6.3Mo+0.9Si+0.15Al) + Al - 6 hours annealed at 600 °C.

To eliminate the molybdenum leaving from the γ-U phase for the intermetallic phase, depleting in this way the γ phase solid solution in Mo, a thermodynamic analysis using phase diagrams was implemented. As a rule, the alloying of UMo alloy with elements that form intermetallic compounds with uranium leads to the undesired type of the phase diagram with ternary intermetallic phases that comprise molybdenum, e.g., U-Mo-Al, U-Mo-Si, U-Mo-Sn etc systems (Fig. 3a). For molybdenum not to enter an intermetallic phase but to remain in a solid solution with uranium, the type of the phase diagram (Fig. 3b) has to be realized, where the phase triangle is restricted by U-U_2Mo-UX phases, where UX is a binary intermetallic compound of uranium and an alloying element. This version is feasible in the U-Mo-C system (Fig. 3b) in which theoretically ternary compounds must not form close to the uranium angle of the phase diagram. This can be confirmed by forming carbide phase inclusions along the grain boundaries of the γ-solid solution in U-10Mo alloy with carbon impurities. These carbon phase inclusions did not contain molybdenum.

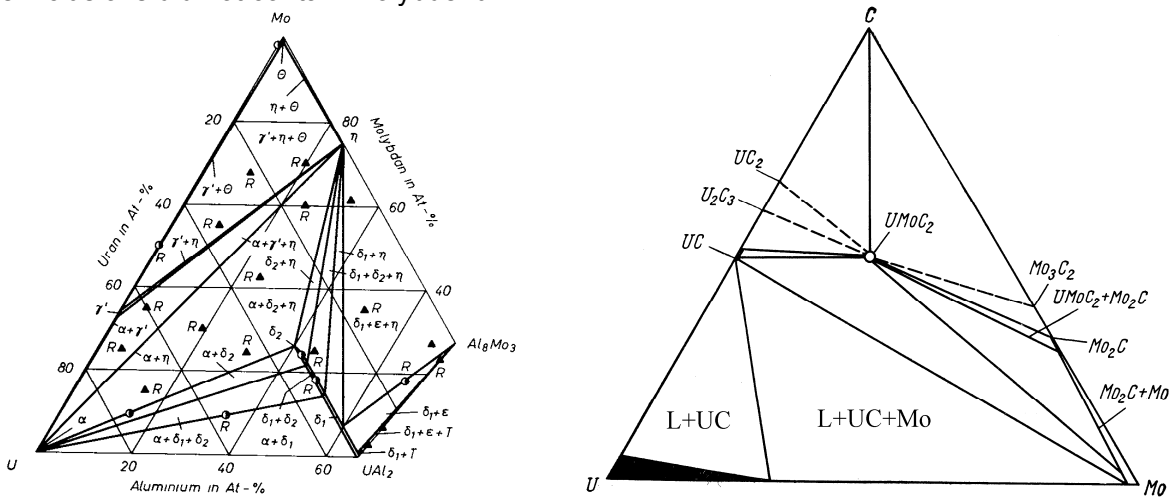

a) **b)**

Fig. 3. Types of phase diagrams of UMo alloy with elements that form intermetallic compounds with uranium, a – system with ternary compounds (U-Mo-Al) [3], b – isothermal section of U-Mo-C phase diagram at 1500 °C.

References

[1] G.L. Hofman, M.R. Finlay, Y.S. Kim, H.J. Rue and J. Rest "Observations of the Nucleation and Evolution of Porosity in U-Mo Fuels", Proc. 2005 International Meeting on Reduced Enrichment for Research and Test Reactor, Nov. 6-11, 2005, Boston, USA.

[2] A. Savchenko, E. Malamanova, I. Konovalov, Y. Petrov. Novel Trends in Fuel and Matrix Alloying to Reduce Interaction, Proceedings of the Research Reactor Fuel Management (RRFM-2007) Conference, Lion, France, 11.03-14.03.2007, available through the European Nuclear Society (ENS) website.

Fuel Cycle Concept with Advanced METMET and Composite Fuel in LWRs

A.Savchenko, M.Skupov, A.Vatulin, A.Glushenkov, G.Kulakov, K.Lipkina

A.A. Bochvar Institute of Inorganic Materials (VNIINM), P.O.Box 369, Rogova Street 5A, 123060, Moscow, Russia
e-mail : sav-alex111@mail.ru

Generation II Light Water Reactors (LWRs) are the dominant world commercial nuclear power plant. Currently, 90% of the installed reactors worldwide operate on a once-through nuclear fuel cycle, utilizing uranium dioxide fuel. To optimize the fuel cycle MOX fuel has been considered for thermal reactors, although some limitations exist, that make MOX fuel be used only in one fuel cycle. The most relevant are: the degradation of Pu isotopic vector, the insufficient uranium density, high operating fuel temperature and the low serviceability under transients.
We suggest replacing the container design fuel rod, for which possibilities are practically exhausted, by dispersion type fuel elements. Structurally, advanced METMET dispersion type fuel consists of uniformly distributed higher density fuel granules of U-Mo, U-Nb-Zr or U_3Si alloys that are metallurgically bonded between themselves and to fuel cladding with specially developed Zr-based matrix alloys. A fuel meat retains controllable porosity in the range of 16- 38% to accommodate fuel swelling [1-2].

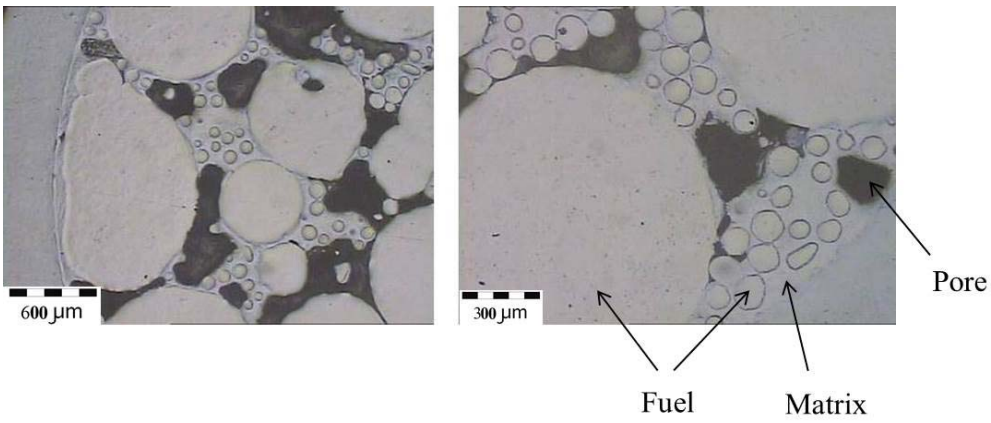

Fig. 1. Microstructure of modified composite fuel with higher uranium content. Conditions: 72% volume fraction of fuel under the cladding, technological parameters: t = 900°C and τ =60 s, fuel column length: 800 mm.

The primary advantages of advanced METMET fuel for application in thermal reactors are high uranium content (25-50% higher in comparison with the standard UO_2 pelletized fuel rod), low temperature of fuel (<500 ºC, cold fuel), the extension of burn-up (100 MW*d/kgU) and serviceability under transient conditions.
Due to high uranium content and hence intermediate neutron spectrum the main economically significant characteristics for PWR's can be improved:
1. Larger quantities of generated plutonium (~2.5-3 times higher).
2. Increasing of fissionable plutonium isotopes up to 75-78% in spent fuel (harder neutron spectrum).
3. Increasing the breeding ratio up to 0.7-0.8 (by reducing the hydrogen-to-heavy metal ratio).
4. The prolongation of the campaign will be more than 30% in effective days (up to 500 additional effective days).
5. Increasing the time between refueling, in other words, increasing the Unit Capacity Factor (UCF). In this case instead of a year or a year and a half fuel cycle at two year cycle becomes feasible.

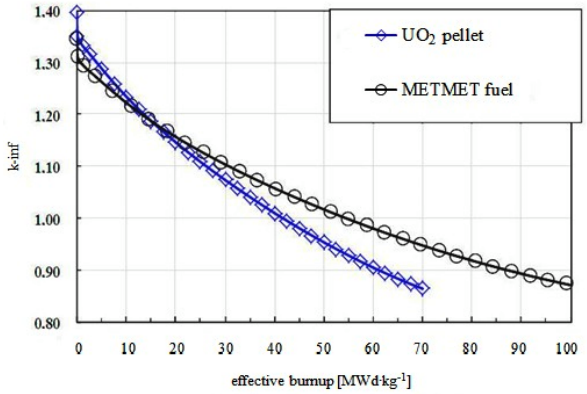

Fig. 2. K-inf versus effective burn-up for UO_2 and advanced METMET fuel

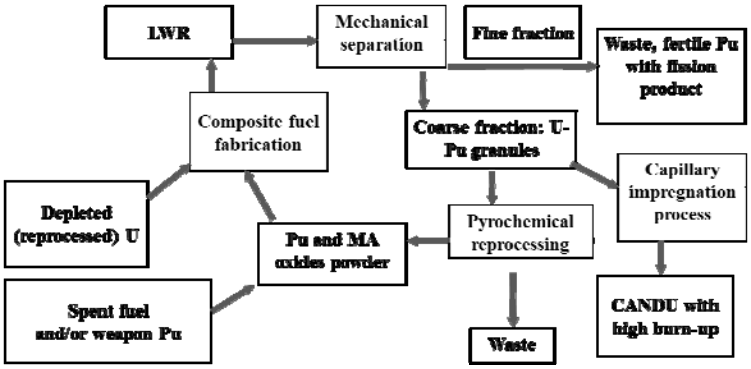

Fig. 3. LWR fuel cycle with composite fuel and multiply recycling of Pu

On the basis of METMET fuel, composite U(Th)-PuO_2 fuel (an analogue of MOX) can be fabricated where depleted uranium alloy and dioxide plutonium powder have initially separate arrangement [1-2]. The fuel element development approach consists of individual operations used to fabricate a fuel element with uranium as the main component and to fill it with plutonium dioxide powder, which minimizes dust producing operations on the fuel element fabrication. According to new fuel element design, a framework fuel element having a porous uranium alloy meat (U-Mo or U-Zr alloys) is filled with standard PuO_2 powder of less than 70 micron fraction prepared by pyrochemical or other methods. In this way a high uranium content fuel meat metallurgically bonded to cladding forms a heat conducting framework, pores of which contain PuO_2 powder. Instead/or in combination with Pu dioxide powder, other MA oxides can be used based on Am and Np. This approach can be also implemented with the use of Th granules in place of depleted uranium alloy granules. In this case the conversion ratio is increased.

Due to this as compared to MOX fuel the new one features higher thermal conductivity, higher uranium content, hence, high conversion ratio, does not interact with fuel cladding and fabrication technology is more environmentally clean. Composite fuel is intended for use in thermal and fast reactors as it features higher characteristics in comparison to MOX or metallic (U-Pu-Zr) fuel.

Mechanism of composite fuel operation: first PuO_2 burns up in metmet fuel form while Pu generates in the metmet fuel that first serves as a breeding blanket and then begins to burn up. Consequently, the components of the composite fuel have different Pu isotope compositions at the cycle end. The plutonium dioxide powder will basically accumulate non-fissionable isotopes while the METMET fuel – fissionable species.

In composite fuel U alloy and PuO_2 powder have initially separate arrangement in a fuel composition, so we can separate fissile Pu from fertile one. Mechanically evoked from cladding granules of generated U-Pu alloy can be used repeatedly in PWR and CANDU reactors using capillary impregnation method as they have high content of generated Pu. Hence in comparison to MOX we can multiply use of generated Pu in spent fuel and instead of partial recycling implement full recycling which drastically reduces the fuel waste.

Thus, using novel concept based on high density dispersion and composite fuel the closed U-Pu cycle in thermal reactors can be implemented – as the fuel available to these reactors may be increased by ~48% (18% in case of MOX). The remained Pu fissile isotopes can be used from the accumulated thermal reactor spent fuels.

References

[1] A. Savchenko, A. Vatulin, K. Lipkina, G. Kulakov, et all, Journal of Progress in Nuclear Energy in press,1-7 (2013), http://dx.doi.org/10.1016/j.pnucene.2013.10.007.

[2] A. Savchenko, et all, Journal of Progress in Nuclear Energy **138-144**, 57 (2012).

Thermodynamic and transport properties of $U_3Cu_4Si_4$ and $U_3Cu_4Ge_4$

Oleksandr Bednarchuk,[1] Mathieu Pasturel[2], Dariusz Kaczorowski[1]

[1] *Institute of Low Temperature and Structure Research, Polish Academy of Sciences, P.O.Box 1410, 50-950 Wrocław, Poland*
e-mail: O.Bednarchuk@int.pan.wroc.pl
[2] *Laboratoire de Chimie du Solide et Matériaux, UMR CNRS 6226, Université de Rennes 1, Avenue du Général Leclerc, 35042 Rennes, France*

Uranium-based germanides and silicides containing d-electron transition elements continue to attract much research interest due to their unusual physical properties that are principally governed by the degree of localization of the 5f electrons that is largely dependent on the strength of their interactions with the conduction and valence electrons of neighboring atoms. The ternary compounds $U_3Cu_4Si_4$ and $U_3Cu_4Ge_4$ crystallize with the orthorhombic $U_3Ni_4Si_4$- and $Gd_3Cu_4Ge_4$-type structures, respectively, which are closely related to those of intensively studied phases UTX and UT_2X_2 (T stands for a transition metal, X = Si or Ge) [1]. In line with the structural relationship, also the magnetic properties $U_3Cu_4Si_4$ and $U_3Cu_4Ge_4$ are fairly similar to those of UCuX and UCu_2X_2 counterparts. Both compounds were reported to order magnetically at low temperatures and exhibit metallic electrical conductivity governed in their paramagnetic state by Kondo effect [1]. The subsequent studies, however, provided some mutually contradictory findings as regards the character of the ordered phases [2-3]. In the present work, we reinvestigated $U_3Cu_4Si_4$ and $U_3Cu_4Ge_4$ by means of detailed magnetization, heat capacity and magnetotransport measurements, aiming at verification of the reported data and possibly clearing up the controversies.

The silicide was reported to order antiferromagnetically at $T_N \approx 135$ K, and then to undergo another phase transition near $T_1 \approx 70$ K to a magnetic state bearing sizeable ferromagnetic component [1]. The more recent study [4] confirmed the presence of two anomalies in the temperature variations of the DC magnetization, and proved ferromagnetic-like nature of the low-temperature phase evident in the AC magnetic susceptibility data. Surprisingly, the neutron diffraction experiment performed down to 1.5 K did not reveal any change in the collinear antiferromagnetic structure that set in at T_N [4]. This finding implied that either the ferromagnetic component is too small to be detected by standard powder neutron diffraction or the bulk magnetic features near and below T_1 have just short-range character. In accord with the latter scenario, the corresponding peak in the AC susceptibility showed some frequency dependence, reminiscent of spin-glass behavior. Another result reported in Ref. 4 was a clear irreversibility effect between the magnetization curves measured as a function of magnetic field upon cooling the sample in zero (ZFC) and finite (FC) field. Unexpectedly, the onset in the ZFC-FC bifurcation, characteristic of ferromagnetic-like or spin-glass properties, was found at $T_2 = 145$ K, i.e. not only much above T_1 but also T_N. This fairly strange behavior remained unexplained so far.

Some new light on the magnetic behavior $U_3Cu_4Si_4$ has been shed by our reinvestigation of the compound. Our detailed measurements of the temperature- and field-dependent bulk magnetization mostly corroborated the key features reported in Refs. 1 and 4, and provided a complete characterization of the low-temperature magnetic behavior. The heat capacity studies revealed two lambda-type anomalies occurring at 128 K and 148 K (see the Figure). While the former peak can be related to the antiferromagnetic phase transition elaborated before, the latter one matches very well with the onset of the irreversibility in the magnetic data. Markedly, no anomaly in the specific heat was found near the hypothetical transition at T_1. Also, the electrical resistivity was found featureless at T_1, in agreement with the result published before [1]. In the magnetically ordered state, the transverse magnetoresistance of $U_3Cu_4Si_4$ is negative and very small. It systematically increases with decreasing temperature and reaches a value of about -0.9% at 2K in a magnetic field of 9 T.

In contrast to $U_3Cu_4Si_4$, the magnetic properties of $U_3Cu_4Ge_4$ appear comprehensible. The compound was reported to order ferromagnetically below T_C = 67 K [1,2]. The ferromagnetic state was then confirmed in neutron diffraction experiment [3] that was interpreted in terms of collinear arrangement of uranium magnetic moments directed along the a-axis. Interestingly, despite the presence of two inequivalent U atoms in the $Gd_3Cu_4Ge_4$-type crystallographic unit cell, characterized by notably different coordination polyhedra [2], the magnetic moments associated with these sites have the same magnitude [3]. As shown in the Figure, the magnetic phase transition in the germanide manifests itself as a pronounced peak in the heat capacity. The onset of the ferromagnetic state results in a rapid drop in the electrical resistivity, due to suppression in spin-disorder scattering. In the ordered region, both the specific heat and the electrical transport of $U_3Cu_4Ge_4$ show evidence of sizable contributions due to magnon excitations.

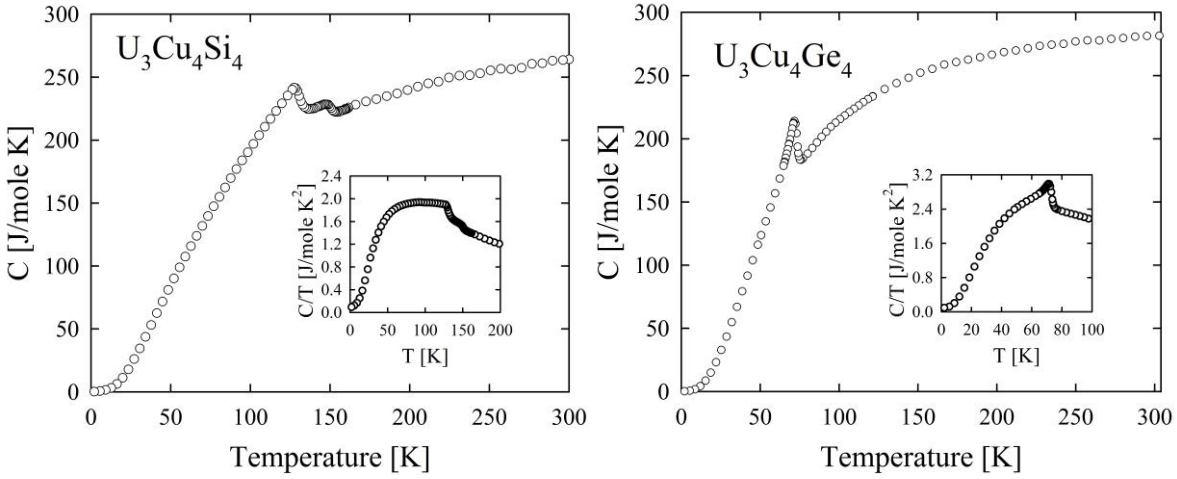

References

[1] D. Kaczorowski et al., *Physica B* **206&207** (1995) 457.
[2] S. Pechev et al. *J. Alloys Compd.* **243** (1996) 77.
[3] S. Pechev et al., *J. Alloys Compd.* **271-273** (1998) 448.
[4] S. Pechev et al., *J. Magn. Magn. Mater*. **191** (1999) 282.

A self-consistent thermodynamic modeling of thermal and elastic properties of $PuCoGa_5$ and $PuRhGa_5$

Filanovich A.N., Povzner A.A, Nogovitsyna T.A.

Physics department, Ural Federal University, Mira st, 19, Ekaterinburg, 620002, Russia
e-mail: a.n.filanovich@urfu.ru

The 115-family superconducting compounds based on actinides attract extensive attention of the scientific community. This is caused by that the most well-known representative of this family – $PuCoGa_5$ possess an anomalously high value of the transition temperature to the superconducting state (T_c~18,5 K) and the question about the nature of the superconductivity in $PuCoGa_5$ remains open. In order to answer the question, which physical mechanisms cause the unusual properties of the 115-family compounds, besides studying their magnetic and electrical properties, it is necessary to investigate their thermal and elastic properties. In the present study we develop a self-consistent thermodynamic model [1] for the $PuCoGa_5$ and $PuRhGa_5$ compounds, which enables to account for the impact of phonon anharmonicity. In the framework of this model we have calculated the temperature dependencies of the thermal and elastic properties of $PuCoGa_5$ and $PuRhGa_5$.

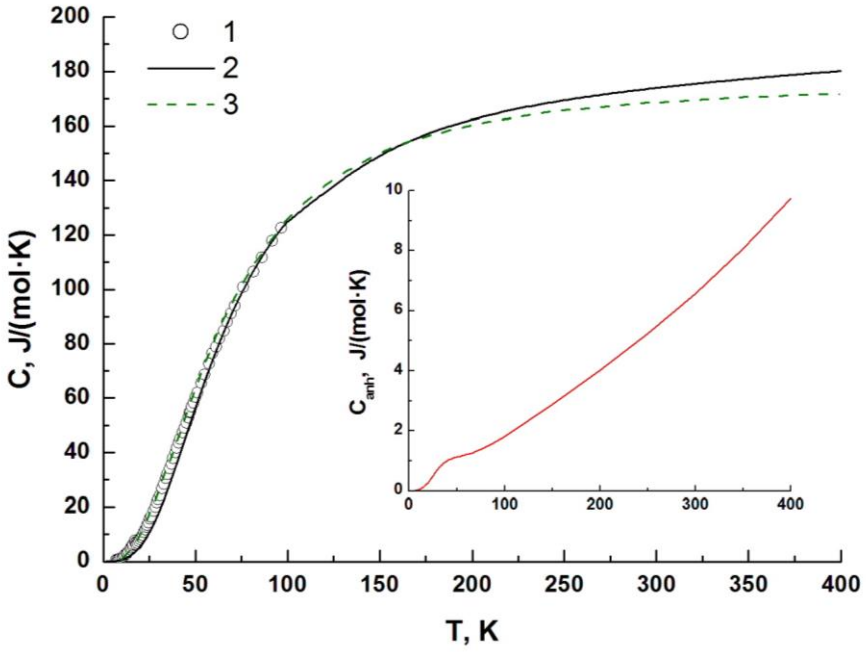

Fig. 1. Temperature dependence of molar heat capacity of $PuCoGa_5$: 1 – experimental data [2], 2 – lattice heat capacity C_p obtained in the present study, 3 – lattice heat capacity at constant volume C_v obtained in [3]; inset – the contribution of phonon anharmonicity to the specific heat of $PuCoGa_5$

The calculated temperature dependencies of the lattice specific heats C_p of $PuCoGa_5$ and $PuRhGa_5$ are shown in Fig. 1 and 2 in comparison with the experimental data [2]. Also in Fig. 1 we show the lattice specific heat at constant volume C_v of $PuCoGa_5$ obtained in [3] by using the ab initio calculated phonon spectra of $PuCoGa_5$. One can see that at low temperatures the lattice heat capacity C_p, calculated in the present study, is in good agreement with the results [3] on the C_v. However, as the temperature increases, a contribution to specific heat associated with the phonon anharmonicity begins to appear, leading to divergence of our calculation of C_p (anharmonicity included) and the calculation [3] of C_v. To underline the effect of anharmonicity in inset to Fig. 2 we show the temperature dependence of this

phonon anharmonicity contribution to the specific heat capacity of $PuCoGa_5$, which was calculated as the difference C_p–C_v (both calculated in the present study). From Fig. 1 and 2 it also follows that the experimental specific heats of $PuCoGa_5$ and $PuRhGa_5$ can be almost completely described by the lattice contribution. This can be explained as follows. Each unit cell of $PuMGa_5$ contains five atoms of Ga, which have small electronic heat capacities (as compared to Pu and Co), while having a "normal" (roughly the same as Pu and Co) lattice heat capacities. Thus the total lattice heat capacity of $PuMGa_5$ is essentially larger than its total electronic heat capacity.

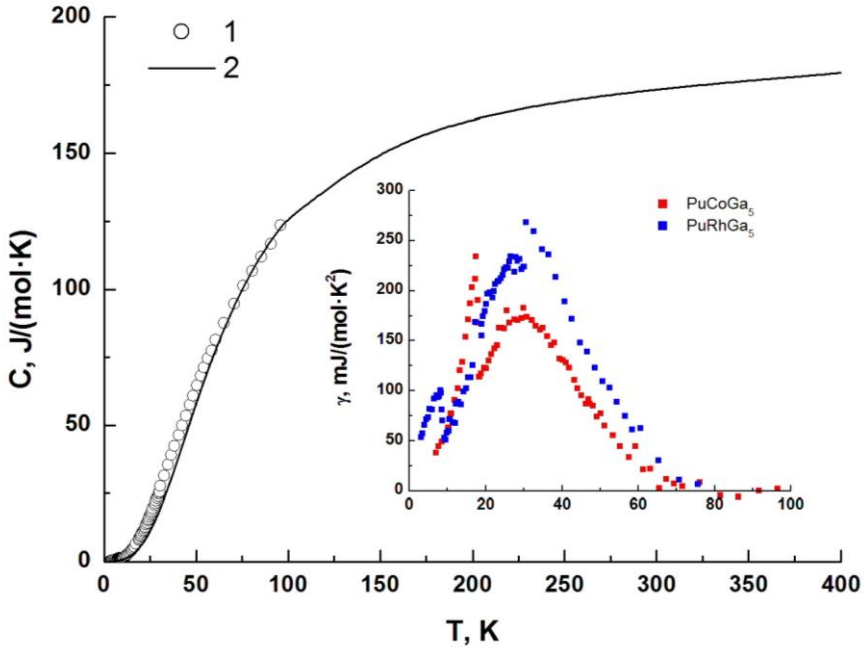

Fig. 2. Temperature dependence of molar heat capacity of $PuRhGa_5$: 1 – experimental data [2], 2 – lattice heat capacity C_p obtained in the present study; inset – the coefficients of electronic heat capacities

The coefficients of electronic heat capacities γ of $PuCoGa_5$ and $PuRhGa_5$ obtained by subtracting the calculated C_p from the experimental data are shown in inset to Fig. 2. One can see the peaks corresponding to the phase transitions to the superconducting state and that for both compounds γ has a complicated nonlinear dependence on temperature, which, however, does not change significantly when going from $PuCoGa_5$ to $PuRhGa_5$. The values of γ estimated in [2] are within the range 80-150 mJ/(mol·K^2), which in general is consistent with the values obtained in the present study. Further we have calculated the temperature dependencies of bulk modulus, thermal expansion coefficient and Debye temperature of $PuCoGa_5$ and $PuRhGa_5$.

References

[1] A. Filanovich, A. Povzner. *Journal Of Nuclear Materials* **437**, 102 (2013).

[2] P. Javorsky et al. *Physical Review B*. **75**, 184501 (2007) and references therein.

[3] P. Piekarz et al. *Physical Review B.* **72**, 014521 (2005).

Ab initio atomistic thermodynamics of water reacting with UO_2 surfaces

Pablo Maldonado[1], Lena Zetterstöm Evins[2], Peter M. Oppeneer[1]

[1] *Department of Physics and Astronomy, Uppsala University, Box 516, S-75120 Uppsala, Sweden*
[2] *Swedish Nuclear Fuel & Waste Management Co., Blekholmstorget 30, SE-10124 Stockholm, Sweden*

e-mail: peter.oppeneer@physics.uu.se

The dissolution of UO_2 surfaces in ground waters is important for the long-term "safe" storage of spent nuclear fuel in deep-underground geological repositories. Utilizing first-principle simulations [based on density functional theory (DFT) corrected for on-site Coulomb interactions (DFT+U)], we develop a model to explain the experimental stability in solution of materials having the fluorite structure (which is the crystal structure of the most common nuclear fuel UO_2). It is shown that the stability of a surface is mainly dependent on its atomic structure and the presence of sites where atoms are deficiently bonded. Hence, we are able to predict the surface formation energy and the surface energy of any high Miller-indexed plane. Comparisons with experimental results performed on surrogate fluorite materials CaF_2 and CeO_2 show a correlation between the trends of dry surface energies and surface stabilities during dissolution of both CaF_2 and CeO_2, even though the chemical processes of dissolution of CeO_2 and CaF_2 are different [1].

Moreover we study the thermodynamics of water reacting with flat and with stepped UO_2 surfaces, using the DFT+U method in combination with ab initio molecular dynamics simulations (AIMD) to capture the temperature dependence of the reaction. We compute the pressure-temperature phase diagrams and establish the thermodynamic boundaries that govern the feasibility of water adsorption at these surfaces. Effects of water coverage on the surface adsorption reaction have been taken into account. We find that the dissociative adsorption reaction of water on stepped surfaces can be analyzed as two separated reactions, the dissociative water adsorption on the step edge and the water adsorption on the terrace. The most stable water adsorption upon modification of the water partial pressure and temperature is adsorption on the (211) step edge (see Fig. 1), followed by adsorption on the (221) step edge and being the least favorable for the (111) surface. We conclude that these UO_2 surfaces will always react with water at room temperature and atmospheric pressure, leading to water dissociation and a modification of the step morphology [2].

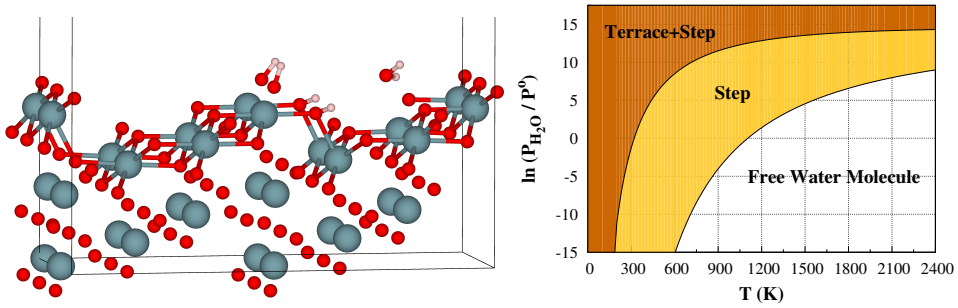

Fig. 1. Left: side view of the three-molecules water adsorption on the (211) UO_2 surface. Right: the computed pressure-temperature phase diagram of the reaction. The shadowed areas indicate the regions where the reaction is feasible, only at the step (yellow) or at the step and the terrace (brown).

References

[1] P. Maldonado, J. Godinho, L.Z. Evins, and P.M. Oppeneer, J. Phys. Chem. C **117**, 6639 (2013).
[2] P. Maldonado, L.Z. Evins, and P.M. Oppeneer, J. Phys. Chem. C, accepted (2014).

Electronic structure of Np_2Co_{17}, experimental and theoretical studies

A. HEN[1, 2], I. HALEVY[2, 3, 4], I. ORION[2], E. COLINEAU[1], R. ELOIRDI[1], J.-C. GRIVEAU[1], P. GACZYŃSKI[1], F. WILHELM[5], A. ROGALEV[5], J.-P. SANCHEZ[6], M. L. WINTERROSE[4], N. MAGNANI[7], A. B. SHICK[1, 8], aned R. CACIUFFO[1]

[1]European Commission, Joint Research Centre, Institute for Transuranium Elements, Postfach 2340, DE-76125 Karlsruhe, Germany
[2]Nuclear Engineering Department, Ben Gurion University, IL84105 Beer-Sheva, Israel
[3]Physics Department, Nuclear Research Center Negev, P.O. Box 9001, IL84190 Beer-Sheva, Israel
[4]California Institute of Technology, W. M. Keck Laboratory 138-78, Pasadena, California 91125, USA
[5]European Synchrotron Radiation Facility (ESRF), Boîte Postale 220, FR-38043 Grenoble, France
[6]SPSMS, UMR-E CEA/UJF-Grenoble 1, INAC, FR-38054 Grenoble, France
[7]Lawrence Berkeley National Laboratory, Chemical Sciences Division, 1 Cyclotron Road, Berkeley, California 94720, USA
[8]Institute of Physics, Academy of Sciences of the Czech Republic, Na Slovance 2, CZ-182 21 Prague, Czech Republic

We report the results of a study carried out on a neptunium-transition-metal binary compound Np_2Co_{17} that has been synthesized and characterized by means of Powder X-Ray Diffraction, ^{237}Np Mössbauer spectroscopy (Fig. 1), Superconducting-Quantum-Interference-Device magnetometry (SQUID, Fig. 2), and X-Ray Magnetic Circular Dichroism (XMCD, Fig. 3).
The compound crystallizes in a Th_2Ni_{17}-type hexagonal structure with room-temperature lattice parameters a = 8.3107(1) Å and c = 8.1058(1) Å.
Magnetization curves indicate the occurrence of ferromagnetic order below $T_C > 350$ K and a total magnetic moment of $\mu = 30.0(5)\ \mu_B$.
Mössbauer spectra suggest a Np^{3+} oxidation state ($5f^4$ configuration) and give an ordered moment of $\mu_{Np} = 1.57(4)\ \mu_B$ and $\mu_{Np} = 1.63(4)\ \mu_B$ for the Np atoms located, respectively, at the 2b and 2d crystallographic positions of the $P6_3/mmc$ space group.
Combining these values with a sum-rule analysis of the XMCD spectra measured at the neptunium $M_{4,5}$ absorption edges, allowed us to obtains the spin and orbital contributions to the site-averaged Np moment [$\mu_S = -1.88(9)\ \mu_B$, $\mu_L = 3.48(9)\ \mu_B$].
The calculated ratio between the expectation value of the magnetic-dipole moment and the spin magnetic moment ($m_{md}/\mu_S = +1.36$) is positive as predicted for localized *5f* electrons and lies between the values calculated in intermediate-coupling (IC) and jj approximations.
The expectation value of the angular part of the spin-orbit-interaction operator is in excellent agreement with the IC estimate. The ordered moment averaged over the four inequivalent Co sites, as obtained from the saturation value of the magnetization, is $\mu_{Co} \approx 1.6\ \mu_B$.
Experimental results are discussed against the predictions of first-principles electronic-structure calculations (Table 1) based on the spin-polarized local-spin-density approximation plus the Hubbard interaction [1].

Acknowledgement: "The high purity Np metals required for the fabrication of the compound were made available through a loan agreement between Lawrence Livermore National Laboratory and ITU, in the frame of a collaboration involving LLNL, Los Alamos National Laboratory and the US Department of Energy."

References
[1] I. Halevy et al. Phys. Rev. B. 85, 014434 (2012).

E-mail for corresponding author: amir.hen@mail.huji.ac.il

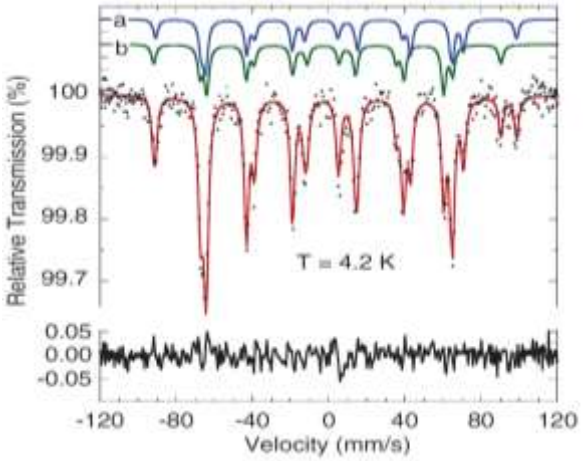

Fig. 1 ^{237}Np Mössbauer spectrum of Np_2Co_{17} taken at 4.2 K in the ferromagnetic state, red line – best fit to the data, given by the superposition of 2 sub-spectra (blue and green lines).

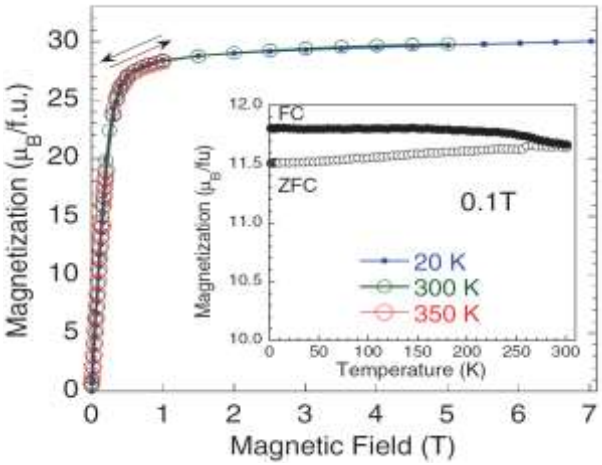

Fig. 2 Magnetic field dependence of Np_2Co_{17} magnetization measured in the range of 20-350 K. Inset – magnetization temperature dependence measured up to 300 K in a field μ_0H = 0.1 T in field cooled (FC) and zero-field cooled (ZFC)

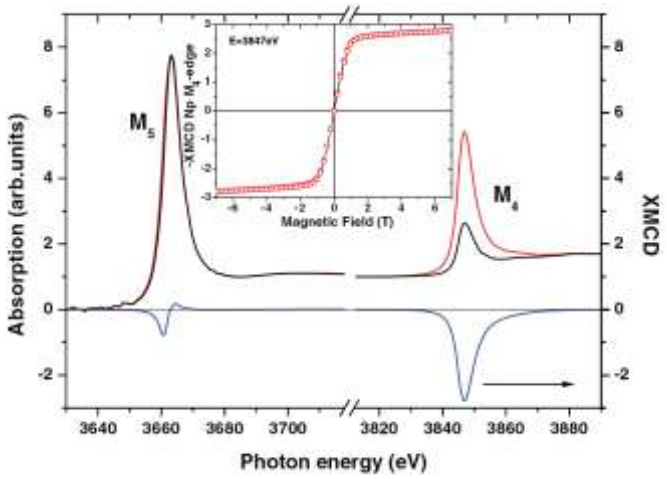

Fig. 3 X-ray absorption spectra $\mu^{+,-}$ measured at 50 K at the $M_{4,5}$ Np absorption edges in Np_2Co_{17}.
Red line - photon helicity parallel, black line - antiparallel with respect to a 7T magnetic field applied along the beam direction, Blue line - The XMCD signal, given by $\mu^+ - \mu^-$. Inset – field dependence of the XMCD signal at the M_4 edge.

		LSDA(+SOC)			AMF−LSDA+U			
Atom	Site	μ_S	μ_L	μ	μ_S	μ_L	μ	$\mu_{expt.}$
Np_1	2*b*	−3.15	1.97	−1.18	−1.96	3.50	1.54	1.57(4)
Np_2	2*d*	−3.14	1.87	−1.27	−2.09	3.94	1.85	1.63(4)
Co_1	4*f*	1.58	0.05	1.63	1.59	0.05	1.64	1.58
Co_2	6*g*	1.50	0.08	1.58	1.50	0.09	1.59	1.58
Co_3	12*j*	1.38	0.10	1.48	1.37	0.13	1.50	1.58
Co_4	12*k*	1.50	0.09	1.59	1.51	0.08	1.59	1.58
Total		17.56	5.26	22.82	20.14	9.12	29.26	30.0(5)

Table 1 Spin (μ_S), orbital (μ_L), and total ($\mu = \mu_S + \mu_L$) magnetic moments in the "muffin-tin" spheres around the Np and Co atoms (in μ_B units) together with total values (including interstitial contributions) per formula unit of μ_S , μ_L, and μ. Experimental values obtained from the ^{237}Np Mössbauer spectra and SQUID-magnetization measurements are given in the last column.

Recent progress in the investigation of the electronic and magnetic properties of $NpNi_5$

A. Hen,[1,2] E. Colineau,[1] R. Eloirdi,[1] J.-C. Griveau,[1] J.-P. Sanchez,[5] F. Wilhelm,[6] A. Rogalev,[6] A. B. Shick,[7] I. Halevy,[2,3,4] I. Orion,[2] and R. Caciuffo[1]

[1]European Commission, Joint Research Centre, Institute for Transuranium Elements, Postfach 2340, D-76125 Karlsruhe, Germany
E-mail: amir.hen@mail.huji.ac.il
[2]Nuclear Engineering Department, Ben Gurion University, IL84105 Beer-Sheva, Israel
[3]Physics Department, Nuclear Research Center Negev, P.O. Box 9001, IL84190 Beer-Sheva, Israel
[4]California Institute of Technology, W. M. Keck Laboratory 138-78, Pasadena, California 91125, USA
[5]SPSMS, UMR-E CEA/UJF-Grenoble 1, INAC, FR-38054 Grenoble, France
[6]European Synchrotron Radiation Facility (ESRF), B.P.220, F-38043 Grenoble, France
[7]Institute of Physics, Academy of Sciences of the Czech Republic, Na Slovance 2, CZ-182 21 Prague, Czech Republic

ReT_5 (Re = rare earth, T = Transition metal) compounds have been studied in the past in the frame of its magnetic properties (small Re to T stoichiometric ratio, large spontaneous magnetization and high Curie temperature) [1-2]. Extending these investigations to actinide analogues is interesting, as the wider radial extension of the *5f* electronic shell compared to the *4f* one should result in a larger inter-sublattice exchange interaction, and in non-negligible An-An exchange coupling. The spin-orbit interaction in the *5f* configuration for the actinide atoms is also larger than the *4f* spin-orbit interaction. For these reasons, a magnetic behaviour even richer than the one observed in the rare earth compounds is expected.

$NpNi_5$ [3] was synthesized by arc-melting and X-Ray powder diffraction enabled to confirm a $CaCu_5$ (D_{6h}) P6/mmm hexagonal crystallographic structure having one Np atom per unit cell, with room-temperature lattice parameters a = 4.8501 (5) Å and c = 3.9841 (5) Å. Physical properties were measured by the means of Superconducting – Quantum – Interference – Device (SQUID) magnetometry, ^{237}Np Mössbauer spectroscopy (Fig. 1), specific heat measurements (Fig. 2) and X-Ray magnetic circular dichroism (XMCD) (Fig. 3).

$NpNi_5$ is a ferromagnetic binary system, where the Np *5f* electrons seem to be essentially localized. Magnetization curves (not shown) indicate that $NpNi_5$ is a soft ferromagnet with a T_C ~16 K with a clear Curie–Weiss behaviour above T_C (μ_{eff} ~ 3.7 μ_B, θ_P ~ 14.6 K).
Mössbauer spectroscopy data (Fig. 1) suggests a Np^{3+} oxidation state ($5f^4$ electronic configuration), The hyperfine field inferred from the spectrum at 4.2 K (~439 T) yields an ordered moment at the Np site μ_{Np} ~ 2 μ_B. Comparison with saturated magnetization suggests an average moment of only 0.04 μ_B on the Ni sites.
The specific heat (Fig. 2) shows a clear and narrow anomaly at ~16 K corresponding to the onset of magnetic order. In applied magnetic fields the peak is shifted towards higher temperature and broadened (not shown), as expected for a ferromagnet. The magnetic transition can be extracted form the total specific heat by subtracting the phonons, electron, and nuclear contributions. Inset shows the low temperature part indicating the presence of the nuclear Schottky contribution.

In this communication we will present the results obtained (including preliminary data from XMCD) and discuss them in the light of theoretical considerations.

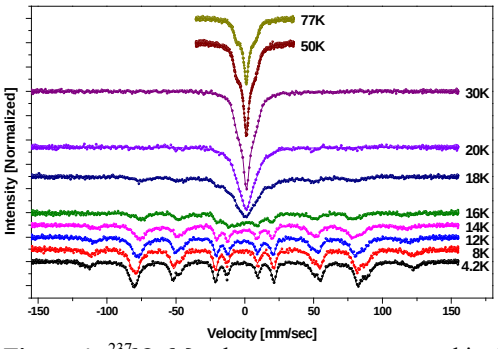

Figure 1: ^{237}Np Mössbauer spectra measured in the temperature range 4.2 - 77 K.

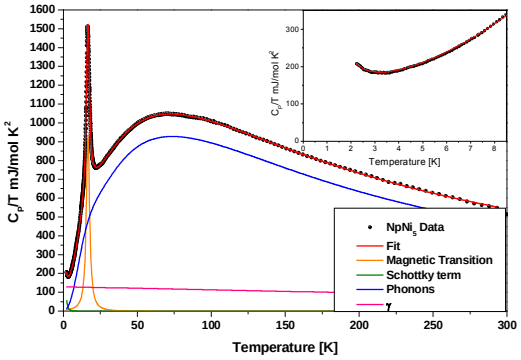

Figure 2: Normalized specific heat as a function of temperature, Solid lines – theoretical fit and its components. Insert – low temperature specific heat.

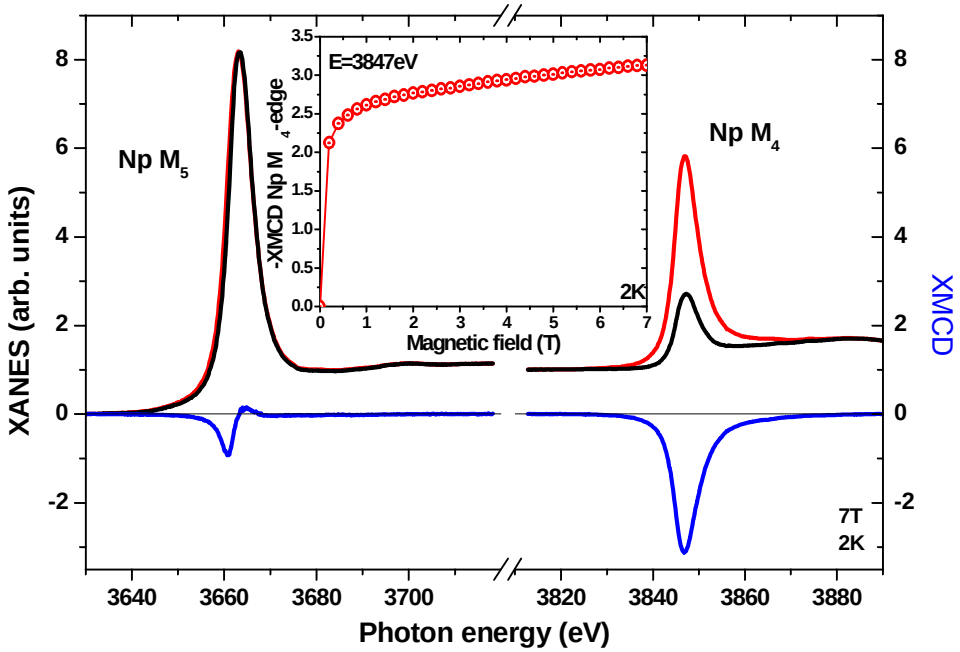

Figure 3: X-ray absorption spectra μ^+ (red line), μ^- (black line) measured at 2 K and H_{ext}=7 T at the $M_{4,5}$ Np absorption edges; Blue line – XMCD signal, inset – field dependence of the XMCD signal at the M_4 edge.

Acknowledgements

The high purity Np metals required for the fabrication of the compound were made available through a loan agreement between Lawrence Livermore National Laboratory and ITU, in the frame of a collaboration involving LLNL, Los Alamos National Laboratory and the US Department of Energy.

References

[1] S. Nasu *et al.,* Journal of Physics and Chemistry of Solids, **32**, 2779 (1971).
[2] R. M. Gale´ra *and* A. Rogalev, Journal of Applied Physics **85**, 4889 (1999).
[3] M. Akabori *et al.*, Journal of Alloys and Compounds **257** 268 (1997).

Mössbauer and NMR spectroscopy of $U_{0.15}Np_{0.85}O_2$

A. Hen,[1,2] L. Martel,[1] Y. Tokunaga,[3] E. Colineau,[1] J.-C. Griveau,[1] and R. Caciuffo[1]

[1]European Commission, Joint Research Centre, Institute for Transuranium Elements, Postfach 2340, D-76125 Karlsruhe, Germany
[2]Nuclear Engineering Department, Ben Gurion University, IL84105 Beer-Sheva, Israel
E-mail: amir.hen@mail.huji.ac.il
[3]Advance Science Research Center, Japan Atomic Energy Research Institute, Tokai, Ibaraki 319-1195, Japan

Actinide dioxides form solid solutions with each other and the resulting compounds retain the CaF_2 lattice structure, with the different actinide species randomly distributed over the anion sublattice. $U_{1-x}Np_xO2$ solutions are interesting to investigate due to the nature of two-ion interactions and for the possible exotic states which they may display.

The magnetic behavior of these compounds has been investigated by powder neutron diffraction, Mössbauer spectroscopy, and magnetic susceptibility measurements (see [1] for a comprehensive list of previous works on actinide dioxides and their solid solutions). The Np ions are tetravalent, with $5f^3$, $^4I_{9/2}$ electronic configuration, independently of temperature and composition. Magnetic order has been detected in all composition range, with T_N decreasing within the range $0 \le x \le 0.75$ and increasing within $0.85 \le x \le 1$: $T_N \sim 31$ K for x=0 (UO_2 orders antiferromagnetically, with a transverse noncollinear 3-**k** magnetic dipole structure accompanied by a similar order of electric quadrupoles), and $T_N = 25$ K for x = 1 (NpO2 develops a longitudinal 3-**k** order of triakontadipole, rank 5, magnetic multipoles accompanied by a similar order of electric quadrupoles).

The substitution of Np for U reduces the importance of dipolar exchange interactions, which eventually become irrelevant in the multipolar-ordered states. For x smaller than 0.4 the magnetic structure is transverse AF type I, like in UO_2, whereas for larger Np content the magnetic order is short range and incommensurate. The behaviour of T_N across the solid solution (Fig. 1), with a minimum for intermediate compositions, can be understood by observing that the primary order parameter (OP) is different in the two pure compounds. Hence, on both limits, the minority component acts as a dilution agent for the dominant two-ion interaction. The presence of several active degrees of freedom on U and Np ions and the richness of the associated interactions make it difficult to identify a unique model providing an overall unified description of $U_{1-x}Np_xO_2$ compounds, whose properties result from the subtle interplay between the intrinsic complexity of these materials and the effect of disorder.

Some qualitative observations can be formulated from a virtual-crystal-approximation (VCA) perspective. For $x \to 1$, U ions are particularly effective on the multipolar-ordered state since they act as dilution centres for the primary OP of NpO_2, being the corresponding ionic magnetic multipoles (MMP) quenched on these ions. On the contrary, the secondary quadrupolar OP does not experience dilution since the corresponding ionic moment is not quenched on U. On the opposite side, $x \to 0$, Np ions dilute neither the magnetic primary OP of UO_2, nor the secondary quadrupolar OP, but do of course modify the behaviour of pure UO_2 by their different single-ion response and two-ion interactions. In particular, the decrease of T_N with increasing x shows that the presence of Np ions destabilizes the magnetically ordered state. Even if calculations based on the VCA provide a qualitatively satisfactory theoretical framework, the properties of solid solutions with long-range magnetic order have not yet been completely understood, and neither are the short-range ordered intermediate-x compounds, where the effect of disorder is maximal and so is the competition between the different OPs of the pure compounds.

The study of the composition range $0.75 < x < 0.95$ is particularly interesting to understand where and how the MMP order of NpO_2 is eventually destabilized by U doping, therefore the intermediate composition $U_{0.15}Np_{0.85}O_2$ was produced and characterized by means of SQUID magnetization, NMR and ^{237}Np Mössbauer spectroscopy.

Magnetization and susceptibility measurements indicate that $U_{0.15}Np_{0.85}O_2$ undergoes an antiferromagnetic transition below $T_N \approx 17$ K (Fig. 2), Mössbauer spectra (inset of Fig. 3) in the paramagnetic phase consist of a single peak (as expected from the symmetry) centred at ~8.1 mm/sec, which corresponds to an isomer shift δ_{IS} ~ -5.5 mm/sec relative to the calibration standard $NpAl_2$ and indicates a Np^{4+} charge state ($5f^3$ electronic configuration).
At 17K, the spectrum broadened, indicating the proximity to a phase transition. Below this temperature, the spectra show a magnetically split, unresolved pattern. The spectra cannot be reproduced by assuming a simple static hyperfine magnetic field but may be accounted for by assuming dynamic effects (relaxation [2]). The fitted magnetic hyperfine field reaches 60 T at 4.2 K, which corresponds to a magnetic moment μ_{Np} (4.2 K) ~ 0.3 μ_B.
The transition is shown in the temperature dependence of field-sweep ^{17}O NMR spectrum by a broadening of the spectral lines below T_N (Fig. 4) confirming SQUID and Mössbauer data.

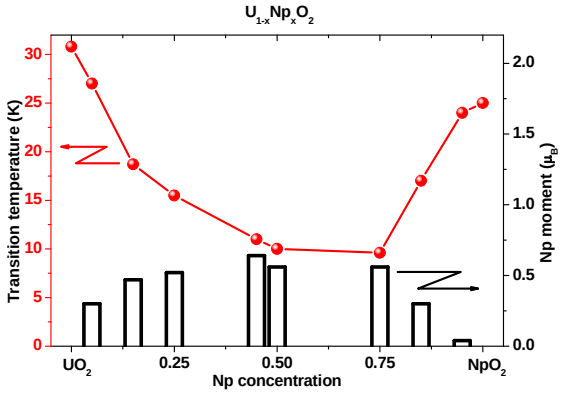

Fig. 1: Transition temperatures (red dots) and ordered Np moments (black bars) as a function of Np concentration (red line serves as guide for the eyes only). In all cases of data inconsistency between literature sources – values derived from Mössbauer spectroscopy were used.

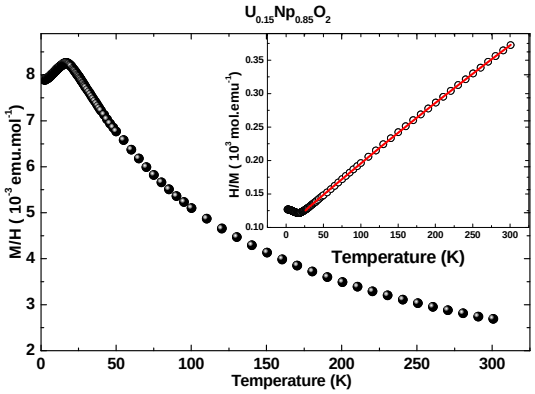

Fig. 2: Temperature dependence of the magnetic susceptibility indicating magnetic transition below $T_N \approx 17$ K, inset – fit of the data to the Curie–Weiss law.

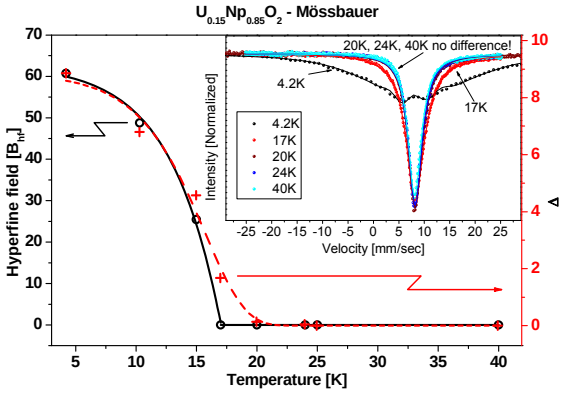

Fig. 3: Temperature dependence of the hyperfine field (Bhf) and the broadening parameter (Δ). Inset – Mössbauer spectra taken at typical temperatures.

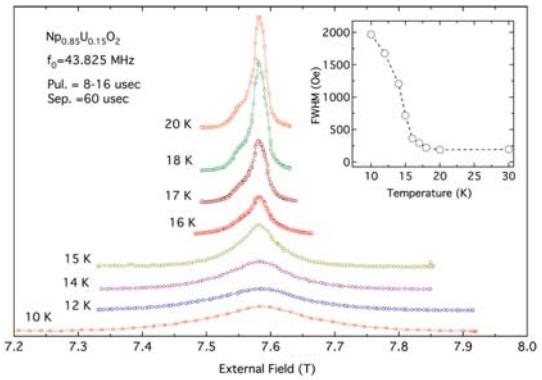

Fig. 4: Temperature dependence of field-sweep ^{17}O NMR spectrum.
Inset shows the temperature dependence of the full width at half maximum (FWHM)

References

[1] P. Santini et al, *Reviews of Modern Physics* 81, 807 (2009).
[2] A. Tabuteau et al., Solid State Comm. 50 (1984) 357.

Superconductivity of strongly correlated 5f- electron systems with a magnetic instability (on example of americium)

Volkov A.G., Oskina V.A., Povzner A.A.

Department of Physics, Ural Federal University, Mira str., 19, Ekaterinburg, 620002, Russia
e-mail: v.a.oskina@gmail.com

Strongly correlated 5f-metals and their compounds reveal a series of singularities specific to a number of high-temperature superconductors. The mechanism leading to their superconductivity is not identified. Andreev-reflection measurements indicate the d-symmetry of the superconducting order parameter and in formation of Cooper pairs the possibility of paramagnon mechanism.

As a part of s(p)df- model which Hamiltonian includes Hamiltonians of free s(p) -, d- and f-electrons and Hubbard interaction of d- and f-electrons conditions of the superconducting phase with singlet order parameter due to coherent scattering by spin-density fluctuations (FSD) were analyzed. Procedure of functional integration, based on Laplace transformation and used in the calculations of the statistical sum and in derivation of the scattering matrix, allow us to reduce the original multiparticle problem to the study of electron motion in fluctuating internal exchange and charge fields. Estimates of anomalous Green's functions are similar to calculations in the BCS theory. The main difference from the BCS procedure is the substitution of quantum-statistical averaging of phonon operators to functional integrals calculation for all possible configurations of stochastic exchange and charge fields.

Summation of series in perturbation theory at superconducting parameter of order was performed in the following hierarchy of characteristic lengths: $r_{SC} > r_c > r_e$, where r_e - electronic hopping length, r_c - correlation length of FSD, r_{SC} - the size of the Cooper pair. In these conditions, the single electrons move against the background of like set magnetic structure. At the same time electrons are combining into the Cooper pairs moving in different fluctuation volumes (in which the direction of the internal fields is opposite). It is shown that electron pairing occurs due to the transverse components of spin fluctuations.

It is shown that electron pairing occurs due to the transverse components of spin fluctuations. The presence of non-zero solution of the equation for the order parameter is the result of charge fluctuations induced by FSD. The most favorable case for the occurrence of the superconducting state due to the spin-fluctuation pairing is the occasion of negative values of the spin-stiffness coefficient (κ<0).

Quantitative analysis of obtained expressions for Am shows spin-fluctuation renormalization of the electron spectra, which leads to redistribution of electrons between the f-, d- and sp-states, significantly increase calculated values of superconductivity temperature [1]. Critical values calculations of temperature and magnetic field induction that associated with Am transition from normal into a superconducting phase was made on the base of the density of electronic states function and values U, ε_F. These values were found in the self-consistent calculation scheme of the electronic structure, the FSD amplitude and paramagnetic susceptibility. We established that in Am is implemented instability in the superconductivity formation of f-electron system. The calculated values of $T_C \approx$1K and $h_C \approx$0.1T are in a good agreement with experimental data [2]: T_C =0.67-0.8K and h_C = 0.075-0.1T. A shift of the Fermi level on a scale of energy to the right as well as to the left leads to a decrease of the calculated values with following conversion to zero.

References

[1] A.A. Povzner, A.N. Filanovich, V.A. Oskina et al., *Journal of Technical Physics,* **58**(12), 1844 (2013);

[2] A.A. Povzner, A.G. Volkov, P.V. Bayankin*, Journal of Low Temp. Phys.,* **23**, 792 (1997).

Magnetic susceptibility and features of electronic structure of $PuRhGa_5$

Povzner A. A., Volkov A. G., Golubeva L. R.

Department of Physics, Ural Federal University, Mira str. 19, Ekaterinburg, 620002, Russia
e-mail: a.a.povzner@ustu.ru

The existence of a crossover region of the superconducting and magnetically ordered states points to strong electron-electron correlations in the 5f-metals and their compounds [1]. A prominent place belongs to the Pu-115 superconducting compounds for their features possessed also by strongly correlated high-temperature superconductors (see, for example [2]). The assumption that electron pairing is due to phonon exchange and is describable in terms of the classical BCS theory does not agree with the experimental data on the temperature T_C [3, 1], while the dependence of the Andreev reflection points to the d-symmetry of the superconducting order parameter [4]. It is therefore expected that the superconductivity of these materials is due to the spin-fluctuation mechanism of Cooper pairing [5]. However, the electronic structure and its relationship with the magnetic subsystem of these compounds (in particular, the connection with the observed temperature dependence of the normal phase) have not been studied adequately.

In the present study, we develop a self-consistent model based on the LDA+U+SO method [6] for calculating the density of states, electron-electron interaction parameters and magnetic susceptibility. This model is then used for investigating spin fluctuations caused by the Hubbard interaction of the d-and f-electrons. To describe many-body electron-electron interactions, we use the Stratonovich-Hubbard transformation technique, which reduces the many-body problem to a study of non-interacting d,f-electrons in fluctuating exchange and charge fields. A method for calculating the partition function has been developed within the framework of the spin-fluctuation theory [7].

The density of states and the electron-electron interaction parameters have been calculated within the framework of the LDA+U+SO scheme on the LAPW basis supplemented by an agreement with the results of calculating the amplitudes of spin fluctuations and magnetic susceptibility. The results of calculating the electronic structure and magnetic susceptibility are shown in Fig. 1, 2. It is seen that the results are consistent with the experiment.

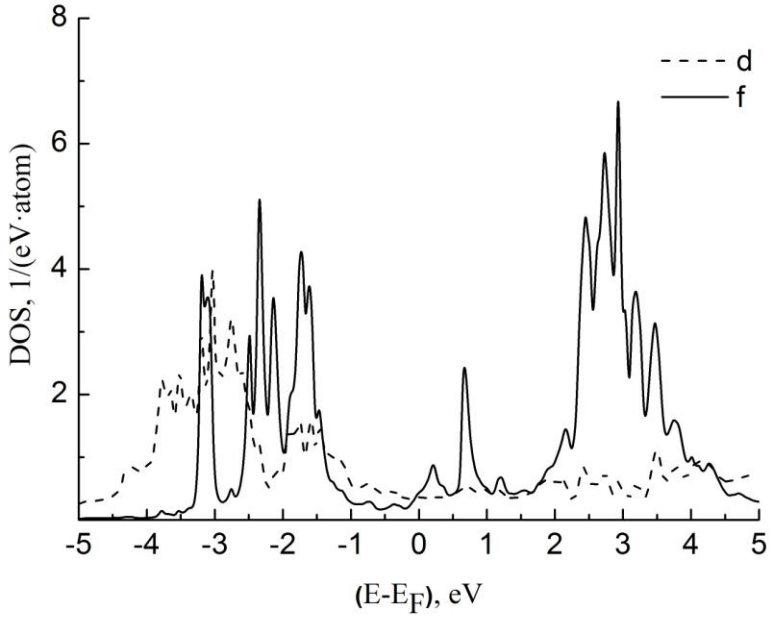

Fig. 1. Density of states of f- and d-electrons of $PuRhGa_5$. The origin of energy consideration corresponds to the location of the Fermi level.

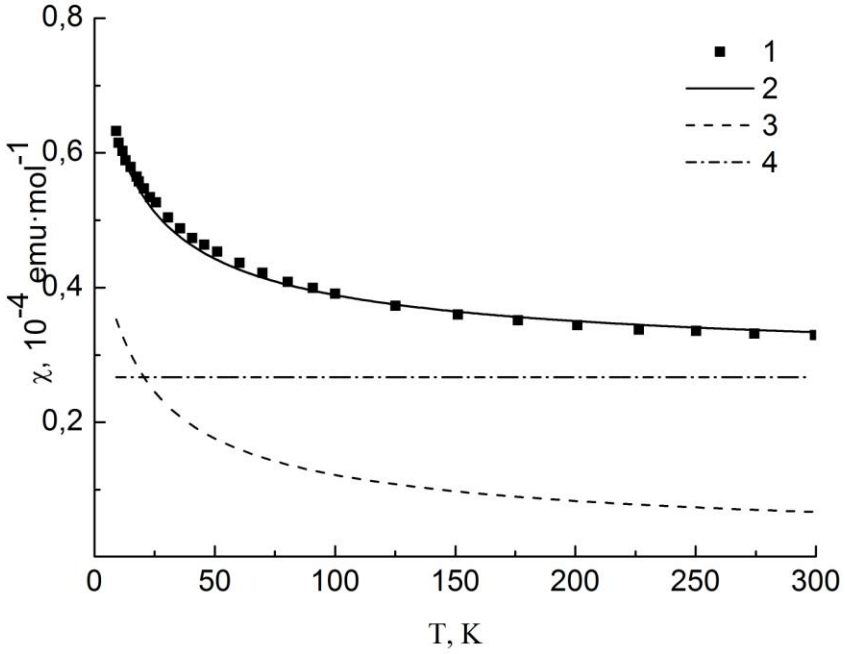

Fig. 2. Temperature dependence of the magnetic susceptibility of $PuRhGa_5$: 1 – the experimental data [5]; 2 – the magnetic susceptibility with respect to orbital contribution; 3 – spin susceptibility; 4 – orbital magnetic susceptibility.

Partially filled f-peak is formed in the overlap of 5/2 and 7/2 multiplets leading to a spin anharmonicity and ferromagnetic instability. This feature arises due to the fact that the lower band of the 5/2 multiplet gets almost completely filled. This leads to the expulsion of its states to higher energies and enhances their hybridization with 7/2 states.

Our analysis of the electronic structure of the superconducting compound $PuRhGa_5$ also suggests a significant spin anharmonicity in the vicinity of the superconductivity onset temperature. A sharp increase in spin anharmonicity in the immediate vicinity of the superconductivity transition point reflects enhanced interaction between the spin and electronic subsystems.

References

[1] K. T. Moore, G. van der Laan, *Rev. Mod. Phys*. **81**, 235 (2009).
[2] T. Das, J.-X. Zhu, and M. J. Graf, *J. Mater. Res*. **28**, 659 (2013).
[3] P. Piekarz, K. Parlinski, P.T. Jochym et al., *Phys. Rev. B* **72**, 014521 (2005).
[4] D. Daghero, M. Tortello, G.A. Ummarino et al., *Nat. Commun*. 3:786 doi:10.1038/ncomms1785 (2012).
[5] P. Boulet, E. Colineau, F.Wastin et al., *Phys. Rev. B* **72**, 104508 (2005).
[6] A. O. Shorikov, A.V. Lukoyanov, M.A. Korotin et al., *Phys. Rev. B* **72**, 024458 (2005).
[7] A. A. Povzner, A.G. Volkov, L.R. Kabirova. *J. Supercond. Nov. Magn.*, **26**, 1653 (2013).

Evolution of the Ferromagnetism in UCoGe Induced by Ru Doping

M. Vališka, J. Pospíšil and V. Sechovský

DCMP, Faculty of Mathematics and Physics, Charles University,
Ke Karlovu 5, 12116 Prague 2, Czech Republic

UCoGe is a weak itinerant 5f electron ferromagnet which becomes superconducting at ambient pressure [1]. A widely accepted scenario of superconductivity in UCoGe involves the spin-triplet pairing mediated by critical spin fluctuations occurring in the vicinity of a ferromagnetic QCP. The low T_C = 3 K together with tiny spontaneous magnetic moment μ_s = 0.03 μ_B/f.u. indicate proximity of a ferromagnetic instability. We have observed that a small substitution of Fe or Ru for Co stabilizes the ferromagnetic state, which is manifest by a considerable increase both of the T_C and spontaneous magnetic moment [2] despite the fact that both, UFeGe and URuGe, behave as an enhanced Pauli paramagnet without any sign of magnetic ordering down to the lowest temperatures [3]. Recently, it has been shown that further substitution of Fe for Co leads to a ferromagnetic QCP [4]. This observation motivated us to study the development of the magnetism in the $UCo_{1-x}Ru_xGe$ system. Consequently, we have performed investigation of structure, magnetization, AC susceptibility, specific heat and electrical resistance on numerous polycrystalline samples with various x over the entire concentration range.

All samples were found possessing the same orthorhombic TiNiSi-type structure (space group Pnma) as the boundary compounds UCoGe and URuGe. The unit cell volume of the ferromagnetic UCoGe is smaller (V = 208.3 Å^3) of about 5% than that of the Pauli paramagnet URuGe (V = 219.5 Å^3). As seen in Fig. 1, the observed concentration dependence of all the three lattice parameters and also the unit cell volume is linear, i.e. it obeys the Vegard's law. The parameters *b* and *c* increase with increasing *x,* whereas the parameter *a* simultaneously decreases. The volume expansion seems to be reflecting the increase of the covalent radii from 126 pm Co to Ru to 146 pm. Refinement of diffraction patterns confirmed that the Ru atoms really substitute the Co atoms on their sites.

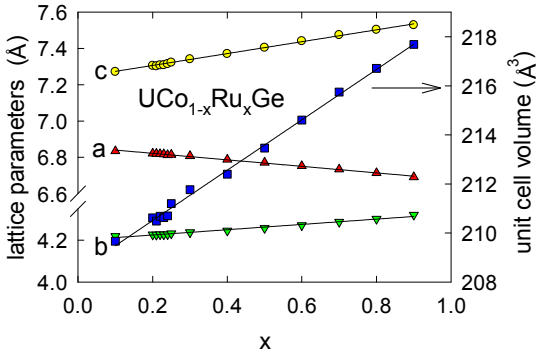

Fig. 1 - Concentration dependence of the lattice parameters and unit cell volume in $UCo_{1-x}Ru_xGe$ system. The lines serve as guides for the eye.

Magnetization measurements showed simultaneous development of T_C and μ_s with increasing Ru content, first a rapid increase of the spontaneous moment up to 0.1μ_B for x ≈ 0.1 which is followed with gradually decreasing values for x > 0.12 (see the phase diagram in Fig. 2). The $T_C(x)$ and $\mu_s(x)$ tend to zero at the critical concentration for ferromagnetism x_{cr} ≈ 0.3.

The values of spontaneous magnetic moment μ_s have been estimated from the magnetization curves M(B) measured at 1.85 K by extrapolation from high magnetic fields to zero T. The corresponding T_C values have been determined by Arrott plot (M^2 over H/M) analysis of magnetization isotherms. These values are in good agreement with the corresponding temperatures of the inflection point of the M(T) dependence measured in 10

mT, of the maximum of the real AC susceptibility χ' and with the inflection point on the C(T) dependence measured in zero magnetic field.

The other two panels of Fig. 2 display evolution of parameters derived from temperature dependencies of the electrical resistivity. The results are discussed with respect to the expected ferromagnetic QCP at $x_{cr} \approx 0.3$.

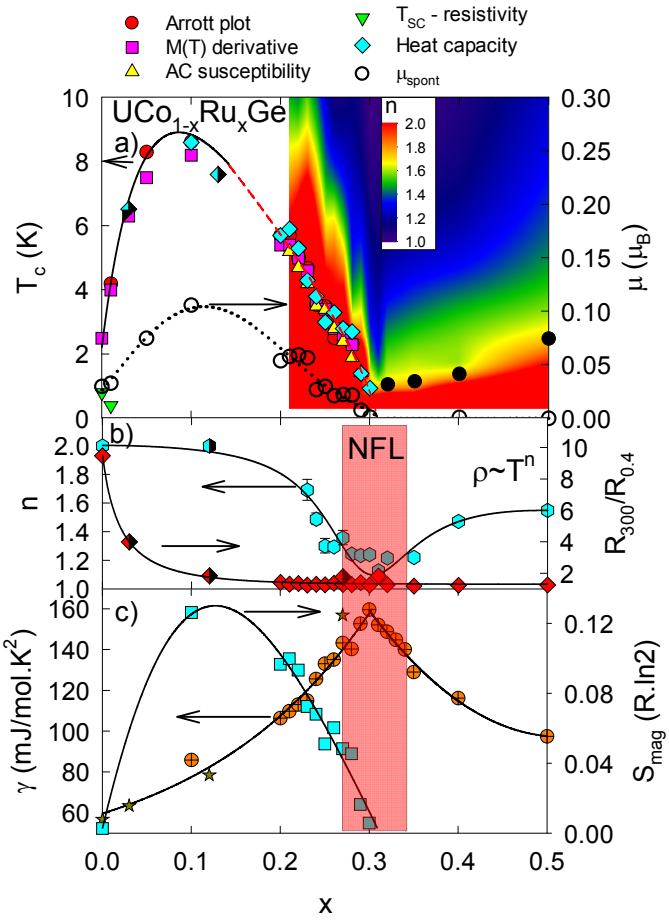

Fig. 2 - Panel a) shows the phase diagram based on measurements of polycrystalline samples. Curie temperatures are estimated with various methods mentioned in the text. The black solid line is only guide for the eye while the red dashed part is a fit of $Tc \approx (x_{cr}-x)^{3/4}$. The right axis shows development of the spontaneous magnetic moment (dashed line is only guide for the eye). Contour plot shows local exponent in the resistivity obtained as $n = d\ln(\rho-\rho_0)/d\ln T$. Panel b) shows coefficients n from fitting of the low temperature dependence of resistivity with equation $\rho = \rho_0 + AT^n$ for $T>T_C$. Right axis shows RRR = $R_{300K}/R_{0.4K}$ as a function of x. Panel c) shows development of Sommerfeld γ coefficient obtained from the C(T) data and magnetic entropy S_{mag}.

In order to study also anisotropy of magnetic and transport properties in the $UCo_{1-x}Ru_xGe$ system we have grown three single crystals. We also prepared single crystals with specific Ru concentrations. Single crystals with final composition verified by EDX as $UCo_{0.97}Ru_{0.03}Ge$ (fastest increase of T_C), $UCo_{0.88}Ru_{0.12}Ge$ (maximum T_C) and $UCo_{0.73}Ru_{0.27}Ge$ (close to the expected QCP). The obtained results will be also a part of the presentation at JdA.

References

[1] N. T. Huy, et al., Physical Review Letters **99**, 067006 (2007).
[2] J. Pospisil et al., Jornal of Applied Physics **105**, 07E114 (2009).
[3] R. Troc and V. H. Tran, Journal of Magnetism and Magnetic Materials **73**, 389 (1988).
[4] K. Huang et al., Physical Review B 87, 054513 (2013).

New scientific possibilities provided by the ESS for neutron scattering experiments on actinide-based compounds

Arno Hiess

European Spallation Source AB, Lund, Sweden
e-mail : arno.hiess@esss.se

ESS will provide unique possibilities for neutron research due to its beams of unparalleled brightness, delivering more neutrons than the world's most powerful reactor-based neutron source with higher peak intensities than other spallation sources. The ESS science drivers include soft condensed matter research, life science, studies of magnetic and electronic phenomena, chemistry of materials, energy research, engineering materials and geosciences, archaeology and heritage conservation, as well as fundamental and particle physics. ESS's high brightness allows to probe weak signals, study phase transitions and systems that change over time, or to measure within a small volume. This last ability is particularly useful for real-world heterogeneous samples or for materials for which only small sample quantities are available or can be used.
ESS presented its Technical Design Report [1] in early 2013 with a reference suite of 22 neutron instruments illustrating its wide-spread scientific potential. To study phenomena in a broad range of length and time scales, the instruments will use the range of scattering and non-scattering techniques and methods developed over the years: diffraction, imaging, small-angle scattering, reflecometry, spectroscopy and instrumentation for fundamental physics. Many instrument concepts have been developed during the last two years and several are now under scientific and technical evaluation prior to entering the construction phase. Most of those state-of-the-art instruments envisage to boost the sensitivity to study increasingly challenging scientific problems.
In this presentation I will illustrate the scientific possibilities by some recent inelastic neutron scattering (INS) experiments on actinide-based superconductors performed at the Institut Laue Langevin, France, and the Maier-Leibnitz Zentrum, Germany. INS has been of particular importance to appreciate the interrelation of magnetism and superconductivity by studying the microscopic spin dynamics in momentum and energy space. As in the case of high temperature superconductors, the spin dynamics changes on entering the superconducting state in cerium- and uranium-based intermetallic superconductors: a gap opens at low energies and inelastic neutron scattering experiments reveal that an increased magnetic intensity is present above the gap, forming in most cases a sharp inelastic peak (so-called 'spin resonance peak'). Its momentum space dependence is related to the symmetry of the superconducting order parameter but its relevance for the pairing mechanism is still subject of debate.
For the archetypical cubic actinide-based superconductor UBe_{13} (T_c = 0.85 K) a dynamic magnetic response has been observed at selected momentum space positions below T ~ 50 K. The energy dependence in the normal state reflects the energy scales determined from specific heat measurements and changes upon entering the superconducting state. I will also present INS results mapping the normal state spin dynamics of the magnetic superconductor UNi_2Al_3 (T_N = 5 K, T_c = 1 K) and confront our data with those obtained on the isostructural compound UPd_2Al_3 (T_N = 14K, T_c = 2K) to discuss the aspect of competing magnetic interactions.
Nevertheless, specialised instruments will not be sufficient by themselves to fully exploit the potential of ESS. This is especially true for experiments using actinide-based materials. In my presentation I will also touch on the extensive support systems required to enable future users to make the most productive use of research instruments. This endeavour includes scientific coordination, scientific support laboratories and sample environment.

References

[1] ESS Technical Design Report; http://esss.se/documents/tdr/TDR_final.pdf

Aerial Measuring System (AMS)/ Israel Atomic Energy Commission (IAEC) Joint Comparison Study

I. Halevy [1], P. Wasiolek [2], S. Dadon[1], M. Sheinfeld[1], A. Broide[1], S. Rofe[1] and I.Yaar[1]

1. Israel Atomic Energy Commission, Israel

2. U.S. Department of Energy National Nuclear Security Administration Remote Sensing Laboratory, USA

Israeli Team: I. Halevy, S. Dadon, M. Sheinfeld, A. Broide, S. Rofe and I.Yaar
American Team: AMS team – RSL LV
Piotr Wasiolek, Rusty Malchow, Carson Riland, Manuel Avaro, Ray Arsenault
Ed Zachman, Mike Lukens, Joe Keller, Jaz Stampahar and John Gelsthorpe

In support of the U.S. Department of Energy (DOE) International Emergency Management and Cooperation (IEMC/NA-46) Program, the comparison of the U.S. and Israeli Aerial Measuring Systems (AMS) study was proposed and accepted. The study, organized by the DOE/National Nuclear Security Administration (NNSA) Remote Sensing Laboratory (RSL), involved the DOE/NNSA Aerial Measuring System Project based at the RSL and operated under a contractor agreement by National Security Technologies, LLC (NSTec), and the Israel Atomic Energy Commission (IAEC) Aerial Measuring System. The operational comparison was conducted at RSL-Nellis in Las Vegas, Nevada, during week of June 24–27, 2013. The Israeli system, Air RAM 2000 (figure 1, down), was shipped to RSL-Nellis and mounted together with the DOE Spectral Advanced Radiological Computer System, Model A (SPARCS-A, figure 1 up) on U.S. DOE Bell-412 helicopter for a series of aerial comparison measurements at local test ranges, including the Desert Rock Airport and Area 3 at the Nevada National Security Site (NNSS). A four-person Israeli team from the IAEC, Nuclear Research Center – Negev (NRCN) supported the activity.
The main objective of this joint comparison was use the DOE/RSL Bell-412 helicopter aerial platform, perform the comparison study of measuring techniques and radiation acquisition systems utilized for emergency response by IEAC and NNSA AMS [1].

MEASURING SYSTEMS

One advantage of acquiring aero-radiometric measurements lies in the high collection rate of data over large areas and rough terrain. Typical aero-radiometric systems record and save gamma-ray spectra, correlated with the Global Positioning System (GPS) derived location information (latitude, longitude, elevation over GPS ellipsoid=GPS altitude) in regular time intervals of 1 to 2 seconds. Such data can be used to locate radiation anomalies on the ground, map ground contamination, or track a radioactive airborne plume. Acquiring spectral data of this type allows separation of natural radioactivity from that of man-made sources and identification of specific isotopes, whether natural or man-made.
During the acquisition the flight altitude is kept constant, with typical values recorded between 50 and 985 feet (ft) (15 and 100 meters [m]) above ground level (AGL). The helicopter ground speed is maintained constant, in the case of DOE Bell-412, 70 knots (130 km/h).
For the comparison study, AMS and IAEC used their emergency response radiation detection systems, Israel's Air RAM 2000, and the DOE's SPARCS. For altitude measurements the AirRAM 2000 system uses a barometric altimeter with the range of 0–8000 ft, which is calibrated at 1000 ft by a radar altimeter. The SPARCS system uses radar altimeters for vertical positioning (altitude over the ground) and Differential GPS for location.

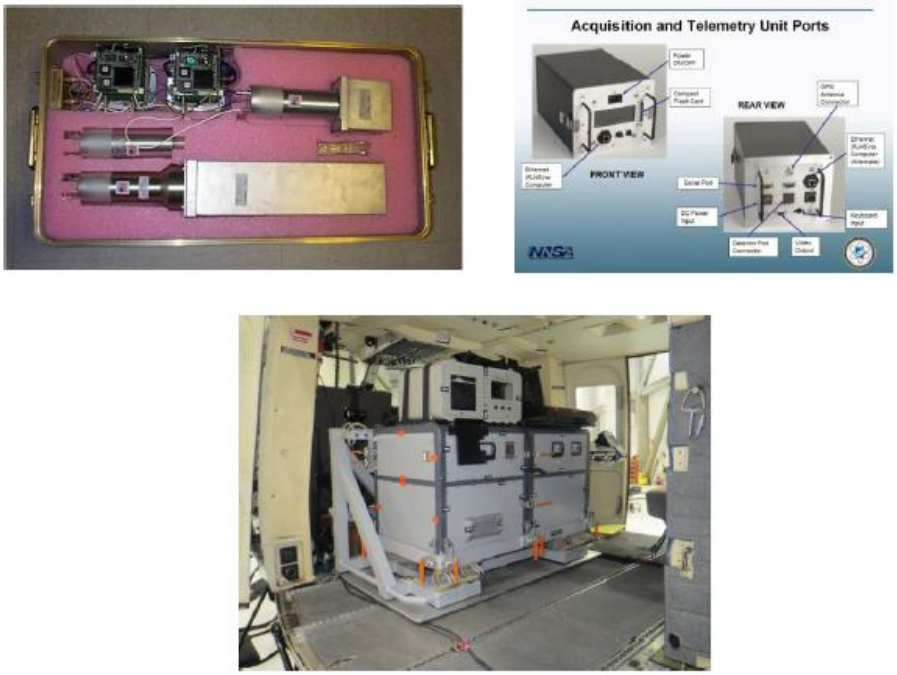

Figure 1. Interior of the SPARCS-A pod and The SPARCS ATU connections, up.
The Air ram2000, down.

Survey Aircraft

The DOE Bell-412 helicopter was used as the airborne platform to carry out the comparison study (figure 2). The Bell-412 is a twin engine utility helicopter that has been manufactured by Bell Helicopter since 1981. With a standard fuel capacity of 330 gallons, it is capable of flying for up to 3.7 hours, with a maximum range of 356 nautical miles and a cruising speed of 122 knots. However, with the AMS radiation survey configuration of 12 detectors, four crew members (two pilots, a mission scientist, and an equipment operator), with a survey speed of 70 knots (120 ft/sec) at survey altitude of 300 ft AGL, the Bell-412 was capable of 2.5 hours of flight time.

Figure 2. DOE Bell-412 helicopter during survey

RESULTS
Attenuation and Sensitivity
Lake Mohave Calibration Line

The altitude spiral flight over the Lake Mohave Calibration Line was used to derive the local effective air attenuation coefficient, obtain the sensitivity of both acquisition systems, and estimate their inherent background. The altitude spiral consists of passes between two waypoints programmed into helicopter navigation system over the land calibration line and water line at several different altitudes. During the exchange, the altitudes were 50, 100, 200, 300, 750, 1500, and 3000 ft AGL. The path plots of the altitude spiral flight plotted independently by both groups are presented in Figure 3.

Figure 3. The AirRAM 2000 inside the DOE Bell-412 helicopter

The count rate ratio of the SPARCS single 2″ × 4″ ×16″ NaI detector to the AirRAM 2000 two 2″ × 2″ inch detectors of about 18 (Table 1) compares very well with the ratio of volumes between systems of 16 [128 $inch^3$ (2″ × 4″ × 16″)/8 $inch^3$ (2″ × 2″ × 2″)]. From the altitude spiral, the effective air attenuation coefficient and sensitivity of the detectors can be derived by plotting each altitude flight's net gross counts versus altitude on a semi-log plot (Figure 4) and exponentially fitting the gross counts expression:

$$Calt = CGC \times e\exp[\mu air \times (H - Havg)]$$

Where:
Calt = gross counts normalized to the averaged survey altitude, (cps).
CGC = total terrestrial count rate or gross counts, (cps).
μair = gamma ray air attenuation coefficient, ft^{-1}.
H,Havg = average radar altitude, ft AGL.
The difference in sensitivity between the SPARCS single 2″ × 4″ ×16″ NaI detector to the AirRAM 2000 two 2″ × 2″ inch detectors is remarkable, ~18 times.

Table 1. Average count rate from different detectors at the calibration line

Altitude (ft)	Count rate (cps)					
	Land Line			Water Line		
	SPARCS NaI 2″×4″×16	AirRAM two NaI 2″×2″	Count Ratio	SPARCS NaI 2″×4″×16	AirRAM two NaI 2″×2″	Count Ratio
50	2620	151	17	159	11	14
100	2450	141	17	155	10	16
200	2139	118	18	165	11	15
300	1887	102	18	172	10	17
750	993	53	19	190	12	16
1500	405	22	18	173	11	16
3000	223	13	17	196	12	16

The slope in figure 4 is the gamma ray air attenuation coefficient (0.00186 ft^{-1}).
From the graph it is clear that the heights altitude for detecting 8.5 μR/hr is ~1950 ft.

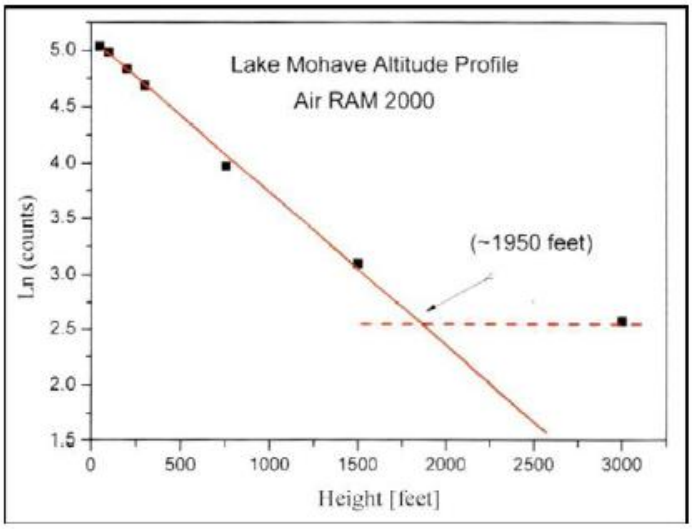

Figure 4. Results of the curve fit of the altitude spiral data collected with AirRAM and analyzed by IAEC

Desert Rock Airport Sources Overfly

Three radioactive sources listed in Table 2 were placed approximately 1500 ft (450 m) apart along the runway at the Desert Rock Airport (Figure 5). Using the visual flight rules, several passes directly over the sources (marked with orange cones) were executed. To study the response of the SPARCS and AirRAM, the flight altitude and speed were varied from 50 to 150 ft AGL and from 35 to 150 knots. The results of the source flyover are presented in Figure. The SPARCS data (gross counts from the 2″ × 4″ × 16″ NaI crystal) show an elevated count rate at any combination of flight altitude and speed tested, from 50 ft AGL at 50 knots to 150 ft AGL at 100 knots. The AirRAM, due to much lower detector volume, failed to detect the smaller 60Co source at 100 ft and both 60Co sources at 150 ft AGL. A higher flight speed of 100 knots, combined with lower sampling frequency (sample every 2 seconds) affected the AirRAM capability to spatially locate the sources.

Table 2. Activity and location of the radioactive sources used in the study

	Activity (mCi)	Longitude	Latitude
^{137}Cs	20.6	−116.028505	36.624740
^{60}Co	3.6	−116.031402	36.621293
^{60}Co	1.7	−116.034129	36.617998

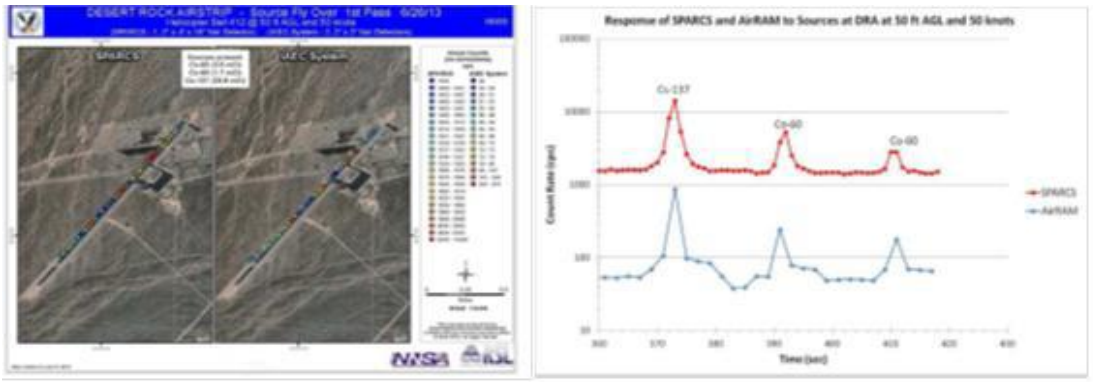

Figure 5. Source flyover at Desert Rock Airport at 50 ft AGL altitude at 50 knots ground speed presented spatially (left) and as time series (right)

Contours
Natural Background

To compare responses of the SPARCS and AirRAM to variable natural radiation background, the AMS test/evaluation area (Government Wash) was surveyed using standard AMS techniques of flying uniformly spaced parallel lines over survey area. The actual flight lines flown during the exchange are shown in Figure 6.

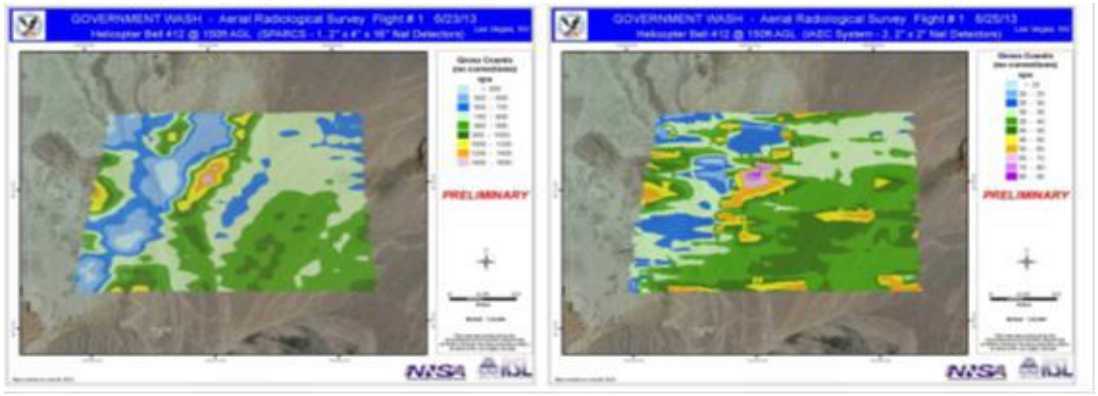

Figure 6. Gross-count contour of the natural background area (Government Wash) created using IAEC AirRAM detection system and AMS data processing techniques

[1] PIOTR WASIOLEK and ITZHAK HALEVY, AERIAL MEASURING SYSTEM (AMS)/ ISRAEL ATOMIC ENERGY COMMISSION (IAEC) JOINT COMPARISON STUDY REPORT, Nevada National Security Site June 24–27, 2013 , DOE/NV/25946--1941

Radioactive Contamination Estimation from micro-copters or helicopter Airborne survey: Simulation and real measurements

I. Halevy, M. Ghelman, Y. Yehuda-Zada, A. Manor, S. Dadon A. Sharon and I. Yaar

Nuclear Research Center – Negev, P. O. Box 9001, Beer-Sheva 84190, Israel

One of the main advantages of acquiring aero-radiometric measurements lies in the high collection rate of data over large areas and rough terrain. Typical aero-radiometric system records and saves gamma ray spectrum, correlated with the GPS derived location information in regular time intervals of one to two seconds. Such data can be used to locate radiation anomalies on the ground, map ground contamination or track a radioactive airborne plume. Acquiring spectral data of this type allows separation of natural radioactivity from that of man-made sources and identification of specific isotopes, natural or man-made.

The data acquisition can be done by helicopter or micro-copters at wide range of heights from few meters to few kilometers.

Usually the flight altitude will be kept constant to make the data analysis easier. Rough terrain will jeopardize that assumption. The radioactive particles are not always on the ground, they can be in a cloud above the ground or on roofs or trees. Speed of survey with a helicopter is in the range from hovering to ~120 Knots, while the speed of micro-copters is much lower, from hovering to ~30 Knots. Both, the helicopter and the micro-copters are suffering from limited abilities while severe weather conditions.

The main advantages of micro-copters are the ability to fly even indoor and without exposing the measuring team to radiation or extra flight risks.

When the survey is done or even during the survey, the main challenge is to estimate the radiation field and the contamination in the scene.

An iterative algorithm was suggested to estimate the radioactive contamination for analyzing an airborne survey [1].

In that work this algorithm will be tested on real scenario while spreading radioactive material, ^{99m}Tc, simulating an RDD events by explosion [2, 3].

In those simulations it is clear that a lower-height survey can improve the space resolution. Slow flight will improve the detection sensitivity but will take much more time.

This survey can be for detection only or it can bring also isotope identification by energy resolution. In our software, four energies windows can be set as our PDS-1000 flying detector.

We simulated a spread of radioactive sources on a radioactive background. A radioactive field at a survey height was calculated. From that data we found the spread of radioactive sources by our iterative algorithm.

There is no clear proof that the results are unique. The highest background we have the less significant map of spread radioactive sources can be achieved.

Few new results of simulation and real surveys are depicted in the next figures.

Figure 1: Mikro-Kopter / multi-rotor (upper)
Airborne radiation survey of ^{99m}Tc from “Green field” (Open field) test compared with ground survey (lower) [2].

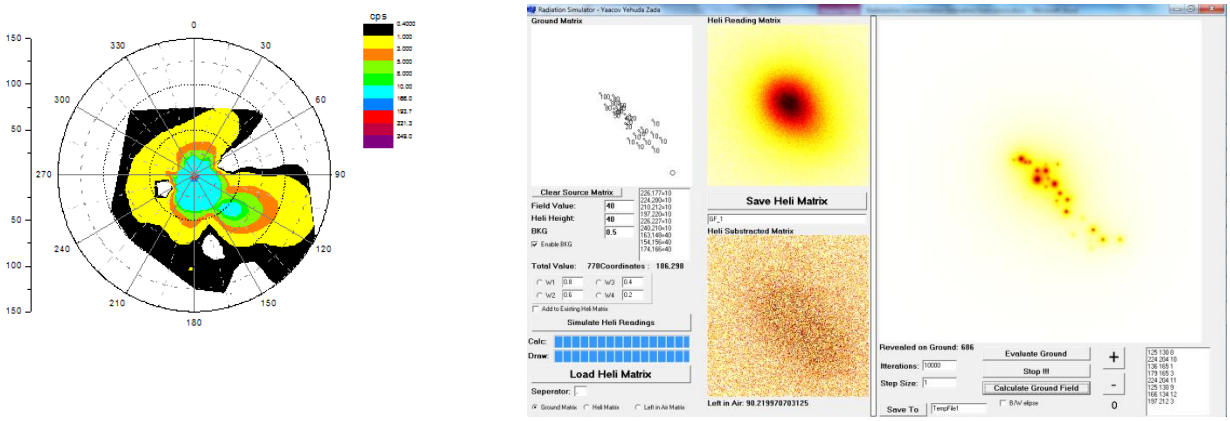

Figure 2: Airborne radiation survey analysis of ^{99m}Tc from "Green field" (Open field) test compared with ground survey [2].

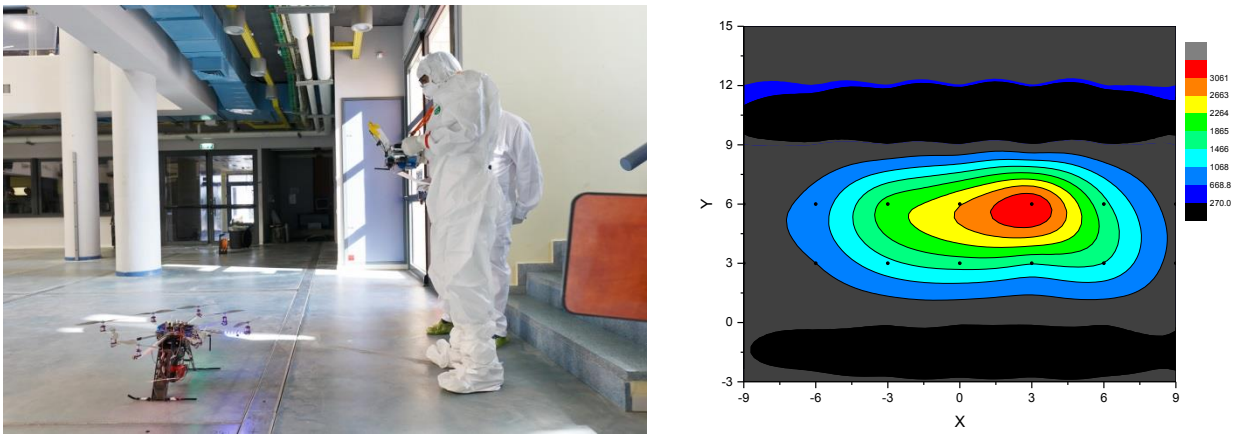

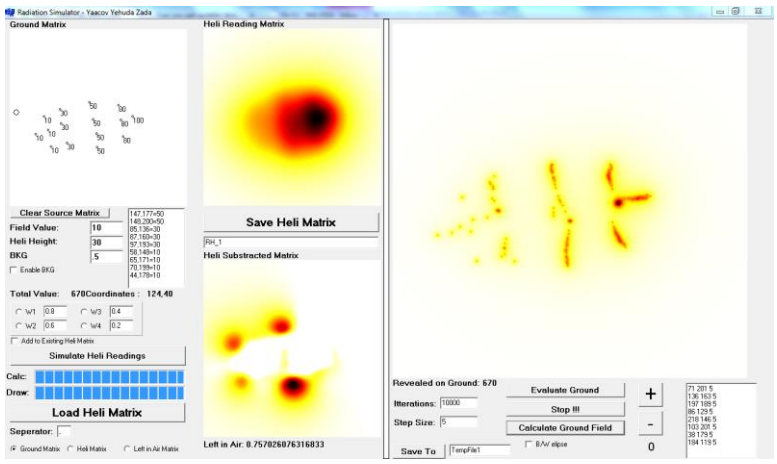

Figure 3: Airborne radiation survey of ^{99m}Tc from "Red-House" (Indoor) test compared with ground survey [3].

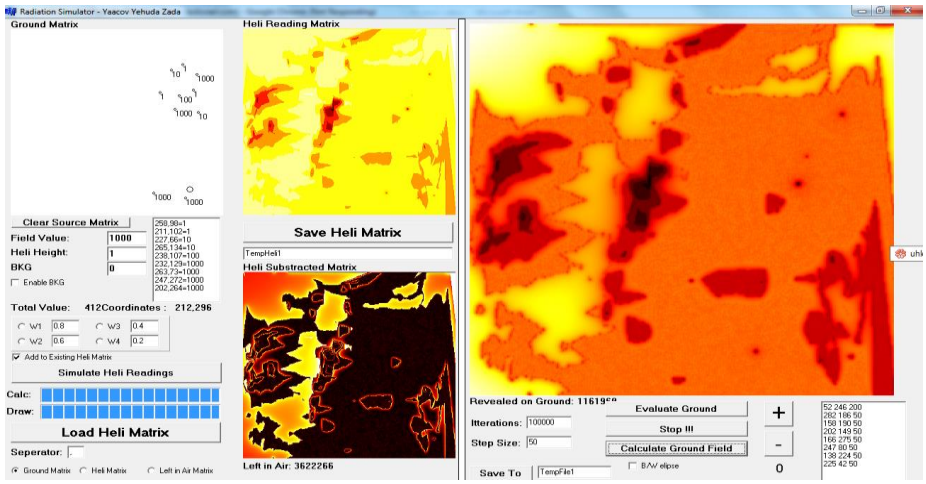

Figure 4: Airborne radiation survey of natural background from Air RAM 2000 measurements at the Government Wash area [4].

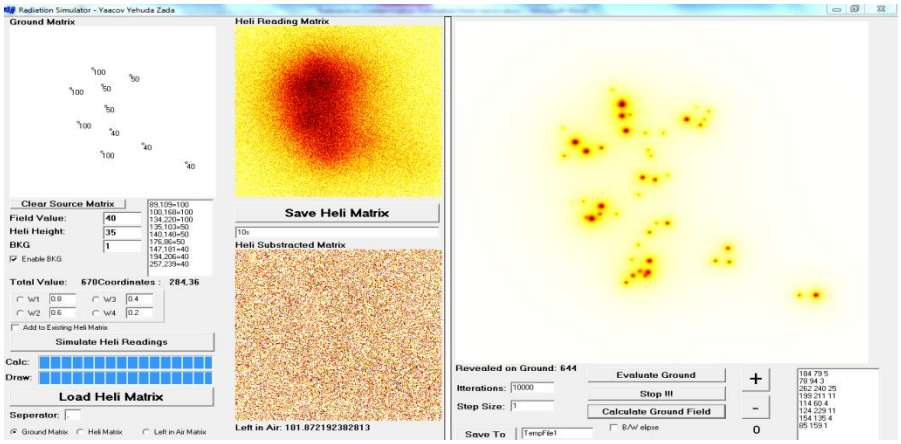

Figure 5: Airborne radiation simulation of natural background with ten spread sealed sources.

REFERENCES

[1] M. Ghelman, M. Sheinfeld, A. Manor, E. Vax, Y. Kadmon and D. Tirosh
The 25th Conference of the Nuclear Societies in Israel
16-18 February 2010, Crown Plaza Hotel, Dead Sea, Ein Bokek, ISRAEL

[2] A. Sharon, D. Sattinger, I. Halevy, R. Neuman, A. Ashkenazi and I. Yaar
Cloud Rise Model for a "Dirty Bomb" Event
The 25th Conference of the Nuclear Societies in Israel
16-18 February 2010, Crown Plaza Hotel, Dead Sea, Ein Bokek, ISRAEL

[3] Cloud Rise Model for an Explosion Inside a Building
A. Sharon, D. Sattinger, I. Halevy, R. Neuman, A. Ashkenazi and I. Yaar
The 25th Conference of the Nuclear Societies in Israel
16-18 February 2010, Crown Plaza Hotel, Dead Sea, Ein Bokek, ISRAEL

[4] Aerial Measuring System (AMS) / Israel Atomic Energy Commission (IAEC) Joint Comparison Study Report
Piotr Wasiolek and Itzhak Halevy: DOE/NV/25946-1941

Electron Transport in Solids – Inelastic Mean Free Path Measurements in the 5 to 15 keV Energy Range

Eitan Tiferet[1], Alon Givon[2], Itzhak Orion[2]

1 Department of Materials, Nuclear Research Center-Negev, Israel
2 Department of Nuclear Engineering, Ben-Gurion University of the Negev, Israel

In the past two decades the advanced in third generation synchrotrons and new x-ray sources enable the use of photoelectrons with higher kinetic energy than before. This created a void in the IMFP data, which was filled recently with the publication of calculated IMFP values over the 50 eV to 30 keV energy range. Yet, the indispensible experimental data for the validation of calculated IMFP values is lacking in energies above 5 keV.
In this study we investigate bulk electronic properties of low Z materials in the 5 to 15 keV energy range, and present two methods for measuring the electron IMFP. Full description of both the wide energy spectrum approach and the total current measurement approach is presented. In addition, a new algorithm that does not rely on the signal electron for measuring film thickness, and is based on the wide energy spectrum approach is presented. The wide energy spectrum approach relies on the multiple inelastic scattering theory and thus requires experimental spectrum validation. We show experimental results, performed at the Spanish CRG BM25 beam-line (SpLine) in ESRF, that substantiate our wide energy spectrum approach, and demonstrate the distinct characteristics of the electron multiple inelastic scatterings. These characteristics match the theoretical calculations and give IMFP values that agree with the published IMFP data.
The advancement in the study of electron IMFP measurements at energies above 5 keV was achieved by applying the electron multiple inelastic scattering theory on new concepts that integrates experimental measurements and Monte Carlo simulations. For the simulations, a new Monte Carlo code that meets the methods demands was developed.
The new methods were shown to accurately describe the bulk transport of electrons in the 5 to 15 keV energy range. Our wide energy spectrum approach was confirmed in a synchrotron experiment, and the IMFP of carbon graphite was measured in various energies. The measured electron IMFP at energies of 8860 eV and 7854 eV compared to the IMFP reported in the literature showed a difference of 1.9% and 1.7% respectively. These innovative methods and the novel MC simulation opened new possibilities for the study of electron IMFPs at energies between 5 and 15 keV that previously were not available.

Towards measurement of the $^{209}Bi(n,\gamma)^{210m,g}Bi$ cross sections at SARAF

A. Shor,[1]D. Berkovits[1], Y. Eisen[1], G. Feinberg[1], A. J. M. Plompen[2], G.Giorginis[2], M. Hult[2], A. Krása[2], M. Friedman[3], D. Cohen[3], M. Paul[3] and M. Tessler[3]

[1] *Nuclear physics and engineering division, Soreq Nuclear Research Center, Yavne, Israel, 81800*
e-mail: shor@soreq.gov.il
[2] *European Commission, Joint Research Centre, Institute for Reference Materials and Measurements, 2440 Geel, Belgium*
[3]*Racah Institute of Physics, The Hebrew University, Jerusalem, Israel, 91904*

The main incentives for this work is to exploit the large proton currents and high neutron flux capabilities at the Soreq Applied Research Accelerator Facility (SARAF)along witha liquid lithium target to perform sensitive measurements of interest in reactor design and safety. The first measurement to be performed is neutron activation of^{209}Bi. This measurement is important for proposed Pb-Bi eutectic coolants for Gen IV reactors and for targets for accelerator driven systems (ADS). The activity of one of the reaction products,^{210m}Bi, is very difficult to measure because of long half-life (3 million years). Successful measurements and comparison with the activation of ^{210g}Bi (the ^{210}Bi ground state) requires high neutron flux and very sensitive measurements. We plan to perform the activation using the 30 keVMaxwellian-like neutron spectrum produced by the ^{7}Li(p,n)^{7}Be reaction near threshold. Subsequent to the activation, the plan is to measure directly the γ-decays from the decay products,^{206}Tl for the ^{210m}Biand ^{206}Pb for the ^{210g}Bi activation, in the underground laboratory HADES at SCK-CEN in Mol, Belgium.Level diagram and previous measurements of this ratio are shown in figure 1. This reaction is also of significance for nuclear astrophysics since it is the end of the chain for s-process for nucleo-synthesis in heavy stars, with the Maxwellianneutrons mimicking environment in asymptotic giant branch (AGB) stars.

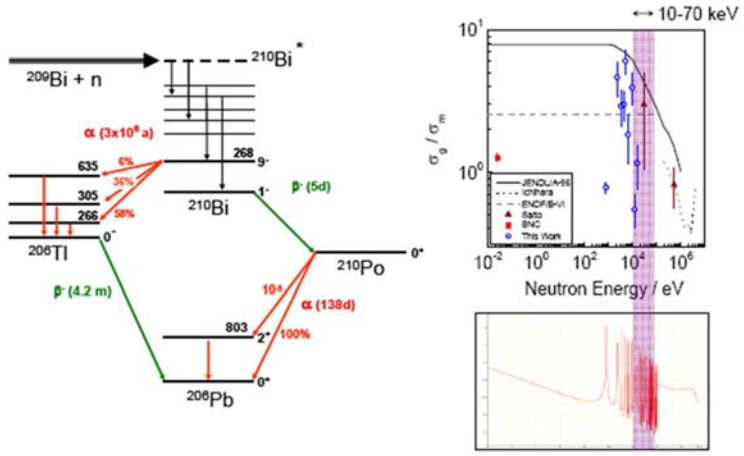

Figure 1. Level diagram of ^{210m,g}Bi and existing measurements with uncertainty

Preliminary measurements were performed at the IRMM Van de Graafffacility to characterize the neutron energy distribution with a narrow and broad energy proton beam, with Ep=1.912 MeV, as anticipated at SARAF, and to corroborate the gold activation cross section which is considered the "standard" for these types of activation measurements. Neutron spectra obtained with broad energy beam provides better agreement with semi-Maxwellian distribution required for astro-physical studies, as shown figure 2. A simulation code,'SiMLiT', was written for the ^{7}Li(p,n)^{7}Be reaction, and it compares favorably to spectra measured at IRMM. Table 1 shows the cross section obtained for the gold activation, obtained with both a narrow and a broad energy proton beam at Ep=1.912 MeV.

TABLE I. Experimental cross sections (mb) of the $^{197}Au(n,\gamma)^{198}Au$ reaction measured in this paper for neutrons from the thick-target $^{7}Li(p,n)$ reaction.

	Narrow energy	Broad energy
Au sample No. 1 ($\theta < 84°$)	608 ± 17	620 ± 17
Au sample No. 2 ($\theta < 66°$)	626 ± 18	619 ± 17
Average	616 ± 17	620 ± 16

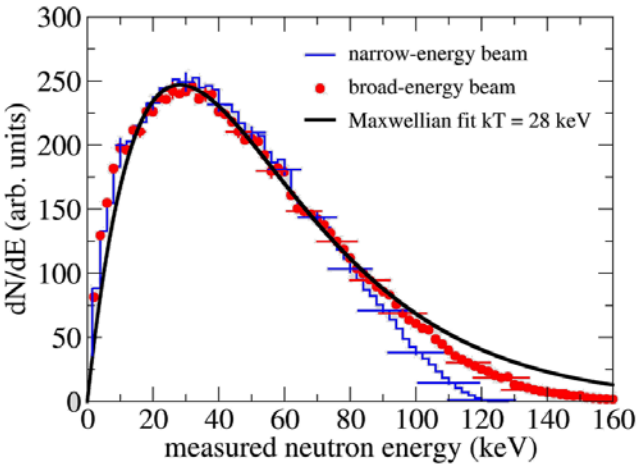

Figure 2. Measurements taken at IRMM VdG neutron spectrum for narrow-energy and broad energy proton beam and fit to semi-Maxwellian.

SARAF accelerator Phase I (figure 3) currently provides 2 mA proton beam via external beam line. LiLiT liquid lithium target was operated successfully at 1.5 mAproton current. We will soon perform irradiation studies of bismuth with thermal neutron to confirm branching ratio for ^{210}Po decay via the excited and ground states of ^{206}Pb.We will later perform preliminary study of bismuth activation with moderate neutron flux, using gamma detection system at Soreq, and subsequently at HADES. Bismuth activation with high flux of neutrons, followed by sensitive measurements at HADES, will begin towards the end of 2014.

Figure 3. SARAF Phase I – photograph showing EIS ion source, low energy beam transport (LEBT), radio-frequency quadrupole (RFQ), and prototype superconducting module (PSM) consisting of six have-wave resonator accelerating cavities.

Acknowledgment: this work is partially support by the IAEC-JRC collaboaration.

References

[1] Feinberg, M. Friedman,A. Krasa, A. Shor, Y. Eisen, D. Berkovits, G.Giorginis, T. Hirsh, M. Paul, A. Plompen, E. Tsuk, Phys.Rev.C 85,055810 (2012).
[2] Feinberg, M. Friedman,A. Krasa, A. Shor, Y. Eisen, D. Berkovits, G.Giorginis, T. Hirsh, M. Paul, A. Plompen, E. Tsuk, , Journal of Physics Conf. 337, 012044(2012).
[3] M. Friedman, D. Cohen, M. Paul, D. Berkovits, Y. Eisen, G. Feinberg, G. Giorgios, S. Halfon, A. Krasa, A. Plompen, and A. Shor, , Nucl.Inst.Meth. A698, 117-126 (2012).
[4] M. Tessler, M. Friedman S. Schmidt, A. Shor, D. Berkovits, D.Cohen, G. Feinberg, S. Fiebiger, A. Krasa, M. Paul, R. Plag, A. Plompen and R. Reifarth, to be published , Journal of Physics: Conference Series (JPCS) 2014.
[5] M. Friedman, D. Cohen, M. Paul, D. Berkovits, Y. Eisen, G. Feinberg, G. Giorgios, S. Halfon, A. Krasa, A. Plompen, and A. Shor, to be Phys.Rev.C.

Synthesis of novel UC_x nanomaterials for online production of exotic isotope ion beams

M.S. Henriques,[1] A. Cruz[1], J. Marçalo[1], T. Stora[2], L. Havela[3], Z. Weishauptová[4], A.P. Gonçalves[1]

[1] *Nuclear and Technological Campus-IST, University of Lisbon, 2695-066 Bobadela, Portugal*
e-mail: mish@ctn.ist.utl.pt
[2] *ISOLDE-CERN, CH-1211 Geneva 23, Switzerland*
[3] *Dept. Condensed Matter Physics, Faculty of Mathematics and Physics, Charles University, 121 16 Prague, Czech Republic*
[4] *Institute of Rock Structure and Mechanics, ASCR, V Holešovičkách 41, 182 09 Prague, Czech Republic*

Radioactive ion beams (RIBs) provide unique opportunities to study nuclear, atomic, surface and solid-state physics, astrophysics, nuclear forensics, medicine, and biology. The isotope separation online (ISOL) method is used at ISOLDE - CERN [1] to create RIBs through the bombardment of thick high-temperature targets by an accelerated primary proton beam. As a result, radionuclides are generated in the target material via induced spallation, fragmentation and fission nuclear reactions. Once produced, the isotopes must first diffuse from the interior of the target to the surface and then evaporate from it, followed by ionization, acceleration, mass separation and further beam manipulation until delivered at the final user. From the experimental point of view, high intensity RIBs can be obtained by increasing the overall efficiencies, high isotope diffusion and short delay times, or by increasing the power of the primary beam. Minimum delay times can be achieved in targets with highly-permeable, low-density, open-structures operating at high temperatures. However, increased driver beam intensity might carry serious concerns for the target as thermal loads, radiation damage, or physical integrity under irradiation. Thus to find the ideal material for a thick target is a tremendous technological challenge for the ISOL technique. Nearly five decades after the first irradiation tests, micrometric uranium carbide-based materials are still the reference materials for radioactive ion-beam production. Nevertheless, it was recently proved that a significant increase of the release and yields of exotic isotopes can be obtained on submicron and nanostructured porous materials [2]. The objective of this study is to produce submicron structured carbides of U to be tested as target materials at ISOLDE.

For this purpose, three different approaches were tested: (1) solid - gas reaction between U metal and CH_4, (2) electrospinning of precursor solutions containing U salts (Fig. 1), and (3) mechanical alloying in liquid medium of pre-alloyed uranium carbide.

In the path (1), U sub-micron powders were prepared by hydrogen decrepitation: UH_3 was first prepared by reaction of U with H_2, followed by its decomposition at 250ºC under vacuum. The UC_x nanopowders were then prepared by the reaction of the uranium powders with CH_4 at 700ºC, with a crystallite size in the range 20 – 30 nm, but upon heat treatment they are very reactive with oxygen, and a mixture of UC + UO_2 forms readily.

In the approach (2), an exploratory work was first made with lanthanides and then extended to U. Acetate salts and/or acetylacetonate were synthesized for the different metals (M = Eu, Er, Yb and U) and mixed with cellulose acetate. The solutions were then electrospun in different conditions. The dried electrospun materials were subsequently heat-treated at temperatures from 800 to 1550ºC in a flowing argon atmosphere. Scanning electron microscopy observations show that for the same M/C = 4 ratio the spinnability of the solutions is dissimilar for each M and changes for the different salts of the same element. For 4f metals, micrometric fibers are well formed for the Er case, while for Eu the fibers are nanometric and exhibited many and large beads. For Yb no fibers are formed. In the case of U, the formation of nanometric fibers was only achieved for the acetylacetonate solutions (Fig. 1). The heat treatment of the electrospun materials lead to the material densification and to the formation of highly porous samples, with an open porosity and large distribution of pore sizes. CO_2 adsorption isotherms have shown that the Er sample treated at 800ºC has a

surface area of 527 m^2/g. X-ray diffraction indicated the formation of MC_2 or MC for all studied samples, with estimated average crystallite sizes of 13, 10 and <10 nm for ErC_2, EuC_2 and YbC_2, respectively. For U carbides, the starting crystallite size is <10 nm for the acetate salt and 28 nm for the acetylacetonate solution, increasing with annealing temperature up to 66 nm for the maximum temperature tested (1550ºC).
In the method (3), after an exploratory trial with Y and graphite, a powdered pre-alloyed UC was mixed with excess of graphite together with an organic solvent. The mixture was then inserted in a WC carbide crucible containing WC carbide balls in a ratio 1/18 and milled in a planetary ball-mill. The evolution of the milling procedure was followed by X-ray diffraction analysis at regular intervals of time.
The results have shown that nanostructured UC_x materials can be successfully produced by all the techniques. Yet electrospinning is the most versatile method to tune the desired surface-interface features for these materials. However, serious drawbacks are the low yields, the complicated production of precursors and polymeric solutions. Batches of some of these materials are now under preparation for in-situ proton irradiation.

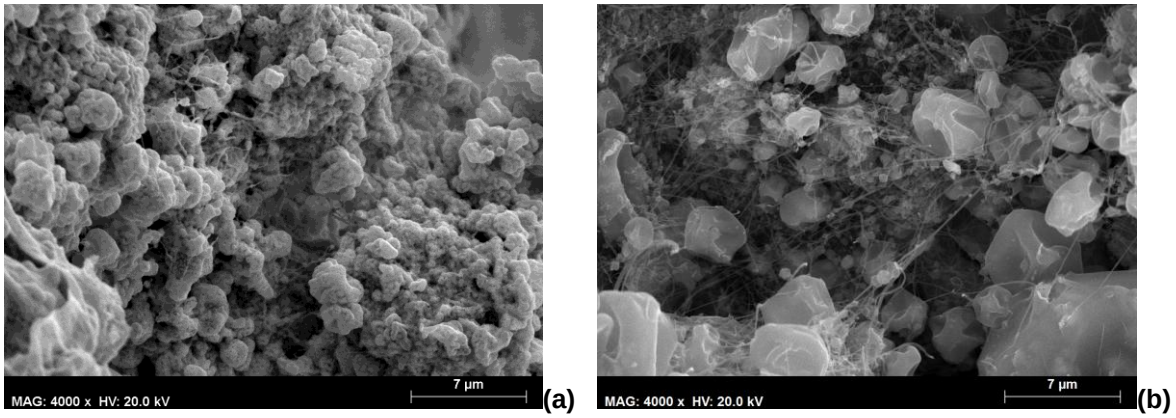

Fig. 1. Scanning electron microscopy images of a U precursor solution produced by electrospinning, showing the formation of nanofibers: as electrospun (a) and after heat treatment (b).

References

[1] A. Herlert, *Nuclear Phys. News* **20**, 4 (2010).
[2] T. Stora, *Nucl. Instr. Meth. B* **317**, 402 (2013).

Acknowledgements: This work was carried within the financial support of FCT, Portugal, through the project CERN/FP/123588/2011 and the grant SFRH/BD/66161/2009 (MSH).

Magnetism in hydrides of γ-Uranium alloys.

M. Paukov, I. Tkach, Z. Matěj, L. Havela

Department of Condensed Matter Physics, Faculty of Mathematics and Physics, Charles University, Ke Karlovu 5, 121 16, Prague 2, Czech Republic
e-mail: Michael.Paukov@gmail.com

The *bcc* form of Uranium metal, its alloys, and their hydrides have been used in various applications, such as low-enriched nuclear fuel. The γ-Uranium metal is stable at elevated temperatures. The only possibility to retain this phase to low temperatures is to combine doping (by Mo, Zr, Ti, Nb, Re, Ru, Pd, or Pt) with quenching. It opens the possibility to study the ground state properties in this form of U. We have been testing the possibility to reduce the necessary amount of the dopant using ultrafast cooling [1].

As next, we decided to test the interaction with hydrogen. The common α-U phase is known to react readily with H at low pressures already, producing a fine pyrophoric powder of β-UH_3, which is ferromagnetic with the Curie temperature around 170 K. Experiments revealed that the Mo stabilized γ-U absorbs H only at elevated pressure. The product is surprisingly not powder. We obtained brittle but compact pieces of hydrides denoted as UH_3Mo_x with practically amorphous crystal structure, most likely related to β-UH_3 [2]. Varying the Mo concentration, we found that the Curie temperatures increase up to 200 K. The Curie temperature has a maximum for $UH_3Mo_{0.18}$ (see Fig. 1a).

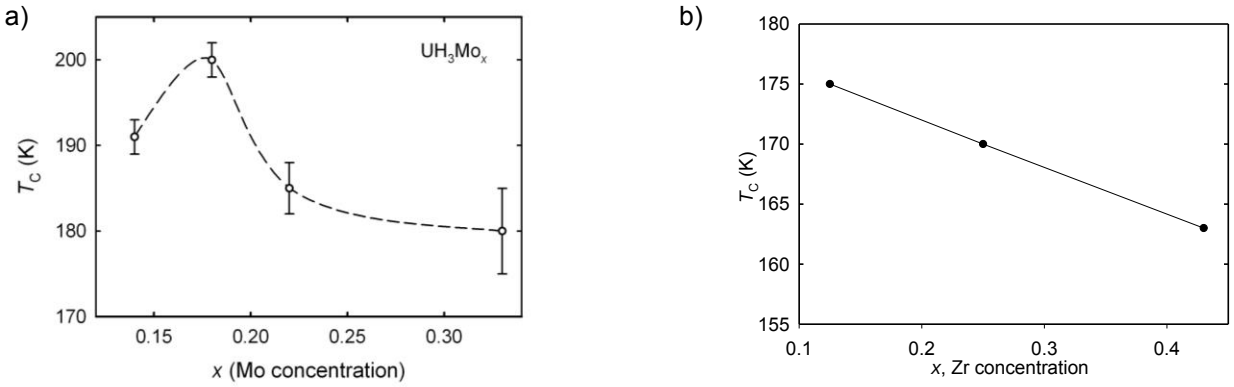

Fig. 1. The dependence of Curie temperature on a) Mo, b) Zr concentration.

The magnetic moment per U atom increases, as well [2]. The saturation magnetization of the U-Mo hydrides is higher than that in β-UH_3 (see Fig. 2a).

The type of hysteresis loops at T = 2 K can be associated with pinning of domain walls in highly disordered systems with high anisotropy (see Fig. 2b). There exists extended evidence of similar behavior among such materials, called as High Anisotropy Random Distribution, for example on the basis of $SmCo_5$ or amorphous $TbFe_2$. With increasing concentration of Mo the coercive force increases extremely up to 5 Tesla.

For comparison with U-Mo, we undertook the same type of study with *bcc* U doped by Zr. The U-Zr alloys absorb hydrogen (pressures above 5 bar H_2 are necessary) up to the stoichiometry UH_3Zr_x, forming a crystalline material with the cubic structure corresponding to α-UH_3, which represents a *bcc* U lattice filled with H.

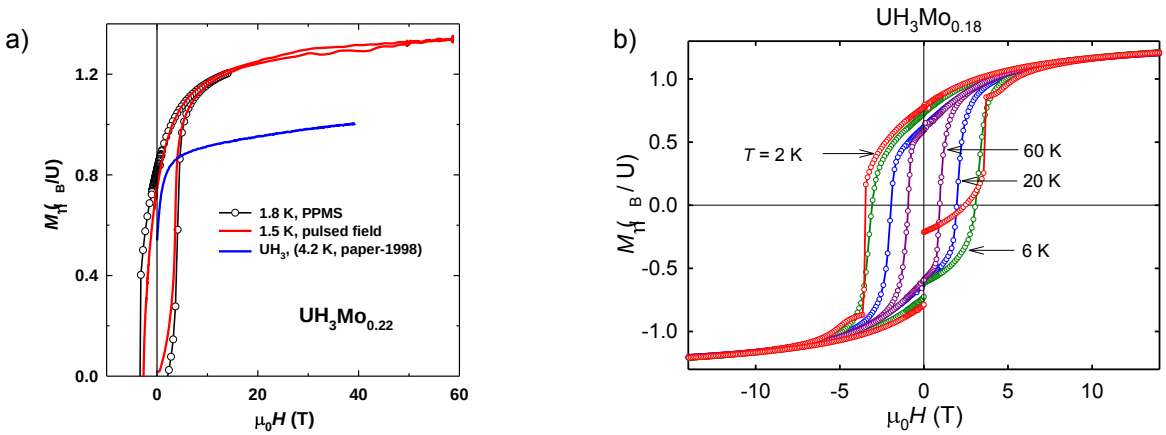

Fig. 2. a) Approach to saturation in high magnetic fields for $UH_3Mo_{0.22}$ compared with β-UH_3 b) temperature variations of hysteresis loop for $UH_3Mo_{0.18}$.

We assume that Zr occupies randomly the U lattice sites, as the atomic radius of Zr and U are similar. $T_C \approx 175$ K slightly exceeds that of β-UH_3 for low Zr concentrations, but decreases with increasing Zr concentration (see Fig. 1b). U moments remain on the level of 1 μ_B. The study reveals a surprising fact that magnetic properties of α-UH_3 and β-UH_3 are similar, despite different atomic spacing. A striking feature of UH_3Zr_x systems is enormous magnetic coercivity, with the width of hysteresis loop exceeding 11 T at low temperatures (see Fig. 3).

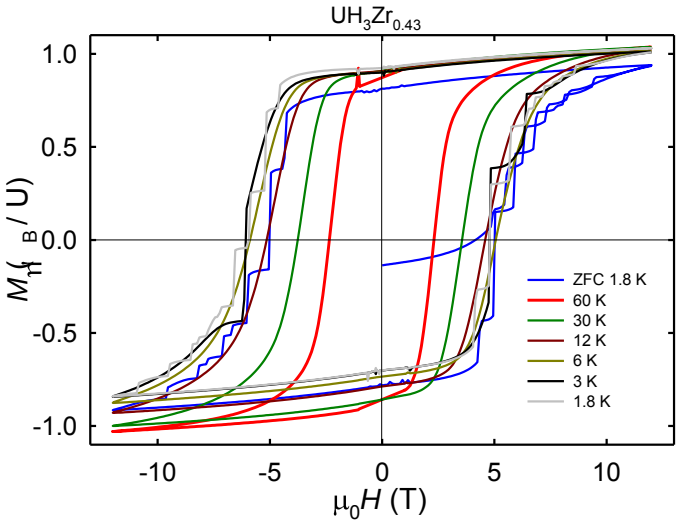

Fig. 3. Hysteresis loops of $UH_3Zr_{0.43}$ measured at various temperatures.

It can be again attributed to the statistical distribution of Zr leading to randomness of easy-magnetization direction.

Our results indicate that interestingly large variability can be achieved for the UH_3 hydrides. The amorphous phase may allow for diverse other dopants tuning magnetic properties. At present we try to dope U by both Mo and Zr.

[1]. I. Tkach, N.-T. H. Kim-Ngan, S. Mašková, M. Dzevenko, L. Havela, A. Warren, C. Stitt, T. Scott, J.Alloys Comp. 534 (2012) 101-109.
[2]. I. Tkach, S. Mašková, Z. Matěj, N.-T. H. Kim-Ngan, A.V. Andreev and L. Havela, Phys. Rev. B 88 (2013) 060407(R).

Dr. Moshe Kuznietz
(1937 - 2006)

This well-known experimentalist in the studies of physics of the Actinides was born in Haifa (Israel) in 1937 and passed away in 2006 at the age of almost 69, having been a long-standing scientist of the Nuclear Research Centre-Negev, in Beer-Sheva (Israel). From the beginning of his pioneering work he had been interested in NMR and neutron diffraction investigations of various uranium materials. After graduating from the Department of Sciences/Physics of the Technion-Israel Institute of Technology in Haifa in 1960, he continued studying and teaching there, through his Ph.D. thesis research entitled “Magnetic properties of uranium hydride” under supervision of Prof. Grunzweig-Genossar. He obtained his Ph.D. degree in 1967. In the same year, he started his post-doctoral appointment at Argonne National Laboratory (Argonne, Illinois, USA) .

He was co-working with Gerry Lander, at present known as an outstanding actinide physicist. They worked together on the magnetic and electronic properties of monopnictides (UPn) and monochalcogenides (UCh) and their solid solutions. Owing to the above studies, these researchers recognized for the first time the complex nature of such solid solutions presenting novel types of magnetic arrangement of uranium moments. This kind of studies he continued in years 1984/85 at the Centre d’Etudes Nucleaires de Grenoble, cooperating also with an already famous rare-earth and actinide physicist, Prof. Jean Rossat-Mignod. They together determined e.g. the most complex magnetic phase diagram (existing in actinides up to date) between UAs and USe using highly precise neutron-diffraction measurements and single crystals of various compositions. Electronic structure of actinide compounds was also his main-interest subject during a one-year stay at the Physics Department of Imperial College in London (England, 1971/72).

His first regular working place as a research scientist was the Soreq Nuclear Research Centre in Yavne (Israel) during the period of 1972-1976 and then the Institute mentioned above in Beer Sheva during years 1976-2006. During that time, his research activities were concentrated on the properties of systems of uranium with transition metals, but especially on their magnetic structures investigated by neutron diffraction in many different solid solutions. Also in those years he worked abroad in many laboratories, as for example at the Laboratoire Leon Brillouin, Centre d’Etudes de Saclay (France, 1991/92), National Research Institute for Metals, Tsukuba (Japan, 1998), the Departamento de Química, Instituto Tecnológico e Nuclear, Sacavém (Portugal, 1998/2000), International Frontier Center for Advanced Materials (IFCAM), Institute for Materials Research (IMR), Tohoku University (Japan, 2003) and he also worked several times, usually for one month, at the Department of Magnetic Investigation of the Institute of Low Temperature and Structure Research of Polish Academy of Sciences, Wrocław (Poland). His interest was always concentrated on magnetic properties of various intermetallic materials containing rare-earth or actinides.

The results of his investigations in Israel and in many laboratories abroad were presented in numerous publications and review articles and on many international conferences. He was also a co-organizer and main-organizer of the 13^{émes} and 32^{émes} Journées des Actinides at Eilat and Ein-Gedi (Israel) in 1983 and 2002, respectively.

Written by his colleague Prof. Robert Troć

Prof. Bernard R. Cooper
(1936-2013)

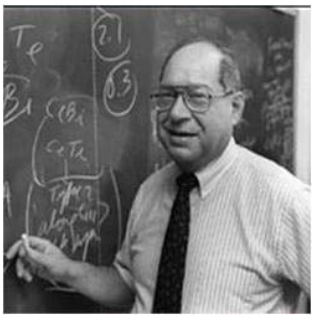

Bernard (Barry) R. Cooper, Claude W. Benedum professor emeritus at West Virginia University, passed away at age 77 on June 10, 2013 in Morgantown, West Virginia. A fellow of the American Physical Society, Barry was a theoretical condensed matter physicist best known for his contributions to the fundamental understanding of the magnetic and electronic properties of transition, rare earth, and actinide metals. He also contributed to early efforts to accurately calculate and predict the properties of materials using first-principles methods.

Barry was born on April 15, 1936 in Everett, Massachusetts. He received his S.B. degree in Physics from MIT in 1957 and his Ph.D. from the University of California – Berkeley in 1961 where we worked with Charles Kittel. After completing his Ph.D., he held positions at the Atomic Energy Research Establishment in Harwell, England, Harvard University, and the General Electric Research Laboratory. During this time his research focused on the magnetic properties of transition and rare earth metals. While at GE he developed a band parameterization scheme using a Green's function method that allowed an efficient calculation of band structures of transition metals. He also developed models that explain the unusual magnetic behavior of antiferromagnets, many of them containing cerium, that have strong magnetic anisotropies (i.e. comparable to the exchange energy).

In 1974 he left General Electric to become the Claude W. Benedum Professor of Physics at West Virginia University. At WVU his research focused on magnetic ordering and associated properties of correlated electron systems as well as the thermo-mechanical properties, phase separation, and interfacial behavior of structural and magnetic metallic systems. Together with investigators at the Los Alamos National Laboratory, in particular John Willis, Barry studied the electronic properties of actinides using ab-initio techniques, specifically working with a full-potential linear muffin-tin orbital method (FPLMTO) that takes into account relativistic effects. One of his major contributions in this field was the development of a band and model Hamiltonian theory for weakly hybridizing *f*-electron systems based on the FPLMTO. This technique has since been used by others in a wide array of ab-initio calculations involving transition metals, rare-earth metals, and actinides where relativistic effects, including spin-orbit coupling, are important.

In collaboration with Willis and other scientists at Los Alamos, he also worked on plutonium, where he was able to calculate its surface electronic structure and explain experimental photoemission data in terms of delta-like surface states. In the field of intermetallic compounds, he developed techniques for calculating bonding energies of carbide-based systems in collaboration with David Price, who later worked at Memphis State University (now University of Memphis). At WVU during the late 1990's and early 2000's he also made contributions to the study of wide-bandgap semiconductors, devising algorithms to determine the role of various types of defects in GaN.

He collaborated closely with Nancy Giles, Larry Halliburton, and Thomas Myers on this project. While at WVU Barry was a champion of the research mission of the University. He initiated and organized (with Gabor Fodor of the WVU Chemistry Department) the Benedum Public Lecture series, the yearly Lakeview Conference on Computational Materials, and played a key role in the early years (1980's and 1990's) of the Experimental Program to Stimulate Competitive Research (EPSCoR) program at WVU.

He was also a mentor to numerous post-doctoral researchers, students, and junior faculty at WVU. Barry was deeply concerned with issues related to social justice and freedom in the world. During the 1970's and 1980's he was an advocate for refusnik scientists from the Soviet Union and for human rights in Asia, Latin America, and Eastern Europe. In an article in Technology Review, written in 1980 with Earl Callen and John Parmentola, he argued that scientists and human rights issues are inextricably linked to each other. He was a member of the executive board of the Committee of Concerned Scientists and chairman of the Committee on International Freedom of Scientists of the American Physical Society. Barry retired in 2003 when his health started deteriorating. Despite this, he continued to collaborate with Ning Ma and Bruce Kang (from the WVU Mechanical and Aerospace Engineering Department) for several years to successfully model the electronic behavior of intermetallic alloys, and co-authored several journal papers between 2003 and 2008.

He was interested in science until the end. As a junior faculty in the WVU Physics Department I had the privilege of working with Barry on several projects. He was a kind and supportive mentor to me. I will miss his intelligence, sense of humor, and most of all his genuine concern for the well-being of myself and the other faculty members, students, staff, and postdocs and their families at WVU.

David Lederman, Physics Today, 2013

Prof. Oscar Vogt
(1927-2014)

On 21st. Jan. 2014 Oscar Vogt left us. Born in 1927, he lived a long and fulfilling life.
One of us (PW) first met Oscar Vogt and his wife Ditta in 1962, when we both investigated in the Laboratorium für Festkörperphysik of ETH Zürich (Swiss Federal Institute of Technology) the magnetic properties of rare-earth compounds. Oscar was a son of the owner of Vogt and Co. (VoCo), a wire-fabrication company, which could also make exotic wires like tungsten. He received his PhD at ETH Zürich with Prof G. Busch, who mentioned that he was the only graduate student not asking for payment. He enjoyed interesting hobbies and was much involved in cultural activities. He engaged himself with great enthusiasm, initially in the research of rareearth compounds, and then later in the actinides. We had a long-lasting and fruitful friendship.
When his father died in the 1970s, Oscar faced a choice – physics or the family business. He managed both! Every Monday he spent in the Institute, and with his competent technical assistant Kurt Mattenberger, grew large and well-defined single crystals of rare-earth compounds and investigated their magnetic properties. The production of crystals was especially challenging as these compounds melt only near 2000 °C, and special tungsten crucibles had to be maintained at constant temperature for long periods.
But what were the scientific questions behind the research on such rare-earth compounds? The ferromagnetism of iron, cobalt and nickel even today is not completely understood. It originates in the partially filled 3*d* electron shells of the atoms, which become in solids partially filled bands. In contrast, the magnetic 4*f* shells of the rare earths are shielded from the valence electrons and they retain their localized, or atomic-like, properties even in solids. The magnetism of these materials has been completely explained by quantum-mechanical rules within the last 30 years, and the results from research at ETH did much to cement this view of 4*f* magnetism. In the 1970s Oscar Vogt became interested in the actinide series and in conversations with Gerry Lander (then at Argonne National Laboratory, USA) started making similar samples to the rare-earth compounds, but with uranium instead of a rare earth.
Experiments on these materials presented a myriad of interesting properties, and did much to show that the light actinides were by no means a simple analogue of the light rare earths. In fact, for uranium, at least, it became clear that a band-structure approach was probably more fruitful – thus placing them with some similarities to systems with 3*d* electrons. During this period Oscar Vogt developed a long friendship with Barry Cooper, a theorist at WVU, and who passed away in June 2013. The two, one an experimentalist, the other a theorist, presented many important papers and Barry was a frequent visitor to Zurich.
It was already suggested that the actinides would *localize* (i.e. become more rare earth like) when more electrons were added to the 5*f* shell (i.e. the transuranium elements), and Oscar looked at this possibility with much interest. However, given the radioactivity present in these materials, an extension of the work at ETH, Zurich was impossible. Oscar then formed a collaboration with the Institute of Transuranium Elements, funded by the European Commission, in Karlsruhe, Germany, and his methods developed at ETH were transferred and applied to the heavier actinides, Np, Pu, and Am.
Again, many different experiments were done on these materials, and, as long as they were well encapsulated, they could even be used at ETH and a number of other places. The results showed the localization of the 5*f* states, but they showed, in addition, that the 5*f* electrons interact with the conduction electrons, and this has a strong influence on the magnetic properties.
Oscar Vogt published at least 500 papers as author or co-author, together with book chapters and reviews.
But Oscar Vogt was still, principally, the technical director of his wire-fabrication company. When the high T_c superconductors with critical temperatures up to about 136K were discovered, the question of producing superconducting wire was of great importance. And a wire factory was available! Oscar was rapidly motivated to produce superconducting wires in his factory, and he was the first in the world to produce a 1km long such wire. A graduate student was always at international conferences with rolls of silver wire filled with superconductors, whereas competitors only had 10cm long wires.
So Oscar had a rich scientific life; at home his wife Ditta made invitations a real sensation. Ditta, his children and grandchildren will miss him as husband, father and grandfather.

Peter Wachter, ETH Zürich
Gerry Lander, Argonne National Laboratory & ITU, Karlsruhe

Adamska Anna	am.adamska@bristol.ac.uk	*University of Bristol, United Kingdom*
Almog Yossi	almog@mail.huji.ac.il	*Hebrew University of Jerusalem, Israel*
Andreev V Alexander	a.andreev@seznam.cz	*Institute of Physics, AVCR, Czech Republic*
Andreeva Liudmila	a.andreev@seznam.cz	*Prague, Czech Republic*
Argaman Nathan	argaman@mailaps.org	*NRCN, Israel*
Avila Miguel	miguelavila_arg@yahoo.com.ar	*Argentina*
Baker Robert	bakerrj@tcd.ie	*Trinity College, Dublin, Ireland*
Banos Antonis	ab13306@bristol.ac.uk	*University of Bristol, United Kingdom*
Batrice Rami	batricer@gmail.com	*Technion - Israel Institute of Technology, Israel*
Bednarchuk Oleksandr	O.Bednarchuk@int.pan.wroc.pl	*Institute of Low Temperature and Structure Research, Poland*
Beeri Ofer	ofer.beeri@gmail.com	*Ben Gurion University, Israel*
Berkovits Dan	berkova@soreq.gov.il	*Soreq NRC, Israel*
Bouchet Johann	johann.bouchet@cea.fr	*CEA, France*
Boukobza Erez	erezbou@gmail.com	*NRCN, Israel*
Bram Avraham	avrambram@gmail.com	*Ben Gurion University, Israel*
Brincat Nick	n.brincat@bath.ac.uk	*University of Bath, United Kingdom*
Broide Amir	broide@post.bgu.ac.il	*NRCN, Israel*
Caciuffo Roberto	roberto.caciuffo@ec.europa.eu	*Institute for Transuranium Elements, Germany*
Caspi El‘ad	caspie@nrcn.org.il	*NRCN, Israel*
Chorev Shaul		*Israel Atomic Energy Commission, Israel*
Cohen Dror	dror@post.bgu.ac.il	*Ben Gurion University, Israel*
Colineau Eric	eric.colineau@ec.europa.eu	*Institute for Transuranium Elements, Germany*
Dadon Shay	shay_d5@walla.co.il	*NRCN, Israel*
Danieli David		*Israel Atomic Energy Commission, Israel*
Dolgin Bella	dbella9@gmail.com	*NRCN, Israel*
Dubi Chen	chendb331@gmail.com	*NRCN, Israel*
Edelstein Norman	nmedelstein@lbl.gov	*Lawrence Berkeley National Lab, USA*
Eidelstein Eitan	eitan.eidelstein@gmail.com	*NRCN, Israel*
Eisen Moris	chmoris@tx.technion.ac.il	*Technion - Israel Institute of Technology, Israel*
Ettedgui Hanania	hananiae@hotmail.com	*NRCN, Israel*
Fabrice Wilhelm	wilhelm@esrf.eu	*ESRF, France*
Filanovich Anton	a.n.filanovich@urfu.ru	*Ural Federal University, Russia*
Friedman Moshe	moshe.friedman@mail.huji.ac.il	*Hebrew University of Jerusalem, Israel*
Furman David	sirok4@gmail.com	*NRCN, Israel*
Gal Joseph	jgal@bgu.ac.il	*Nano Institute Ben Gurion University, Israel*
Geeson David	jeremy.allard@awe.co.uk	*AWE, United Kingdom*
Genossar Jan	phr08jg@techunix.technion.ac.il	*Technion,, Israel*
Glam Benny	glam@soreq.gov.il	*Soreq NRC, Israel*
Gonçalves António Pereira	apg@ctn.ist.utl.pt	*Instituto Superior Técnico, Universidade de Lisboa, Portugal*
Gorbunov Denis	gorbunov@fzu.cz	*Institute of Physics, AVCR, Czech Republic*
Gouder Thomas	thomas.gouder@ec.europa.eu	*Institute for Transuranium Elements, Germany*
Gumeniuk Roman	gumeniuk@cpfs.mpg.de	*Max Planck Institut, Germany*
Halevy Dotan	halevyi@caltech.edu	*TCB, Israel*
Halevy Itzhak	halevyi@caltech.edu	*NRCN, Israel*
Hallam Keith	k.r.hallam@bristol.ac.uk	*University of Bristol, United Kingdom*
Hambsch Franz-Josef	franz-josef.hambsch@ec.europa.eu	*Institute for Reference Materials and Measurements, Belgium*
Haquin Gustavo	gustavo@soreq.gov.il	*Soreq NRC, Israel*
Harker Robert	robert.harker@awe.co.uk	*AWE, United Kingdom*
Hen Amir	amir.hen@mail.huji.ac.il	*Institute for Transuranium Elements, Germany*
Hen Or	or.chen@mail.huji.ac.il	*Tel-Aviv University, Israel*
Henriques Margarida	mish@ctn.ist.utl.pt	*University of Lisbon, Portugal*
Hiess Arno	arno.hiess@esss.se	*ESS AB, Sweden*
Izosimov Igor	izig@mail.ru	*Joint Institute for Nuclear Research, Russia*
Kaczorowski Dariusz	D.Kaczorowski@int.pan.wroc.pl	*Institute of Low Temperature and Structure Research, Poland*

Karmel Isabell Sarah	karmel@tx.technion.ac.il	*Technion, Israel*
Karpas Zeev	zeevkar44@gmail.com	*NRCN, Israel*
Kessel Ronit	ronit.kessel@mail.huji.ac.il	*Hebrew University of Jerusalem, Israel*
Kimmel Giora	kimmel@bgu.ac.il	*Ben Gurion University, Israel*
Kochavi Eiran	eranc@nrcn.org.il	*NRCN, Israel*
Kogan Anna	annak@bgu.ac.il	*NRCN, Israel*
Landau Alex	landaho@post.bgu.ac.il	*NRCN, Israel*
Landau Peri	landperi@gmail.com	*NRCN, Israel*
Lander Gerard	lander@ill.fr	*Institute for Transuranium Elements, Germany*
Levin Orit		*Ben Gurion University, Israel*
Levy Ohad	lohad@bgu.ac.il	*NRCN, Israel*
Ling Michael	michael.ling@awe.co.uk	*AWE, United Kingdom*
Lipkina Ksenia	ksenia.lipkina@gmail.com	*A.A. Bochvar Institute, Russia*
Livneh Tsachi	t.livneh@nrcn.org.il	*NRCN, Israel*
Makov Guy	makovg@bgu.ac.il	*Ben Gurion University, Israel*
Maltsev Dmitry	d.s.maltsev@gmail.com	*Ural Federal University, Russia*
Maskova Silvie	maskova@mag.mff.cuni.cz	*Charles University, Czech Republic*
May-Tal Beck Sharon	smtbeck@gmail.com	*NRCN, Israel*
Melchakov Stanislav	s.yu.melchakov@gmail.com	*Ural Federal University, Russia*
Melchior Aviva	avimel@gmail.com	*NRCN, Israel*
Meyer Karsten	karsten.meyer@fau.de	*Friedrich-Alexander University Erlangen – Nürnberg, Germany*
Ocherashvili Aharon	ocherash@bezeqint.net	*NRCN, Israel*
Oppeneer Peter	peter.oppeneer@physics.uu.se	*Uppsala University, Sweden*
Orion Itzhak	iorion@bgu.ac.il	*Ben Gurion University, Israel*
Oskina Varvara	v.a.oskina@gmail.com	*Ural Federal University, Russia*
Pasturel Mathieu	mathieu.pasturel@univ-rennes1.fr	*Institut des Sciences Chimiques de Rennes, France*
Paukov Mykhaylo	Michael.Paukov@gmail.com	*Charles University, Czech Republic*
Popescu Ioana-Carmen	janepopescu@gmail.com	*R&D National Institute for Metals and Radioactive Resources, Romania*
Povzner Alexander	a.a.povzner@urfu.ru	*Ural Federal University, Russia*
Rafailov Gennady	grafailov@gmail.com	*NRCN, Israel*
Raison Philippe	Philippe.raison@ec.europa.eu	*European Commission, Germany*
Reiffers Marian	reiffers@unipo.sk	*Presov University, Slovakia*
Salem Ran	ran.salem@gmail.com	*NRCN, Israel*
Samsel-Czekala Malgorzata	m.samsel@int.pan.wroc.pl	*Institute of Low Temperature and Structure Research, Poland*
Savchenko Aleksei	sav-alex111@mail.ru	*A.A. Bochvar Institute, Russia*
Schweke Danielle	daniela.schweke@gmail.com	*NRCN, Israel*
Sechovsky Vladimir	sech@mag.mff.cuni.cz	*Charles University, Czech Republic*
Shamir Noah	noah.shamir@gmail.com	*NRCN, Israel*
Sharon Avi	asharon68@gmail.com	*NRCN, Israel*
Shick Alexander	shick@fzu.cz	*Institute of Physics, AVCR, Czech Republic*
Shor Asher	shor@soreq.gov.il	*Soreq NRC, Israel*
Snir Yoav	snirys@gmail.com	*NRCN, Israel*
Tereshina Evgeniya	teresh@fzu.cz	*Institute of Physics, AVCR, Czech Republic*
Tiferet Eitan	tiferete@gmail.com	*NRCN, Israel*
Troc Robert	r.troc@int.pan.wroc.pl	*Institute of Low Temperature and Structure Research, Poland*
Venkert Arie	venkert@gmail.com	*NRCN, Israel*
Volkovich Vladimir	volkovich@dpt.ustu.ru	*Ural Federal University, Russia*
Yaar Ilan	ilany@energy.gov.il	*Israel Ministry of National Infrastructures, Energy & Water Resources, Israel*
Yahel Eyal	eyalyahel@hotmail.com	*NRCN, Israel*
Zalkind Shimon	s_zalkind@yahoo.com	*NRCN, Israel*
Zeiri Yehuda	yehuda.zeiri@gmail.com	*NRCN, Israel*
Zilbermann Israel	israelz2003@gmail.com	*NRCN, Israel*